

Cover Page



Universiteit Leiden



The handle <http://hdl.handle.net/1887/62351> holds various files of this Leiden University dissertation.

Author: Stammes, M.A.

Title: Multimodal image-guided interventions using oncological biomarkers

Issue Date: 2018-05-22

**Multimodal image-guided interventions using
oncological biomarkers**

Marieke A. Stammes

Multimodal image-guided interventions using oncological biomarkers

© M.A. Stammes, 2018, Leiden, the Netherlands. All rights reserved. No parts of this thesis may be reproduced, distributed, stored in a retrieval system or transmitted in any forms or by any means without prior written permission of the author.

ISBN: 978-90-9030924-8

Lay-out by: M.A. Stammes

Printing by: ProefschriftMaken || www.proefschriftmaken.nl

Cover photo/artwork by: M.A. Stammes

The research described in this thesis was financially supported by the project grant H2020-MSCA-RISE grant number 644373 – PRISAR, the European Union Seventh Framework Programme FP7-PEOPLE-2013-IAPP grant number 612360 – BRAINPATH, the Center for Translational Molecular Medicine: 03O-202 MUSIS, the European Research Council (ERC) through an ERC Advanced Grant grant number 323105-SURVive and a TI Pharma project number D4-603 - IMMUNOCOLOURS.

Financial support by the department of Radiology of the Leiden University Medical Center and iThera Medical GmbH for printing of this thesis was gratefully acknowledged.

**Multimodal image-guided interventions using
oncological biomarkers**

Proefschrift

ter verkrijging van
de graad van Doctor aan de Universiteit Leiden,
op gezag van Rector Magnificus prof.mr. C.J.J.M. Stolker,
volgens besluit van het College voor Promoties
te verdedigen op dinsdag 22 mei 2018
klokke 11.15 uur
door

Marieke Alice Stammes

geboren op 25 januari 1986

te Alkmaar

Promotor	Prof. dr. L.F. de Geus-Oei
Co-promotores	Dr. A.L. Vahrmeijer Dr. L.J. Cruz-Ricondo
Promotiecommissie	Prof. dr. C.A.M. Marijnen Prof. dr. F. Alves (Max Planck Institut & Universitätsmedizin Göttingen, Göttingen, DE) Prof. dr. M.A. van Buchem Prof. dr. ir. M. de Jong (Erasmus MC, Rotterdam) Prof. dr. A.C. Perkins (University of Nottingham, Nottingham, UK) Prof. dr. C.J.H. van de Velde

Patience is wisdom

Table of Contents

Chapter 1	General introduction and outline	9
-----------	----------------------------------	---

Part I – Image-guided Surgery

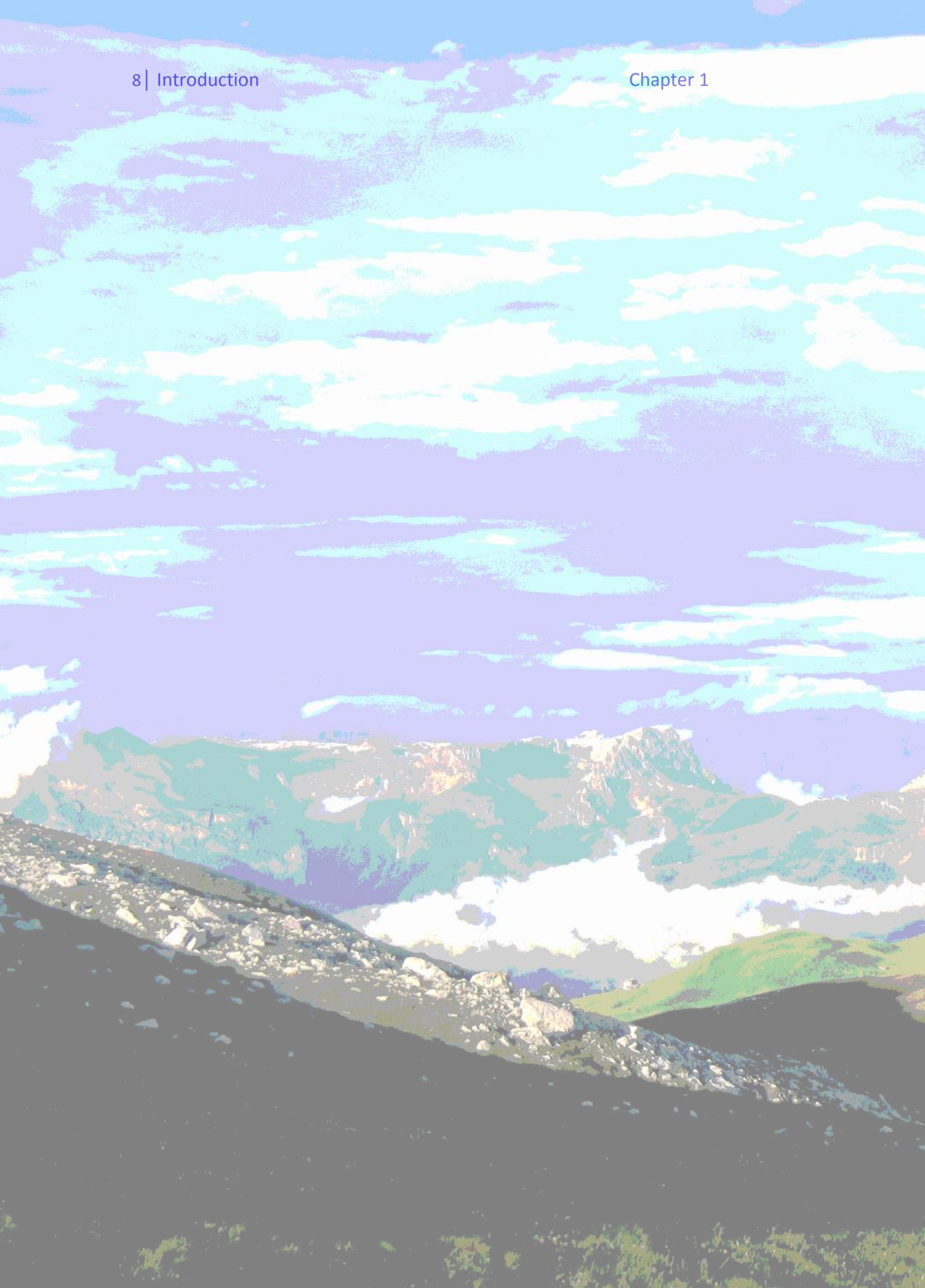
Chapter 2	Modalities for image- and molecular-guided cancer surgery	27
Chapter 3	Evaluation of EphA2 and EphB4 as targets for image-guided colorectal cancer surgery	57
Chapter 4	Fluorescence- and multispectral optoacoustic imaging for an optimised detection of deeply located tumors in an orthotopic mouse model of pancreatic carcinoma	73

Part II – Necrosis Imaging

Chapter 5	Necrosis avid near infrared fluorescent cyanines for imaging cell death and their use to monitor therapeutic efficacy in mouse tumor models	103
Chapter 6	Pre-clinical evaluation of a cyanine based SPECT probe for multimodal tumor necrosis imaging	133
Chapter 7	The necrosis-avid small molecule HQ4-DTPA as a multimodal imaging agent for monitoring radiation therapy-induced tumor cell death	159
Chapter 8	General discussion, summary, and future perspectives	183

Appendices

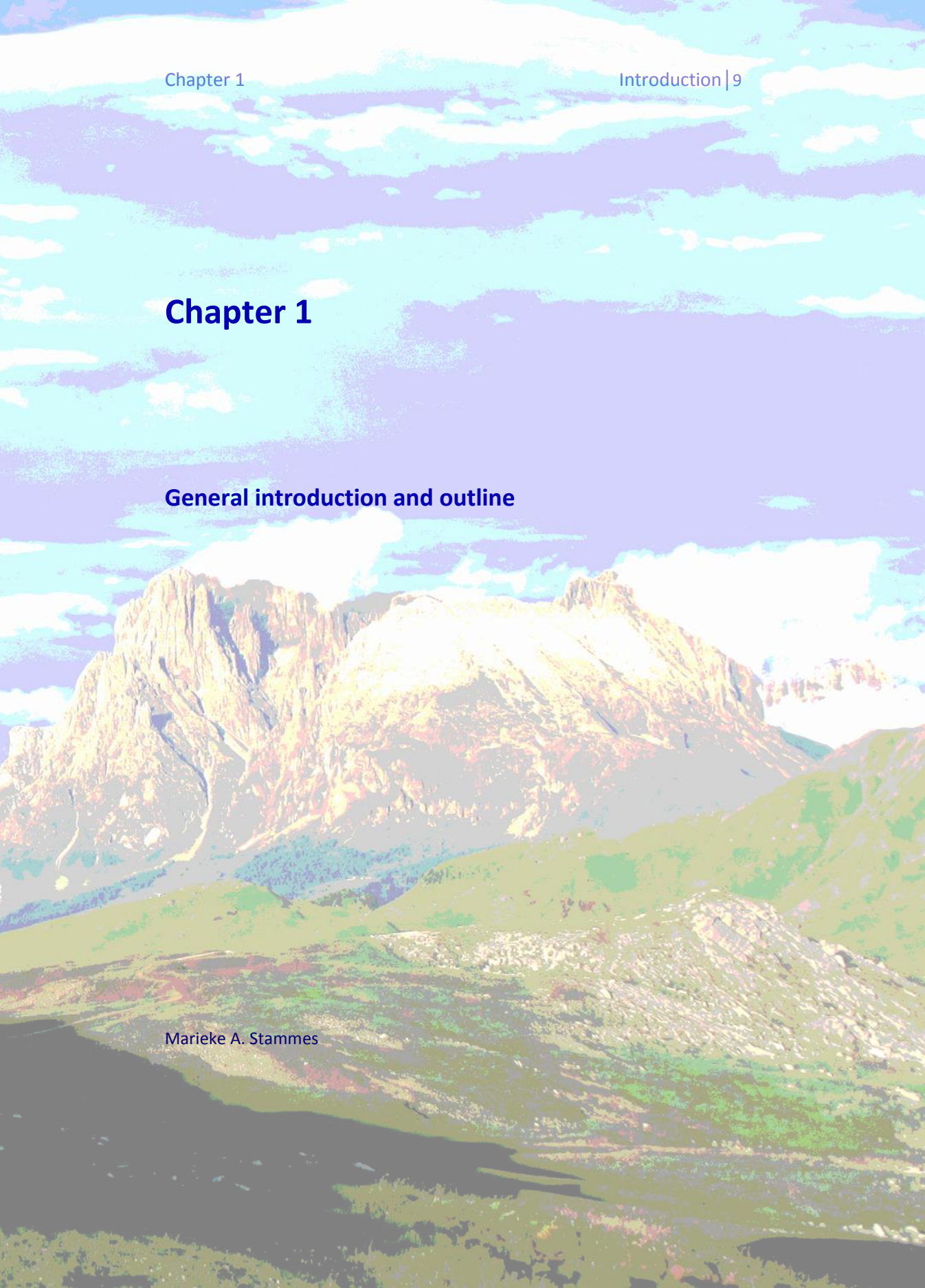
Nederlandse Samenvatting	203
List of Abbreviations	209
Curriculum Vitae	213
List of Publications & Conference Abstracts	215
Dankwoord	219



Chapter 1

General introduction and outline

Marieke A. Stammes

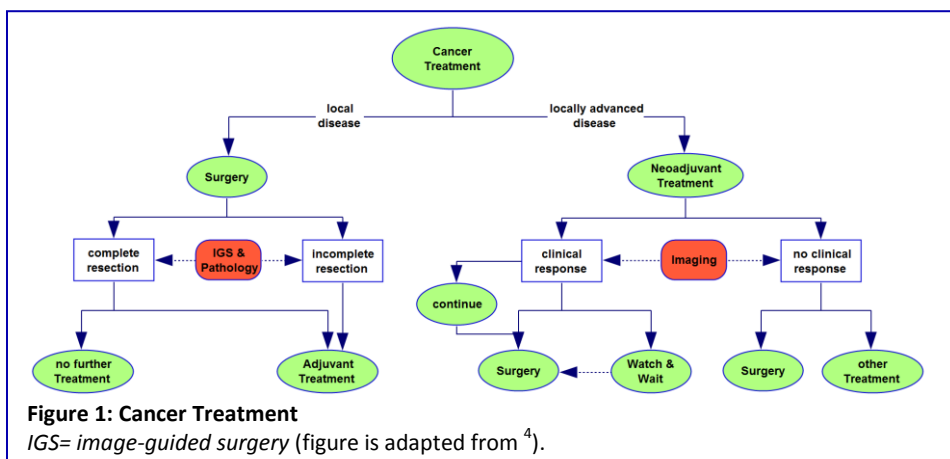


General introduction

Cancer is one of the leading causes of mortality worldwide, with around 14 million new cases in 2012 ¹. It is expected that this number will increase up to 20 million around 2025, which means that the cumulative risk factor of people who will be afflicted with a form of cancer, which is now already 18.5%, will increase further over the upcoming years. The common goal of many research institutes around the world is to decrease the cancer related morbidity and mortality rate ^{1,2}.

Cancer biology

Cancer can be defined as the rapid creation of abnormal cells that have the ability to divide and grow uncontrollably beyond their usual boundaries, after which they can spread and invade in other organs ³. Although this definition is clear, a tumor is more complex than a mass of proliferating cancer cells. It is a heterogeneous and complex disease regulated by genomic alterations. The complexity is due to the different locations and number of alterations or mutations between cancer types and between patients with the same type of cancer. Some mutations will create oncogenes which will work in favor of the tumor and others will lead to a loss of function of tumor suppressor genes. In addition, the transformation from a normal cellular environment into a malignant tumor environment, tumorigenesis, is a multi-step process. This process is reflected by genetic alterations in the regulatory circuits of cells which normally would maintain homeostasis. Although a lot of processes are involved, some molecular, biochemical, and cellular characteristics are shared by most tumors. Those alterations are rationalized by the well-known cancer hallmarks as described by Hanahan and Weinberg ^{6,7}. Unfortunately,



nowadays, these molecular alterations do not play a major role in the treatment decision process.

Cancer treatment

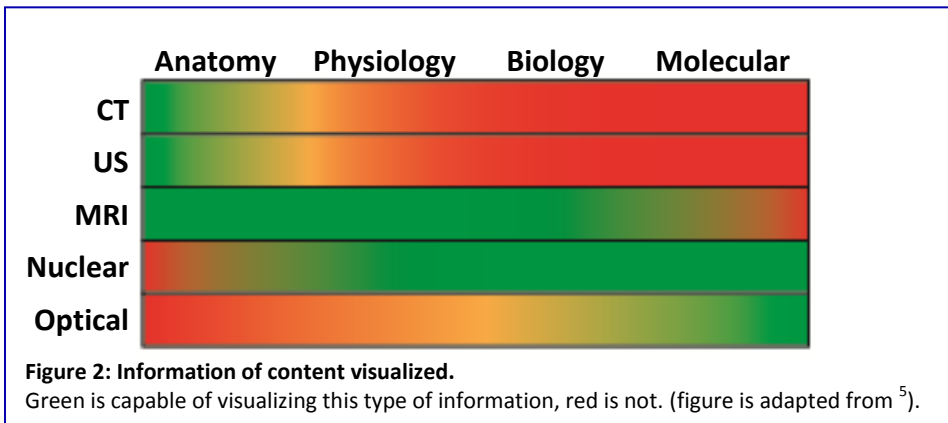
There is no doubt that cancer will remain a significant healthcare problem for the years to come. Fortunately, early diagnosis and improvements in therapy, including neo-adjuvant treatments, have led to serious improvements in survival rates and quality of life. However, due to the fact that there are more survivors, there is also an increase in late toxic side effects which will influence the quality of life in a negative manner^{8,9}. Surgical interventions, systemic treatments and radiotherapy or a combination thereof, are the main treatment modalities for cancer¹⁰. Whenever possible, surgery is the first choice to treat localized disease (**Figure 1**)^{4,11}. In case of locally advanced disease, patients can be offered neo-adjuvant treatment before surgery (as shown in **Figure 1**). The goal of this therapy is to reduce tumor invasion and size of the primary tumor allowing radical or more organ sparing surgery and to improve locoregional disease control^{12,13}.

Cancer research

Imaging

With the aim of improving the clinical outcome of cancer patients, cancer research is directed towards developing personalized and targeted treatments to increase the specificity in eradicating the cancer cells and sparing healthy tissue¹⁰. Diagnosis, staging and treatment planning are determined by several techniques, and imaging is indispensable to provide information about the tumor biology and anatomical structures. Frequently used imaging modalities to gain information about the anatomical structures involved are computed tomography (CT), magnetic resonance imaging (MRI), ultrasound (US) and conventional radiography. Although anatomical imaging provides information about tumor morphology, it does not always give functional information about the tumor. Molecular imaging techniques can provide valuable functional information. In general, with molecular imaging it is possible to non-invasively visualize, characterize and measure biological processes of the tumor and the tumor micro-environment at a molecular level¹⁴. The most well-known and clinical used molecular imaging techniques are single photon emission tomography (SPECT) and positron emission tomography (PET).

For intra-operative imaging, the use of optical imaging is gaining interest and



is nowadays widely used in both clinical and pre-clinical research ¹⁵. The additional value of near-infrared fluorescence in the range of 700-900 nm over lower wavelength fluorescence is a higher tissue penetration of up to a centimeter and low auto fluorescence ¹⁶. The drawbacks are the lack of whole body overview and still the limited penetration depth. Therefore, combining techniques like optical and nuclear imaging can have synergistic effects (**Figure 2**). The same is true for the introduction of PET-CT as hybrid imaging modality. Both single modalities, PET as molecular modality and CT as morphological modality, lack the requirements for an accurate and complete *in vivo* assessment. However, together providing anatomical, physiological, biological and molecular information this problem will be solved ^{5,15}. The specifications of several imaging techniques and the use of hybrid techniques are discussed more in depth in **Chapter 2**.

Targets

For molecular imaging the use of a-specific contrast agent the so-called molecular imaging agent is required as the goal is to assess the expression or function of a dedicated molecular target ^{14,17}. There are two main approaches of developing a targeting agent by conjugation or by structure-mimicking. The first is the most widely used method in which a contrast agent consists out of a targeting moiety associated with the molecule of interest, a contrast-enhancing agent dependent on the type of imaging modality and a linker to connect those two parts. The other approach is to chemically modify a molecule that naturally interacts with the molecule of interest. With this approach a targeting moiety can directly be converted in a contrast agent ¹⁸.

Using a targeted contrast agent is called active targeting, however, passive targeting is also possible via the enhanced permeability and retention effect (EPR) by which molecules leak into the tumor¹⁹. The drawback of passive targeting in combination with surgery is that the targeting is a-specific and, as discriminating the boundary of a tumor is essential during surgery, agents that leak into the core of the tumor are not the best candidates¹⁹⁻²¹.

In general, targets can be divided in a genetic and a mechanistic class. The first represents genes or gene products that carry mutations or that lead to a higher disease risk. In our genome, which consists out of 25.000 genes, around 1800 genes are involved in diseases such as cancer. This means, including post-translational modifications, over 40.000 different proteins are available as possible target²². The second class of targets consists of receptors and enzymes which are, in general, not different from the normal population, they do not have any mutation. However, biological observations detected that their behavior differs from a normal situation. This suggests that they might be involved in a tumor process and by this be an interesting target^{21,23}. When an interesting target is found, an agent is developed towards a binding pocket in the target of interest and, when necessary, afterwards modified to enhance the pharmacokinetics and pharmacodynamics before it could be used as targeted contrast agent²⁴.

The general aim of this thesis is double, first to improve image-guided surgery (IGS) via innovative imaging modalities in combination with targeted contrast agents which will lead to improved intra-operative visualization of resection margins during surgery. Second, for patients who undergo neo-adjuvant therapy, the aim is to ameliorate treatment response monitoring already in an early stage after start of treatment. Therefore, the second part of this thesis will focus on detecting the amount of necrosis, as biomarker, after chemotherapy and/or radiotherapy. The background information of each part is separately discussed below, followed by an overview of the content of the chapters.

Part I: Image-guided Surgery

As mentioned above multiple imaging modalities have proven to be essential for cancer diagnostics, providing much information about the tumor before surgery^{25,26}. However, during surgery, when the anatomy changes due to manipulation, the surgeon relies on palpation and visual inspection to accurately determine whether the resection margins are tumor free²⁷⁻²⁹. In oncologic surgery, clean and clear demarcation of the tumor boundaries is essential for proper removal of the tumor. There is a fine balance between achieving tumor free resection margins and sparing healthy tissue and organ function. Therefore, visualization of the tumor borders with a high sensitivity is essential for an optimal and safe removal of the cancer lesion^{30,31}. The eyes and hands of a surgeon are useful, but cannot determine the boundaries of a tumor at a microscopic level²⁹. Therefore, the risk remains of an irradical resection of the tumor, also known as an R1 resection. For instance, in breast cancer patients, undergoing breast sparing surgery, the percentage of R1 resections is around 20%^{27,28,32,33}. To improve cure rates, it is important to decrease local recurrence rates as well as complication rates. To reach this goal, intra-operative assistance, using additional visualization tools could be helpful. Nowadays, during oncologic surgery intra-operative ultrasound or x-ray fluoroscopy are the only two modalities which provide real-time visualization. Drawbacks of these modalities are the necessity of direct contact with the body, the use of ionizing radiation and the current lack of availability of targeted contrast agents²⁷. The details about the imaging systems are discussed more in depth in **Chapter 2**.

Up to now, in clinical trials, tumor specific optical IGS is already performed with several agents, such as 5-ALA for gliomas³⁴, folate-near infrared (NIR) fluorophore for ovarian cancer^{35,36} and bevacizumab-IRDye800CW (in combination with hyperthermic intra-peritoneal chemotherapy (HIPEC)) for peritoneal carcinomatosis³⁷. Results obtained from these trials are two-sided with promising results and hurdles which need to be overcome for a broader clinical implementation. These studies demonstrated that fluorescence imaging did not interfere with the standard surgical procedure, showed real-time identification of the tumor and was able to reduce overtreatment, due to a higher number of R0 resections. The two main problems encountered are the high amount of false-positive findings of lymph nodes in particular and the limited penetration depth of optical imaging^{34,35,37,38}. For the development of new IGS approaches, there is a need for dedicated targeted contrast agents

with high tissue specificity and a high tumor to background ratio (TBR) for a more detailed visualization of the tumor (**Chapter 3**) in combination with alternative imaging modalities (**Chapter 2 & 4**)^{19,28}.

Part II: Necrosis Imaging

Treatment evaluation

Most systemic anticancer therapies are effective only for a subgroup of patients. Unfortunately, up to now there are only limited possibilities to stratify patients for specific treatments. Therefore, it is difficult to predict upfront which patient will benefit from a certain treatment and which one will not³⁹. Currently, the treatment regimen is based on population based statistics, which have limited value for the individual patient. Evaluation of the treatment is nowadays generally based on measuring tumor shrinkage at a late stage during and after treatment mostly based on the RECIST criteria; Response Evaluation Criteria in Solid Tumors. Those criteria are generally used as end points in clinical trials or for routine clinical decision making in order to decide to stop, continue or switch to another treatment⁴⁰⁻⁴². Nevertheless, monitoring the anti-cancer efficacy of a therapy at an early stage of treatment would have multiple advantages³⁹. Existing methods for the determination of tumor markers in blood lack the accuracy for a broad routine application for treatment response monitoring^{43,44}. Early evaluation of the therapy efficacy would facilitate the growing interest for individualized cancer treatment, allowing the clinician to adjust the therapy based on tumor response and might result in improved survival rates, quality of life and cost-efficacy^{45,46}.

As discussed above, morphologic changes often can only be detected several weeks to months after the start of treatment. Functional and molecular alterations, on the other hand, occur much faster, already in the first weeks after start of treatment. Most of those molecular alterations are in a way related to restoring homeostasis and creating cell death. For this reason cell death is a biological process which can also be used as biomarker of tumor response in the treatment of cancer patients^{39,47}.

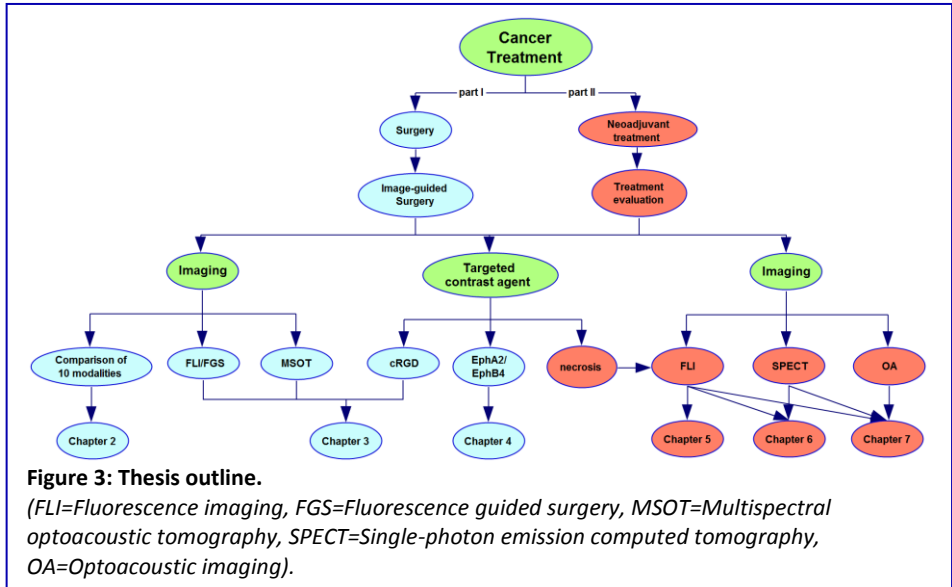
Cell death

Cell death is a process that is reversible until the first irreversible step is made. Different steps could represent this phase but a cell is considered death when

the cell has lost its membrane integrity, undergone complete fragmentation and when the cell corpse is engulfed by an adjacent cell. This diversity leads to a high variety of types of cell death which are classified according to its morphology, enzyme involvement, functional aspects and immunological characteristics⁴⁸. Nevertheless, it is possible to narrow it down to the two fundamental and most well-known types of cell death; apoptosis and necrosis^{39,45,48,49}. In general, apoptosis is required to maintain homeostasis and the main mechanism by which cells die in the human body^{39,49}. Necrosis is the result of metabolic failure and usually occurs in response to acute hypoxic or ischemic injury⁴⁹. Based on the facts above, it implies that the process of cell death in apoptosis and necrosis are clearly distinct from each other. However, when the number of cells in apoptosis is too high for the phagocytes to eradicate them, this will lead to secondary necrosis. Secondary necrosis is also a form of necrosis, although the dying mechanism is still regulated by apoptosis⁵⁰.

In part II of this thesis, the value of intra-tumor necrosis, as unique biomarker, is investigated. Necrosis is used to monitor the anti-cancer efficacy of a treatment at an early stage after start of treatment. Necrotic cell death plays a prominent role in multiple pathological and physiological disorders; especially in cancer as tumor necrosis is associated with tumor aggressiveness and negatively correlated with disease prognosis⁵¹⁻⁵³.

Chapter overview



In **Figure 3** a graphical overview of the thesis is visualized, when comparing this figure to **Figure 1** a close comparison can be found between a cancer treatment and this thesis.

In **Chapter 2**, an overview is provided of the state of the art imaging modalities which can be used intra-operatively. Next to the imaging modalities, mentioned in this thesis, several applications of molecularly IGS will be discussed. The image quality of most of these techniques can be improved by using a dedicated contrast agent. Targets upregulated at the cell surface, abundantly present on tumor cells and absent on surrounding healthy cells are the best candidates to be used for IGS.

In **Chapter 3**, two proteins, the transmembrane receptor tyrosine kinase EphA2 and EphB4, are evaluated as possible targets for IGS in colorectal cancer on a tissue microarray. In this chapter, EphA2 is derived from the National Cancer Institute (NCI) prioritization list and is known to be highly overexpressed on a high variety of tumor types, including colorectal cancer. EphA2 is compared to the family member EphB4 from another class²¹. EphB4, a member of the B class of the same family is upregulated in many solid tumors. However, for both EphA2 and EphB4 their expression in healthy tissue has not been investigated. In this chapter, the TBR of both proteins will be

determined and discussed whether EphA2 and EphB4 are valuable candidates for IGS⁵⁴⁻⁵⁶.

In **Chapter 4** the additional value of a new imaging modality, multispectral optoacoustic tomography (MSOT) is assessed. MSOT uses light as a source and acoustics for signal detection to create images which enables the visualization of optical absorbing agents at a high resolution similar to optical imaging. However, the main advantage of MSOT compared to optical imaging is the accurate spatial localization within deep tissue since the detection is not limited by photon scattering enabling a higher depth penetration^{57,58}. In this chapter, the additional value of MSOT is compared to a couple existing fluorescence imaging modalities. The value and the results obtained with MSOT and the other modalities are validated both *in* and *ex vivo* by using an orthotopic pancreatic ductal adenocarcinoma (PDAC) mouse model targeted by cRGD in combination with the fluorescent dye IRDye800CW⁵⁹⁻⁶¹.

The second part of the thesis will focus on different imaging techniques to visualize tumor necrosis.

In **Chapter 5**, two novel optical necrosis avid contrast agents, IRDye800CW and HQ5 are identified and evaluated. Those contrast agents both belong to the group of carboxylated cyanine dyes which are in general mentioned as non-reactive and control compounds. In addition, IRDye800CW and HQ5 both belong to the group of near-infrared dyes. Their necrosis avidity is validated *in vitro* and *in vivo* in mouse breast cancer tumor models of spontaneous necrosis or necrosis induced by chemotherapy.

In **Chapter 6**, one of the family members of HQ5, HQ4, is equipped with a radioactive moiety to facilitate the clinical translation in the future. Near-infrared dyes have a tissue penetration of up to a centimeter. However, a tissue penetration of one centimeter still limits a broad clinical application. By using radioactivity the penetration depth is unlimited. In addition, with the use of radioactivity, quantitative biodistribution studies were performed to get more insight in the behavior of the agent.

In **Chapter 7**, the knowledge gained in the previous two chapters is further extrapolated by evaluating HQ4 for monitoring tumor cell death induced by radiation therapy in a clinically relevant MCF-7 human breast cancer mouse model. Furthermore, the multimodal imaging properties of the necrosis avid contrast agent were assessed with the addition of a third imaging modality, optoacoustic or photoacoustic imaging. Optoacoustic imaging is similar to MSOT with the only difference that MSOT uses a multispectral illumination

approach in order to differentiate even more specific spectral signatures of exogenous or endogenous contrast agents⁶². This modality is tested because it has the benefit of a higher tissue penetration as compared to optical imaging and it overcomes the drawbacks associated with the use of ionizing radiation.

Finally, in **Chapter 8** a general discussion is provided, including a summary and the future perspectives of multimodal image-guided interventions are addressed.

References

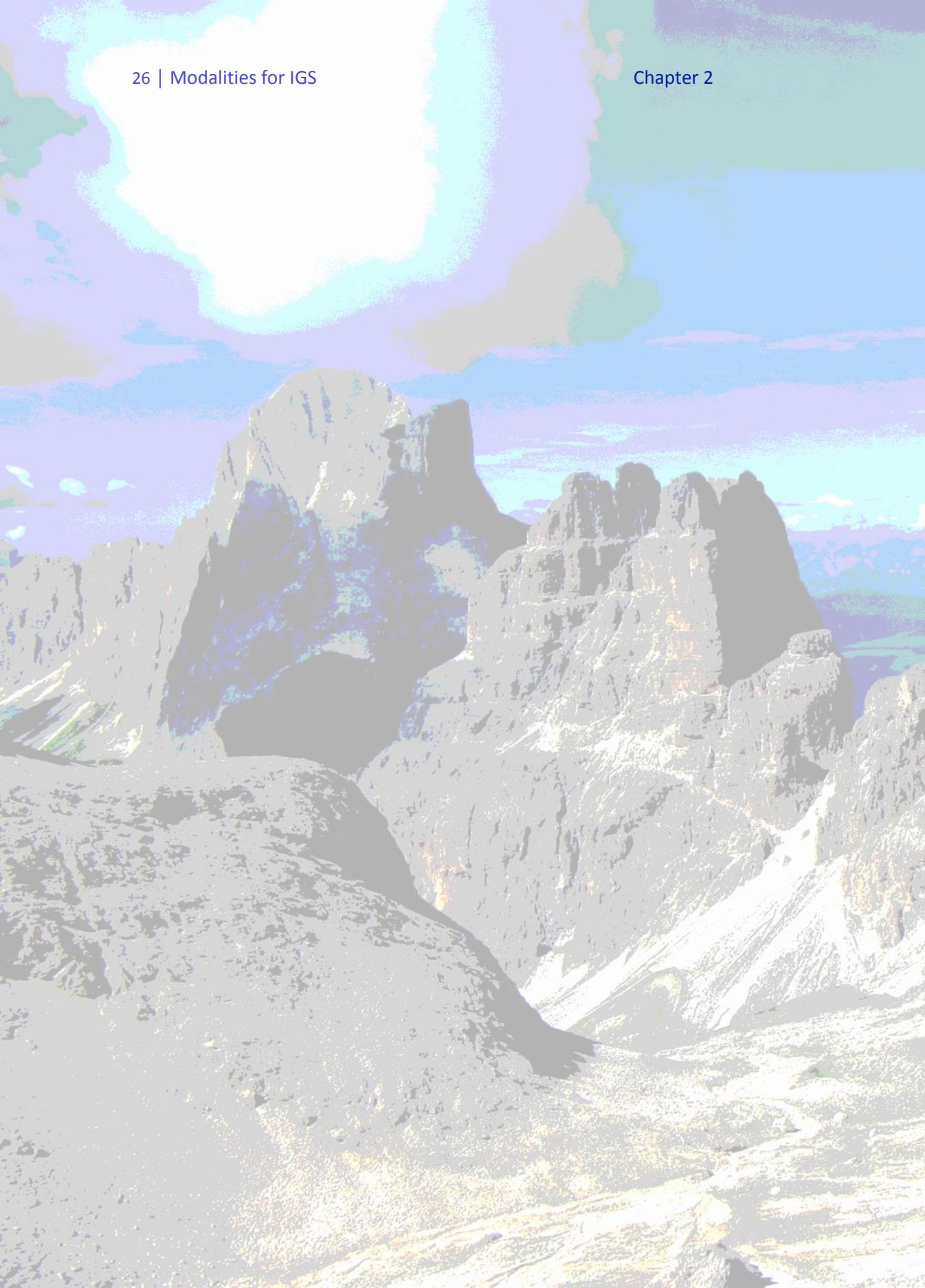
1. Ferlay J, Soerjomataram I, Dikshit R, et al. Cancer incidence and mortality worldwide: sources, methods and major patterns in GLOBOCAN 2012. *Int J Cancer*. 2015;136(5):E359-386.
2. van de Loo JW, Trzaska D, Berkouk K, Vidal M, Draghia-Akli R. Emphasising the European Union's Commitment to Cancer Research: a helicopter view of the Seventh Framework Programme for Research and Technological Development. *Oncologist*. 2012;17(10):e26-32.
3. Cancer - Fact sheet. <http://www.who.int/mediacentre/factsheets/fs297/en/>. Accessed January 2017.
4. Kummel S, Holtschmidt J, Loibl S. Surgical treatment of primary breast cancer in the neoadjuvant setting. *Br J Surg*. 2014;101(8):912-924.
5. Weissleder R, Mahmood U. Molecular imaging. *Radiology*. 2001;219(2):316-333.
6. Hanahan D, Weinberg RA. Hallmarks of cancer: the next generation. *Cell*. 2011;144(5):646-674.
7. Hanahan D, Weinberg RA. The hallmarks of cancer. *Cell*. 2000;100(1):57-70.
8. Drury A, Payne S, Brady AM. Cancer survivorship: Advancing the concept in the context of colorectal cancer. *Eur J Oncol Nurs*. 2017;29:135-147.
9. Aaronson NK, Ahmedzai S, Bergman B, et al. The European Organization for Research and Treatment of Cancer QLQ-C30: a quality-of-life instrument for use in international clinical trials in oncology. *J Natl Cancer Inst*. 1993;85(5):365-376.
10. Padma VV. An overview of targeted cancer therapy. *Biomedicine (Taipei)*. 2015;5(4):19.
11. Sohal DPS. Adjuvant and neoadjuvant therapy for resectable pancreatic adenocarcinoma. *Chin Clin Oncol*. 2017;6(3):26.
12. Rubovszky G, Horvath Z. Recent Advances in the Neoadjuvant Treatment of Breast Cancer. *J Breast Cancer*. 2017;20(2):119-131.
13. Croner RS, Sevim M, Metodiev MV, et al. Identification of Predictive Markers for Response to Neoadjuvant Chemoradiation in Rectal Carcinomas by Proteomic Isotope Coded Protein Label (ICPL) Analysis. *Int J Mol Sci*. 2016;17(2):209.
14. Mankoff DA. A definition of molecular imaging. *Journal of nuclear medicine : official publication, Society of Nuclear Medicine*. 2007;48(6):18N, 21N.
15. Grenier N, Brader P. Principles and basic concepts of molecular imaging. *Pediatr Radiol*. 2011;41(2):144-160.
16. Frangioni JV. In vivo near-infrared fluorescence imaging. *Curr Opin Chem Biol*. 2003;7(5):626-634.
17. Graham MM, Weber WA. Evaluation of the Efficacy of Targeted Imaging Agents. *Journal of nuclear medicine : official publication, Society of Nuclear Medicine*. 2016;57(4):653-659.
18. Vithanarachchi SM, Allen MJ. Strategies for Target-Specific Contrast Agents for Magnetic Resonance Imaging. *Curr Mol Imaging*. 2012;1(1):12-25.
19. Vats M, Mishra SK, Baghini MS, Chauhan DS, Srivastava R, De A. Near Infrared Fluorescence Imaging in Nano-Therapeutics and Photo-Thermal Evaluation. *Int J Mol Sci*. 2017;18(5).

20. Boonstra MC, de Geus SW, Prevoo HA, et al. Selecting Targets for Tumor Imaging: An Overview of Cancer-Associated Membrane Proteins. *Biomark Cancer*. 2016;8:119-133.
21. Cheever MA, Allison JP, Ferris AS, et al. The prioritization of cancer antigens: a national cancer institute pilot project for the acceleration of translational research. *Clin Cancer Res*. 2009;15(17):5323-5337.
22. Azmi AS, Wang Z, Philip PA, Mohammad RM, Sarkar FH. Proof of concept: network and systems biology approaches aid in the discovery of potent anticancer drug combinations. *Mol Cancer Ther*. 2010;9(12):3137-3144.
23. Sams-Dodd F. Target-based drug discovery: is something wrong? *Drug Discov Today*. 2005;10(2):139-147.
24. Azmi AS, Mohammad RM. Rectifying cancer drug discovery through network pharmacology. *Future Med Chem*. 2014;6(5):529-539.
25. Mondal SB, Gao S, Zhu N, Liang R, Gruev V, Achilefu S. Real-time fluorescence image-guided oncologic surgery. *Adv Cancer Res*. 2014;124:171-211.
26. Weissleder R, Pittet MJ. Imaging in the era of molecular oncology. *Nature*. 2008;452(7187):580-589.
27. Vahrmeijer AL, Hutteman M, van der Vorst JR, van de Velde CJ, Frangioni JV. Image-guided cancer surgery using near-infrared fluorescence. *Nat Rev Clin Oncol*. 2013;10(9):507-518.
28. de Boer E, Harlaar NJ, Taruttis A, et al. Optical innovations in surgery. *Br J Surg*. 2015;102(2):e56-72.
29. Tempny CM, Jayender J, Kapur T, et al. Multimodal imaging for improved diagnosis and treatment of cancers. *Cancer*. 2015;121(6):817-827.
30. Keereweer S, Van Driel PB, Snoeks TJ, et al. Optical image-guided cancer surgery: challenges and limitations. *Clin Cancer Res*. 2013;19(14):3745-3754.
31. Benckert C, Bruns C. The Surgeon's Contribution to Image-Guided Oncology. *Viszeralmedizin*. 2014;30(4):232-236.
32. Rosenthal EL, Warram JM, Bland KI, Zinn KR. The status of contemporary image-guided modalities in oncologic surgery. *Ann Surg*. 2015;261(1):46-55.
33. Sanguinetti A, Lucchini R, Santoprete S, et al. Surgical margins in breast-conserving therapy: current trends and future prospects. *Ann Ital Chir*. 2013;84(6):595-606.
34. Stummer W, Pichlmeier U, Meinel T, et al. Fluorescence-guided surgery with 5-aminolevulinic acid for resection of malignant glioma: a randomised controlled multicentre phase III trial. *Lancet Oncol*. 2006;7(5):392-401.
35. van Dam GM, Themelis G, Crane LM, et al. Intraoperative tumor-specific fluorescence imaging in ovarian cancer by folate receptor-alpha targeting: first in-human results. *Nature medicine*. 2011;17(10):1315-1319.
36. Hoogstins CE, Tummers QR, Gaarenstroom KN, et al. A Novel Tumor-Specific Agent for Intraoperative Near-Infrared Fluorescence Imaging: A Translational Study in Healthy Volunteers and Patients with Ovarian Cancer. *Clinical cancer research : an official journal of the American Association for Cancer Research*. 2016;22(12):2929-2938.
37. Harlaar NJ, Koller M, de Jongh SJ, et al. Molecular fluorescence-guided surgery of peritoneal carcinomatosis of colorectal origin: a single-centre feasibility study. *Lancet Gastroenterol Hepatol*. 2016;1(4):283-290.

38. Tummers QR, Hoogstins CE, Gaarenstroom KN, et al. Intraoperative imaging of folate receptor alpha positive ovarian and breast cancer using the tumor specific agent EC17. *Oncotarget*. 2016;7(22):32144-32155.
39. De Saint-Hubert M, Prinsen K, Mortelmans L, Verbruggen A, Mottaghy FM. Molecular imaging of cell death. *Methods*. 2009;48(2):178-187.
40. Weber WA. Assessing tumor response to therapy. *J Nucl Med*. 2009;50 Suppl 1:1S-10S.
41. Therasse P, Arbuck SG, Eisenhauer EA, et al. New guidelines to evaluate the response to treatment in solid tumors. European Organization for Research and Treatment of Cancer, National Cancer Institute of the United States, National Cancer Institute of Canada. *J Natl Cancer Inst*. 2000;92(3):205-216.
42. Eisenhauer EA, Therasse P, Bogaerts J, et al. New response evaluation criteria in solid tumours: revised RECIST guideline (version 1.1). *Eur J Cancer*. 2009;45(2):228-247.
43. Kinahan PE, Fletcher JW. Positron emission tomography-computed tomography standardized uptake values in clinical practice and assessing response to therapy. *Semin Ultrasound CT MR*. 2010;31(6):496-505.
44. Mehta S, Shelling A, Muthukaruppan A, et al. Predictive and prognostic molecular markers for cancer medicine. *Ther Adv Med Oncol*. 2010;2(2):125-148.
45. de Bruin EC, Medema JP. Apoptosis and non-apoptotic deaths in cancer development and treatment response. *Cancer Treat Rev*. 2008;34(8):737-749.
46. Venkatramani R, Wang L, Malvar J, et al. Tumor necrosis predicts survival following neo-adjuvant chemotherapy for hepatoblastoma. *Pediatr Blood Cancer*. 2012;59(3):493-498.
47. Elvas F, Stroobants S, Wyffels L. Phosphatidylethanolamine targeting for cell death imaging in early treatment response evaluation and disease diagnosis. *Apoptosis : an international journal on programmed cell death*. 2017;22(8):971-987.
48. Kroemer G, Galluzzi L, Vandenabeele P, et al. Classification of cell death: recommendations of the Nomenclature Committee on Cell Death 2009. *Cell death and differentiation*. 2009;16(1):3-11.
49. Hotchkiss RS, Strasser A, McDunn JE, Swanson PE. Cell death. *N Engl J Med*. 2009;361(16):1570-1583.
50. Silva MT. Secondary necrosis: the natural outcome of the complete apoptotic program. *FEBS Lett*. 2010;584(22):4491-4499.
51. Kato T, Kameoka S, Kimura T, Tanaka S, Nishikawa T, Kobayashi M. p53, mitosis, apoptosis and necrosis as prognostic indicators of long-term survival in breast cancer. *Anticancer Res*. 2002;22(2B):1105-1112.
52. Park SY, Lee HS, Jang HJ, Lee GK, Chung KY, Zo JI. Tumor necrosis as a prognostic factor for stage IA non-small cell lung cancer. *Ann Thorac Surg*. 2011;91(6):1668-1673.
53. Pollheimer MJ, Kornprat P, Lindtner RA, et al. Tumor necrosis is a new promising prognostic factor in colorectal cancer. *Human pathology*. 2010;41(12):1749-1757.

54. Herath NI, Boyd AW. The role of Eph receptors and ephrin ligands in colorectal cancer. *International journal of cancer Journal internationale du cancer*. 2010;126(9):2003-2011.
55. Xi HQ, Wu XS, Wei B, Chen L. Eph receptors and ephrins as targets for cancer therapy. *J Cell Mol Med*. 2012;16(12):2894-2909.
56. Pasquale EB. Eph receptors and ephrins in cancer: bidirectional signalling and beyond. *Nat Rev Cancer*. 2010;10(3):165-180.
57. Sarantopoulos A, Beziere N, Ntziachristos V. Optical and opto-acoustic interventional imaging. *Ann Biomed Eng*. 2012;40(2):346-366.
58. Tzoumas S, Nunes A, Deliolanis NC, Ntziachristos V. Effects of multispectral excitation on the sensitivity of molecular optoacoustic imaging. *J Biophotonics*. 2015;8(8):629-637.
59. Verbeek FP, van der Vorst JR, Tummers QR, et al. Near-infrared fluorescence imaging of both colorectal cancer and ureters using a low-dose integrin targeted probe. *Annals of surgical oncology*. 2014;21 Suppl 4:S528-537.
60. Huang R, Vider J, Kovar JL, et al. Integrin alphavbeta3-targeted IRDye 800CW near-infrared imaging of glioblastoma. *Clinical cancer research : an official journal of the American Association for Cancer Research*. 2012;18(20):5731-5740.
61. Liu L, Lin G, Yin F, Law WC, Yong KT. Near-infrared fluorescent peptide probes for imaging of tumor in vivo and their biotoxicity evaluation. *J Biomed Mater Res A*. 2016;104(4):910-916.
62. Ma R, Taruttis A, Ntziachristos V, Razansky D. Multispectral optoacoustic tomography (MSOT) scanner for whole-body small animal imaging. *Optics express*. 2009;17(24):21414-21426.

Part I – Image-guided Surgery



Chapter 2

Modalities for image- and molecular-guided cancer surgery

Marieke A. Stammes, Sarah L. Bugby, Tiffany Porta, Keely Pierzchalski, Tim Devling, Cees Otto, Jouke Dijkstra, Alexander L. Vahrmeijer, Lioe-Fee de Geus-Oei, J. Sven D. Mieog

Adapted from: Modalities for image- and molecular-guided cancer surgery, Br J Surg 2018 Jan; 105(2): e69-e83.

Abstract

Purpose

Surgery is the cornerstone of treatment for many solid tumors. Whereas a wide variety of imaging modalities are available before surgery for staging, surgeons still primarily rely on visual and haptic cues in the operating environment. Image- and molecular-guidance might improve the adequacy of resection through enhanced tumor definition and detection of aberrant deposits. Available intra-operative modalities for image- and molecular-guided cancer surgery are reviewed here.

Procedures

Intra-operative cancer detection techniques were identified through a systematic literature search selecting peer-reviewed publications from January 2012 to January 2017. Modalities are reviewed, described and compared according to twenty-five pre-defined characteristics. To summarize the data in a comparable way, a three-point rating scale was applied to quantitative characteristics.

Results

Our search identified ten image- and molecular-guided surgery techniques, which can be divided in four different groups: conventional, optical, nuclear and endogenous reflectance modalities. The conventional modalities are the most well-known imaging modalities unfortunately have the drawback of a defined resolution and long acquisition time. Optical imaging is a real-time modality, however, the penetration depth is limited. Nuclear modalities have excellent penetration depth, however, their intra-operative use is limited by the use of radioactivity. The endogenous reflectance modalities provide high resolution, although with a narrow field of view.

Conclusions

Every modality has its own strengths and weaknesses, not one single modality will be suitable for all surgical procedures. Strict selection of modalities per cancer type and surgical requirements is required as well as combining modalities in order to find the most optimal balance.

Introduction

Over the last decades, multiple imaging modalities have emerged as essential tools in cancer diagnostics, providing information about the molecular and functional processes in normal and diseased tissues¹. New technologies have been developed to enhance our understanding of the diversity and behavior of cancer *in vivo*². Despite these resources, surgeons still primarily rely on their eyes and hands as tools during surgeries³⁻⁵. In oncologic surgery, clean and clear demarcation of the tumor boundaries is pivotal to determine the balance between excising too little or too much tissue. Therefore, a careful examination of the tumor borders is essential^{6,7}. Preoperative imaging does not always correlate well with intra-operative images due to tumor growth, deformation of soft tissue, shifting of organs or misalignment of the image display compared to the surgical field⁸.

As Rosenthal et al. discussed for breast, melanoma and head-neck cancer patients, surgical excision requires 3 detection steps: initial assessment before resection; initial assessment during incision including detection of regional metastasis as well as lymph nodes; and post resection margin analysis by the pathologist⁹. Eyes and hands cannot detect the exact boundaries of a tumor or create a clear 3D morphologic or functional overview of the operative site⁵. As a result, histologic tumor involvement of the resection margins may be observed in patients with breast cancer at least 20% of the time^{3,4,9,10}. In order to improve cure and complication rates, the use of intra-operative *in vivo* and real-time tools would be useful. To achieve this requires spatial resolution better than the human eye, minimal interference with daily practice, operator friendly instrumentation that is time efficient¹¹. To go beyond visualization of anatomic boundaries, real-time molecular information would provide additional information to optimize surgical resection.

The focus of this review was intra-operative modalities for image- and molecular-guided cancer surgery.

Methods

Twenty-five characteristics were selected to evaluate and compare the ten different IGS modalities reviewed here (**Table 1-6**). As Weissleder and Pittet state: *“for imaging technologies to be adapted more widely and to be complementary to other types of imaging the read-outs need to meet certain criteria; they need to be quantitative, high resolution, longitudinal, comprehensive, standardized, digital and sensitive”*². This statement refers to cancer imaging in general but the requirements apply equally well to image- and molecular-guided surgery in cancer patients².

The chosen characteristics are based on relevant articles, which were found through PubMed searches (January 2012-January 2017) using one or more of the following keywords; “surgery,” “cancer,” “oncology,” and the specific names of the (imaging) modalities. Further searches were carried out for specific performance characteristics, e.g., resolution. Abstracts were reviewed and full-text articles obtained where possible. References and linked articles from included papers were studied to identify further relevant information.

To summarize the data in a comparable way, a three-point rating was applied to quantitate image-guided surgery (IGS) characteristics. These ratings are detailed as footnotes to the tabulated results. User friendliness was determined from discussions with end-users but differ from user to user, these were scored as easy (+), intermediate (-/+), or challenging (-).

Results

Our study identified ten modalities which could be used for image guidance during surgery. Example imaging systems for each modality, along with a representative clinical image, are visualized in **Figure 1-3**. In general, the modalities can be classified into four groups: conventional, optical, nuclear, and endogenous reflectance. Each modality is discussed below, and the characteristics of each are tabulated for comparison (conventional in **Table 1 & 4**, optical & nuclear in **Table 2 & 5** and endogenous reflectance in **Table 3 & 6**⁹).

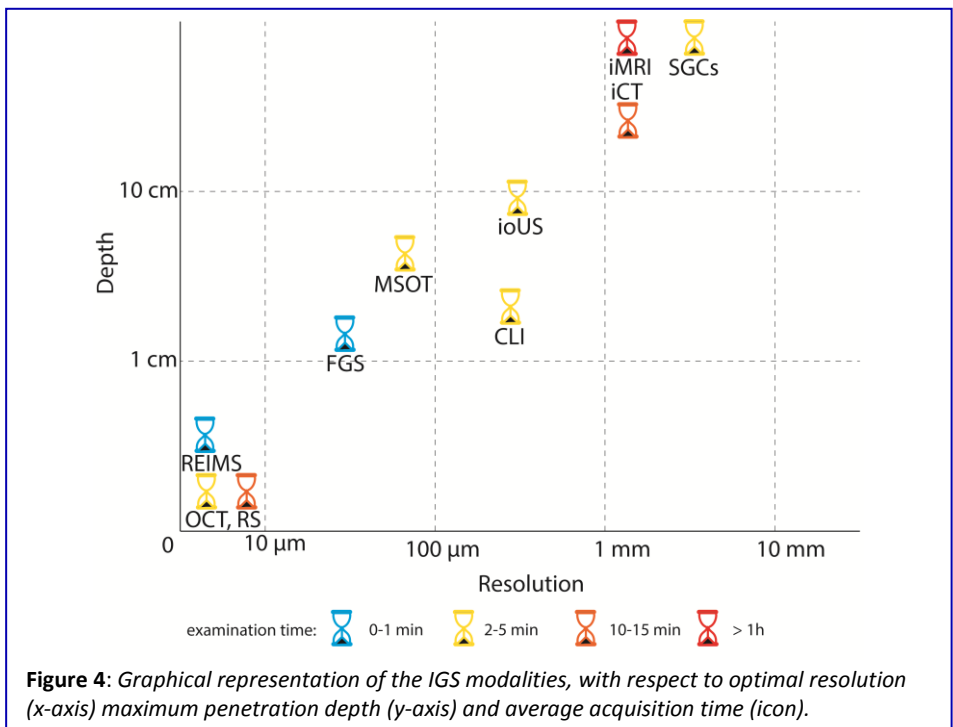
Comparison between modalities

Modalities within each group are compared in tables below, and it is also possible to compare between groups (across multiple tables).

Table 1 provides information for conventional modalities already familiar to many practitioners, the imaging modalities are described along with the type of information that is obtained together with the surgical interference and associated risks. **Table 2** and **Table 3** provide the same information for optical and nuclear, and endogenous reflectance techniques respectively.

The same groupings are used for **Tables 4, 5 and 6**, which compare the performance of each modality during surgery, including the criteria that Weissleder and Pittet mention as being essential ². **Tables 4-6** additionally provide information about the clinical potential and major challenges for clinical implementation of each of the ten modalities.

Figure 4 provides a fast comparison of all ten modalities based on characteristics most interesting in clinical practice - penetration depth, resolution and acquisition. This clearly demonstrates a common trade off in image-guided surgery, a greater penetration depth often coincides with a degradation of resolution.



Conventional modalities

The use of non-invasive imaging for disease diagnosis has become a standard operating procedure and these conventional modalities are widely available. The current golden standard consists of conventional imaging modalities that yield anatomical and macroscopic structure information. The images and information obtained with any new technologies must be compared with these established imaging modalities³⁵.

iMRI (intraoperative Magnetic Resonance Imaging)

To be able to use an MRI intraoperatively, MR compatibility of surgical equipment needs to be guaranteed together with special policies for safety and staff training. The implementation of these special policies can be prohibitively expensive although the costs are dependent on the field strength of the system. High field systems (>1.0 T) require far more investment as shielding of the operating room is essential but provide high resolution images within a shorter acquisition time. Low-field systems (< 0.3T) are cheaper since no additional requirements for the operating room (OR) are necessary and so they can be integrated into existing ORs¹⁷. Another advantage of using a low-field system is the availability of open systems, which is more useful during surgery. Nevertheless, the lower the field strength the lower the image quality or the longer the scan time^{21,26}.

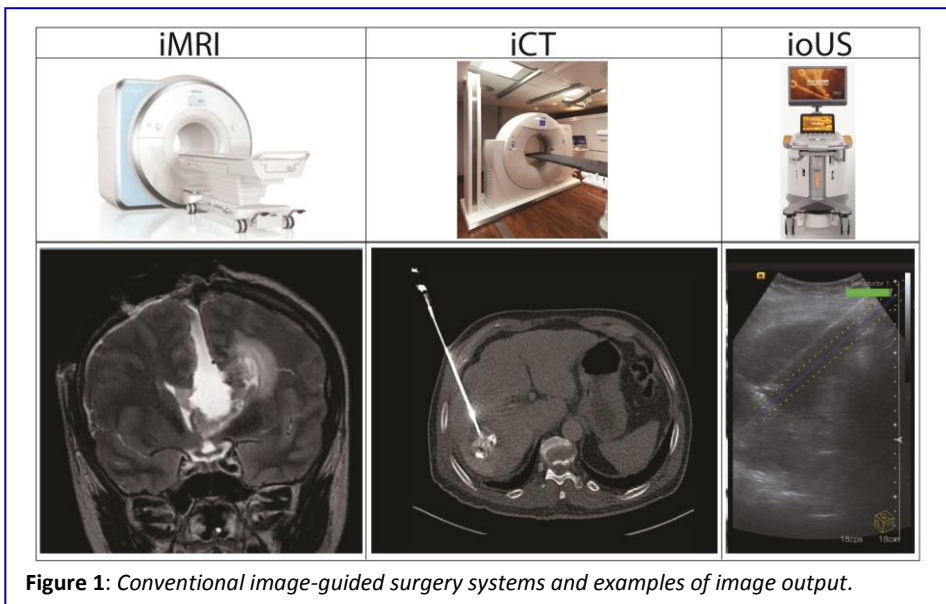


Figure 1: Conventional image-guided surgery systems and examples of image output.

The main reason to still make use of an MRI during surgery, despite these limitations, in neurosurgery it has been proven that the maximum amount of tumor could be removed in a safe manner²¹.

iCT (intraoperative Computed Tomography)

In general CT offers high throughput with high-resolution imaging, however, this is not the case when used as an intraoperative imaging modality. Acquiring a CT during surgery takes 10-15 minutes, partly due to the interference caused by the shape of the gantry, as using a bore will cause more interference compared to a C-arm. When using the CT for assessing surgical specimens instead of the cavity, a micro-CT can be used in this way there is less interference of the surgery and a high spatial resolution of <1 μm . Nevertheless, the accuracy of margin assessment is variable due to specimen orientation and there can be a high rate of nonspecific findings due to dense parenchyma and architectural distortion due to the surgery³⁶.

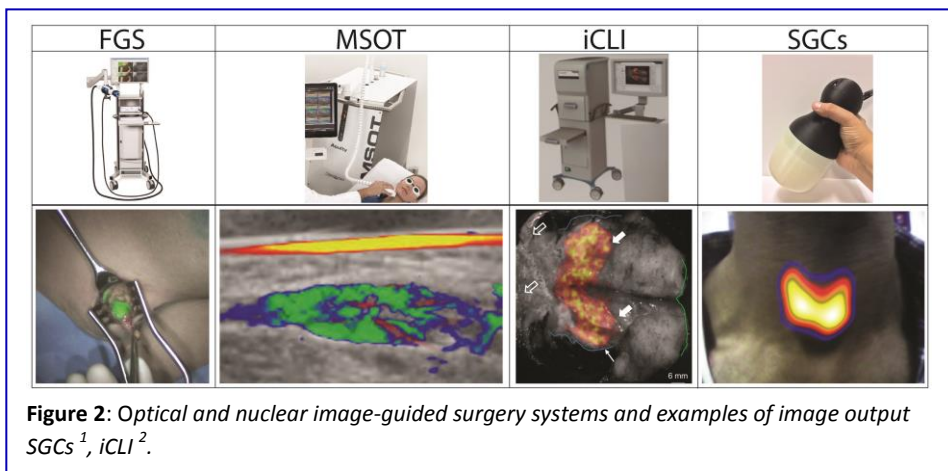
ioUS (intraoperative Ultrasound)

Of the conventional imaging modalities ultrasound is the easiest technique to incorporate intraoperatively as it does not cause interference with surgery or logistical challenges, gives real time information and surgeons are already used to interpreting the images obtained. In addition, ioUS is one of the most sensitive imaging modalities for assessing small lesions due to the high frequency transducer which can be used. In addition to sensitivity, the specificity of discrimination between healthy tissue and residual disease is a benefit of this technique²⁵. As ioUS can be used in an iterative mode one, should be aware of an essential drawback - surgical manipulation can cause artifacts so the image quality will decrease as the surgery proceeds³⁷.

Optical imaging

Optical imaging techniques such as fluorescence guided surgery (FGS) and multispectral optoacoustic tomography (MSOT) can provide real-time feedback with limited workflow disruption. They require a targeted probe which consists of a fluorophore belonging to the near infrared window (~700 nm to 900 nm) which has the largest penetration depth in tissue of optical light. In this window, penetration is one centimeter for FGS or a few centimeter with MSOT compared to only a couple of millimeters for wavelengths below 700 nm^{3,4,6,19}. There is also a window above 900 nm, the

so called second-window near infrared light (NIR2) ranging from 900 nm-1450 nm. This window has the advantages of even deeper tissue penetration and low tissue auto fluorescence signals which will lead to higher tumor to background ratios (TBRs). Animal study *in vivo* testing has shown a penetration depth of up to 18 mm, and simulations suggest that this might be increased to up to 10 cm³¹⁻³³. To make use of this NIR2 window new instrumentation will be required. Specific probes for use in this range goes beyond the scope of this review, however single-walled carbon nanotubes or upconversion nanoparticles are encouraging opportunities³¹⁻³³.



FGS (Fluorescence Guided Surgery)

FGS has the advantage of providing real-time, relatively cheap, user friendly, and not interfering the surgical area. However, also several disadvantages exists, such as the limited penetration depth of maximum 10 mm and challenges in quantification due to other processes that are associated with the use of light, such as photobleaching, transmission and reflection changes. Light in general is attenuated by absorption and scatter in tissue, the total attenuation (the sum of attenuation from absorption and scatter) has an exponential relationship with depth. This means practically that less than 0.0001% of the photons transmitted into tissue can be detected and that of this amount only 10-25% of the photons generated in tissue will be really recovered. This is due to the relatively small quantum yield of most fluorophores and especially NIR fluorophores. Another limitation for quantification are absorption and scatter as those characteristics are highly

variable in tissue. Full correction, by measurements of the absorption, scatter and anisotropy of tissue, can lead to quantitative measurements, however this is still in its infancy³. Another limitation for a full clinical translation is the lack of specific contrast agents. So far only 3 tumor specific agents are registered for clinical use. Several tumor-specific agents are in the process of clinical translation however, their clinical translation is dependent on the approval of the fluorophore³.

MSOT (Multispectral Optoacoustic Tomography)

In general, MSOT deals with the same advantages and disadvantages as FGS with the difference that MSOT has a greater penetration depth. In addition, both FGS and MSOT are based on photon delivery but in optoacoustic tomography low frequency ultrasonic pulses are also detected. Those pulses are generally unaffected by tissue absorption and scattering, essentially removing a large component of the limiting factor in development of quantitative methods for fluorescence based imaging at depth. Given that the strength of an optoacoustic signal within a pixel is a function of both the diffusive light reaching that pixel and the concentration of absorber present, it is apparent that by determining or modeling the light propagation through the tissue, the concentration of a local chromophore can be determined. Work by both Tzoumas et al and Brochu et al has recently demonstrated that this result can be achieved both in phantoms and more importantly *in vivo*, giving a glimpse that quantitation in clinical optoacoustic tomography is a possibility³⁸⁻

⁴⁰.

Nuclear Imaging

Nuclear modalities use a radioactive tracer to generate images with, in general although dependent on the tracer of choice, a high sensitivity and specificity³⁴. However, the use of radioactive material requires special biosafety permits, additional training, and safety procedures both for personnel and patients.

CLI (Cherenkov Luminescence Imaging)

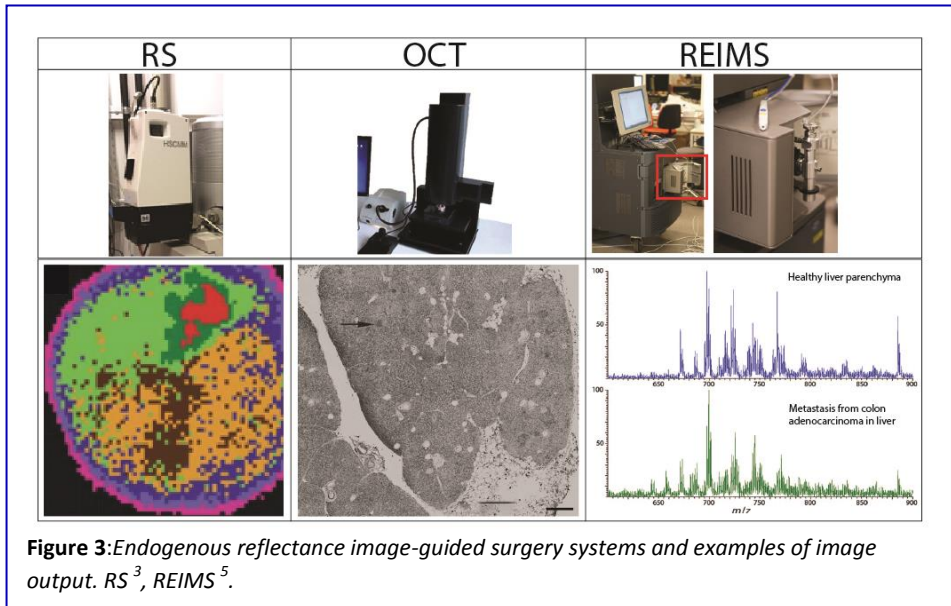
CLI is actually a combination of optical and nuclear imaging as the radioactive tracer in CLI is used to create optical photons. A drawback of this is that CLI has a similar tissue penetration as optical imaging of only a centimeter. On the other hand, the advantage is that the resolution is also similar to optical imaging which means that this is higher than any other nuclear imaging modality. Nevertheless, the intensity of the optical photons generated is about a billion times lower than the illumination in an operating room which makes it hardly suitable to use for open surgery, endoscopic applications would be favorable ⁴¹. This low light level negatively influences the sensitivity which can be improved by injecting a higher amount of radioactivity. The amount of radioactivity is well correlated with the light output, radiance, though an increase in radioactivity will also lead to an increase in radiation burden.

SGCs (Small Gamma Cameras)

Gamma cameras, like single-photon emission computed tomography (SPECT) can be considered a conventional modality. However, those systems face similar drawbacks as MRI and CT in that the size and shape of the machine causes a lot of surgical interference and actually need a dedicated scanning room. To circumvent this, a handheld gamma probe is already used in clinical practice for sentinel lymph node detection. Although useful, these probes can only indicate the amount of activity within their field of view and do not have imaging capabilities. Innovative radiation detector design allow the generation of compact gamma cameras, small gamma cameras (SGCs) ⁴². The differences between SPECT imaging and SGCs is that with gamma imaging the sensitivity is dependent on the tracer but independent of the depth of the tumor and for SGCs there is a tradeoff between sensitivity and spatial resolution dependent on the imaging distance. In addition, the field of view (FOV) is smaller but dependent on the detector design.

Endogenous reflectance

The last group of techniques encompasses a variety of endogenous reflectance/signals modalities. The advantage of this group is that no additional contrast agents are necessary to generate relevant and very detailed information based on the characteristics of the tissue itself. Nevertheless, creating high resolution output may require substantial acquisition times.



RS (Raman Spectroscopy)

In general, RS uses intrinsic properties of molecules to generate contrast which means RS is not limited to a certain tissue type although it requires a more specialized approach for skin pigments such as in melanoma. To create additional contrast, plasmonic particles or organic polymers coupled with antibodies could be used. Stimulated Raman scattering can be used to monitor dynamic changes, alterations in tissue cellularity, axonal density and protein / lipid ratio²².

A possible limitation of translating RS into clinical practice is the question of how small fields of view could be applied to the validation of a tumor bed, which is relative large. A clinical trial using this technique has detected low-grade gliomas instead of the tumor bed. For this an image-resect-image

technique was used in which the arm movement was predefined. This method led to an additional operation time of 10 minutes for image acquisition which was not considered obstructive to surgical workflow^{22,30}.

OCT (Optical Coherence Tomography)

OCT has the advantage of being analogous to US which makes the images easy to interpret for a surgeon as they are already used to those types of images. Instead of sound, OCT uses the reflections of light. This means that OCT does not need direct contact with the surgical area however, due to differences in refractive index direct contact is desirable^{11,43,44}. Similarly to RS, OCT does not require a contrast agent but can use the same agents as used in optical imaging to generate additional contrast if needed. This opportunity to image without a contrast agent shortens the pathway towards full clinical translation as the regulatory issues and risks associated with contrast agents can be circumvented⁴⁵.

REIMS (Rapid Evaporative Ionization Mass Spectrometry)

Intra-operative molecular diagnostics based on mass spectrometry have recently gained attention from the medical field as it offers the possibility of *in vivo*, *in situ*, and real-time mass spectrometric analysis of tissue^{13,14}. In combination with electrosurgical devices¹⁵, REIMS promises to guide and optimize surgical resection in real-time as it is performed within a couple of seconds. Within this timeframe, the smoke generated by electrocautery is aspirated through tubing and a chemical analysis takes place, followed by real-time data processing and finally quasi-instant visual feedback. Nevertheless, to keep this speed there is the need for validated tissue-specific databases which require time to generate and a large clinical cohort to account for inter-individual variability. It is expected that when this database is available any tissue can be analyzed^{12,13,28}. In addition, complex molecular signatures can be identified which can increase the specificity over a single biomarker¹². Although it is not truly an 'imaging' technique, REIMS has the potential to improve surgical margins by molecular sampling of them¹⁶ comparable to Mohs surgery for skin cancer in which, during surgery, the removed specimen is examined for cancer cells⁴⁶.

Table 1: Description of conventional image-guided surgery modalities and interference with surgical workflow.

	iMRI	iCT	ioUS
Principle	MRI is based on the different spin relaxation rates of atoms within tissue under a static magnetic field and radiofrequency pulses via the excitation of hydrogen nuclei ⁴⁷ .	X-rays pass through the patient, are attenuated and subsequently measured by detectors which rotate around the patient ⁴⁸ .	The US probe transmits ultrasound waves, which are (partially) reflected and/or scattered by tissue inhomogeneities and interfaces and sent back to the probe ⁴⁹ .
Type of information	Soft tissue discrimination and a multiplanar visualization ²⁶ .	Structural differences due to differences in absorbance ^{36, 48} .	Contrast is based on scattering/ reflectance differences between different types of tissue: soft tissue, fat, and fluid ^{43, 49} .
Anatomical information	Yes, what, is dependent on the sequence ¹⁷ .	Yes ³⁶ .	Yes, although orientation is limited due to the different planes ^{27, 37} .
2D/3D	3D.	3D.	2D, 3D with specialized transducers or a stacked 2D volume ³⁷ .
Need for contrast agent	Not necessary discrimination between two types of tissue can be improved ^{17, 21} .	Not necessary discrimination between two types of tissue can be improved ²³ .	Not necessary discrimination between two types of tissue can be improved and real time vascular phase images ^{18, 25} .
Cost machine&facility	€€€ ¹⁷ .	€€€ ²⁴ .	€ ^{27, 37} .
Acq. Cost	€€€ ^{50, 51} .	€€ ^{50, 51} .	€ ^{50, 51} .
Time acquisition& reconstruction	Max 2h ^{21, 27} , not real time.	10-15min ^{23, 27, 36} , not real time.	Real time interactive information ^{25, 27} . Delay is dependent on the operator (max. a few minutes) ³⁷ .
Interference of surgery	Yes, highly interfering. Position wise maybe even impossible ¹⁷ .	Yes, dependent on the modality and the possibility of a sliding gantry on a railtrack ^{23, 27} .	Not in general and it gives no logistical challenges ³⁷ . Yes, it needs direct contact with the specimen ^{4, 43} .
Endoscopic options	No.	No.	Yes.
Safety	No, it can even detect complications in an earlier stage ^{17, 21, 26} .	No complications or infections related to iCT and surgical complications were directly recognized ²³ .	Relatively safe and well tolerated ²⁵ . It gives direct feedback to the surgeon ⁵² .

Table 2: Description of optical and nuclear image-guided surgery modalities and interference with surgical workflow.

	FGS	MSOT	CLI	SGCs
Principle	An injected/ endogenous fluorophore is excited at a specific wavelength and the emitted fluorescent photons are detected ⁶ .	Light is used as input energy and acoustics for signal detection, similar to US. Molecules absorbing light undergo transient thermos-elastic expansion which generates US waves ¹¹ .	Charged particles emitted from radionuclides transfer energy as they move through a medium. If they travel faster than the speed of light, the transferred energy is released, through relaxation, as light ⁴¹ .	Radionuclides introduced to the patient emit gamma radiation. Gamma photons have sufficient energy to pass relatively unimpeded through tissue to be detected by an external camera ⁵³ .
Type of information	Presence of a fluorophore or specific tissue properties in a certain area ^{6,9} .	The differences of optical absorption inside tissue is visualized ¹¹ .	Functional images based on the distribution of an externally administered particle-emitting radiotracer ⁵⁴ .	Quantitative functional images based on the distribution of an externally administered gamma-emitting radiotracer ⁵⁵ .
Anatomical information	No, however, autofluorescence provides information about tissue properties ⁹ .	Yes, by strong endogenous absorbers like blood and melanin ¹¹ . Interleaved with US images for mechanical contrast.	No.	No.
2D/3D	2D.	2D and 3D.	2D ⁴¹ .	2D or 3D depending on the detector system used
Need for contrast agent	Yes typically, however when using endogenous fluorescence signal a contrast agent is not necessary ^{4,9} .	Yes/no, detects endogenous tissue absorbers or exogenous contrast agents ⁴ .	Yes, a particle-emitting radiotracer ⁴¹ .	Yes, a gamma-emitting radiotracer.
Cost machine&facility	€ ⁴ .	€€.	€ ⁴¹ .	€€.
Acq. Cost	€.	€.	€€ ⁵¹ .	€€ ^{50,51} .
Time acquisition& reconstruction	Real time, in the millisecond range, and related to the surgical field ^{3,4} .	Image generation is in real time. Possible to perform advanced analysis post process.	Several minutes ^{41,53} .	Depends on the amount of activity vs SNR. In general, one minute is sufficient ^{29,53} .
Interference of surgery	No, as there is no direct contact with the specimen as the optimal working distance is between 5-45cm ¹⁹ . A dark environment is beneficial ⁷ .	Not in general but yes, it needs to be contact based, similar to iOUS.	Yes. Complete darkness is required for imaging. In addition, the use of radioactive tracers may have implications for working practice ⁴¹ .	Not in general, there is no direct contact necessary with the specimen. However, the use of radioactive tracers, may have implications for working practice.
Endoscopic options	Yes, with the Cellvizio® system ⁵⁶ .	Yes.	Yes ⁵⁷ .	No.
Safety	NIR imaging is a safe technique only laser illumination levels needs attention ³ .	Similar to US in technique, so relative safe. Only the direct contact can cause problems.	Radiation exposure for both patients and surgeons ⁴ .	Radiation exposure for both patients and surgeons ⁴ .

Table 3: Description of endogenous reflectance image-guided surgery modalities and interference with surgical workflow.

	RS	OCT	REIMS
Principle	Monochromatic light from a certain wavelength illuminates tissue and scatters light with new wavelengths. The energy related to the wavelength shift is a function of the vibrational energies of molecular bonds in tissues ^{22,30} .	Is analogous to US, only reflections of near-infrared light are detected instead of sound ^{45,58} , the information is obtained by differences in reflected energy and scattering intensity ⁴³ .	An ambient ionization technique. Connected to an unmodified surgical handpiece, the system directly aspirates and analyses the smoke created by the electro-surgical device from the surface of the tissue.
Type of information	Cellular structures can be distinguished based on the chemically specific Raman spectrum of metabolites, lipids, proteins, DNA ³⁰ .	Cross-sectional images are generated mimicking the intensity of optical backscatter of light passed through tissue ⁵⁸ .	The identification is based on tissue-specific libraries (molecular profiles or fingerprints) to identify the tissue type ¹² .
Anatomical information	Yes, dependent on the technique ³⁰ .	Yes ^{43,58} , tomographic images of biological tissue are generated (morphology) ^{11,30,44} .	No, it is based on tissue-specific molecular signatures ²⁸ .
2D/3D	2D, 3D is possible by using stacked images or measure on a different depth.	2D and 3D depending on the detector used ⁴⁵ .	There is a spectrum generated and not an image ^{13,15,59} .
Need for contrast agent	No, it is a label-free method as it uses intrinsic properties of molecules ²² .	No, depends on the optical scattering and reflectance of tissue to generate contrast ^{30,44,45} .	No, it is a label-free technique ^{13,15,59} .
Cost machine&facility	€.	€.	€€ ²⁸ .
Acq. Cost	€.	€.	€.
Time acquisition& reconstruction	Short (1-10 min) ³⁰ . Spontaneous Raman scattering : acq time of 0.05 second for a single high quality spectrum. Coherent Raman imaging is faster (μ s/pixel) ^{22,30} , with limited spectral quality.	Real time ^{11,45} , an image can be taken every 5s ^{43,58} . Total acquisition time can be up to 5min ^{30,44} .	A couple of seconds (< 3s) ^{13,28} . The use of a real-time recognition algorithm allows for rapid identification of tissue being analyzed.
Interference of surgery	There is no direct contact needed. ³⁰	Yes/No, does not require direct contact with the specimen ^{11,43,44} , rapidly scan large areas of tissue ⁵⁸ .	No, no modification of surgical procedure is required ¹³ . The tissue which is measured is destroyed during this process but this is the tissue that the surgeon is cutting ^{12,15} .
Endoscopic options	Yes	Yes ^{43,45,58} .	Yes ⁵⁹ .
Safety	Reasonable, due to the weak signal high levels of light energy and exposure times are often needed ⁶⁰ .	Relative safe, similar to ultrasound and fast image acquisition ^{43,58} .	Relative safe ¹² . For the mass analyzer system, European norms have to be complied with.

Table 4: Performance and clinical potential of conventional image-guided surgery modalities.

	iMRI	iCT	ioUS
Resolution	Resolution around 0.3-1.3 mm ^{61, 62} . Improves with the scan time, and field strength ^{17, 21, 62} .	Spatial resolution of 0.4-0.6mm ^{4, 27} . For micro-CT <1um ³⁶ .	High spatial and temporal resolution around 0.3-1mm ^{4, 25, 27, 43} .
Field of View (FOV)	Up to 20cm, although the distortion increases with the FOV ⁶³ .	14cm ³⁶ .	Dependent on the transducer curved transducer > linear transducer in the range 10-60mm ⁴ .
Iterative	Yes, but mostly one scan is obtained ²¹ .	Yes.	Yes ³⁷ .
When to use during surgery.	Can be used for surgical (re-) orientation and as quality control of the resection cavity ^{17, 21, 26} .	Can be used for surgical (re-) orientation and the micro-CT for lump margin assessment ^{23, 36} .	Used for real-time surgical guidance in all stages ^{25, 37, 52} .
Depth	Whole body.	Whole body.	Several cm ⁴ .
Inter-operator variability	Medium ¹⁷ .	Low.	High ^{18, 27, 52} .
User friendly	-/+, depends on the familiarity of the surgeon with MR image interpretation ⁹ .	+	+ ^{27, 37, 52} .
Availability	-/+, Due to the high price and requirement, limited ¹⁷ .	+, For CT and limited use of Micro-CT ³⁶ .	++, Widely available ^{27, 37, 52} .
Status Machine	Clinical.	Clinical.	Clinical.
Status contrast agent.	Non-tumor specific are available.	Non-tumor specific are available.	Three agents available in Europe ^{18, 27} .
Quantification of size/ signal	Yes, absolute ² .	Yes, absolute ² .	Yes, absolute ² .
Cancer type	Neuro ^{4, 9, 17, 21, 26} .	Lump margin assessment ³⁶ , neuro ²³ , spinal ²⁰ .	Abdomen ^{18, 25, 9} , H&N area ^{37, 52} , breast ⁹ , neuro ⁹ .
Artifacts/ Limitations	-Vascularized tumors will lead to poorly visualized operation fields - hematomas that produces imaging artifacts ¹⁷ .	-Dense parachyma and architectural distortion making margin assessment difficult ³⁶ . -Bone anatomy is well visualized but limited on the lesion itself ²⁰ . - Radiation exposure ²⁴ .	-Cirrhosis, can be improved by using CA ²⁵ . -Steatosis (induced by chemo) ¹⁸ . - lack of anatomical orientation ³⁷ .
Sensitivity, specificity of the system.	Increases with the field strength ^{21, 26, 34} .	. The specificity is > 90% but sensitivity only 60% ³⁶ .	Both the sensitivity and specificity are high ²⁵ .

Table 5: Performance and clinical potential of optical and nuclear image-guided surgery modalities.

	FGS	MSOT	CLI	SGCs
Resolution	10um ⁴ , dependent on the camera system ¹⁹ .	Dependent on the detector. Typically higher resolution is achieved with a depth trade off 15um till 3mm, 200-300um up to 3cm ¹¹ .	Fundamental spatial resolution limit of 0.3mm, further degraded by scattering in tissue ^{41, 64} .	Spatial resolution can range from 3mm – 30mm ^{4, 29, 53} .
Field of View (FOV)	Dependent on the camera system between 20-250mm ¹⁹ .	Similar to ioUS, when the resolution increases the FOV is decreasing.	Typical endoscopic FOVs. An open field FOV is 80x80mm ⁶⁵ .	Dependent on the camera system, between 40-120mm is typical. Can vary with pinhole cameras ^{29, 53} .
Iterative	Yes.	Yes.	Yes, though limited by the half-life of the radiotracer used.	Yes, though limited by the half-life of the radiotracer used.
When to use during surgery.	Used for tumor margin/SLN localization and quality control of the resection cavity ^{3,4,19} .	Usage is similar to FGS but with more anatomical information ^{11, 66} .	Mostly used for quality control of the resection cavity and lump assessment ^{41, 67} .	Used for SLN detection, for surgical orientation and as quality control of the resection cavity ^{29, 68} .
Depth	0.5-2cm ^{3,4} .	Several cm ⁴ .	1 cm, dependent on the radiotracer used ^{41, 69} .	No limit ⁴ .
Inter-operator variability	Low.	Medium.	Low.	Low.
User friendly	+, NIR light does not alter the appearance of the surgical field ^{3, 30} .	+	+, does not alter the appearance of the surgical field. -, Radiation burden. -, exclusion of all ambient light.	+, does not alter the appearance of the surgical field. -, Radiation burden.
Availability	+, Available ³ .	-/+, Available in limited centers.	-/+, Available in limited centers.	+, Available.
Status Machine	Clinical ^{3, 19} .	Clinical trials ongoing.	Clinical trials, some systems available for clinical use ⁴¹ .	Some systems available for clinical use, some undergoing trials ⁵³ .
Status contrast agent.	Only 3 tumor a-specific CA are registered for clinical use ³ .	Likely that the agents under investigation for FGS will also be studied for MSOT ⁷ .	Clinically available for the available PET tracers and more tumor-specific tracers are in clinical development.	Clinically available for the available SPECT tracers more tumor-specific tracers are in clinical development.
Quantification of size/ signal	Relative, absorption and scatter limit the ability for absolute quantification ² .	Yes, via the amount of signal in an area ³⁸⁻⁴⁰ .	Relative absorption and scatter limit the ability for absolute quantification ⁴¹ .	Absolute or relative depending on camera design ² .
Cancer type	Primary tumor, lymph nodes, vascularization, metastases ³ .	Hollow organs for endoscopic else all solid tumors ¹¹ .	Broad range of solid tumors.	For numerous cancer types; SLN, parathyroid, colon ²⁹ .
Artifacts/ Limitations	-Attenuation correction of the excitation light can help with target detection, over-compensation can cause false-positives ³ . - Penetration depth ^{3, 19} .	Requires surface contact.	-High radiation burden. -Exclusion of ambient light is essential, endoscopic applications would be favorable ⁴¹ . - Scattering can cause signal to be visualized in the incorrect area ⁶⁴ .	-Radiation burden -Tradeoffs between dose, acquisition time, sensitivity, spatial resolution and FOV.
Sensitivity, specificity of the system.	Superficial tissue can be detected with a high sensitivity. Sensitivity is decreased with the depth ^{4, 19} .	Nanomolar sensitivity with high specificity based on multispectral imaging.	- Lack of sensitivity due to low light levels ⁴¹ . - Specificity is dependent on the tracer ³⁴ .	- An increase in imaging distance degrades sensitivity and spatial resolution ^{29, 53} . - Are dependent on the system and tracer ³⁴ .

Table 6: Performance and clinical potential of endogenous reflectance image-guided surgery modalities.

	RS	OCT	REIMS
Resolution	High, in the submicron range ²² .	High, 1-15µm, limited by the depth penetration which is, depending on the tissue, up to 5mm ^{11, 30, 43-45} .	Not applicable, as it does not generate an image but a profile.
Field of View (FOV)	~ 0.1 mm ³⁷ , at highest far-field optical resolution ^{22, 30} .	Around 1cm ^{2, 30} .	Around a surgical dissection rate of 1mm/s which leads to a FOV of 1mm ^{3 13} .
Iterative	Yes ³⁰	Yes ^{43, 45, 58} .	Yes, however not on the same piece of tissue ^{12, 28} .
When to use during surgery.	Mostly used for quality control of the resection cavity and lump assessment ²² .	Mostly used for quality control of the resection cavity and lump assessment ^{30, 45} .	Mostly used for quality control of the resection cavity and lump assessment ^{12, 28} .
Depth	Hundreds of micrometer ^{22, 30} .	0.2cm ^{30, 43, 45, 58} .	Not applicable/ limited.
Inter-operator variability	Low, when incorporated in a robotics system	High/medium ⁴⁵ .	Low as a reference library is used for feedback and tissue classification ¹³ .
User friendly	+, when incorporated in a robotics system, otherwise low.	+ ⁴⁵	+, does not change the procedure of electrosurgical dissections ¹³ .
Availability	-/+, Available in limited number of centers.	-/+, Not in routine clinical use for surgery available for other approaches ^{11, 44, 45} .	-/+, Available in limited centers for research purpose only.
Status Machine	Mostly <i>ex vivo</i> studies, only one study <i>in vivo</i> so far published ³⁰ .	Mostly <i>ex vivo</i> , <i>in vivo</i> clinical trials are needed ⁴³ . Handheld probes are in development ^{11, 30} .	Clinical research, mainly on <i>ex vivo</i> tissue and few papers reporting <i>in vivo</i> tissue analysis ^{12, 13, 28} .
Quantification of size/ signal	Relative quantification ²	Yes, absolute.	Only relative, comparison based on different molecular fingerprints from one tissue type to another ¹³ .
Cancer type	Neurology ^{22, 30} , gastrointestinal, bladder, cervical ²²	Bladder, prostate, kidney ⁴³ breast ^{45, 58} , melanoma, thyroid ⁴⁵ , ovary ⁴⁴ .	All solid tumors like breast, liver, colorectal, brain ¹³
Artifacts/ Limitations	- interrogate a small region of tissue, - SNR can be a limiting factor - the intrinsic weak signals can be partly solved by high quality instruments ^{22, 30} .	-limited penetration depth ⁴³ . -optical scattering and coherent speckle artifacts from cellular structures limits the visualization of small cells ⁵⁸ .	-The tissue needs to be disrupted for analysis and cannot be measured again ¹² . -The need for validated tissue-specific databases ¹³ .
Sensitivity, specificity of the system.	Accuracy, Sensitivity and Specificity >90% to distinguish normal brain from tumor invaded brain ²² .	High, sensitivity rates between 80-100% could be found and specificity 60-100% ^{11, 30, 45} .	High, >90% depends on the accuracy of the classification library

Discussion

Tumor removal is an incremental and iterative process so there should also be the possibility to obtain intra-operative images linked to those obtained by initial staging scans¹². This may require merging of more than one modality. US is a well-established technique for interventional procedures but is rarely the choice for definitive staging. In comparison, single-photon emission computed tomography (SPECT) and positron emission tomography (PET) may be used to perform tumor staging but cannot be used during surgery due to size limits whereas portable SGCs may suffice¹¹. For this purpose, a conventional anatomic technique (e.g. MRI, CT or US) can be combined with a biological imaging modality such as optical or nuclear imaging, with the use of a targeted tracer. Or else a technique used during surgery for (re-)orientation can be combined with a technique which is used for quality control of the resection cavity or lump assessment as mentioned in **Table 4-6**. Another option is the use of a technique with a high penetration depth but a somewhat lower resolution complementary to one of the imaging modalities of the endogenous reflectance group to compensate for the loss of resolution. Both options will lead to more complete overview of the actual situation in a patient. **Figure 4** visualizes the differences between the techniques in relation to depth, resolution and acquisition time^{2,70}. One has to be aware that techniques which are further apart from each other in the figure may gain the most in combination. So far, the biggest challenge remains the fusion of the images generated by different techniques which can lead to a certain degree of uncertainties, the greater the distance between two modalities in **Figure 4**, the greater the challenge.

Over the past decade, imaging has broadened from the conventional anatomical overview to state-of-the-art methods giving a molecular description of structure or function⁷¹. The overall goal of imaging is to provide a better outcome. It should be noted that a “better outcome” can be defined—and may often differ—from different perspectives, i.e., from the patient, surgeon, instrument manufacturer, and society¹⁶. In iMRI, for example, surgeons appreciate the fact that they have a better visualisation and a higher chance of a complete resection of the tumor but, in contrast, they prefer shorter procedure times and with the use of iMRI these can be

increased up to two hours^{21,27}. In addition, a reduction of complications, like tumor-bed hematoma formation may be achieved with iMRI detection^{17,21}. From a manufacturing standpoint, iMRI is viewed as successful due to the reputation and competitive benefits from good system performance in an operating room¹⁶.

For the imaging modalities discussed above, when used in open surgery, the surgeon must look away from the operative field to review the images on a screen; this is not the most ideal situation. With augmented reality the imaging results are projected onto the operative field which allows the visualization of different types of images merged with each other. Those images can be obtained pre-operatively, which allow more detailed planning of the operation beforehand. The major limitation with this approach is the deformation of soft tissue during the surgical procedure and the orientation of the image display in relation to the surgical field. The application of augmented reality is most promising in the treatment of tumors associated with bone structures⁸. However, the challenges for minimal invasive surgery are shifted to limited depth perception and haptic feedback leading to a disconnection between the hand and eye⁷². With augmented reality a patient-specific virtual model can be created for open or minimal invasive surgery to assist surgeons in maintaining 3D interpretations as in robotic procedures^{8,73}.

It should be noted that none of the modalities described provide comprehensive medical information. Due to improvements in conventional imaging modalities the expectations placed on imaging systems have increased and none of them are without any limitations^{74,75}. Hybrid or multimodality imaging is commonly employed in diagnostics (e.g. PET-CT or SPECT) to combine functional and anatomical information.

Is it necessary to have the amount of signal intensity or contrast agent in each cubic centimeter or is the signal intensity/amount of contrast agent in arbitrary units per pixel/voxel sufficient? Surgical decisions are generally based on visual interpretation of data, which gives only an impression and does not lead to linear obtained results. What data is necessary for a particular medical/clinical outcome? Does an improved clinical outcome rely on absolute numbers during surgery? And can this data be generated in sufficient time for

the patient/surgeon? Most imaging modalities are unable to provide absolute quantification due to noise, scattering and motion, or the absence of a standard. All ten modalities reviewed here allow relative quantification, assuming that the signals are independent of the position in the sample and no motion artefacts are present. Although absolute quantification is preferred, particularly in therapy-response monitoring, relative quantification is sufficient in practice and for most other indications. The future of medical imaging is in the transfer of images to data with a high negative power and a focus on sensitivity.

Finally, standardization is necessary to achieve reproducible and reliable information, which makes interinstitutional comparisons feasible and facilitates the implementation of new techniques from one site to another. Especially in case of quantification, standardization is a prerequisite. To achieve images which are intuitive to interpret, reproducibility and reliability are key parameters. Each modality requires technical standardization for both signal acquisition and image reconstruction, and to account for the biological factors of the contrast agent and the heterogeneity of every patient. The technical factors can be standardized relatively easily with the use of standard operating protocols (SOPs) and an accurate quality assurance program, including validated libraries or calibration curves for the contrast agent. As an example, the REMARK study gave recommendations for how to report results about tumor markers in a standardized way for assessment of the quality and generalizability for further research⁷⁸. A similar protocol should be developed for imaging and molecular modalities used in surgery.

In conclusion, every modality has its own strengths and no single modality will be suitable for all surgical procedures and fields. Strict selection of modalities per cancer type and surgical requirements is required as well as combining modalities in order to increase visibility and decrease noise. The range of available modalities at differing levels of development makes comparison necessarily qualitative. Eventually, standardization of data across the different imaging and molecular modalities will enable data to be compared in an equipollent manner.

Acknowledgment/Disclosure of funding

This research has been made possible with the support of a European Union H2020-MSCA-RISE grant (644373– PRISAR) and by the Bas Mulder Award (UL2015-7665) from the Alpe d’Huzes Foundation/Dutch Cancer Society. The research performed at M4I was made possible with the support of the LINK program of the Dutch Province of Limburg. The financial support for this study did not have any influence on the collection, analysis, and interpretation of the data as the authors declare that there is no conflict of interest. We are grateful for the assistance of Alan Chan, Hang Nguyen, Ron Heeren, Alan Perkins and John Lees with the manuscript. We thank Siemens Healthcare for providing the images shown in **Figure 1**.

References

1. Mondal SB, Gao S, Zhu N, Liang R, Gruev V, Achilefu S. Real-time fluorescence image-guided oncologic surgery. *Adv Cancer Res* 2014;**124**: 171-211.
2. Weissleder R, Pittet MJ. Imaging in the era of molecular oncology. *Nature* 2008;**452**(7187): 580-589.
3. Vahrmeijer AL, Hutteman M, van der Vorst JR, van de Velde CJ, Frangioni JV. Image-guided cancer surgery using near-infrared fluorescence. *Nat Rev Clin Oncol* 2013;**10**(9): 507-518.
4. de Boer E, Harlaar NJ, Taruttis A, Nagengast WB, Rosenthal EL, Ntziachristos V, van Dam GM. Optical innovations in surgery. *Br J Surg* 2015;**102**(2): e56-72.
5. Tempany CM, Jayender J, Kapur T, Bueno R, Golby A, Agar N, Jolesz FA. Multimodal imaging for improved diagnosis and treatment of cancers. *Cancer* 2015;**121**(6): 817-827.
6. Keereweer S, Van Driel PB, Snoeks TJ, Kerrebijn JD, Baatenburg de Jong RJ, Vahrmeijer AL, Sterenberg HJ, Lowik CW. Optical image-guided cancer surgery: challenges and limitations. *Clin Cancer Res* 2013;**19**(14): 3745-3754.
7. Benckert C, Bruns C. The Surgeon's Contribution to Image-Guided Oncology. *Viszeralmedizin* 2014;**30**(4): 232-236.
8. Nijmeh AD, Goodger NM, Hawkes D, Edwards PJ, McGurk M. Image-guided navigation in oral and maxillofacial surgery. *Br J Oral Maxillofac Surg* 2005;**43**(4): 294-302.
9. Rosenthal EL, Warram JM, Bland KI, Zinn KR. The status of contemporary image-guided modalities in oncologic surgery. *Ann Surg* 2015;**261**(1): 46-55.
10. Sanguinetti A, Lucchini R, Santoprete S, Bistoni G, Avenia S, Triola R, Avenia N. Surgical margins in breast-conserving therapy: current trends and future prospects. *Ann Ital Chir* 2013;**84**(6): 595-606.
11. Sarantopoulos A, Beziere N, Ntziachristos V. Optical and opto-acoustic interventional imaging. *Ann Biomed Eng* 2012;**40**(2): 346-366.
12. Calligaris D, Norton I, Feldman DR, Ide JL, Dunn IF, Eberlin LS, Cooks RG, Jolesz FA, Golby AJ, Santagata S, Agar NY. Mass spectrometry imaging as a tool for surgical decision-making. *J Mass Spectrom* 2013;**48**(11): 1178-1187.
13. Balog J, Sasi-Szabo L, Kinross J, Lewis MR, Muirhead LJ, Veselkov K, Mirnezami R, Dezso B, Damjanovich L, Darzi A, Nicholson JK, Takats Z. Intraoperative tissue identification using rapid evaporative ionization mass spectrometry. *Sci Transl Med* 2013;**5**(194): 194ra193.
14. Balog J, Szaniszló T, Schaefer KC, Denes J, Lopata A, Godorhazy L, Szalay D, Balogh L, Sasi-Szabo L, Toth M, Takats Z. Identification of biological tissues by rapid evaporative ionization mass spectrometry. *Anal Chem* 2010;**82**(17): 7343-7350.
15. Takats Z, Strittmatter N, McKenzie JS. Ambient Mass Spectrometry in Cancer Research. *Adv Cancer Res* 2017;**134**: 231-256.
16. Jolesz FA, Kettenbach J, Grundfest WS. Cost-effectiveness of image-guided surgery. *Acad Radiol* 1998;**5 Suppl 2**: S428-431.
17. Buchfelder M, Schlaffer SM. Intraoperative magnetic resonance imaging during surgery for pituitary adenomas: pros and cons. *Endocrine* 2012;**42**(3): 483-495.

18. Cantisani V, Grazhdani H, Fioravanti C, Rosignuolo M, Calliada F, Messineo D, Bernieri MG, Redler A, Catalano C, D'Ambrosio F. Liver metastases: Contrast-enhanced ultrasound compared with computed tomography and magnetic resonance. *World J Gastroenterol* 2014;**20**(29): 9998-10007.
19. Chi C, Du Y, Ye J, Kou D, Qiu J, Wang J, Tian J, Chen X. Intraoperative imaging-guided cancer surgery: from current fluorescence molecular imaging methods to future multi-modality imaging technology. *Theranostics* 2014;**4**(11): 1072-1084.
20. D'Andrea K, Dreyer J, Fahim DK. Utility of Preoperative Magnetic Resonance Imaging Coregistered with Intraoperative Computed Tomographic Scan for the Resection of Complex Tumors of the Spine. *World Neurosurg* 2015;**84**(6): 1804-1815.
21. Ginat DT, Swearingen B, Curry W, Cahill D, Madsen J, Schaefer PW. 3 Tesla intraoperative MRI for brain tumor surgery. *Journal of magnetic resonance imaging : JMRI* 2014;**39**(6): 1357-1365.
22. Hollon T, Lewis S, Freudiger CW, Sunney Xie X, Orringer DA. Improving the accuracy of brain tumor surgery via Raman-based technology. *Neurosurg Focus* 2016;**40**(3): E9.
23. Hosoda T, Takeuchi H, Hashimoto N, Kitai R, Arishima H, Kodera T, Higashino Y, Sato K, Kikuta K. Usefulness of intraoperative computed tomography in surgery for low-grade gliomas: a comparative study between two series without and with intraoperative computed tomography. *Neurol Med Chir (Tokyo)* 2011;**51**(7): 490-495.
24. Ji S, Fan X, Paulsen KD, Roberts DW, Mirza SK, Lollis SS. Intraoperative CT as a registration benchmark for intervertebral motion compensation in image-guided open spinal surgery. *Int J Comput Assist Radiol Surg* 2015;**10**(12): 2009-2020.
25. Joo I. The role of intraoperative ultrasonography in the diagnosis and management of focal hepatic lesions. *Ultrasonography* 2015;**34**(4): 246-257.
26. Patel KS, Yao Y, Wang R, Carter BS, Chen CC. Intraoperative magnetic resonance imaging assessment of non-functioning pituitary adenomas during transsphenoidal surgery. *Pituitary* 2016;**19**(2): 222-231.
27. Prada F, Del Bene M, Moiraghi A, Casali C, Legnani FG, Saladino A, Perin A, Vetrano IG, Mattei L, Richetta C, Saini M, DiMeco F. From Grey Scale B-Mode to Elastasonography: Multimodal Ultrasound Imaging in Meningioma Surgery-Pictorial Essay and Literature Review. *Biomed Res Int* 2015;**2015**: 925729.
28. Santagata S, Eberlin LS, Norton I, Calligaris D, Feldman DR, Ide JL, Liu X, Wiley JS, Vestal ML, Ramkissoon SH, Orringer DA, Gill KK, Dunn IF, Dias-Santagata D, Ligon KL, Jolesz FA, Golby AJ, Cooks RG, Agar NY. Intraoperative mass spectrometry mapping of an onco-metabolite to guide brain tumor surgery. *Proc Natl Acad Sci U S A* 2014;**111**(30): 11121-11126.
29. Tsuchimochi M, Hayama K. Intraoperative gamma cameras for radioguided surgery: technical characteristics, performance parameters, and clinical applications. *Phys Med* 2013;**29**(2): 126-138.
30. Valdes PA, Roberts DW, Lu FK, PhD, Golby A. Optical technologies for intraoperative neurosurgical guidance. *Neurosurg Focus* 2016;**40**(3): E8.

31. Ghosh D, Bagley AF, Na YJ, Birrer MJ, Bhatia SN, Belcher AM. Deep, noninvasive imaging and surgical guidance of submillimeter tumors using targeted M13-stabilized single-walled carbon nanotubes. *Proceedings of the National Academy of Sciences of the United States of America* 2014;**111**(38): 13948-13953.
32. Welsher K, Sherlock SP, Dai H. Deep-tissue anatomical imaging of mice using carbon nanotube fluorophores in the second near-infrared window. *Proc Natl Acad Sci U S A* 2011;**108**(22): 8943-8948.
33. Gao W, Wang Z, Lv L, Yin D, Chen D, Han Z, Ma Y, Zhang M, Yang M, Gu Y. Photodynamic Therapy Induced Enhancement of Tumor Vasculature Permeability Using an Upconversion Nanoconstruct for Improved Intratumoral Nanoparticle Delivery in Deep Tissues. *Theranostics* 2016;**6**(8): 1131-1144.
34. Liu J, Chen Z, Wang T, Liu L, Zhao L, Guo G, Wang D. Influence of Four Radiotracers in PET/CT on Diagnostic Accuracy for Prostate Cancer: A Bivariate Random-Effects Meta-Analysis. *Cell Physiol Biochem* 2016;**39**(2): 467-480.
35. Kircher MF, Willmann JK. Molecular body imaging: MR imaging, CT, and US. part I. principles. *Radiology* 2012;**263**(3): 633-643.
36. Tang R, Buckley JM, Fernandez L, Coopey S, Aftreth O, Michaelson J, Saksena M, Lei L, Specht M, Gadd M, Yagi Y, Rafferty E, Brachtel E, Smith BL. Micro-computed tomography (Micro-CT): a novel approach for intraoperative breast cancer specimen imaging. *Breast cancer research and treatment* 2013;**139**(2): 311-316.
37. Moiyadi AV, Shetty P. Direct navigated 3D ultrasound for resection of brain tumors: a useful tool for intraoperative image guidance. *Neurosurg Focus* 2016;**40**(3): E5.
38. Tzoumas S, Nunes A, Deliolanis NC, Ntziachristos V. Effects of multispectral excitation on the sensitivity of molecular optoacoustic imaging. *J Biophotonics* 2015;**8**(8): 629-637.
39. Tzoumas S, Nunes A, Olefir I, Stangl S, Symvoulidis P, Glasl S, Bayer C, Multhoff G, Ntziachristos V. Eigenspectra optoacoustic tomography achieves quantitative blood oxygenation imaging deep in tissues. *Nat Commun* 2016;**7**: 12121.
40. Brochu FM, Brunker J, Joseph J, Tomaszewski MR, Morscher S, Bohndiek SE. Towards Quantitative Evaluation of Tissue Absorption Coefficients Using Light Fluence Correction in Optoacoustic Tomography. *IEEE Trans Med Imaging* 2016.
41. Das S, Thorek DL, Grimm J. Cerenkov imaging. *Adv Cancer Res* 2014;**124**: 213-234.
42. Ng AH, Blackshaw PE, Alqahtani MS, Jambi LK, Bugby SL, Lees JE, Perkins AC. A novel compact small field of view hybrid gamma camera: first clinical results. *Nucl Med Commun* 2017;**38**(9): 729-736.
43. Gupta M, Su LM. Current and evolving uses of optical coherence tomography in the genitourinary tract. *Curr Urol Rep* 2015;**16**(3): 15.
44. Peters IT, Stegehuis PL, Peek R, Boer FL, van Zwet EW, Eggermont J, Westphal JR, Kuppen PJ, Trimbos JB, Hilders CG, Lelieveldt BP, van de Velde CJ, Bosse T, Dijkstra J, Vahrmeijer AL. Noninvasive Detection of Metastases and Follicle

- Density in Ovarian Tissue Using Full-Field Optical Coherence Tomography. *Clin Cancer Res* 2016.
45. Erickson-Bhatt SJ, Nolan RM, Shemonski ND, Adie SG, Putney J, Darga D, McCormick DT, Cittadine AJ, Zysk AM, Marjanovic M, Chaney EJ, Monroy GL, South FA, Cradock KA, Liu ZG, Sundaram M, Ray PS, Boppart SA. Real-time Imaging of the Resection Bed Using a Handheld Probe to Reduce Incidence of Microscopic Positive Margins in Cancer Surgery. *Cancer research* 2015;**75**(18): 3706-3712.
 46. Highsmith JT, Highsmith MJ, Monheit GD. Histologic Accuracy of Mohs Micrographic Surgery. *Dermatologic surgery : official publication for American Society for Dermatologic Surgery [et al]* 2017.
 47. Wu B, Warnock G, Zaiss M, Lin C, Chen M, Zhou Z, Mu L, Nanz D, Tuura R, Delso G. An overview of CEST MRI for non-MR physicists. *EJNMMI Phys* 2016;**3**(1): 19.
 48. Seeram E. *Computed Tomography, physical principles, clinical applications, and quality control* (4th edn). Elsevier: St. Louis, 2016; 474.
 49. Khokhlova TD, Haider Y, Hwang JH. Therapeutic potential of ultrasound microbubbles in gastrointestinal oncology: recent advances and future prospects. *Therap Adv Gastroenterol* 2015;**8**(6): 384-394.
 50. Sistrom CL, McKay NL. Costs, charges, and revenues for hospital diagnostic imaging procedures: differences by modality and hospital characteristics. *J Am Coll Radiol* 2005;**2**(6): 511-519.
 51. Saini S, Seltzer SE, Bramson RT, Levine LA, Kelly P, Jordan PF, Chiango BF, Thrall JH. Technical cost of radiologic examinations: analysis across imaging modalities. *Radiology* 2000;**216**(1): 269-272.
 52. Clayburgh DR, Byrd JK, Bonfili J, Duvvuri U. Intraoperative Ultrasonography During Transoral Robotic Surgery. *Ann Otol Rhinol Laryngol* 2016;**125**(1): 37-42.
 53. *Gamma Cameras for Interventional and Intraoperative Imaging*. CRC Press, 2016; 209.
 54. King MT, Carpenter CM, Sun C, Ma X, Le QT, Sunwoo JB, Cheng Z, Prax G, Xing L. beta-Radioluminescence Imaging: A Comparative Evaluation with Cerenkov Luminescence Imaging. *J Nucl Med* 2015;**56**(9): 1458-1464.
 55. Herrmann K, NOE, Povoski S.P. *Radioguided Surgery: Current Applications and Innovative Directions in Clinical Practice*. Springer International Publishing: Switzerland, 2016; 503.
 56. Pavlov V, Meyronet D, Meyer-Bisch V, Armoiry X, Pikul B, Dumot C, Beuriat PA, Signorelli F, Guyotat J. Intraoperative Probe-Based Confocal Laser Endomicroscopy in Surgery and Stereotactic Biopsy of Low-Grade and High-Grade Gliomas: A Feasibility Study in Humans. *Neurosurgery* 2016;**79**(4): 604-612.
 57. Kothapalli SR, Liu H, Liao JC, Cheng Z, Gambhir SS. Endoscopic imaging of Cerenkov luminescence. *Biomed Opt Express* 2012;**3**(6): 1215-1225.
 58. Boppart SA, Luo W, Marks DL, Singletary KW. Optical coherence tomography: feasibility for basic research and image-guided surgery of breast cancer. *Breast Cancer Res Treat* 2004;**84**(2): 85-97.
 59. Alexander J, Gildea L, Balog J, Speller A, McKenzie J, Muirhead L, Scott A, Kontovounisios C, Rasheed S, Teare J, Hoare J, Veselkov K, Goldin R, Tekkis P,

- Darzi A, Nicholson J, Kinross J, Takats Z. A novel methodology for in vivo endoscopic phenotyping of colorectal cancer based on real-time analysis of the mucosal lipidome: a prospective observational study of the iKnife. *Surg Endosc* 2016.
60. Bauer NJ, Hendrikse F, March WF. In vivo confocal Raman spectroscopy of the human cornea. *Cornea* 1999;**18**(4): 483-488.
61. Krishnamurthy U, Neelavalli J, Mody S, Yeo L, Jella PK, Saleem S, Korzeniewski SJ, Cabrera MD, Ehterami S, Bahado-Singh RO, Katkuri Y, Haacke EM, Hernandez-Andrade E, Hassan SS, Romero R. MR imaging of the fetal brain at 1.5T and 3.0T field strengths: comparing specific absorption rate (SAR) and image quality. *J Perinat Med* 2015;**43**(2): 209-220.
62. Dula AN, Pawate S, Dortch RD, Barry RL, George-Durrett KM, Lyttle BD, Dethrage LM, Gore JC, Smith SA. Magnetic resonance imaging of the cervical spinal cord in multiple sclerosis at 7T. *Mult Scler* 2016;**22**(3): 320-328.
63. Torfeh T, Hammoud R, McGarry M, Al-Hammadi N, Perkins G. Development and validation of a novel large field of view phantom and a software module for the quality assurance of geometric distortion in magnetic resonance imaging. *Magn Reson Imaging* 2015;**33**(7): 939-949.
64. Yamamoto S, Hamamura F, Watabe T, Ikeda H, Kanai Y, Watabe H, Kato K, Ogata Y, Hatazawa J. Development of a PET/Cerenkov-light hybrid imaging system. *Med Phys* 2014;**41**(9): 092504.
65. Grootendorst MR, Cariati M, Kothari A, Tuch DS, Purushotham A. Cerenkov luminescence imaging (CLI) for image-guided cancer surgery. *Clin Transl Imaging* 2016;**4**(5): 353-366.
66. He H, Wissmeyer G, Ovsepian SV, Buehler A, Ntziachristos V. Hybrid optical and acoustic resolution optoacoustic endoscopy. *Optics letters* 2016;**41**(12): 2708-2710.
67. Grootendorst MR, Cariati M, Pinder S, Kothari A, Douek M, Kovacs T, Hamed H, Pawa A, Nimmo F, Owen J, Ramalingam V, Sethi S, Mistry S, Vyas K, Tuch D, Britten A, Van Hemelrijck M, Cook G, Sibley-Allen C, Allen S, Purushotham A. Intraoperative Assessment of Tumor Resection Margins in Breast-Conserving Surgery using 18F-FDG Cerenkov Luminescence Imaging - A First-in-Human Feasibility Study. *J Nucl Med* 2016.
68. Lees JE, Bugby SL, Alqahtani MS, Jambi LK, Dawood NS, McKnight WR, Ng AH, Perkins AC. A Multimodality Hybrid Gamma-Optical Camera for Intraoperative Imaging. *Sensors (Basel)* 2017;**17**(3).
69. Xiaowei Ma WY, Shuang Zhou, Wenhui Ma, Zhenhua Hu, Jimin Liang and Jing Wang. Study of penetration depth and resolution of Cerenkov luminescence emitted from (18)F-FDG and (131)I. *J Nucl Med* 2012;**53**(supplement 1, 55).
70. Tichauer KM, Wang Y, Pogue BW, Liu JT. Quantitative in vivo cell-surface receptor imaging in oncology: kinetic modeling and paired-agent principles from nuclear medicine and optical imaging. *Phys Med Biol* 2015;**60**(14): R239-269.
71. Blasberg R, Piwnica-Worms D. Imaging: strategies, controversies, and opportunities. *Clin Cancer Res* 2012;**18**(3): 631-637.
72. Schostek S, Ho CN, Kalanovic D, Schurr MO. Artificial tactile sensing in minimally invasive surgery - a new technical approach. *Minim Invasive Ther Allied Technol* 2006;**15**(5): 296-304.

73. Hallet J, Soler L, Diana M, Mutter D, Baumert TF, Habersetzer F, Marescaux J, Pessaux P. Trans-thoracic minimally invasive liver resection guided by augmented reality. *J Am Coll Surg* 2015;**220**(5): e55-60.
74. Culver J, Akers W, Achilefu S. Multimodality molecular imaging with combined optical and SPECT/PET modalities. *J Nucl Med* 2008;**49**(2): 169-172.
75. Garcia-Allende PB, Glatz J, Koch M, Ntziachristos V. Enriching the interventional vision of cancer with fluorescence and optoacoustic imaging. *J Nucl Med* 2013;**54**(5): 664-667.
76. Ghosh P. The role of SPECT/CT in skeletal malignancies. *Semin Musculoskelet Radiol* 2014;**18**(2): 175-193.
77. Sharma P, Jain TK, Reddy RM, Faizi NA, Bal C, Malhotra A, Kumar R. Comparison of single photon emission computed tomography-computed tomography, computed tomography, single photon emission computed tomography and planar scintigraphy for characterization of isolated skull lesions seen on bone scintigraphy in cancer patients. *Indian J Nucl Med* 2014;**29**(1): 22-29.
78. McShane LM, Altman DG, Sauerbrei W, Taube SE, Gion M, Clark GM, Statistics Subcommittee of the NCIEWGoCD. REporting recommendations for tumour MARKer prognostic studies (REMARK). *Br J Cancer* 2005;**93**(4): 387-391.
79. Bugby SL, Lees JE, Ng AH, Alqahtani MS, Perkins AC. Investigation of an SFOV hybrid gamma camera for thyroid imaging. *Phys Med* 2016;**32**(1): 290-296.
80. Liszka BM, Rho HS, Yang Y, Lenferink ATM, Terstappen LWMM, Otto C. A microfluidic chip for high resolution Raman imaging of biological cells. *Rsc Adv* 2015;**5**(61): 49350-49355.



Chapter 3

Evaluation of EphA2 and EphB4 as targets for image-guided colorectal cancer surgery

Marieke A. Stammes, Hendrica A.J.M. Prevoo, Meyke C. Ter Horst, Stéphanie A. Groot, Cornelis J.H. Van de Velde, Alan B. Chan, Lioe-Fee de Geus-Oei, Peter J.K. Kuppen, Alexander L. Vahrmeijer, Elena B. Pasquale and Cornelis F.M. Sier.

Adapted from: Evaluation of EphA2 and EphB4 as Targets for Image-Guided Colorectal Cancer Surgery, *Int J Mol Sci* 2017 Feb 3; 18(2). pii:E307

Abstract

Purpose

Targeted image-guided oncologic surgery (IGOS) relies on the recognition of cell surface-associated proteins, which should be abundantly present on tumor cells but preferably absent on cells in surrounding healthy tissue. The transmembrane receptor tyrosine kinase EphA2, a member of the A class of the Eph receptor family, has been reported to be highly overexpressed in several tumor types including breast, lung, brain, prostate, and colon cancer and is considered amongst the most promising cell membrane-associated tumor antigens by the NIH. Another member of the Eph receptor family belonging to the B class, EphB4, has also been found to be upregulated in multiple cancer types.

Procedures

In this study, EphA2 and EphB4 are evaluated as targets for IGOS of colorectal cancer by immunohistochemistry (IHC) using a tissue microarray (TMA) consisting of 168 pairs of tumor and normal tissue. The IHC sections were scored for staining intensity and percentage of cells stained.

Results

The results show a significantly enhanced staining intensity and more widespread distribution in tumor tissue compared with adjacent normal tissue for EphA2 as well as EphB4.

Conclusions

Based on its more consistently higher score in colorectal tumor tissue compared to normal tissue, EphB4 appears to be a promising candidate for IGOS of colorectal cancer. *In vitro* experiments using antibodies on human colon cancer cells confirmed the possibility of EphB4 as target for imaging.

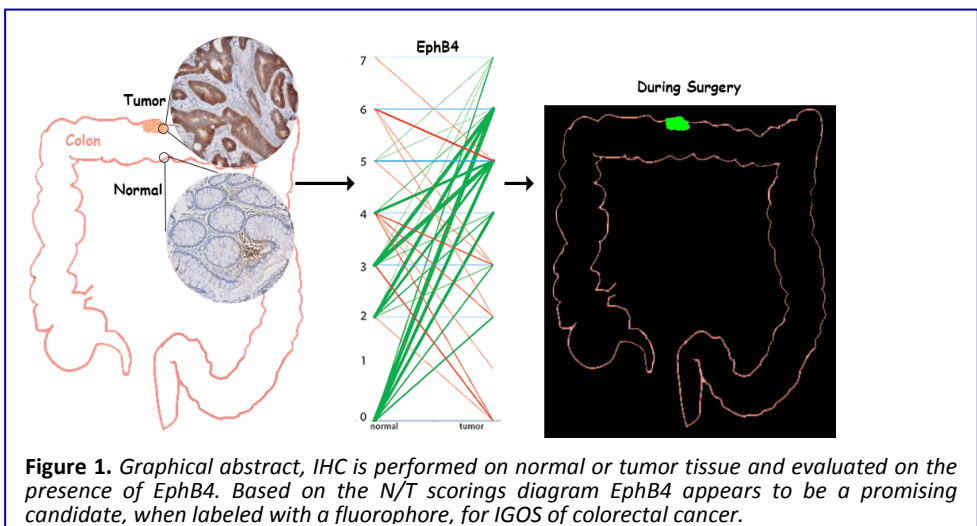


Figure 1. Graphical abstract, IHC is performed on normal or tumor tissue and evaluated on the presence of EphB4. Based on the N/T scorings diagram EphB4 appears to be a promising candidate, when labeled with a fluorophore, for IGOS of colorectal cancer.

Introduction

During oncologic surgery, there is limited information available about the exact boundaries between tumor and healthy tissue. Visual inspection and palpation are often not enough, leading to incomplete resection of the tumor or substantial damage of healthy tissue ¹. Imaging of tumor tissue by targeted real-time near-infrared (NIR) fluorescence is a novel technique that can help the surgeon during an operation ^{1,2}. Besides the quality of the camera system, the effectiveness of this technique relies mainly on the choice of targeted tumor protein. Receptors and adhesion molecules upregulated on the surface of tumor cells are the best candidates for targeted cancer imaging, but the ideal protein for colorectal cancer imaging has not yet been identified ³. Cell surface-associated proteins such as MUC1, EGFR, HER2, PSMA, and CEA are highly ranked on the National Cancer Institute (NCI) prioritization list of cancer antigens and are amongst the most pursued biomarkers for imaging ⁴. We decided to evaluate one of the next candidates on the list, EphA2, a member of the Eph family of receptor tyrosine kinases that is preferentially expressed in tumor tissue compared to normal tissue and plays an important role in cancer malignancy ^{4,5}. Furthermore, we included the family member EphB4 because its overexpression has also been reported in various cancer types ⁶. As a target for tumor imaging, a low grade of expression of both EphA2 and EphB4 in normal tissue is essential and has not been thoroughly investigated ⁵⁻⁷.

EphA2 and EphB4 are known to be upregulated, particularly in the early stages of colorectal cancer ^{5,8,9}. In those early stages, surgery without additional systemic therapy is the main treatment modality, which makes accurate recognition and removal of the tumor essential ^{10,11}. Whether a protein target like EphA2 or EphB4 is suitable for image-guided oncologic surgery (IGOS) is determined by its expression pattern in the tumor in comparison with the surrounding normal tissue. In this study, we evaluate the expression patterns of EphA2 and EphB4 by immunohistochemical (IHC) staining of a tissue microarray (TMA) consisting of pairs of tumor and normal colon tissue. Furthermore, the principle of using these Eph proteins for imaging is evaluated *in vitro* using various cancer cell lines.

Materials and Methods

Tissue Micro Array (TMA)

Formalin-fixed paraffin-embedded (FFPE) tissue blocks of primary tumors and their respective normal tissues were collected from the pathology department of the Leiden University Medical Center (Leiden, the Netherlands). Sections were cut for hematoxylin-eosin staining and histopathologically representative tumor regions were used for preparation of TMA blocks. From each donor block, three 0.6 mm diameter tissue cores were punched from tumor areas and transferred into a recipient paraffin block using a custom-made precision instrument. Because the TMA was designed to evaluate the expression of EphA2 or EphB4 throughout the whole tumor, cores were taken from three different locations across the tumor tissue, plus one outside the tumor, in healthy looking tissue.

Immunohistochemistry

IHC staining of the TMA was performed on 4 μm sections cut from each TMA receiver block. TMA sections were deparaffinized and rehydrated. Endogenous peroxidase was blocked for 20 min in 0.3% hydrogen peroxide in water. The slides were treated for antigen retrieval in citrate buffer (pH 6) for 10 min at 95 °C (DAKO PT Link, Glostrup, Denmark). Sections were incubated overnight with primary antibodies. The antibodies used for EphA2 staining were a polyclonal rabbit (34-7400, Invitrogen/Thermo Fisher Scientific, Waltham, MA, USA) and a polyclonal goat (AF3035, R&D Systems, Minneapolis, MN, USA). Antibodies used for EphB4 were a monoclonal mouse IgG1 (37-1800, Life Technologies/Thermo Fisher Scientific, Waltham, MA, USA) and a polyclonal goat (AF3038, R&D Systems). The optimal dilution for staining colon cancer tissue sections was optimized for all 4 antibodies. After 30 min of incubation with DAKO envision containing horseradish peroxidase conjugated goat anti-rabbit, goat anti-mouse, or rabbit anti-goat antibodies (DAKO Cytomation, Glostrup, Denmark), the sections were visualized using a diaminobenzidine solution (DAB+; DAKO kit). The sections were counterstained with hematoxylin, dehydrated, and mounted with pertex (Histolab). The entire slides were scanned with a Philips Ultra Fast Scanner 1.6 RA (Philips, Eindhoven, the Netherlands) for further analysis.

Scoring Method

The TMA sections were semi-quantitatively scored for EphA2 or EphB4 staining by two independent examiners (MS, HP) using Philips Digital Pathology Solutions-software (Philips, Eindhoven, the Netherlands). TMA cores were used when 50% or more was occupied by tissue. The intensity and percentage of positive tumor cells within each core were scored independently and categorized. The intensity score of epithelial staining was defined as 0 when there was no staining; 1 for weak staining; 2 for moderate staining; or 3 for strong staining. The percentage of cells stained was scored 0 when the percentage was 0%; 1 when <25% was stained; 2 for 25%–50% staining; 3 for 50%–90% staining and 4 when >90% of the cells was stained. The two scored parameters were added up into a final score (0–7) for each core. Only tumors with a minimum of 2 cores were used. The median of the score for each tissue was used for data analysis. Only complete sets of tumor and normal tissue were used for further analysis, for a total of 168 tumors.

Cell Culture, Flow Cytometry, and Chamber Slide Assay

Cancer cell lines A549 (lung), BT-20 (breast), HT-29 (colon), and Jurkat (leukemic T-cell lymphoblast) were grown in RPMI or DMEM (Gibco, LifeTechnologies, Carlsbad, CA, USA) as appropriate, with 10% fetal calf serum and 100 IU/mL penicillin/streptomycin (Gibco) at 37 °C in a humidified incubator with 5% CO₂. The presence of Eph2A and Eph4B on the membranes of these cells was determined by flow cytometry. Cells were cultured until 90% confluence and detached with trypsin/EDTA. Viability of the cells was evaluated with trypan blue. The cells were incubated with 4 µg/mL polyclonal goat antibodies AF3035 and AF3038, against respectively Eph2A and Eph4B for 30 minutes on ice, washed with ice cold phosphate buffered saline pH7.5 (PBS), and incubated with anti-goat secondary antibody conjugated with fluorescein isothiocyanate (FITC) (A11078, Life Technologies). The cells were then centrifuged, washed, and suspended in PBS containing propidium iodide to exclude dead cells and consequently analyzed in a BD LSRII flow cytometer (BD Biosciences, San Jose, CA, USA) with FlowJo (Tree Star Inc., Ashland, OR, USA). For the plate assay, HT-29 colon cancer cells were grown in 8-well chamber slides (Thermo Scientific, Waltham, MA, USA) under conditions described above. At 75–80% confluence, the cells were fixated with 4% paraformaldehyde for 10 minutes. After washings with PBS, the cells were incubated with a rabbit monoclonal anti-EphB4 antibody conjugated with

phycoerythrine (SinoBiological Inc., LuDong Area, BDA, Beijing, P.R. China). The cells were washed and dried. The slides were covered with Prolong Gold with DAPI (Life Technologies) and visualized using a Leica DFC350 FX fluorescence microscope (Leica, Wetzlar, Germany).

Statistical Analysis

Statistical analyses were conducted using SPSS statistical software (version 20.0 for Windows, SPSS Inc., Chicago, IL, USA). Scores are presented as mean \pm standard deviation. Differences between groups are calculated using a Student's paired *t*-test. For the difference in differentiation in relation to tumor stage, a chi-square test was used. All statistical tests were conducted two-sided, and *p*-values of 0.05 or less were considered significant.

Results

A total of 168 tumor/normal pairs were suitable for evaluation of both EphA2 and EphB4. The main characteristics of the patients and the tumors are presented in Table 1. In a preliminary evaluation on five sets of tumor and normal tissue sections, two different antibodies recognizing EphA2 and two different antibodies recognizing EphB4 showed similar staining patterns.

Table 1. Patient and tumor characteristics of the 168 colorectal cancer patients in this study.

Characteristic	Group	Percentage (%)
Gender	Male	48.1
	Female	51.9
Age	<50	11.3
	\geq 50	88.7
Stage	I	20.3
	IIA	25.0
	IIB	1.9
	IIIA	3.8
	IIIB	21.8
	IIIC	8.3
	IV	18.6
Differentiation	Good	25.7
	Moderate	64.2
	Poor	10.2

Therefore, only one antibody recognizing each receptor (rabbit polyclonal 34–7400 for EphA2 and mouse monoclonal 37–1800 for EphB4) was selected for screening the TMA. All stained tissues were evaluated by two examiners and their scores showed a strong positive correlation ($R^2 = 0.86$, $p \leq 0.001$). Inter-observer agreement was obtained by re-evaluation of the respective sections. Staining for EphA2 and EphB4 was generally present in epithelial cells throughout the whole tumor area consisting of 2 or 3 TMA cores (Fig. 2). EphA2 staining was also widely detected in endothelial cells, whereas EphB4 staining was only occasionally found in endothelial cells. In general, tumor tissue showed more staining for both Eph receptors than the corresponding normal mucosa, but there were a few aberrant cases in which normal tissue showed more staining.

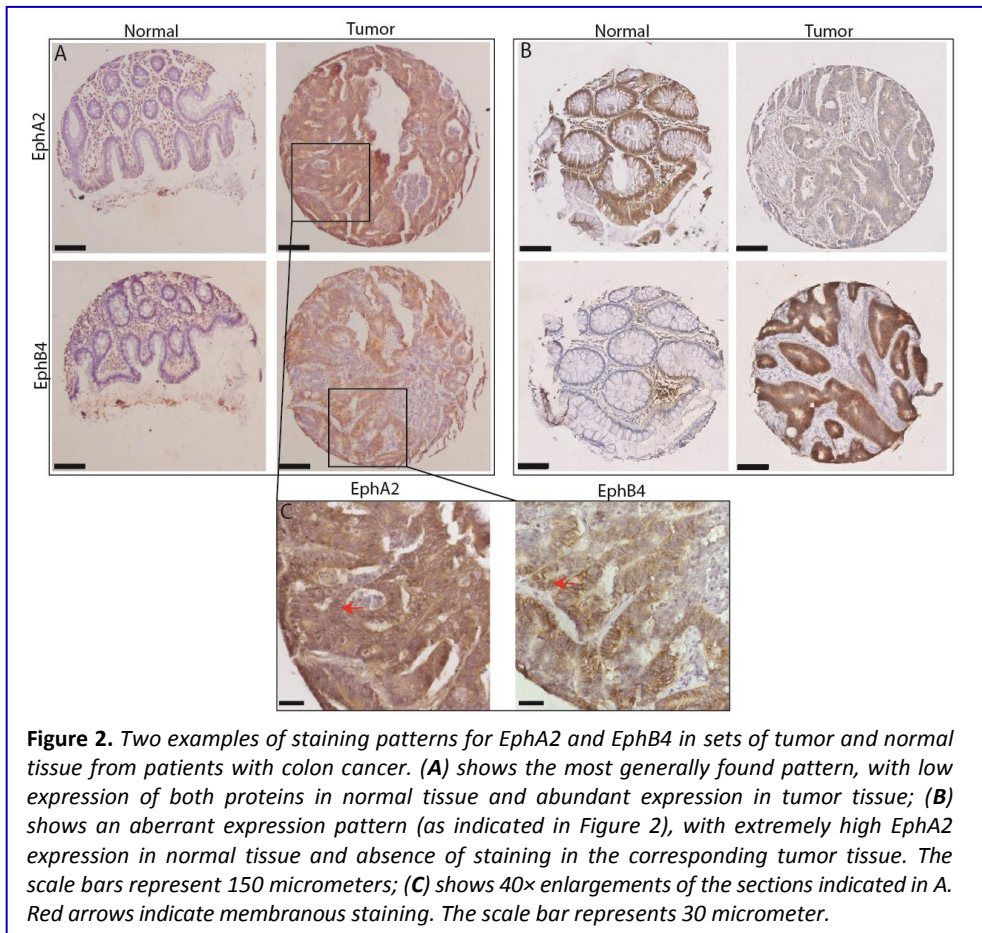
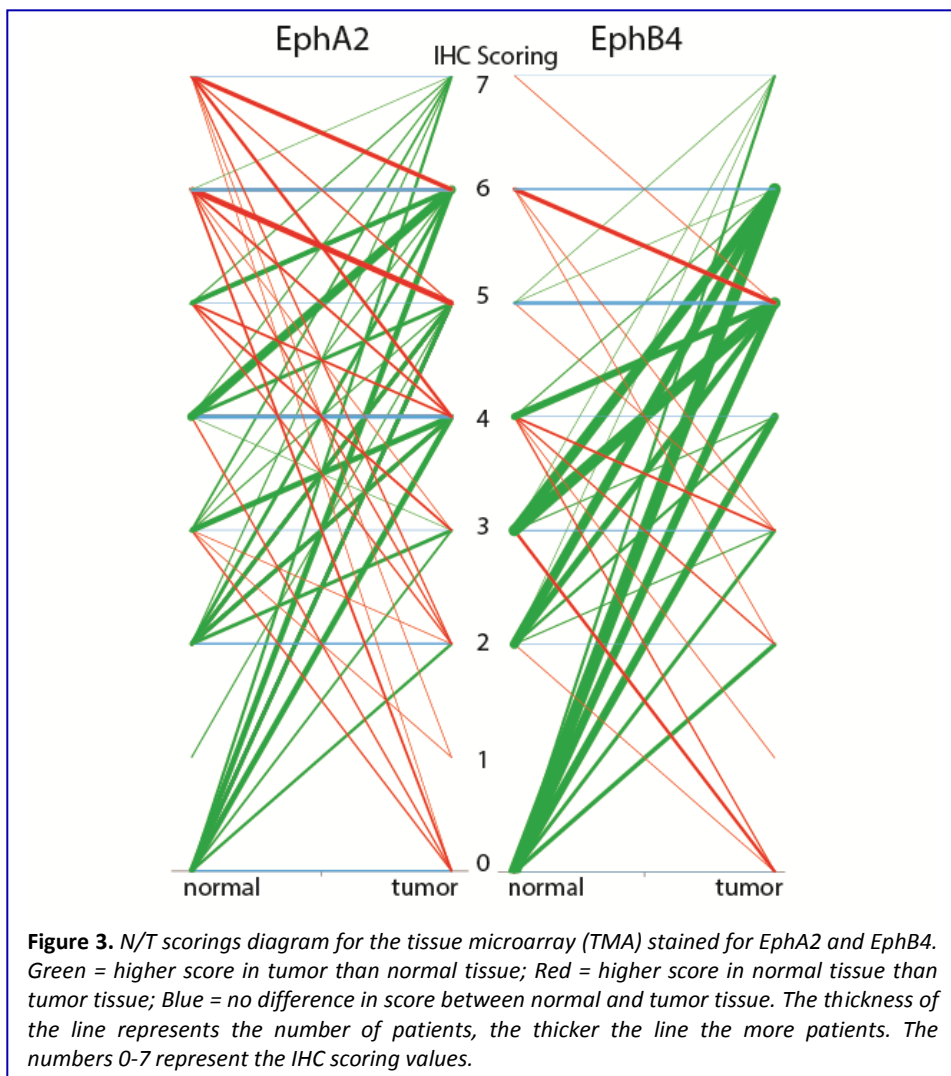


Figure 2. Two examples of staining patterns for EphA2 and EphB4 in sets of tumor and normal tissue from patients with colon cancer. (A) shows the most generally found pattern, with low expression of both proteins in normal tissue and abundant expression in tumor tissue; (B) shows an aberrant expression pattern (as indicated in Figure 2), with extremely high EphA2 expression in normal tissue and absence of staining in the corresponding tumor tissue. The scale bars represent 150 micrometers; (C) shows 40x enlargements of the sections indicated in A. Red arrows indicate membranous staining. The scale bar represents 30 micrometer.

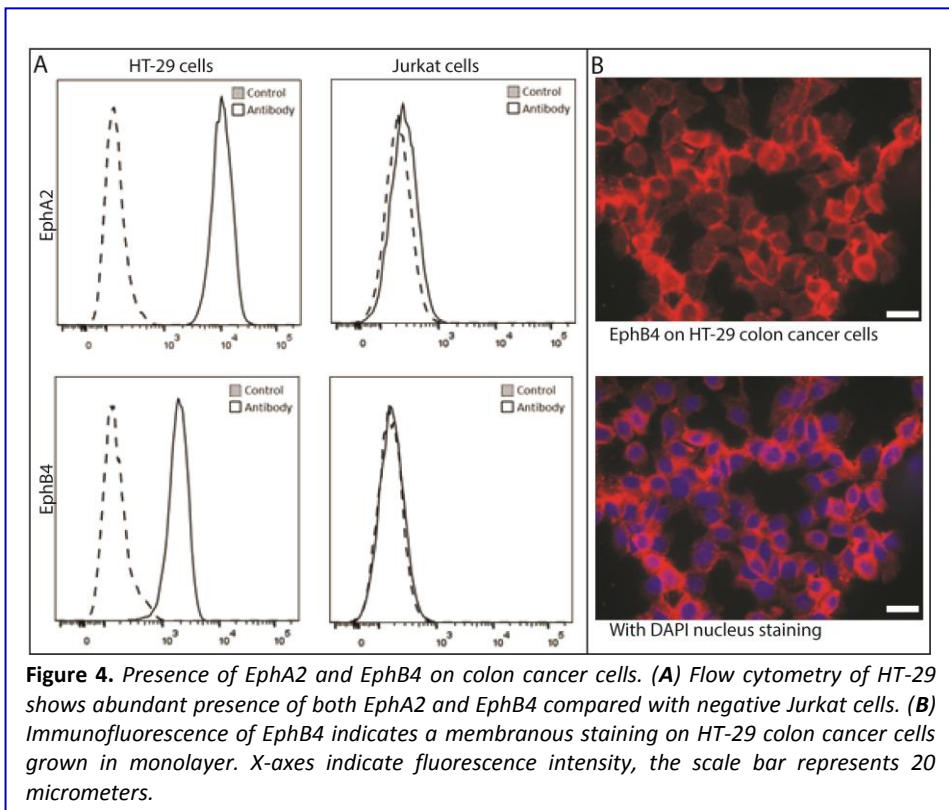
significantly correlate ($R^2 = 0.08$, $p = 0.165$, $n = 336$). Figure 2A shows a typical example of a Stage III patient with high EphA2 and EphB4 staining in the tumor and low staining in normal mucosa. Figure 2B presents a particular case in which normal tissue showed more EphA2 staining than the corresponding Stage III tumor. For EphA2, the mean score for the tumors (4.3 ± 1.8) was significantly higher ($p < 0.001$) compared with the corresponding normal tissue (3.3 ± 2.3). For EphB4, the difference between tumor and normal mucosa was even more pronounced, with scores of respectively 4.6 ± 1.6 versus 2.3 ± 1.9 ($p < 0.001$).

There was no association between the clinical-pathological variables “tumor



stage” or “differentiation” and the score for EphA2 or EphB4 staining. For imaging purposes, the over-expression of a protein target in tumors compared to adjacent normal tissue is more important than high tumor expression per se. Therefore, in the normal to tumor (N/T) scoring diagram in Figure 3, we show a graphical representation of the differences in EphA2 and EphB4 expression in normal versus tumor tissue for individual patients. The IHC score of a normal tissue (left side) is connected by a line with the score of the corresponding tumor tissue (right side).

Green lines indicate that the tumor score was higher than the score of the corresponding normal tissue, whereas red lines indicate the opposite. Blue lines indicate no difference between tumor and normal tissue. The thickness of the lines is proportional to the number of pairs with identical scores; the thicker the line, the more pairs there are. The diagram indicates that there is more variation in the N/T ratios for EphA2 than for EphB4. Although both Eph receptors show some unfavorable red lines, the majority of tissue sets (73% for EphA2 and 88% for EphB4) have green lines. Interestingly, the frequency of pairs with at least two score points difference between N and T is 46% for



EphA2 versus 69% for EphB4. The frequency for a three-point difference becomes 30% for EphA2 versus 52% for EphB4, and for a four-point difference it becomes 23% for EphA2 versus 35% for EphB4.

The other most important characteristic for a protein to become a candidate target for imaging next to upregulation in the tumor cells is the availability on the cell membrane of these cells. Being receptors, the majority of the EphA2 and EphB4 would be expected on the cells rather than inside. **Figure 2C** shows that in our IHC evaluation this is clearly the case for EphB4 and, to a lesser extent for EphA2. Because of the observed advantages of EphB4 with respect to upregulation and cellular localization in

IHC, we performed *in vitro* experiments on various tumor cell lines to evaluate whether EphB4 is targetable on these cells. All cancer cell lines, i.e., lung, breast, and colon, showed an enhanced presence of both EphA2 and EphB4 compared with Jurkat control cells, as shown for colon cancer cell line HT-29 in **Figure 4A**. A chamber slide assay confirmed the accessibility of EphB4 on HT-29 cells grown on chamber slides in monolayer (**Fig. 4B**).

Discussion

In theory, any upregulated protein specifically present in cancer tissue could be a potential target for IGOS, but in practice the proteins expressed on the surface of tumor cells are the best candidates³. Cheever and colleagues ranked EphA2 as one of the highest cell surface antigens for cancer treatment⁴. Therefore, in this study, we evaluated whether the EphA2 receptor and the related EphB4 receptor are suitable for use in image-guided colorectal cancer surgery^{5-7,12,13}.

Our IHC evaluation of 168 sets of N/T tissue showed a statistically significant upregulation in tumor tissue compared with normal tissue for both EphA2 and EphB4 in the majority of the patients. Both Eph receptors were detected in tumors of various stages and grades and in tumor areas that were suitable for imaging. Therefore, both Eph receptors seem to be valid candidate targets for IGOS of colorectal cancer. However, as clearly illustrated by the patient specific N/T scorings diagram, the value of EphA2 as a clinically usable target is problematic because of the presence of high EphA2 staining in some of the normal tissues. This phenomenon is much less evident for EphB4, making this receptor the better candidate target for IGOS. The higher EphB4 expression in colon cancer compared to normal mucosa was previously also shown at the mRNA level in 62 tissue pairs, with validation at the protein level in only a few samples¹⁴. Although we did not find a significant correlation between EphA2 or EphB4 expression and the stage or differentiation grade of the tumors, earlier studies found both EphA2 and EphB4 to be preferentially upregulated in the early cancer stages (Stages I and II)^{5-9,15}. Over-expression in early colorectal cancer stages is particularly advantageous for imaging during surgery, given the increased difficulty in distinguishing normal and tumor tissue morphologically and the fact that, for early stage tumors, surgery is often not accompanied by chemotherapy. Interestingly, earlier studies using Q-PCR to analyze 53 paired normal and colorectal cancer samples showed that EphB4 is more significantly overexpressed in tumor tissue compared to normal tissue than EphA2^{5,12}. This characteristic supports the choice of EphB4 as a target for IGOS.

Multiple publications have shown that EphA2 overexpression is strongly correlated with tumor progression; consequently, high EphA2 levels are associated with worse patient survival^{8,13,16}. High EphB4 expression has also been correlated with poor patient survival¹⁷⁻¹⁹, although some studies have

also found an opposite correlation¹⁵. The signaling effects of EphA2 and EphB4 in cancer are complex, and not only tumor-promoting but also tumor-suppressing effects have been reported for these receptors^{7,20-22}. However, neither a role in carcinogenesis nor the status as a prognostic factor is relevant for the use of a protein as a target for IGOS.

The main disadvantage of our study is the use of a TMA consisting of three cores per tumor, which makes evaluation of the degree of intra-tumor heterogeneity more difficult than with the use of whole tumor sections. Another point of criticism could be the antibodies used for IHC. Although we evaluated a panel of antibodies for EphA2 as well as EphB4, the evaluation of the distribution, the scoring, and the calculations were performed with the antibody that gave the most consistent results. The selected antibodies were commercially available and both raised against C-terminal peptides of respectively EphA2 and EphB4. In general, antibodies against intracellular domains are well suited for IHC, but in most cases these antibodies are not particularly fit for flow cytometry or for determination by IHC, whether the staining is membranous rather than intracellular. Especially the antibody for EphA2 proved to be less suitable for the latter purpose. Based on these results, we cannot conclude that EphB4 is more suitable as a target for IGOS than EphA2. The flow cytometry data, performed with polyclonal antibodies against whole proteins rather than internal domains, indicated that EphA2 is at least as abundantly present on living cancer cells as EphB4. The incubation of these colon cancer cells with labeled antibodies against EphB4 demonstrates the principle that targeting of this receptor could be clinically relevant, but this should be further elucidated in pre-clinical studies using relevant mouse models.

Targeting of Eph receptors for tumor imaging purposes could be achieved using various agents, such as peptides or antibodies^{23,24}. Antibodies offer the advantage of, in general a higher specificity and affinity compared to peptides, and, thanks to molecular engineering, even bi- and tri-specific antibodies have been developed recently, which could enhance tumor specificity^{7,13,25}. Recently, a series of EphB4 antibodies has been evaluated for the use of Positron Emission Tomography (PET) in mice xenografted with human HT-29 colon cancer and MDA-MB-231 breast cells, underscoring the value of EphB4 as a target for tumor imaging²³. A recent study also developed NIR fluorescence probes for targeted imaging using an EphB4 antibody²⁶. While the use of PET for colon cancer is not suitable for routine clinical use²⁷, NIR

fluorescence-based imaging of colorectal cancer shows great potential, especially for rectal cancer²⁸.

In conclusion, both EphA2 and EphB4 show potential as target for image-guided colorectal cancer surgery, but EphB4 seems to have the best characteristics with respect to tumor/normal mucosa distribution, as shown in a relatively large cohort of 168 patients. The *in vitro* binding data confirm the presence of EphB4 on the cell membrane, which is the other important prerequisite for candidate targets for IGOS.

Acknowledgments

This work was supported by the Center for Translational Molecular Medicine: 03O-202 MUSIS, the European Research Council (ERC) through an ERC Advanced Grant (grant number 323105-SURVive) and the project grant H2020-MSCA-RISE (grant number 644373-PRISAR). Elena B. Pasquale is supported by NIH grant CA138390. We acknowledge Geeske Dekker-Ensink, Ronald van Vlierberghe, and Rob Keyzer for their valuable technical assistance during the project.

Supplementary Materials: The following are available online at: <http://www.mdpi.com/1422-0067/18/2/307#supplementary>

References

1. Vahrmeijer AL, Hutteman M, van der Vorst JR, van de Velde CJ, Frangioni JV. Image-guided cancer surgery using near-infrared fluorescence. *Nat Rev Clin Oncol*. 2013;10(9):507-518.
2. Keereweer S, Kerrebijn JD, van Driel PB, et al. Optical image-guided surgery--where do we stand? *Molecular imaging and biology : MIB : the official publication of the Academy of Molecular Imaging*. 2011;13(2):199-207.
3. Boonstra MC, De Geus SW, Prevoo HA, et al. Selecting Targets for Tumor Imaging: An Overview of Cancer-Associated Membrane Proteins. *Biomarkers in Cancer*. 2016;8:15.
4. Cheever MA, Allison JP, Ferris AS, et al. The prioritization of cancer antigens: a national cancer institute pilot project for the acceleration of translational research. *Clin Cancer Res*. 2009;15(17):5323-5337.
5. Herath NI, Boyd AW. The role of Eph receptors and ephrin ligands in colorectal cancer. *International journal of cancer Journal international du cancer*. 2010;126(9):2003-2011.
6. Xi HQ, Wu XS, Wei B, Chen L. Eph receptors and ephrins as targets for cancer therapy. *Journal of cellular and molecular medicine*. 2012;16(12):2894-2909.
7. Pasquale EB. Eph receptors and ephrins in cancer: bidirectional signalling and beyond. *Nat Rev Cancer*. 2010;10(3):165-180.
8. Dunne PD, Dasgupta S, Blayney JK, et al. EphA2 Expression Is a Key Driver of Migration and Invasion and a Poor Prognostic Marker in Colorectal Cancer. *Clin Cancer Res*. 2016;22(1):230-242.
9. Kataoka H, Igarashi H, Kanamori M, et al. Correlation of EPHA2 overexpression with high microvessel count in human primary colorectal cancer. *Cancer Sci*. 2004;95(2):136-141.
10. Barresi V, Reggiani Bonetti L, Ieni A, Branca G, Tuccari G. Histologic prognostic markers in stage IIA colorectal cancer: a comparative study. *Scandinavian journal of gastroenterology*. 2016;51(3):314-320.
11. Compton C, Fenoglio-Preiser CM, Pettigrew N, Fielding LP. American Joint Committee on Cancer Prognostic Factors Consensus Conference: Colorectal Working Group. *Cancer*. 2000;88(7):1739-1757.
12. Herath NI, Spanevello MD, Doecke JD, Smith FM, Pouponnot C, Boyd AW. Complex expression patterns of Eph receptor tyrosine kinases and their ephrin ligands in colorectal carcinogenesis. *European journal of cancer*. 2012;48(5):753-762.
13. Barquilla A, Pasquale EB. Eph receptors and ephrins: therapeutic opportunities. *Annu Rev Pharmacol Toxicol*. 2015;55:465-487.
14. Stephenson SA, Slomka S, Douglas EL, Hewett PJ, Hardingham JE. Receptor protein tyrosine kinase EphB4 is up-regulated in colon cancer. *BMC Mol Biol*. 2001;2:15.
15. Batlle E, Bacani J, Begthel H, et al. EphB receptor activity suppresses colorectal cancer progression. *Nature*. 2005;435(7045):1126-1130.
16. Tandon M, Vemula SV, Mittal SK. Emerging strategies for EphA2 receptor targeting for cancer therapeutics. *Expert opinion on therapeutic targets*. 2011;15(1):31-51.
17. Kumar SR, Masood R, Spannuth WA, et al. The receptor tyrosine kinase EphB4 is overexpressed in ovarian cancer, provides survival signals and predicts poor outcome. *Br J Cancer*. 2007;96(7):1083-1091.

18. Alam SM, Fujimoto J, Jahan I, Sato E, Tamaya T. Coexpression of EphB4 and ephrinB2 in tumour advancement of ovarian cancers. *Br J Cancer*. 2008;98(4):845-851.
19. Guijarro-Munoz I, Sanchez A, Martinez-Martinez E, et al. Gene expression profiling identifies EPHB4 as a potential predictive biomarker in colorectal cancer patients treated with bevacizumab. *Med Oncol*. 2013;30(2):572.
20. Davalos V, Dopeso H, Castano J, et al. EPHB4 and survival of colorectal cancer patients. *Cancer Res*. 2006;66(18):8943-8948.
21. Guo H, Miao H, Gerber L, et al. Disruption of EphA2 receptor tyrosine kinase leads to increased susceptibility to carcinogenesis in mouse skin. *Cancer Res*. 2006;66(14):7050-7058.
22. Yeddula N, Xia Y, Ke E, Beumer J, Verma IM. Screening for tumor suppressors: Loss of ephrin receptor A2 cooperates with oncogenic KRas in promoting lung adenocarcinoma. *Proc Natl Acad Sci U S A*. 2015;112(47):E6476-6485.
23. Liu S, Li D, Park R, et al. PET imaging of colorectal and breast cancer by targeting EphB4 receptor with ⁶⁴Cu-labeled hAb47 and hAb131 antibodies. *J Nucl Med*. 2013;54(7):1094-1100.
24. Riedl SJ, Pasquale EB. Targeting the Eph System with Peptides and Peptide Conjugates. *Curr Drug Targets*. 2015;16(10):1031-1047.
25. Dimasi N, Fleming R, Hay C, et al. Development of a Trispecific Antibody Designed to Simultaneously and Efficiently Target Three Different Antigens on Tumor Cells. *Mol Pharm*. 2015;12(9):3490-3501.
26. Li D, Liu S, Liu R, et al. Targeting the EphB4 receptor for cancer diagnosis and therapy monitoring. *Mol Pharm*. 2013;10(1):329-336.
27. Kijima S, Sasaki T, Nagata K, Utano K, Lefor AT, Sugimoto H. Preoperative evaluation of colorectal cancer using CT colonography, MRI, and PET/CT. *World journal of gastroenterology*. 2014;20(45):16964-16975.
28. Torok JA, Palta M, Willett CG, Czito BG. Nonoperative management of rectal cancer. *Cancer*. 2016;122(1):34-41.



Chapter 4

Fluorescence- and multispectral optoacoustic imaging for an optimised detection of deeply located tumors in an orthotopic mouse model of pancreatic carcinoma

Joanna Napp*, Marieke A. Stammes*, Jing Claussen, Hendrica A.J.M. Prevoo, Cornelis F. M. Sier, Freek J. M. Hoeben, Marc S. Robillard, Alexander L. Vahrmeijer, Tim Devling, Alan B. Chan, Lioe-Fee de Geus-Oei, Frauke Alves.

*equal contribution

Adapted from: Fluorescence- and multispectral optoacoustic imaging for an optimised detection of deeply located tumors in an orthotopic mouse model of pancreatic carcinoma, *Int J Cancer* 2017 Dec 26. Doi:10.1002/ijc.31236

Abstract

Purpose

A crucial point for the management of pancreatic ductal adenocarcinoma (PDAC) is the decrease of R1 resections. Our aim was to evaluate the combination of multispectral optoacoustic tomography (MSOT) with fluorescence-guided surgery (FGS) for diagnosis and perioperative detection of tumor nodules and resection margins in a xenotransplant mouse model of human pancreatic cancer. As MSOT and FGS are novel technologies which can be used to improve visualisation of specifically labeled tissue.

Procedures

The peptide cRGD, conjugated with the near infrared fluorescent (NIRF) dye IRDye800CW and with a transcyclooctene (TCO) tag for future click chemistry (cRGD-800CW-TCO), was applied to PDAC bearing immunodeficient nude mice. 27 days after orthotopic transplantation of human AsPC-1 cells into the head of the pancreas, mice were injected with cRGD-800CW-TCO and imaged with fluorescence- and optoacoustic imaging devices before and 2h, 6h and 24h after injection, before they were sacrificed and dissected with the guidance of a FGS imaging system.

Results

Fluorescence imaging of cRGD-800CW-TCO allowed detection of the tumor area but without information about the depth, whereas MSOT allowed high resolution 3D identification of the tumor area, in particular of small tumor nodules. Highly sensitive delineation of tumor burden was achieved during FGS in all mice. Imaging of whole-mouse cryosections, histopathological analysis and NIRF microscopy confirmed the localization of cRGD-800CW-TCO within the tumor tissue.

Conclusion

In principle all imaging modalities applied here were able to detect PDAC *in vivo* using one NIRF probe. However, the combination of MSOT and FGS provided detailed spatial information of the signal, and achieved a complete overview of the distribution and localization of cRGD-800CW-TCO within the tumor before and during surgical intervention which could lead to a reduction in R1 resections in PDAC surgery.

Introduction

Pancreatic ductal adenocarcinoma (PDAC) has an extremely poor prognosis which is ascribed to the asymptomatic early phase of the disease and its aggressive tumor biology. The challenge in the management of operable pancreatic tumors is an achievement of R0 resections, i.e. complete removal of all tumor nodules. Unfortunately, 80% of pancreatic cancer surgeries are R1 resections, resulting in a further decreased overall survival^{1,2}.

Although surgeons still mostly rely on their visual perception and palpation, novel imaging methods such as fluorescence-guided surgery (FGS) are evolving to assist the differentiation of healthy and tumor tissue. FGS, typically based on near infrared (NIR) fluorescent probes visualises the desired structures in real time³. The application of planar NIR fluorescence imaging for non-invasive detection of tumors is restricted to approximately one cm deep structures^{3,4}. Furthermore, the strong influence of tissue microenvironment and the light scattering hamper signal quantification^{5,6}. Moreover, the detected fluorescence is projected onto the photographic image of the body surface in 2D and attribution to specific organs and structures within the body is not warranted. Nevertheless, planar fluorescence imaging is widely used in preclinical settings and increasingly applied in the clinic as it is non-invasive, easy-to-use, economic and possible in real-time.

Optoacoustic (also called photoacoustic) imaging is an emerging technology, which uses pulsed laser light to excite absorbing molecules. Those molecules undergo thermoelastic expansion leading to the release of acoustic waves^{7,8}. With multispectral optoacoustic tomography (MSOT), tissue can be sequentially illuminated at different wavelengths and images can be processed using spectral unmixing algorithms in order to distinguish and quantify the contribution of different chromophores in tissue which can be spatially resolved and back-projected to reconstruct a three-dimensional (3D) image⁹. MSOT delivers anatomical and functional information simultaneously, with a high spatial resolution and up to 5 cm penetration depths, making it suitable for imaging deeper tissues and tumors within the body^{10,11}. Nevertheless, the depth is dependent on the ultrasound frequency, with lower frequencies allowing for greater imaging depth but with a lower spatial resolution¹². MSOT has been shown to address a number of clinically relevant aspects such as tissue oxygenation or tumor spreading and can potentially overcome a number of other shortcomings in current surgical practice¹³⁻¹⁵.

Both optoacoustic and fluorescence imaging are relying on tumor specific probes^{4,16}. Although there are numerous fluorescent dyes in every desired wavelength, currently, only very few of them are approved for the routine use in patients¹⁷. IRDye800CW is one of the most promising new generation NIRF dyes, which can be detected by both, fluorescence and optoacoustic imaging and is currently widely tested in clinical trials¹⁸. Clinical evaluation is possible, as biocompatibility studies of 800CW did not show evidence of toxicity^{19,20}.

Here, we decided to use a cyclic arginine–glycine–aspartic acid (cRGD) peptide to target integrins, which are overexpressed in various cancer types and are playing a key role in the early phase of tumor angiogenesis and in tumor cell migration²¹. The cRGD peptide contains only one labeling site, for the 800CW dye, in contrast to other targeting molecules, like antibodies, which usually contain multiple labeling sites and can therefore vary in dye to protein ratios. Therefore quenching effects from dye–dye interactions caused by multiple labeling are avoided. In the clinic, several RGD constructs are already applied for tumor detection using PET or SPECT²².

The combination of cRGD and IRDye800CW has already been tested in several preclinical studies, e.g. to specifically target integrins in a transgenic mouse model of glioblastoma or to provide high precision delineation of tumor tissue during fluorescence-guided glioblastoma resection²³. In an orthotopic head and neck cancer model cRGD-800CW was efficiently combined with a unique handheld spectroscopic device for sensitive detection of integrin overexpression on infiltrating tumor cells for intraoperative visualization of not only invasive tumor margins but also metastatic lymph nodes²⁴. In a subcutaneous PDAC model cRGD-800CW allowed for visualization of the tumor up to 24h post injection using fluorescence tumor imaging²⁵.

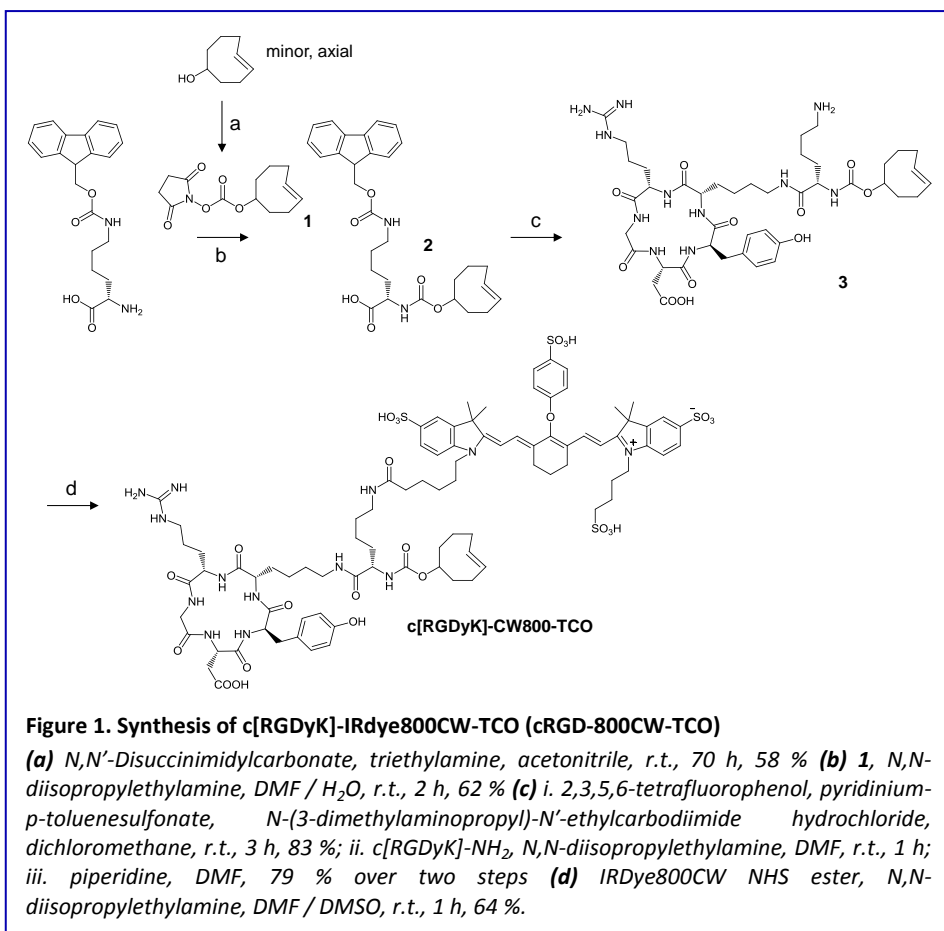
For future pre-targeting possibilities with a radiolabel to irradiate left over tissue a *trans*-cyclooctene (TCO) tag is already added. This system is based on the tumor-binding of a tagged molecule, cRGD-800CW, and the subsequent binding of a small fast-clearing radiolabeled molecule to cRGD-800CW. This will result in improved tumor to background ratios (TBRs) and local radionuclide therapy²⁶.

In this study we evaluated cRGD-800CW-TCO as a potential tool for FGS and more importantly as a tool to compare the diagnostic values of planar fluorescence imaging techniques with MSOT for *in vivo* preclinical imaging of deep seated tumors.

Materials & Methods

Probe preparation

The preparation of cRGD-800CW-TCO composed of *c*[RGDyK]-IRDye800CW-*(trans-cyclooctene)* is extensively described in the supplementary material section and is described in summary in **Figure 1**.



Cell line and culture conditions

The human PDAC cell line AsPC-1 was purchased from ATCC (Rockville, MD), cultivated as described before and used for all tumor models²⁷.

Animal studies

All animal experiments were performed in accordance with German animal ethics regulations, approved by the local ethics office of Lower Saxony (license no. 33.9–42502-04–13/1085). Experiments were performed on male athymic nude mice NMRI-*Foxn1*^{nu} (Charles River Laboratories), housed in ventilated cages and allowed food and water *ad libitum*.

For the subcutaneous (s.c.) transplantation 1×10^6 AsPC-1 cells were resuspended in 100 μ l of PBS and transplanted into the left flank under brief isoflurane gas anesthesia (Abbvie, ~2%, 0.8 l/min). For the orthotopic transplantation 1×10^6 AsPC-1 cells were resuspended in 20 μ l of PBS and implanted under xylazine (15 mg/kg) ketamine (75 mg/kg) anesthesia as described before²⁷. Mice were sacrificed by isoflurane overdose and cervical dislocation.

Imaging

All *in vivo* analyses were preceded by native scans (0h). 27 days after transplantation, AsPC-1 tumor bearing mice received intravenously (i.v.) a single dose of cRGD-800CW-TCO (10 nmol in 100 μ l of 0.9% NaCl) and were scanned under isoflurane gas anesthesia (2%, 0.8 l/min) with planar fluorescence imaging systems Optix MX2 (ART; timedomain system) and IVIS Spectrum (Perkin Elmer; epi-/trans-illumination system) as well as the small animal optoacoustic imaging system MSOT inVision 256-TF (iThera Medical GmbH) at 2h, 6h and 24h post injection (p.i.). Mice were sacrificed either 6h (n=3) or 24h (n=4) p.i. and one mouse per time-point was frozen (-20 °C) directly after sacrifice and used for whole body cryosectioning²⁸, the other for fluorescence-guided dissection (FGD) with the Artemis (Quest Diagnostics; epi-illumination) was performed to mimic FGS²⁹.

Spectrometer measurements

The probe was diluted in a solution of 10% BSA in saline with a final optical density of 0.17. The absorbance spectrum was measured in a 96-well plate between 680 nm and 900 nm at equidistant intervals of 10 nm using SpectraMax™ M2e (Molecular Devices). The probe spectrum was normalized to the maximum peak absorbance value.

Phantom measurement

The same diluted probe sample was then inserted inside 3 mm wide tubes at the center of a scattering cylindrical agar phantom (1.5% agar and 1% intralipid (Sigma); 2 cm diameter). MSOT acquisition was

performed in five imaging planes (~800 μm cross-section) with a 2 mm step size. Images were reconstructed and ROIs were drawn around the insertions to retrieve the mean signal intensities for each measured wavelength (680-900 nm).

***In vivo* NIRF imaging**

In Optix MX2, 730 nm excitation laser and 770 nm LP emission filter were applied for all scans. *In vivo* whole body scans and *ex vivo* imaging of organs were performed with 1.5 mm step size and 0.2 sec integration time per scan-point whereas the high-quality scans over the tumor area with 1.0 mm step size and 1.0 sec integration time. Optix 2.02.01 and OptiView 2.01.00 software (ART) were used to acquire and analyze the Optix MX2 data, respectively.

IVIS scans were performed with an excitation filter of 745 nm with 30 nm bandwidth, emission of 800 nm (range 780-840 nm), field of view (FOV) C for the whole-body scans and FOV B for the focused tumor area scans, medium binning. Living Image software 4.4 (Perkin Elmer) was used for IVIS Spectrum image acquisition and analysis.

Optoacoustic imaging & reconstruction

For optoacoustic imaging, the MSOT inVision 256-TF small animal imaging system (iThera Medical, Munich, Germany) was used³⁰. Briefly, a tunable optical parametric oscillator (OPO) pumped by an Nd:YAG laser provides excitation pulses with a duration of 9 ns at wavelengths from 680 nm to 980 nm at a repetition rate of 10 Hz with a wavelength tuning speed of 10 ms and a peak pulse energy of 100 mJ at 730 nm. Ten arms of a fiber bundle provide even illumination of a ring-shaped light strip of approx. 8 mm width. For ultrasound detection, 256 toroidally focused ultrasound transducers with a center frequency of 5 MHz (60% bandwidth), organized in a concave array of 270° angular coverage and a radius of curvature of 4 cm, are used.

For scanning, isoflurane anesthetized mice were covered with ultrasound gel (Parker), gently and tightly wrapped in cling film and placed in a warm water container. Anesthesia was maintained throughout the procedure.

MSOT images were acquired at six different wavelengths: 715 nm, 730 nm, 760 nm, 775 nm, 850 nm and 900 nm. For each wavelength, 10 consecutive frames were recorded and averaged. Data was fluence-

corrected ($\mu_s = 10 \text{ cm}^{-1}$, $\mu_a = 0.022 \text{ cm}^{-1}$ at 800 nm) to compensate for spectral coloring. Image reconstruction with standard backprojection and spectral unmixing were done using ViewMSOT™ software. Multispectral processing was performed using linear regression on the probe spectrum measured in the phantom. Probe signals were pseudo-colored in jet and overlaid on the corresponding anatomical images (800 nm single wavelength) displayed in grey scale. Maximum intensity images were generated using the 3D ViewMSOT™ software tools. Any adjustment to brightness, color, or contrast has been made to the entire image and applied to all images.

For quantification of probe signals, ROI analysis was performed on single image sections of the spectrally unmixed probe signals with the ROI analysis tool of ViewMSOT

Fluorescence-guided dissection (FGD)

Quest Spectrum clinical system for in vivo FGS supported by Artemis Capture Suite 1.1.2 software (Quest Diagnostics) was used for the dissection guidance applying settings of both visible and NIR light. For the visible light of low-pass filter of <640 nm was used. The NIR light was excited with a wavelength of 785 nm, emission was done with a high-pass filter of >808 nm. In addition, reflected excitation light was blocked by a 750-800 nm filter. The raw data could be saved as individual snapshots or a real-time movie for data analysis. Representative movie frames were selected and FIJI software was used to produce color-coded images³¹.

Excised organs were first imaged with both, the Optix MX2 and IVIS systems and afterwards fresh frozen and stored at -80°C.

Cryoslicing with fluorescence imaging

The samples were cut at equidistant intervals of 0.5 mm throughout the thoraco-abdominal level. For fluorescence imaging of the cryosections a Leica cryostat (CM 1950, Leica Microsystems, GmbH, Wetzlar, Germany) was retrofitted with a self-made fluorescence imaging system with excitation at 740 nm and emission captured with a 780 nm long pass filter. The exposure time was 2.5 seconds²⁸.

Tissue staining

Frozen tissues were sectioned at 2.5 μm slices slice thickness and fixed for 10 min with acetone. For anti-Integrin αv staining, slides were incubated for 1h with rabbit monoclonal anti-Integrin αv antibody (ab179475, Abcam) diluted 1:10.000 in 1% BSA in PBS followed by 30 min incubation with goat ant-rabbit Alexa Fluor 546 (1:400; Mol. Probes). For staining of $\alpha\text{v}\beta\text{3}$ integrins, mouse monoclonal anti-integrin $\alpha\text{v}/\beta\text{3}$ antibody (sc-7312) was transferred to PBS using a Superdex 75 size-exclusion column (500 ml bed volume, GE Healthcare), brought to pH 8.5 before and directly conjugated with Alexa Fluor 488 for 2h slowly rocking in the dark. Slides were incubated for 1h with the labeled anti-integrin $\alpha\text{v}/\beta\text{3}$ antibody diluted 1:200 in 1% BSA in PBS. Three washing steps with PBS, 5 min each, were performed after each incubation steps. Tissues were mounted with ProLong Gold Antifade Reagent (Thermo Fisher) with DAPI. Haematoxylin and Eosin (HE) staining was performed as described elsewhere³².

Tissue imaging and fluorescence microscopy

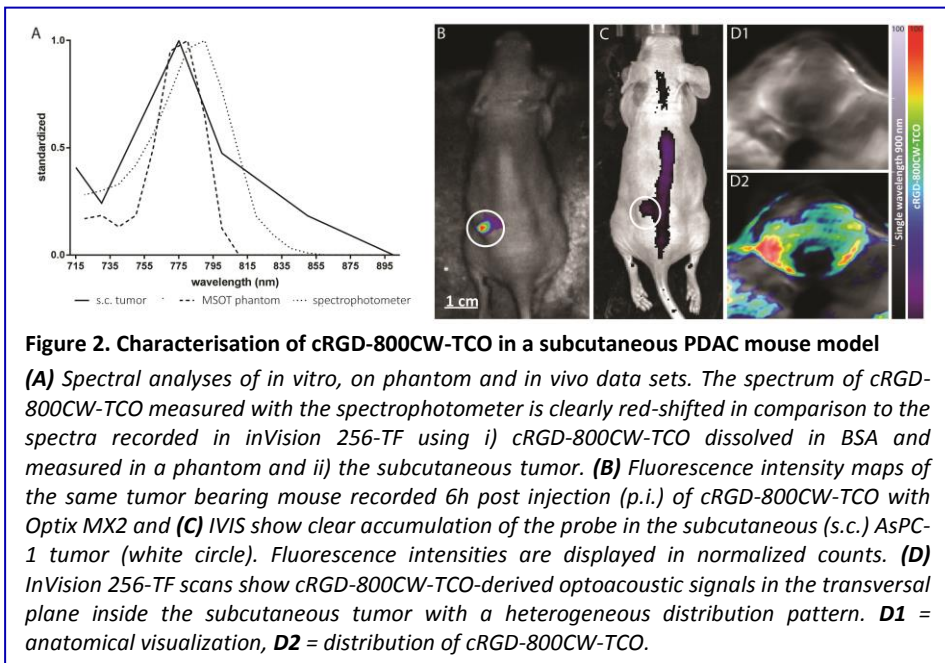
Tissue imaging was performed on 10 μm tumor cryosections obtained from PDAC bearing mice that received 10 nmol cRGD-800CW-TCO, using the Odyssey flatbed scanner (Licor Biosciences) and analyzed with the respective software. Fluorescence microscopy was performed with an Axiovert 200 M inverted microscope (Carl Zeiss Microscopy GmbH) equipped with a NIR-sensitive ORCA-ER digital camera (Hamamatsu). 708 +/-37.5 nm excitation and 809 +/-40.5 nm emission filter was used for the detection of 800CW. A filter was used for the detection of Alexa-Fluor 546 fluorescence and 365 +/- 12.5 nm excitation and 445 +/-25 nm emission filter was used for the detection of DAPI.

Image generation and processing were performed with the software AxioVision Rel.4.6 software and FIJI³¹, respectively.

Results

Spectral features of the cRGD-800CW-TCO-derived signals measured with MSOT *in vivo* in the subcutaneous tumor were compared to MSOT measurements of the same probe embedded in a phantom and to spectroscopic characteristics of the probe *in vitro*. As shown in **Figure 2A**, the *in vitro* cRGD-800CW-TCO spectrum was clearly red-shifted when

compared to MSOT scans *in vivo* and in the phantom. Based on these results, spectral unmixing was performed in all further *in vivo* experiments, using the absorption spectrum found with the MSOT phantom instead of using the spectrophotometer absorption spectrum. The binding of cRGD-800CW-TCO and the specificity of the MSOT signals were first confirmed in mice bearing subcutaneous AsPC-1 tumors (n=3) 6h after i.v. probe injection in comparison to planar fluorescence imaging. In both planar optical imaging systems, Optix MX2 (**Figure 2B**) and IVIS (**Figure 2C**), strong probe-derived fluorescence signals were observed over the palpable tumors. Interestingly, NIR fluorescence signals detected with Optix MX2 were almost exclusively co-localized with the tumor region, whereas with the IVIS system additional relatively strong



background fluorescence was observed, especially in the area surrounding the subcutaneous tumor and along the spine. Optoacoustic tomography revealed comparably strong probe-derived signals within the subcutaneous tumors but less background signals than planar fluorescence imaging, presumably coming from the remaining cRGD-800CW-TCO circulating in the bloodstream (**Figure 2D**). Notably, the transversal scans obtained with the MSOT system revealed

heterogeneous distribution of the probe within the tumor (**Figure 2D1**), suggesting areas with a different degree of cRGD-800CW-TCO accumulation (**Figure 2D2**).

MSOT allows *in vivo* 3D visualization of deeply located tumor nodules in the orthotopic PDAC mouse model

To validate the applicability of cRGD-800CW-TCO as a contrast agent for fluorescence- and optoacoustic imaging of deeply located tumors, an orthotopic mouse model of human PDAC was used in which AsPC-1 cells were transplanted into the head of the pancreas of nude mice. At the time of the imaging experiments - ~3.5 weeks after the transplantation - all mice had developed nodular primary tumors widely spread within the pancreas. The tumors generally showed invasion into the stomach and duodenum, and massive tumor spread to different distant sites and organs adjacent to the pancreas such as the liver, spleen or mesentery as well as growth of a tumor mass at the site of surgical incision (**Fig. 3A-D**). AsPC-1 tumor-bearing nude mice (n=7) were imaged with the OptixMX2, IVIS and MSOT before and 2h, 6h and 24h after i.v. injection of a single dose of cRGD-800CW-TCO (10nmol).

As shown in **Figure 3E**, OptixMX2 detected a strong fluorescence over the upper abdomen, where both, the primary PDAC tumor and the tumor mass at the site of surgical incision are located. The fluorescence intensity was highest at 2h p.i., decreased at 6h p.i., but was still clearly detectable at 24h p.i.. Heterogeneous background fluorescence was detectable at all scan time-points, which was presumably due to the presence of the circulating probe as well as a strong fluorescence signals from the excreted probe within the bladder. The highest tumor to background ratio (TBR) of 1.8 ± 0.3 was measured with the OptixMX2 at 2h p.i. and decreased over time to 1.4 ± 0.3 at 6h and 1.5 ± 0.3 at 24h p.i.. A comparable fluorescence distribution pattern (**Figure 3F**) was obtained with the IVIS system with TBRs of 1.7 ± 0.2 at 2h p.i., 2.0 ± 0.2 at 6h p.i. and 2.2 ± 0.2 at 24h p.i..

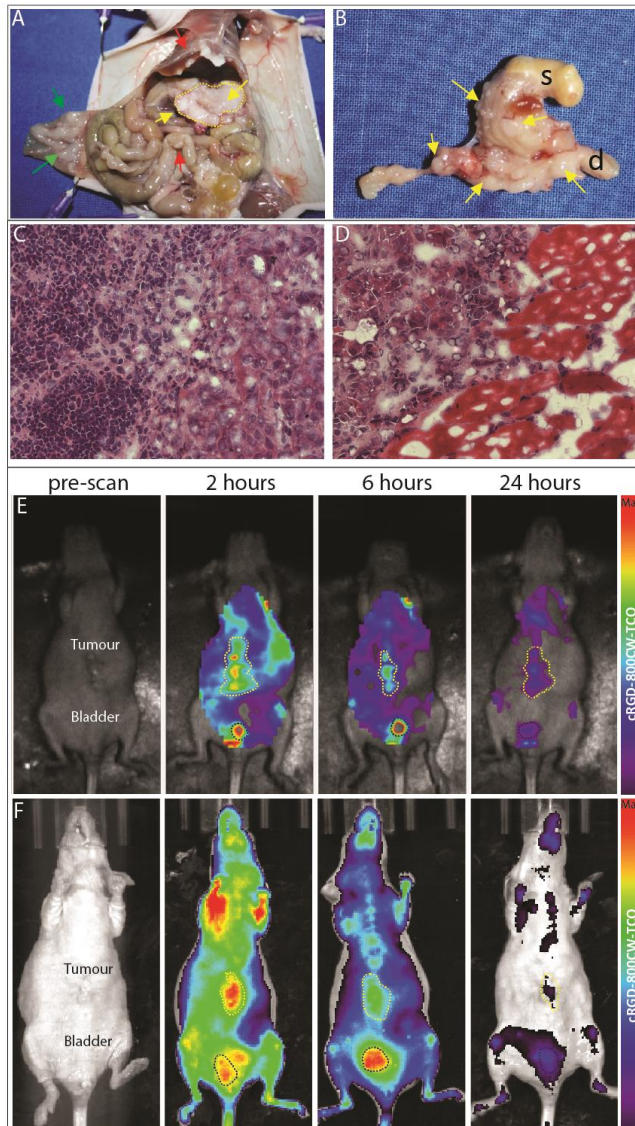
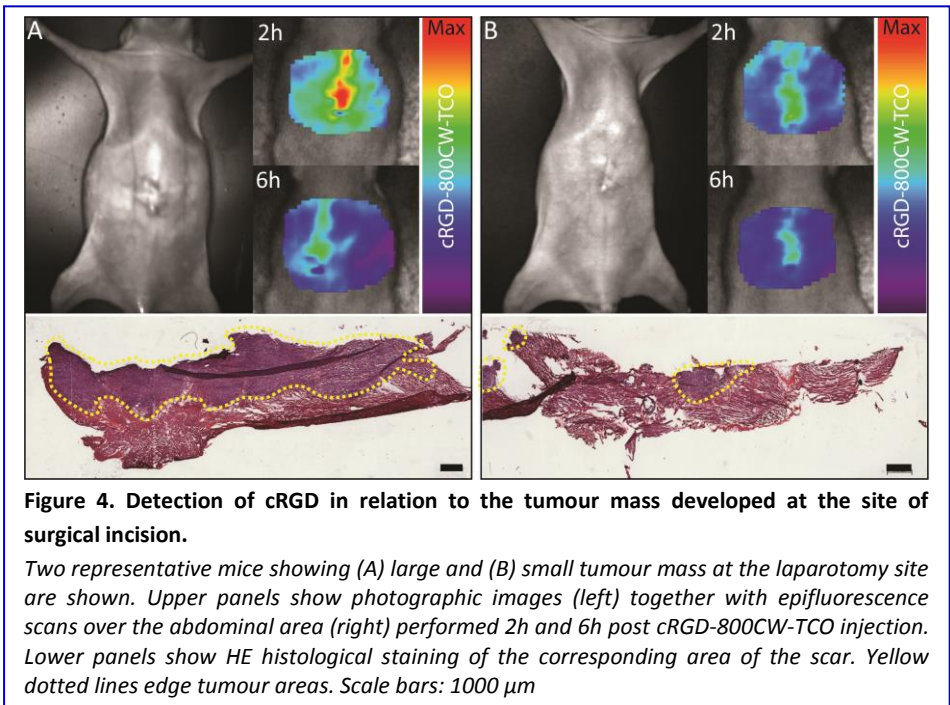


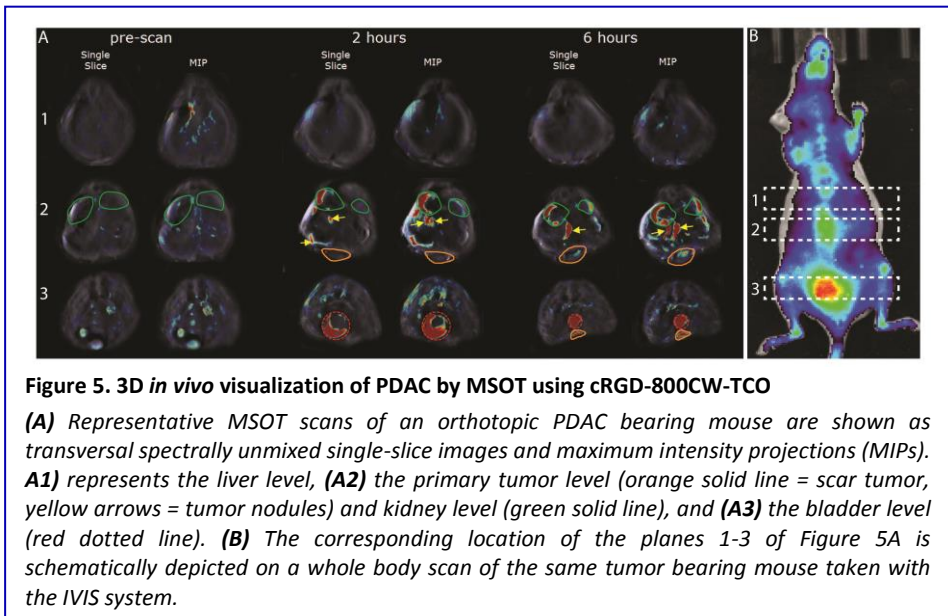
Figure 3. *In vivo* visualization of cRGD-800CW-TCO in an orthotopic PDAC mouse model

(A)-(D) Representative morphological and histological appearance of an AsPC-1 tumour model. **(A)** Image of an AsPC-1 tumour bearing mouse taken during the dissection and showing the typical appearance of the primary tumour and extent of tumour spread within the abdomen (arrows: yellow = primary tumour, red = abdominal metastasis and green = tumour mass at the surgical scar). **(B)** Excised widely spread and nodular primary tumour (arrows) invading stomach (s) and duodenum (d). **(C)** HE staining of the primary tumour and **(D)** of the tumour mass at the site of surgical incision. **(E)** Representative ventral fluorescence whole body images of a mouse bearing an orthotopic AsPC-1 tumour, obtained before (pre-scan) and 2h, 6h and 24h p.i. of cRGD-800CW-TCO with Optix MX2 or **(F)** IVIS. Note the strong fluorescence signals from the excreted probe within the bladder. Fluorescence intensities are displayed in normalized counts.

We observed that mice which developed a large tumor mass at the surgical scar at the abdominal wall also showed higher cRGD-800CW-TCO-derived fluorescence intensities (**Figure 4**). These findings suggest that the epifluorescence signals detected over the abdominal area are the sum of the fluorescence from the probe bound to the primary tumors and to the tumor mass grown at the surgical scar.

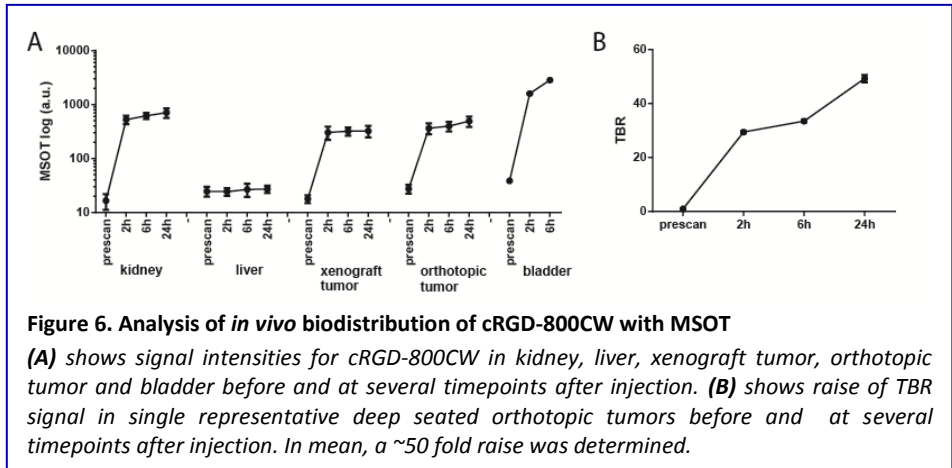


Next, we used MSOT (**Figure 5**) to visualize the position of the primary tumor and tumor nodules in 3D, and to analyze the biodistribution and clearance of the probe over time (see Supplementary Material). **Figure 5A** shows representative MSOT transversal single slices through the mouse body at the level of the liver (1), the kidneys (2) and the bladder (3) and corresponding maximum intensity projections (MIPs) at 6h p.i. of the cRGD-800CW-TCO probe. The virtual positions of the slices are schematically depicted in **Figure 5B** in relation to the planar fluorescence image.



Using MSOT we could not only detect a clear accumulation of cRGD-800CW in the primary tumor but also in several deeply located tumor nodules (**Figure 5A**), which were clearly distinguishable from the primary tumor. Interestingly, we detected only very low background signals from the circulating probe, reflected in high TBRs of 29.5 ± 0.9 at 2h, 33.5 ± 0.9 at 6h, and TBRs of 49.3 ± 2.8 at 24h p.i..

Furthermore, using MSOT, we could clearly confirm the renal excretion pathway of cRGD-800CW-TCO which is typical for small molecules: both, MSOT images (**Figure 5A**) and biodistribution results (see **Figure 6**), revealed a strong detection of probe-derived signals in the kidneys (plane 2; green) and in the bladder (plane 3; red dashed line), but not in the liver (plane 1).



cRGD-800CW-TCO enables FGD of PDAC

Finally, FGD was performed in the orthotopic PDAC model with the guidance of the clinical system Artemis (Quest Spectrum; epillumination), in order to assess the value of cRGD-800CW-TCO for the delineation of the margins between normal and PDAC tissue during surgery. At both, 6h (**Figure 7A**) and 24h (**Figure 7B**) after cRGD-800CW-TCO injection, strong fluorescence signals over the central abdomen were detected with the open field camera even through the skin (*frame 1*). Following median laparotomy and removing the skin, the fluorescence detectable through the peritoneum became more prominent (*frame 2*). Opening the peritoneum revealed that the fluorescence was mainly located over the primary tumor area (*frames 3-5*) as well as over the tumor mass at the site of surgical incision (data not shown). In addition, a strong fluorescence was detectable over the kidneys and bladder, especially at 6h p.i., which most likely corresponds to excreted cRGD-800CW-TCO. Lower fluorescence was also detectable over organs known to have a high integrin expression such as the intestine and the uterus. As shown in **Figure 7C** FGS allowed a clear delineation of the tumor margins. In addition, *ex vivo* imaging shows an increased signal at both, the tumor and scar thereby confirming the findings mentioned above and with MSOT. The real-time images taken before and directly

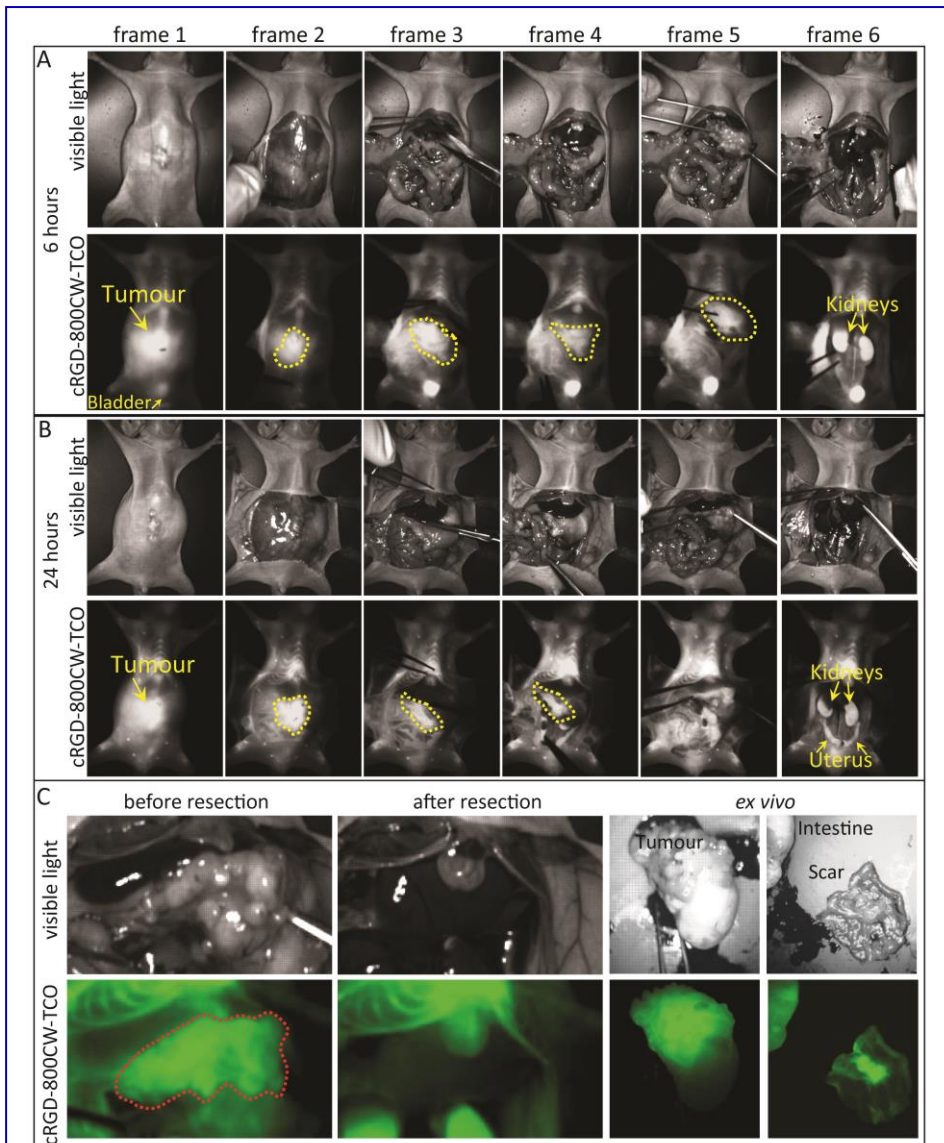


Figure 7. FGD of an orthotopic PDAC bearing mouse model

(A) Representative images of an orthotopic PDAC bearing mouse at 6h and **(B)** 24h p.i. of cRGD-800CW-TCO. Selected frames of representative movies (**frame 1-6**) recorded with the Artemis during different steps of the dissection are shown. At both time-points strong fluorescence intensities are detectable over the primary tumor area (yellow line). In addition, strong fluorescence is detectable over kidneys and bladder, especially at 6h p.i. and lower fluorescence over the intestine and uterus. Red arrows mark strong fluorescence over the tumor mass at the peritoneum. **(C)** Photographic and cRGD-800CW-TCO-derived fluorescence images recorded directly before (left) and after (middle) the resection of a primary tumour attached to the stomach and duodenum are shown. The margins of the primary tumour detected with FGS are delineated with red line. Note, that the fluorescence signals over the sternum and kidneys is still detectable after the resection. Panels on the right show the fluorescence signals over the resected primary tumour attached to the stomach and over the tumour mass at the surgical scar.

after the resection of the pancreatic tumor tissue, together with stomach and duodenum, clearly confirmed that the resection bed is empty of the tumor-derived fluorescent signals upon removal of the cRGD labeled tissue, with only the background fluorescence remaining.

Ex vivo validation confirms accumulation of cRGD-800CW-TCO in an orthotopic PDAC mouse model

To verify the accumulation of cRGD-800CW-TCO within the tumor and to validate the results from the *in vivo* fluorescence- and optoacoustic imaging, we performed various *ex vivo* analyses.

Two mice with orthotopic PDAC were sacrificed and frozen directly after their last scan (one at 6h p.i. and one at 24h p.i.) followed by cryosectioning of the entire body. Fluorescence distribution in the transversal cryosections with respect to the mouse anatomy was then compared to the signals obtained by spectral unmixing of MIPs of MSOT

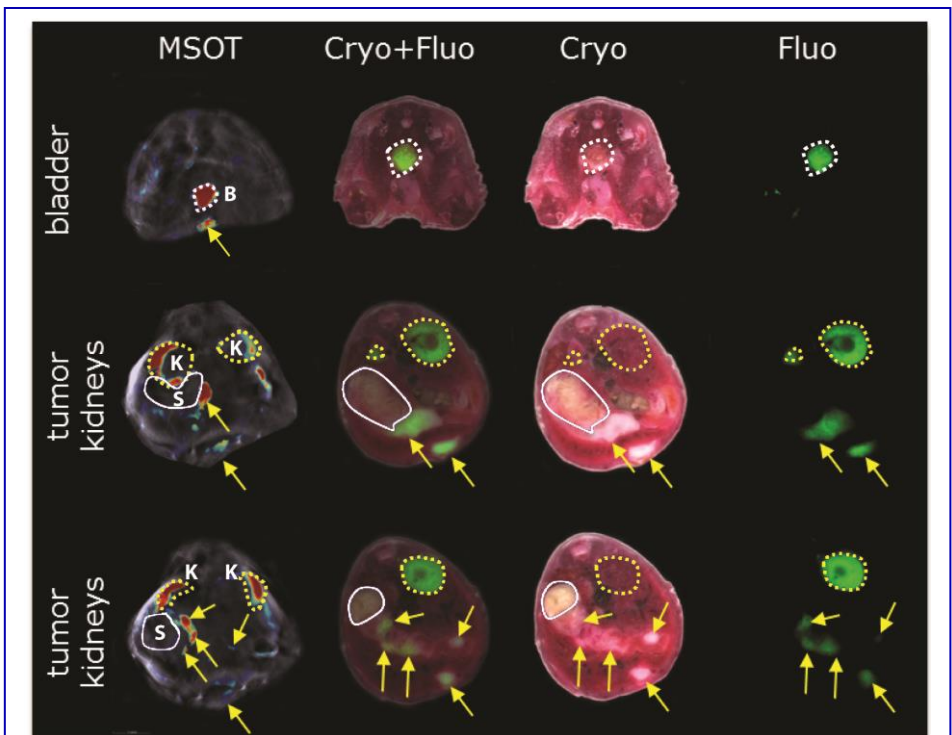


Figure 8. Histological analyses of cryosections in comparison to the fluorescence and optoacoustic images of whole mice

Representative transversal cryoslices (Cryo) of a PDAC bearing mouse sacrificed 6h p.i. of cRGD-800CW-TCO and the matching MSOT MIPs show almost identical distribution of the fluorescence (Fluo) and optoacoustic signals (MSOT) in the tumor pointed out by the yellow arrows. The yellow dotted lines outline the kidneys (K), the white lines the stomach (S) and the white dotted lines the bladder (B).

data. **Figure 8** shows representative transversal slices at the level of the bladder, the tumor and the kidneys for the PDAC mouse sacrificed at 6h p.i.. In both tested mice the *ex vivo* fluorescence measurements revealed a similar distribution pattern as the optoacoustic signals obtained *in vivo* with MSOT (**Figure 8**, yellow arrows).

Finally, excised samples of tumor tissue attached to the stomach and liver were cryosliced and analyzed with a flatbed fluorescence scanner before HE staining was performed. As shown in **Figure 9A-B**, strong cRGD-800CW-TCO fluorescence was predominantly found at the tumor margins allowing for a clear delineation of the tumor nodules (**Figure 9A**), with lower but still well detectable fluorescence within the central tumor mass. On a cellular level, co-staining of the tumor sections with antibodies targeting different integrins was performed, in order to visualize the distribution of the *in vivo* injected probe, cRGD-800CW-TCO, in relation to the target. As shown in **Figure 9C**, the staining pattern of the anti- $\alpha v \beta 3$ integrin antibody (in blue) showed a highly similar pattern to that of the injected cRGD-800CW-TCO probe (in green). In contrast, anti- αv integrin antibody (in red) homogenously stained the tumor tissue, however without any correlation to the cRGD-800CW-TCO binding sites. The same staining pattern was observed on high resolution images (**Fig. 9D**).

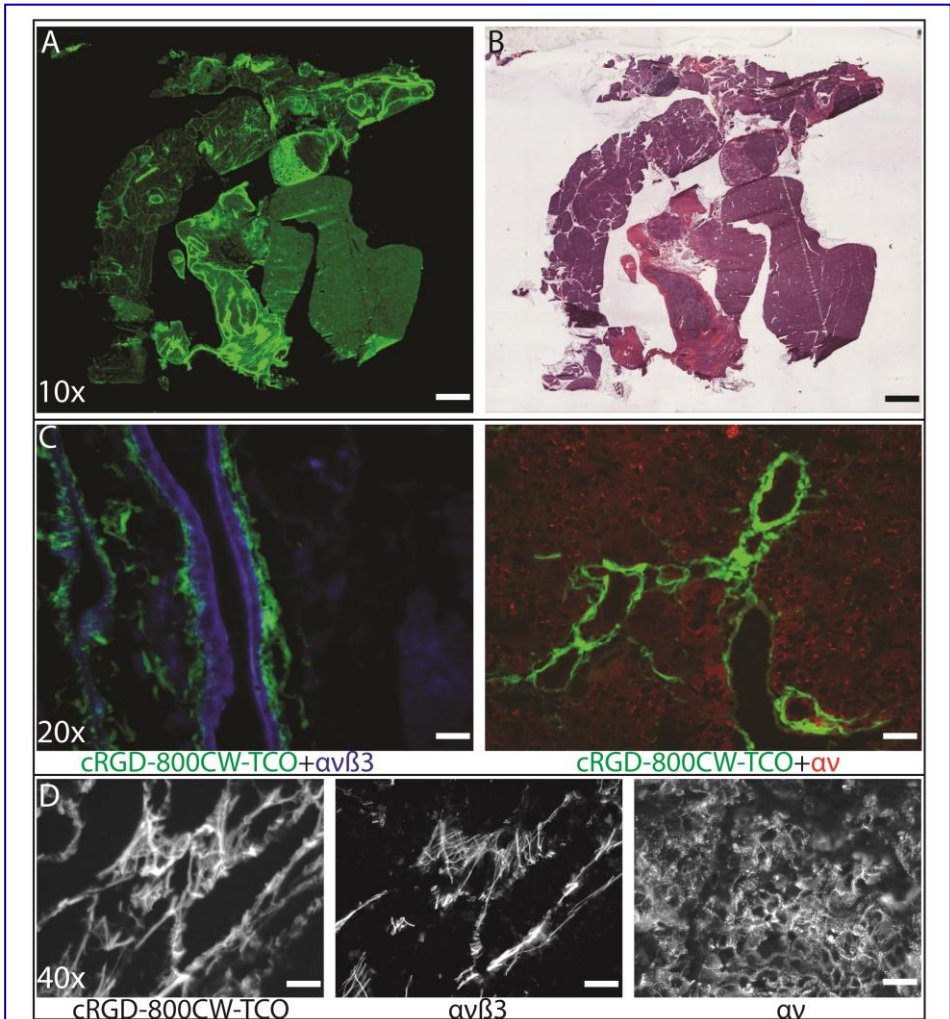


Figure 9. Histological analysis of PDAC samples obtained from FGD

(A) Representative fluorescence scan of a cryoslice of the primary PDAC tumor attached to the stomach and liver and **(B)** corresponding HE staining of the same section demonstrating a strong accumulation of cRGD-800CW-TCO especially at tumor margins/invasion front (arrows). **(C,D)** Fluorescence microscopy of the tumor cryoslices shows co-localisation of cRGD-800CW-TCO only with anti- $\alpha v \beta 3$ integrin antibody but not with anti- αv integrin antibody staining. Scale bars in A and B: 2000 μm , C: 500 μm and D: 250 μm

Discussion

To our knowledge, this is the first study showing the potential and feasibility of MSOT as a pre-operative imaging modality for the detection of deep-seated orthotopic pancreatic tumors in mice with an integrin targeting probe³³. Using cRGD-800CW-TCO as a probe, we were able to distinguish the primary tumor and several small tumor nodules from healthy tissue non-invasively, with high specificity and by notably higher resolution than with planar fluorescence imaging. Finally, during FGD, which we used to mimic PDAC surgery, we not only confirmed the localisation of the tumor nodules detected by MSOT but could also clearly delineate tumor margins with high sensitivity.

In the first part of our study we analyzed the spectral characteristics of cRGD-800CW-TCO and found a clear red-shifted absorbance spectrum of the spectrometer compared to the *in vitro* and *in vivo* results by MSOT. This shift can be assigned to differences in relaxation times of probe molecules as they are excited with light pulses of different lengths³⁴. *In vivo*, spectral coloring, the phenomenon by which light propagating through tissue undergoes wavelength specific fluence attenuation³⁵ or interactions with proteins might occur and cause wavelength shifts. Spectral unmixing of MSOT was performed after fluence correction using a linear regression algorithm and using the spectrum measured from the MSOT phantom in order to maximize the specificity of the unmixed results for cRGD-800CW-TCO. As this was closely correlated with the spectrum derived from the subcutaneous tumor we were confident that using the retrieved spectrum was an appropriate choice.

Using planar *in vivo* fluorescence imaging in cRGD-800CW-TCO injected orthotopic xenotransplants we were able to detect diffuse fluorescence signals over the upper abdomen, indicative of signal emanating from the primary tumor and/or from the tumor mass at the site of surgical incision. This however, did not allow for the precise localization of particular tumor nodules nor did it contain any information about the depth. In contrast, scanning the same mice with the MSOT resulted in high-resolution cross-sectional images from the abdominal area, which enabled the detection and localisation of the primary tumor and several deeply located small tumor nodules. In addition, by applying planar fluorescence imaging we obtained strong background signals, especially at early timepoints p.i. which were much lower in MSOT measurements, resulting in about 15-fold higher TBRs. This can be explained

by the fact that with planar fluorescence imaging all the fluorescence which reaches the object surface from different sources and depths after being subjected to absorbance and scattering, is collected and merged on the intensity maps. Consequently, the fluorescence of deeply located tumors appears less intense and more spread. Furthermore, the fluorescence from the circulating probe, especially in the surface-near areas can appear more intense, increasing the background signal and thereby decreasing the TBR. In this context, one advantage of MSOT over planar fluorescence imaging is the possibility to quantify signals in single slices (see SI) which leads to more reliable TBRs. Nevertheless, similar to fluorescence imaging, MSOT only allows a relative quantification of the signals. In both methods absolute quantification can only be achieved by a full correction for the absorption, scattering and anisotropy of the tissue, the technology to achieve this is still in its infancy^{36,37}. Other methods such as gamma spectroscopy or mass spectrometry could be considered to be applied in future studies if absolute quantification of signals is needed.

Detection of pancreatic tumors with MSOT has previously been described³³. Various probes have been used before, e.g. targeting Syndecan-1^{33,38} or EGFR³⁹ and all of them allowed a clear and specific detection of probe derived optoacoustic signals over the primary tumors. However, in all these studies, pancreatic tumor cells were orthotopically transplanted into the tail of the pancreas which resulted in the development of only locally restricted tumors that grew on the left side of the abdomen next to the spleen and close to the body surface and were therefore relatively easy to localise. By contrast, in our study we transplanted PDAC cells into the head of the pancreas which resulted in the development of nodular primary tumors widely spread within the pancreas and located deep in the abdominal cavity, invading into the stomach and duodenum and accompanied with tumor mass growing at the site of surgical incision as well as multiple abdominal metastasis, as described by us and others^{27,40}. This is a much more relevant model, as in humans about 65% of the pancreatic tumors arise in the head of the pancreas and only 15% in the body and tail⁴¹. Despite of this much more challenging model, we could clearly detect optoacoustic signals over the spread tumor nodules, showing that MSOT is highly suitable for the detection and discrimination of particularly deeply located and disseminated tumors.

Finally, by performing FGD of cRGD-800CW-TCO injected tumor-bearing mice we could confirm that the signals detected by the fluorescence camera during the surgery revealed similar patterns than those detected with MSOT before surgery. This shows that MSOT can provide a specific overview of the distribution and localization of the fluorescence signal at the tumor sites and therefore represents an ideal complement to the FGS. In contrast to planar fluorescence imaging - which has excellent sensitivity for superficial targets but becomes strongly limited by absorption and scattering of the incident and emitted light with increasing depth - MSOT is not susceptible to the scatter of emitted light. This makes MSOT more sensitive for imaging of deeply located tissue, as confirmed by the higher TBRs obtained with MSOT. Nevertheless, despite the clear advantages over planar fluorescence imaging such as high spatial resolution and increased penetration depth, MSOT still has its limitations. The work flow of MSOT is much slower than that of planar fluorescence imaging and includes i.e. multi-wavelength acquisition, reconstruction, spectral unmixing, and further 3D reconstruction, which can require additional post-processing and makes operation in real-time not always possible.

The development of MSOT instrumentation arose from the need for translational imaging. Although handheld optoacoustic devices are emerging, which can be handled similarly to classical ultrasound scan-heads, the current clinical translation of optoacoustic systems is still restricted to the detection of intrinsic absorbers such as haemoglobin, melanin or lipids or FDA approved unspecific contrast agents^{13,42,43}. Several clinical trials using MSOT have already been performed⁴⁴, showing a powerful potential of the technique. However, without the availability of clinical available targeted probes, the full translation of optoacoustic imaging to the clinic is limited. Our study may support a progression in this direction.

Overall, we have demonstrated that cRGD-800CW-TCO can be used as a targeted probe to visualize orthotopic PDAC tumors with several optical imaging modalities. The TCO tag within the probe was designed for future therapeutic approaches based on the two step "click chemistry" principle, aiming future pre-targeting possibilities with a radiolabel to

irradiate left over tumor tissue. This would involve a two-step system with tumor-specific binding of cRGD-800CW-TCO as the first step and the subsequent binding of a small fast-clearing radiolabeled molecule to the TCO tag as the second step of the treatment. Click chemistry via TCO tag has already been shown to improve tumor specificity²⁶.

Nevertheless, in addition to the signals at the disseminated primary pancreatic tumors, we detected both, fluorescence- and optoacoustic signals at the abdominal wall. We ascribed these signals to the tumor mass developed at the scar of the laparotomy site, as the fluorescence intensity was in accordance with the size of the tumor mass present at the scar. Furthermore, we detected relatively high background signals from the circulating probe, as well as relatively high fluorescence from healthy tissue with a high cellular turnover such as intestine or uterus. This is not very surprising, as integrins in general orchestrate cell-cell and cell-extracellular matrix adhesive interactions from embryonic development to mature tissue function. In addition, the $\alpha\beta3$ integrin, which is the major target for cRGD, is connected with angiogenesis, wound healing and cell migration⁴⁵. We thus cannot exclude that some tissue remodelling processes involving integrins still take place at the scar tissue, which could be a source of part of the cRGD-derived signals over the upper abdomen. Taken together, this indicates that the RGD-targeting probe, although sufficient for the perioperative detection of tumor nodules, is not ideal for the improvement of the specificity of therapeutic approaches. Therefore, for clinical use, the choice of the target-ligand combination should be further optimised.

Altogether we showed, that MSOT has the unique ability to give an *in vivo* whole-body 3D overview of the distribution of the probe and its clinical pre-surgery application might provide surgeons with information about the tumor distribution and its interactions with the microenvironment and surrounding organs and structures.

Acknowledgements

We want to acknowledge Thomas C.P. Sardella for the great support during the MSOT recordings, Hannah Puchala, Bärbel Heidrich, Yuedan Li, Katja Bierau, Peter Küppen and Keely Pierzchalski for the help and technical assistance during the experiments, Henk Janssen for the technical assistance during the chemical construction of the probe. We thank Andrea Markus for critical proofreading of the manuscript.

Funding: this work was supported by a European Union project grant from H2020, H2020-MSCA-RISE grant number 644373—PRISAR.

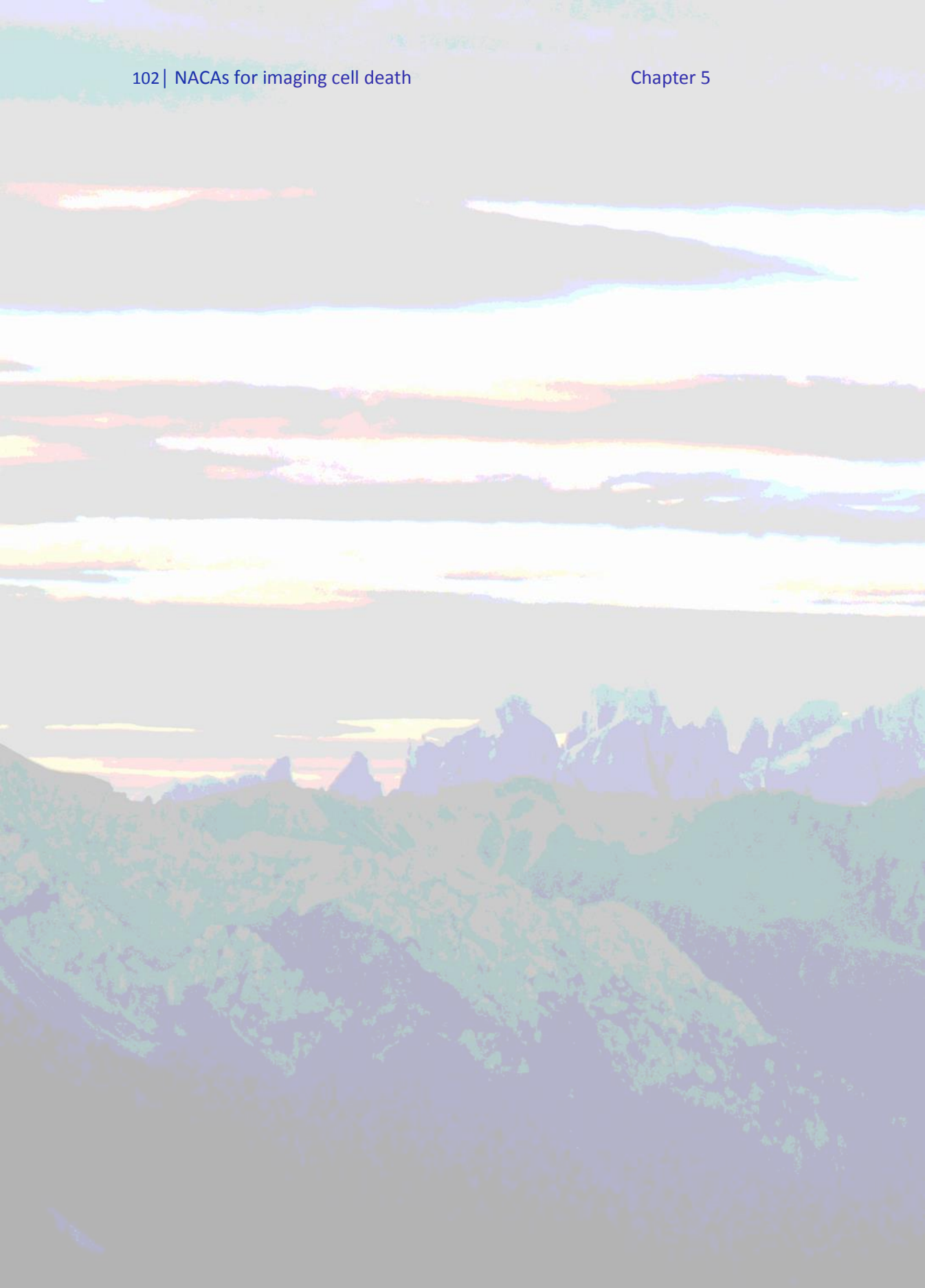
References

1. Gillen S, Schuster T, Meyer Zum Buschenfelde C, Friess H, Kleeff J. Preoperative/neoadjuvant therapy in pancreatic cancer: a systematic review and meta-analysis of response and resection percentages. *PLoS Med.* 2010;7(4):e1000267.
2. Handgraaf HJ, Boonstra MC, Van Erkel AR, et al. Current and future intraoperative imaging strategies to increase radical resection rates in pancreatic cancer surgery. *Biomed Res Int.* 2014;2014:890230.
3. Vahrmeijer AL, Hutteman M, van der Vorst JR, van de Velde CJ, Frangioni JV. Image-guided cancer surgery using near-infrared fluorescence. *Nat Rev Clin Oncol.* 2013;10(9):507-518.
4. de Boer E, Harlaar NJ, Taruttis A, et al. Optical innovations in surgery. *Br J Surg.* 2015;102(2):e56-72.
5. Liu Y, Tseng YC, Huang L. Biodistribution studies of nanoparticles using fluorescence imaging: a qualitative or quantitative method? *Pharm Res.* 2012;29(12):3273-3277.
6. Hawe A, Sutter M, Jiskoot W. Extrinsic fluorescent dyes as tools for protein characterization. *Pharm Res.* 2008;25(7):1487-1499.
7. Mehrmohammadi M, Yoon SJ, Yeager D, Emelianov SY. Photoacoustic Imaging for Cancer Detection and Staging. *Curr Mol Imaging.* 2013;2(1):89-105.
8. Bowen T. Radiation-Induced Thermoacoustic Soft-Tissue Imaging. *IEEE T Son Ultrason.* 1982;29(3):187-187.
9. Taruttis A, Ntziachristos V. Advances in real-time multispectral photoacoustic imaging and its applications. *Nat Photon.* 2015;9(4):219-227.
10. Luke GP, Yeager D, Emelianov SY. Biomedical applications of photoacoustic imaging with exogenous contrast agents. *Ann Biomed Eng.* 2012;40(2):422-437.
11. Kim C, Erpelding TN, Jankovic L, Pashley MD, Wang LV. Deeply penetrating in vivo photoacoustic imaging using a clinical ultrasound array system. *Biomed Opt Express.* 2010;1(1):278-284.
12. Yao J, Wang LV. Photoacoustic Microscopy. *Laser Photon Rev.* 2013;7(5).
13. Knieling F, Neufert C, Hartmann A, et al. Multispectral Optoacoustic Tomography for Assessment of Crohn's Disease Activity. *N Engl J Med.* 2017;376(13):1292-1294.
14. Stoffels I, Morscher S, Helfrich I, et al. Metastatic status of sentinel lymph nodes in melanoma determined noninvasively with multispectral optoacoustic imaging. *Science translational medicine.* 2015;7(317):317ra199.
15. Taruttis A, Timmermans AC, Wouters PC, Kacprowicz M, van Dam GM, Ntziachristos V. Optoacoustic Imaging of Human Vasculature: Feasibility by Using a Handheld Probe. *Radiology.* 2016;281(1):256-263.
16. Cantisani V, Grazhdani H, Fioravanti C, et al. Liver metastases: Contrast-enhanced ultrasound compared with computed tomography and magnetic resonance. *World J Gastroenterol.* 2014;20(29):9998-10007.
17. Nguyen QT, Tsien RY. Fluorescence-guided surgery with live molecular navigation--a new cutting edge. *Nat Rev Cancer.* 2013;13(9):653-662.
18. Mercep E, Burton NC, Claussen J, Razansky D. Whole-body live mouse imaging by hybrid reflection-mode ultrasound and optoacoustic tomography. *Optics letters.* 2015;40(20):4643-4646.

19. Heuveling DA, Visser GW, de Groot M, et al. Nanocolloidal albumin-IRDye 800CW: a near-infrared fluorescent tracer with optimal retention in the sentinel lymph node. *Eur J Nucl Med Mol Imaging*. 2012;39(7):1161-1168.
20. Marshall MV, Draney D, Sevick-Muraca EM, Olive DM. Single-dose intravenous toxicity study of IRDye 800CW in Sprague-Dawley rats. *Mol Imaging Biol*. 2010;12(6):583-594.
21. Verbeek FP, van der Vorst JR, Tummers QR, et al. Near-infrared fluorescence imaging of both colorectal cancer and ureters using a low-dose integrin targeted probe. *Annals of surgical oncology*. 2014;21 Suppl 4:S528-537.
22. Chen H, Niu G, Wu H, Chen X. Clinical Application of Radiolabeled RGD Peptides for PET Imaging of Integrin alphavbeta3. *Theranostics*. 2016;6(1):78-92.
23. Huang R, Vider J, Kovar JL, et al. Integrin alphavbeta3-targeted IRDye 800CW near-infrared imaging of glioblastoma. *Clinical cancer research : an official journal of the American Association for Cancer Research*. 2012;18(20):5731-5740.
24. Yoon Y, Mohs AM, Mancini MC, Nie S, Shim H. Combination of an Integrin-Targeting NIR Tracer and an Ultrasensitive Spectroscopic Device for Intraoperative Detection of Head and Neck Tumor Margins and Metastatic Lymph Nodes. *Tomography*. 2016;2(3):215-222.
25. Liu L, Lin G, Yin F, Law WC, Yong KT. Near-infrared fluorescent peptide probes for imaging of tumor in vivo and their biotoxicity evaluation. *J Biomed Mater Res A*. 2016;104(4):910-916.
26. Rossin R, van Duijnhoven SM, Lappchen T, van den Bosch SM, Robillard MS. Trans-cyclooctene tag with improved properties for tumor pretargeting with the diels-alder reaction. *Molecular pharmaceuticals*. 2014;11(9):3090-3096.
27. Saccomano M, Dullin C, Alves F, Napp J. Preclinical evaluation of near-infrared (NIR) fluorescently labeled cetuximab as a potential tool for fluorescence-guided surgery. *Int J Cancer*. 2016;139(10):2277-2289.
28. Sarantopoulos A, Themelis G, Ntziachristos V. Imaging the bio-distribution of fluorescent probes using multispectral epi-illumination cryoslicing imaging. *Molecular imaging and biology : MIB : the official publication of the Academy of Molecular Imaging*. 2011;13(5):874-885.
29. van Driel PB, van de Giessen M, Boonstra MC, et al. Characterization and evaluation of the artemis camera for fluorescence-guided cancer surgery. *Molecular imaging and biology : MIB : the official publication of the Academy of Molecular Imaging*. 2015;17(3):413-423.
30. Morscher S, Driessen WH, Claussen J, Burton NC. Semi-quantitative Multispectral Optoacoustic Tomography (MSOT) for volumetric PK imaging of gastric emptying. *Photoacoustics*. 2014;2(3):103-110.
31. Schindelin J, Arganda-Carreras I, Frise E, et al. Fiji: an open-source platform for biological-image analysis. *Nat Methods*. 2012;9(7):676-682.
32. Alves F, Contag S, Missbach M, et al. An orthotopic model of ductal adenocarcinoma of the pancreas in severe combined immunodeficient mice representing all steps of the metastatic cascade. *Pancreas*. 2001;23(3):227-235.
33. Yin W, Kimbrough CW, Gomez-Gutierrez JG, et al. Tumor specific liposomes improve detection of pancreatic adenocarcinoma in vivo using optoacoustic tomography. *J Nanobiotechnology*. 2015;13:90.

34. Laufer J, Jathoul A, Pule M, Beard P. In vitro characterization of genetically expressed absorbing proteins using photoacoustic spectroscopy. *Biomed Opt Express*. 2013;4(11):2477-2490.
35. Cox B, Laufer JG, Arridge SR, Beard PC. Quantitative spectroscopic photoacoustic imaging: a review. *J Biomed Opt*. 2012;17(6):061202.
36. Tzoumas S, Nunes A, Olefir I, et al. Eigenspectra optoacoustic tomography achieves quantitative blood oxygenation imaging deep in tissues. *Nat Commun*. 2016;7:12121.
37. Brochu FM, Bruncker J, Joseph J, Tomaszewski MR, Morscher S, Bohndiek SE. Towards Quantitative Evaluation of Tissue Absorption Coefficients Using Light Fluence Correction in Optoacoustic Tomography. *IEEE Trans Med Imaging*. 2017;36(1):322-331.
38. Kimbrough CW, Hudson S, Khanal A, Egger ME, McNally LR. Orthotopic pancreatic tumors detected by optoacoustic tomography using Syndecan-1. *Journal of Surgical Research*. 2015;193(1):246-254.
39. Hudson SV, Huang JS, Yin WY, et al. Targeted Noninvasive Imaging of EGFR-Expressing Orthotopic Pancreatic Cancer Using Multispectral Optoacoustic Tomography. *Cancer Research*. 2014;74(21):6271-6279.
40. Napp J, Dullin C, Muller F, et al. Time-domain in vivo near infrared fluorescence imaging for evaluation of matriptase as a potential target for the development of novel, inhibitor-based tumor therapies. *International Journal of Cancer*. 2010;127(8):1958-1974.
41. Artinyan A, Soriano PA, Prendergast C, Low T, Ellenhorn JDI, Kim J. The anatomic location of pancreatic cancer is a prognostic factor for survival. *Hpb*. 2008;10(5):371-376.
42. McNally LR, Mezera M, Morgan DE, et al. Current and Emerging Clinical Applications of Multispectral Optoacoustic Tomography (MSOT) in Oncology. *Clinical cancer research : an official journal of the American Association for Cancer Research*. 2016;22(14):3432-3439.
43. Valluru KS, Willmann JK. Clinical photoacoustic imaging of cancer. *Ultrasonography*. 2016;35(4):267-280.
44. Whitley MJ, Weissleder R, Kirsch DG. Tailoring Adjuvant Radiation Therapy by Intraoperative Imaging to Detect Residual Cancer. *Semin Radiat Oncol*. 2015;25(4):313-321.
45. Zhao ZQ, Yang Y, Fang W, Liu S. Comparison of biological properties of Tc-99m-labeled cyclic RGD Peptide trimer and dimer useful as SPECT radiotracers for tumor imaging. *Nucl Med Biol*. 2016;43(11):661-669.

Part II – Necrosis Imaging



Chapter 5

Necrosis avid near infrared fluorescent cyanines for imaging cell death and their use to monitor therapeutic efficacy in mouse tumor models

Bangwen Xie, Marieke A. Stammes, Pieter B.A.A. van Driel, Luis J. Cruz, Vicky T. Knol-Blankevoort, Martijn A.M. Löwik, Laura Mezzanotte, Ivo Que, Alan Chan, Jeroen P.H.M. van den Wijngaard, Maria Siebes, Sven Gottschalk, Daniel Razansky, Vasilis Ntziachristos, Stijn Keereweer, Richard W. Horobin, Mathias Hoehn, Eric L. Kaijzel, Ermond R. van Beek, Thomas J.A. Snoeks, Clemens W.G.M. Löwik.

Adapted from: necrosis avid near infrared fluorescent cyanines for imaging cell death and their use to monitor therapeutic efficacy in mouse tumor models, *Oncotarget*. 2015 Nov 17; 6(36):39036-49.

Abstract

Purpose

Necrosis is a unique biomarker in cancer patients. Quantification of tumor necrosis in cancer patients is of diagnostic value as the amount of necrosis is correlated with disease prognosis and it could also be used to predict early efficacy of anti-cancer treatments. The purpose of this study was to show the strong necrosis avid properties of two near infrared fluorescent (NIRF) carboxylated cyanines; HQ5 and IRDye800CW (800CW).

Procedures

Several *in vitro* and *in vivo* mouse models were used, in combination with quantitative structure activity relations (QSAR) modeling, to confirm the necrosis avid properties of HQ5 and 800CW.

Results

In vitro studies showed that both dyes selectively bind to cytoplasmic proteins of dead cells that have lost membrane integrity. Affinity for cytoplasmic proteins was confirmed using quantitative structure activity relations modeling. *In vivo* results, using NIRF and optoacoustic imaging, confirmed the necrosis avid properties of HQ5 and 800CW in a mouse 4T1 breast cancer tumor model of spontaneous necrosis. Finally, in a mouse EL4 lymphoma tumor model, already 24h post chemotherapy, a significant increase in 800CW fluorescence intensity was observed in treated compared to untreated tumors.

Conclusions

We showed, for the first time, that the NIRF carboxylated cyanines HQ5 and 800CW possess strong necrosis avid properties *in vitro* and *in vivo*. When translated to the clinic, these dyes may be used for diagnostic or prognostic purposes and for monitoring *in vivo* tumor response early after the start of treatment.

Introduction

Cell death by necrosis merely occurs under pathological conditions, as a result of physiochemical damage or sudden metabolic failure and is involved in cancer development and treatment^{1,2}. The amount of tissue necrosis is of diagnostic value in many cancer types, since a high degree of necrosis is an indicator of rapid and aggressive tumor growth and is often correlated with poor prognosis³⁻¹⁰. Moreover, necrosis can also be induced by injury caused to tumor tissue by anti-cancer treatments. Finally, therapeutic approaches that initially induce apoptotic cell death often result in secondary necrosis, as a natural outcome of the complete apoptotic program¹¹. Accurate quantification of the amount of tissue necrosis has great potential for pre-clinical and clinical applications, especially in monitoring anti-cancer efficacy at an early stage of treatment instead of at the end of therapy. However, the existing modalities and methods as for example standardized uptake values (SUVs) of FDG-PET, determination of tumor markers or of specific tumor mRNAs all lack the accuracy for a broad and routine application^{12,13}. Therefore, the long lag-time in determining therapy outcome causes loss of valuable treatment time in non-responding patients that will receive expensive treatment and are unnecessarily exposed to side effects. Early evaluation of the therapy efficacy would therefore facilitate the growing call for individualized cancer treatment, allowing the clinician to adjust the therapy based on tumor response, resulting in higher survival rates and cost-efficacy^{1,2}.

In vitro, cell necrosis is often measured using dyes such as Eosin, Propidium iodide (PI), TO-PRO-3 and Trypan Blue, which enter necrotic cells upon loss of membrane integrity and cannot permeate living cells. PI and the cyanine TO-PRO-3 subsequently intercalate into DNA¹⁴⁻¹⁶ rendering them potentially mutagenic, which has hampered their clinical use. Perfetto *et al.* showed that amine-reactive cyanines could also be employed to discriminate between living and dead cells *in vitro*^{17,18}. The amine-reactive group on such cyanines can covalently interact with free amino moieties that are available on every protein. Because these amine-reactive compounds are incapable of passing intact cell membranes, only extracellular membrane proteins of living cells are labeled. However, as soon as cells lose their membrane integrity, cytoplasmic proteins become available for dye binding, leading to an accumulation of these agents in dead cells. Though, this principle cannot be employed *in vivo*,

as immediately after injection, these reactive cyanines will non-specifically interact with all proteins accessible.

In vivo, MRI in combination with non-specific contrast agents, such as Dotarem, have been employed to visualize necrosis. However, with this procedure it was impossible to reliably distinguish healthy from necrotic tissue or neoplastic growth¹⁹. Consequently, the focus shifted towards the development of compounds that could selectively target necrotic tissues. Already in 1988, Epstein and colleagues developed monoclonal antibodies against nuclear antigens, allowing specific targeting of necrotic tissue present in solid tumors²⁰. However, the use of antibodies is limited due to their size, resulting in limited tissue penetration, as well as the induction of unwanted immune responses²¹.

Necrosis avid contrast agents (NACAs) are another class of compounds that specifically accumulate in necrotic tissue, these are categorized in porphyrin or non-porphyrin-based compounds. NACAs, such as the well-known compound hypericin, are assumed to specifically bind proteins, peptides and nucleotides that become available upon loss of cell membrane integrity^{22,23}. However, most of these compounds have poor solubility, high tendency to aggregate, are photo-toxic and lack specificity, which are the main reasons why there are currently no clinically approved NACAs available^{23,24}. Therefore, there is an unmet need for non-toxic, small-molecule based probes that can target necrosis with high specificity for diagnostic imaging and treatment follow-up.

In the present study, using several *in vitro*, cell death, assays, we identified the near infrared fluorescent carboxylated cyanines, HQ5 and 800CW as new non-toxic water soluble NACAs. These NACAs bind to intracellular cytoplasmic proteins of cells that have lost membrane integrity. We employed quantitative structure activity relations (QSAR) modeling to predict the overall trajectory of these dyes to their cellular localization sites. In contrast to amine-reactive or maleimide containing cyanines, used for protein labeling, carboxylated cyanines cannot covalently interact and are therefore indicated as non-reactive. Next to *in vitro* studies, we also characterized the necrosis avid properties of HQ5 and 800CW in an *in vivo* 4T1 mouse breast cancer model of spontaneous tumor necrosis and in an EL4 lymphoma model in which cell death was induced by chemotherapy. In these animal models, due

to their small size, whole body imaging using NIRF imaging, or multi-spectral optoacoustic (OA) imaging, is well suited as a light penetration depth of several cm can be obtained in this part of the spectrum²⁵. The actions of the cyanines were compared to those of the blood pool agent 800CW-PEG.

Materials and Methods

QSAR modeling

Estimation of the structure parameters for carboxylated HQ5 and IRDye 800CW (800CW) and the integration of the parameters with appropriate QSAR models was carried out as detailed elsewhere^{26,27}.

Cyanines

HQ5 carboxylate was obtained from Ilumicare BV (Rotterdam, The Netherlands). The dyes 800CW, 800CW-2-Deoxyglucose (800CW-2DG), 800CW-epidermal growth factor (800CW-EGF) and 800CW-polyethylene glycol (800CW-PEG) were obtained from LI-COR Biosciences.

Cells and culture conditions

4T1-luc2 murine mammary cancer cells (PerkinElmer) was cultured in complete RPMI-1640 medium (Life Technologies, Inc.). EL4 murine lymphoma cells were cultured in complete Iscove's Modified Dulbecco's Medium (Life Technologies). Cells were transduced with a lentivirus for the expression of CBG99 luciferase under the control of the constitutive promoter PGK as described previously to create EL4-CBG99-luc²⁸.

Dry ice dead cell assay

In vitro, cell death was studied using a cryo-induced cell death assay, which detailed procedures have been described previously²⁹. Briefly, a bar of dry ice was applied to the underside of the culture well confluent with 4T1-luc2 cells for 15sec. Subsequently, the cells were incubated with HQ5, 800CW or 800CW-PEG, respectively (100nM, 15min, room temperature (RT), in the dark). After gentle washing with PBS, the samples were scanned for fluorescence imaging (FLI) using an Odyssey Infrared Imager 9120 (LI-COR). For bioluminescence imaging (BLI), D-luciferin solution (25µg/µl; SynChem Inc.) was added for 10min incubation. BLI measurements were then acquired using an IVIS Spectrum imaging system (PerkinElmer).

FACS analyses

The detailed procedures for flow cytometry of cells after inducing cell death have been described previously²⁹. Briefly, 4T1-luc2 cells were incubated in the presence or absence of gambogic acid (GA, 4 μ M, 24h, Calbiochem) or Staurosporine (Sta, 3 μ M, 24h, Sigma-Aldrich). Cells were then collected and re-suspended in 100 μ l PBS. The cell suspensions were incubated in the dark for 15min at RT with one of the cyanines (200nM). Alternatively, cells were stained with the commercially available cell death probes AVF and PI (PromoKine) in accordance with the manufacturer's protocols. Flow cytometry was performed using a BD LSR II or Canto II Flow Cytometer (BD Biosciences). The data was analyzed using FlowJo software.

Confocal microscopy

4T1-luc2 cells were cultured in a glass bottomed culture dish (MatTek Corp.) until 80% confluent. Cell death was induced by incubation with GA (3 μ M, 1h). Subsequently, the cells were washed gently with PBS and incubated in the presence of 80nM HQ5 in the dark for 15 min at RT. AVF and PI were used in accordance with the manufacturer's protocols. Afterwards, samples were imaged using a Leica TCS SP5 confocal microscope (Leica).

SDS-PAGE analysis

Cytoplasmic and membrane protein samples of 4T1-luc2 cells were prepared using a subcellular protein fractionation kit (Thermo Scientific) according to the manufacturer's protocol. Samples of protein extracts (2 μ g per lane) were incubated with either HQ5 or 800CW (1 μ M) for 15min at RT in the dark. For Bovine serum albumin (BSA) commercial preparations of BSA (5 μ g per lane, Life Technologies) were incubate with either HQ5 or 800CW (0.1, 0.5 and 2 μ M, respectively) for 15min at RT in the dark. Subsequently, samples were mixed with SDS-PAGE sample buffer without indicative blue dye and loaded onto reduced 12.5% SDS polyacrylamide gel. The precision plus protein marker (BIO-RAD) was loaded to one extra lane. After running SDS-PAGE, the gel was processed for FLI using the Odyssey Infrared Imager 9120 scanner. Finally, protein samples were stained with Coomassie brilliant blue staining (BIO-RAD) and photographed.

Animals

Female athymic mice (BALB/c *nu/nu*, 6 weeks old) were acquired from Charles River Laboratories (L'Arbresle Cedex, France). All experimental procedures were performed under isoflurane gas anesthesia (3% induction, 1.5-2% maintenance) in 70% pressurized air and 30% O₂, unless stated differently. Animals were sacrificed by cervical dislocation at the end of the experimental period. The animals were housed per 4-5 animals in individually ventilated cages with *ad libitum* access to food and water. All animal experiments were assessed for animal health & ethics and approved by the Animal Welfare Committee of Leiden University Medical Center, the Netherlands. All mice received humane care and were kept in compliance with the *Code of Practice Use of Laboratory Animals in Cancer Research* (Inspectie W&V, July 1999).

Spontaneous tumor necrosis model

Mice (n=5) received orthotopic inoculations of 2×10^4 4T1-luc2 cells beneath the upper mammary fat pad. Trypan Blue (Sigma-Aldrich) exclusion was used to examine the viability of the tumor cells before injection. After three weeks, tumors were formed, containing a spontaneous necrotic core. Whole body BLI and FLI measurements were performed using the IVIS Spectrum, with either 10min post D-luciferin (150mg/kg) per intraperitoneal (i.p.) injection or 24h post HQ5 (2nmole per mouse) per i.v. injection.

3D fluorescent cryomicrotome imaging of a tumor was reconstructed according to the previous published methods³⁰. In brief, tumor samples were immersed in carboxymethylcellulose sodium solvent (Brunschwig Chemie, Amsterdam, The Netherlands) mixed with 5% Indian ink (Royal Talens, Apeldoorn, The Netherlands) and frozen for at least 24hrs at -25°C. After each cut, tumor epi-illumination outline images were acquired at an excitation wavelength of 440nm/20nm (central wavelength and bandwidth) and an emission wavelength of 435nm/25nm, with 300ms illumination time. Images of tumor fluorescence were acquired at an excitation wavelength of 640nm/50nm and an emission wavelength of 712nm/75nm, 5000ms illumination. All tissue samples were imaged in one session with camera binning set at 2048x2048 pixel resolution, with a corresponding in-plane resolution of 17µm. Prior to further analyses, images were converted to 8 bit gray scale.

MSOT imaging

A group (n=3) of female athymic nude-Fox1nu mice was inoculated with 4T1 cells and subjected to MSOT measurements. MSOT measurements were performed using the inVision 256-TF system (iThera Medical GmbH, Munich, Germany) according to the protocol described previously^{31,32}. In brief, the mice were anesthetized and placed in supine position in the animal holder throughout the entire imaging process. Cross-sectional multispectral OA image datasets were acquired through the tumor at eight different wavelengths in the NIR window (690, 700, 710, 740, 760, 780, 800 and 900nm). MSOT datasets are reconstructed using the interpolated model-matrix inversion. Afterwards, linear spectral unmixing is applied to each set of multiwavelength images to resolve biodistribution of the different tissue chromophores and the contrast agent, i.e. oxygenized and deoxygenized hemoglobin and HQ5³³.

Chemotherapy of murine lymphomas

Two randomized groups mice (n=3) received a subcutaneous (s.c.) inoculation with 1×10^5 EL4-CBG99-luc murine lymphoma cells on the upper back. 11 days after inoculation, the animals either received chemotherapy consisting of i.p. injection of a combination of cyclophosphamide (CTX, 100mg/kg; Baxter BV, The Netherlands) and etoposide (ETO, 70mg/kg; Pharmachemie BV, The Netherlands) or remained untreated. After 24h, all animals received an i.v. injection of 800CW (5nmole per mouse). FLI measurements were performed another 24h after injection using the IVIS spectrum. Whole body BLI measurements were performed, before and 24h after injection of the chemotherapeutic agents, 10min after i.p. administering D-luciferin (150mg/kg). After FLI, all mice were sacrificed and the tumors were surgically excised for *ex vivo* FLI and processed for histological analysis. Image analyses were performed using the Living Image software. For quantitative analysis, regions of interest (ROI) from acquired images were selected to cover the tumor regions. Statistical analysis of the average fluorescent radiant efficiency in ROIs was performed using a Student's t-test.

Histopathology analysis

4T1-luc2 and EL4-CBG99-luc tumors were fixed in 4% formaldehyde and embedded in paraffin. 5µm sections were prepared and imaged for FLI using the Odyssey Infrared Imager 9120 scanner. Afterwards, the consecutive sections were subjected to TdT-mediated dUTP Nick-End Labeling (TUNEL)

staining (Promega) to validate accumulation of the NIRF probes in dying and dead cells.

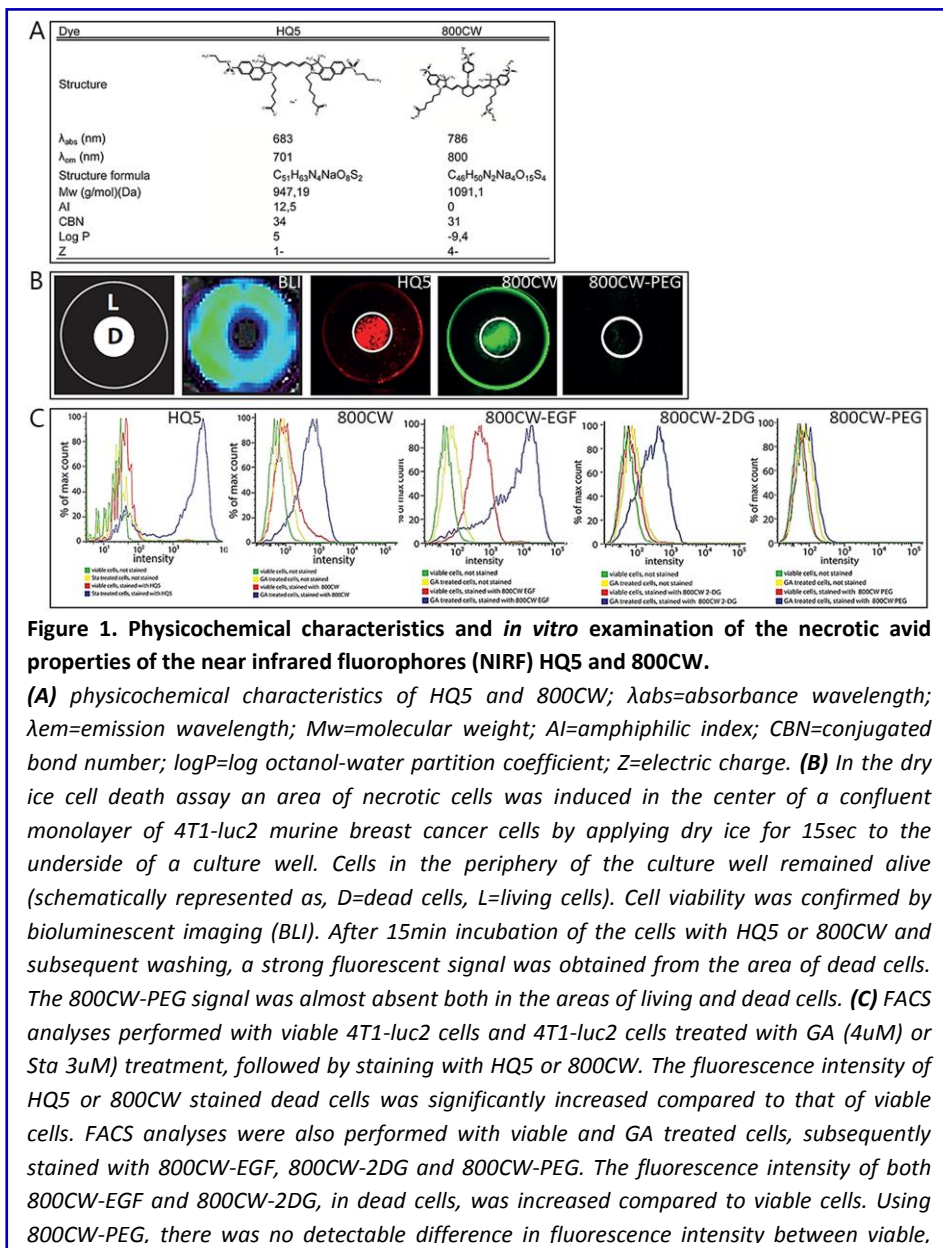
Results

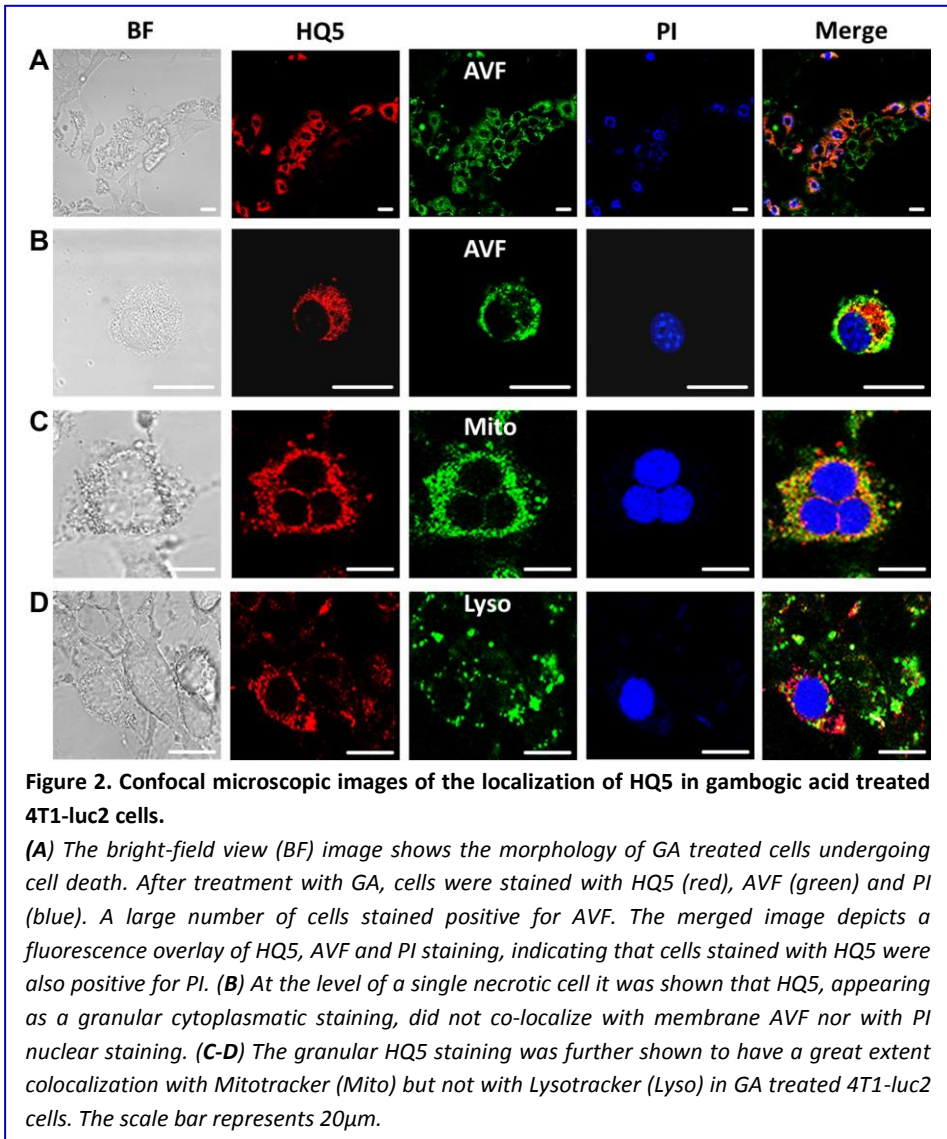
QSAR modeling

Figure 1A shows estimates of the most widely used numerical structure parameters, amphiphilicity index (AI), conjugated bond number (CBN), lipophilicity (logP) and charge (Z), applied to QSAR modeling of the carboxylated cyanines HQ5 and 800CW.

***In vitro* characterization of necrosis avid cyanines**

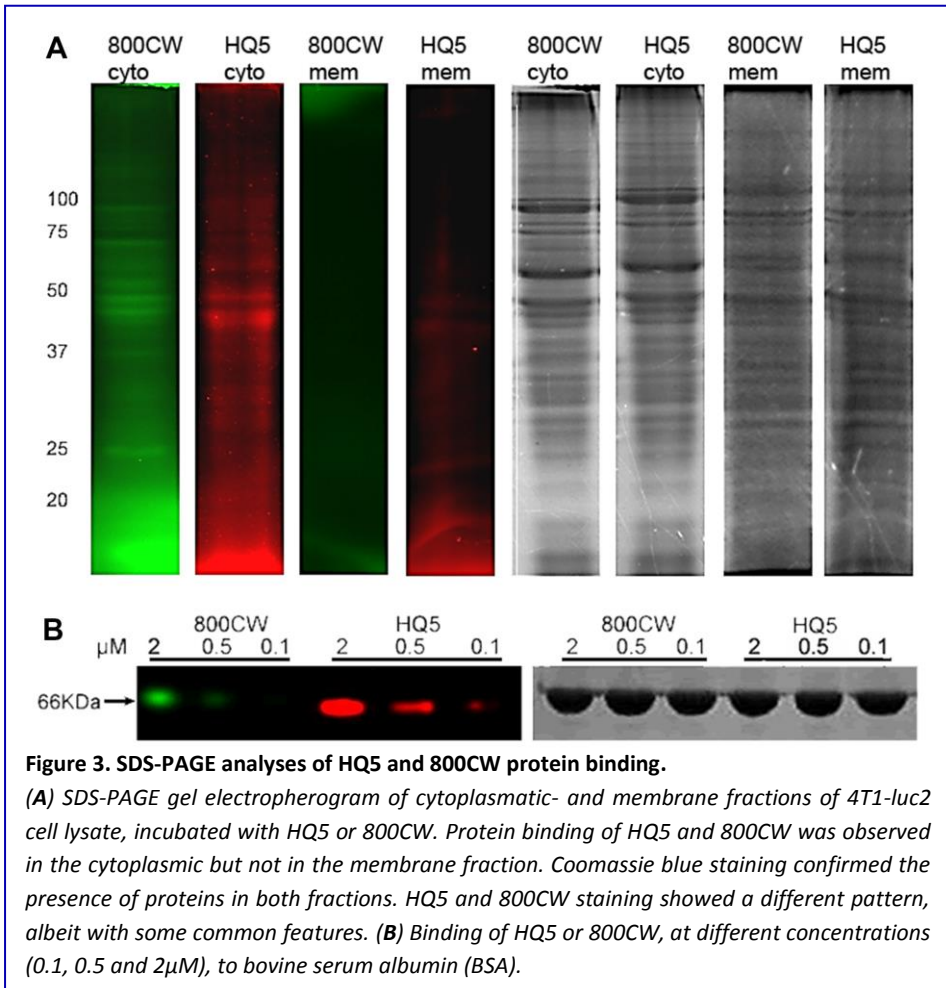
Using a newly developed *in vitro* cell death assay, based on local killing of cells by freezing²⁹, we identified the carboxylated cyanines HQ5 and 800CW to exhibit strong necrosis avid and imaging properties. **Figure 1B** shows a schematic representation of the central, dry ice induced, area of dead 4T1-luc2 cells (D) and the rim of living cells (L) in the periphery. Moreover, BLI measurements, indicated that no bioluminescent signals were obtained from the dead cells in the center of the well while the surrounding living cells produced strong signals. In contrast, HQ5 or 800CW incubated wells showed a strong fluorescent signal in the area of dead cells, but not in the area of living cells. The non-specific contrast agent 800CW-PEG, however, showed minimal affinity for dead cells.





The results obtained from the dry ice assay were confirmed by FACS analysis (**Fig. 1C**). 4T1-luc2 cells which were killed by the cytotoxic agents gambogic acid (GA) or Staurosporine (Sta) stained highly positive for HQ5 and 800CW, this in contrast to living cells. Moreover, our FACS experiments showed that the commercially available NIRF imaging probes 800CW-2DG and 800CW-EGF in which 2-Deoxyglucose (2-DG) or epidermal growth factor (EGF) are conjugated to the side chains of 800CW, also specifically accumulated in dead 4T1-luc2 cells. However, the non-specific contrast agent 800CW-PEG did not accumulate in dead cells.

Figure 2A depicts a confocal microscopic image of a GA treated 4T1-luc2 cell culture stained with HQ5, Annexin V-FITC (AVF) and Propidium Iodine (PI). The bright-field (BF) image shows the morphology of GA treated cells undergoing cell death. Most cells stained AVF positive and a few were positive for HQ5 and PI. The HQ5 positively stained cells coincided with PI nuclear staining and not with AVF phosphatidylserine (PS) staining, as visualized in the merged image. The intracellular distribution of HQ5, PI and AVF staining in a single necrotic 4T1-luc2 cell is shown in **Figure 2B**. PI selectively stained the cell nucleus whereas AVF membrane staining was spread unevenly over the entire cell surface leaving the nucleus unstained. The uneven distribution of the stain may be explained by the loss of membrane integrity. HQ5 showed a more uniform granular staining pattern and did not co-localize with the nuclear stain PI or AVF. Furthermore, **Figure 2C-D** shows that the granular HQ5 staining to a great extent co-localizes with Mito-tracker but not with Lyso-tracker. Moreover, HQ5 also reveals a unique perinuclear staining. Confocal microscopy could not be performed using 800CW as our system is not suitable for the detection of 800nm fluorescence. Specific cyanine affinity towards membrane and cytoplasmatic proteins was examined on SDS-PAGE using isolated membrane- and cytoplasmic protein fractions of 4T1-luc2 cells.



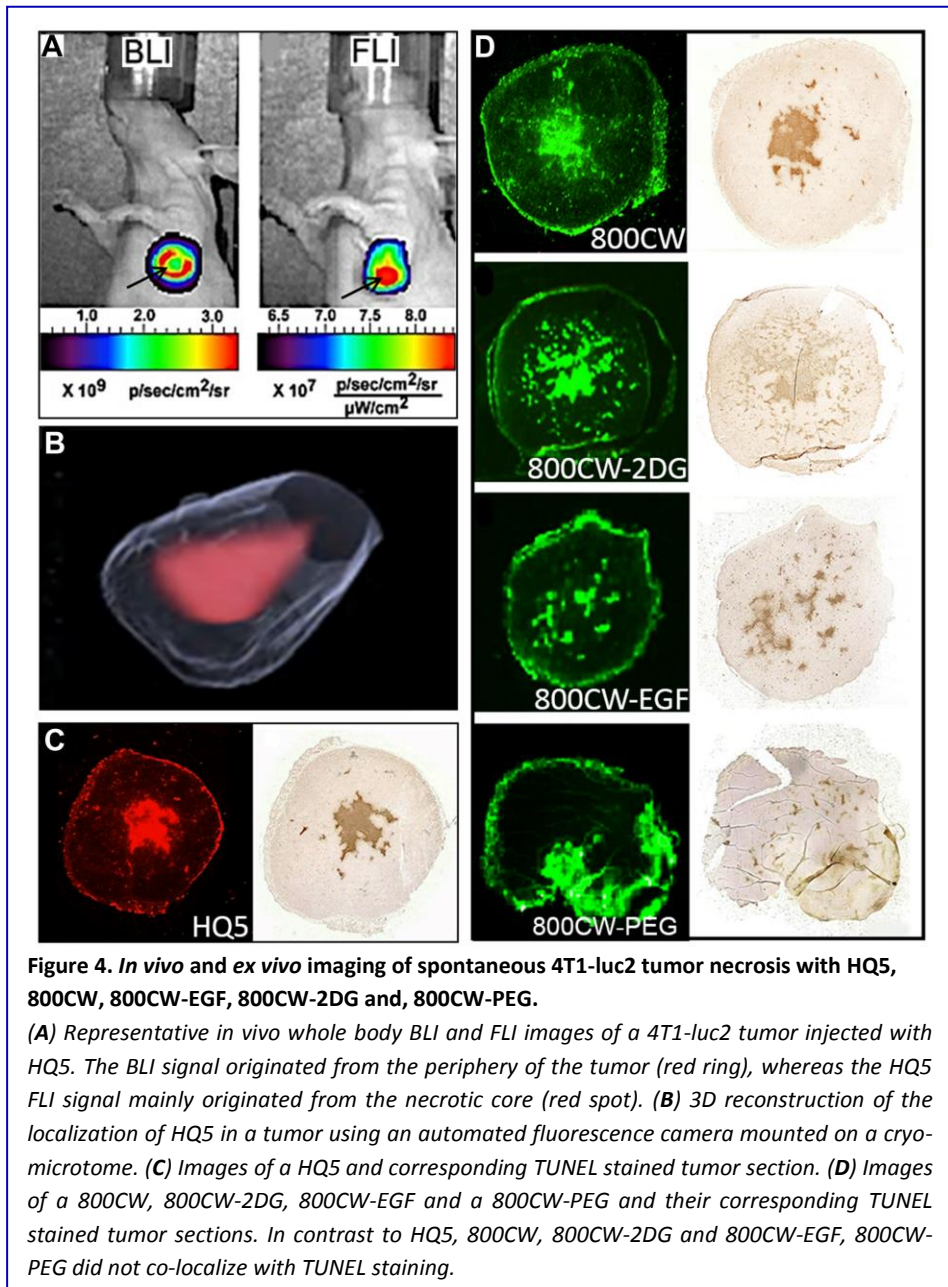
As shown in **Figure 3A**, HQ5 and 800CW strongly stained several protein bands in the cytoplasmic fraction, but not in the membrane fraction. There was some overlap in the staining pattern of the two dyes. Coomassie blue staining indicated that proteins were abundantly present in both fractions.

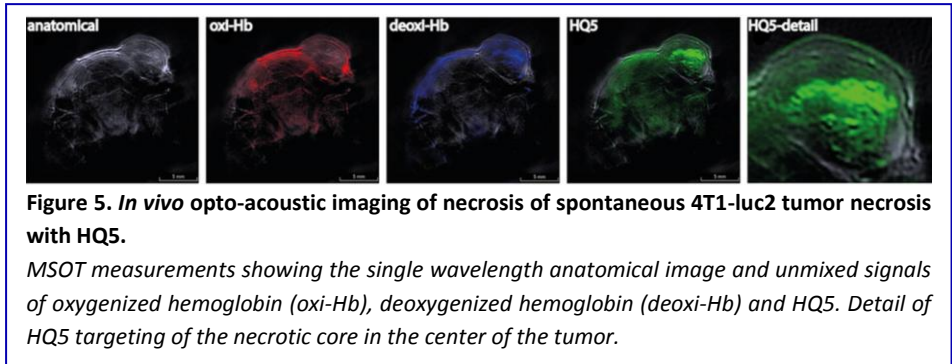
Furthermore, also affinity of the cyanines towards serum albumin was examined using SDS-PAGE analysis. As depicted in **Figure 3B**, HQ5 shows a stronger dose-dependent binding to BSA compared to 800CW, although binding only occurred at micromolar concentrations.

Animal model with tumor necrosis

The necrosis avid properties of the cyanines were evaluated in an animal model of 4T1-luc2 breast tumors, which, during growth, spontaneously develop a necrotic core during progression. As shown in **Figure 4A**, the BLI signal obtained from these tumors has a lower intensity in the center compared to the periphery of the tumor, which is indicative of the presence of a necrotic core. As expected, FLI of the cyanine HQ5 showed strong accumulation of fluorescence in the necrotic center of the tumor. Localization of HQ5 fluorescence in the necrotic core of the tumor was confirmed in 3D reconstructions of cryo-sections (**Fig. 4B**) and showed co-localization with TUNEL staining in parallel paraffin tumor sections (**Fig. 4C**). As shown in **Figure 4D**, 800CW and bio-conjugated receptor targeting probes 800CW-2DG and 800CW-EGF also strongly accumulated in the necrotic areas of tumors, indicated by a co-localization with TUNEL staining. In contrast, 800CW-PEG did not co-localize with TUNEL staining and most of its fluorescence signal was localized in the tumor periphery.

Furthermore, we employed 3D Multi-Spectral Optoacoustic Tomography (MSOT) imaging to visualize the location of HQ5 in the tumor *in vivo*. As shown in **Figure 5**, the HQ5 OA signal co-localized with the deoxygenated hemoglobin signal present in the center of the tumor and not with the oxygenated hemoglobin signal present in the viable rim of the tumor, confirming necrotic core localization.

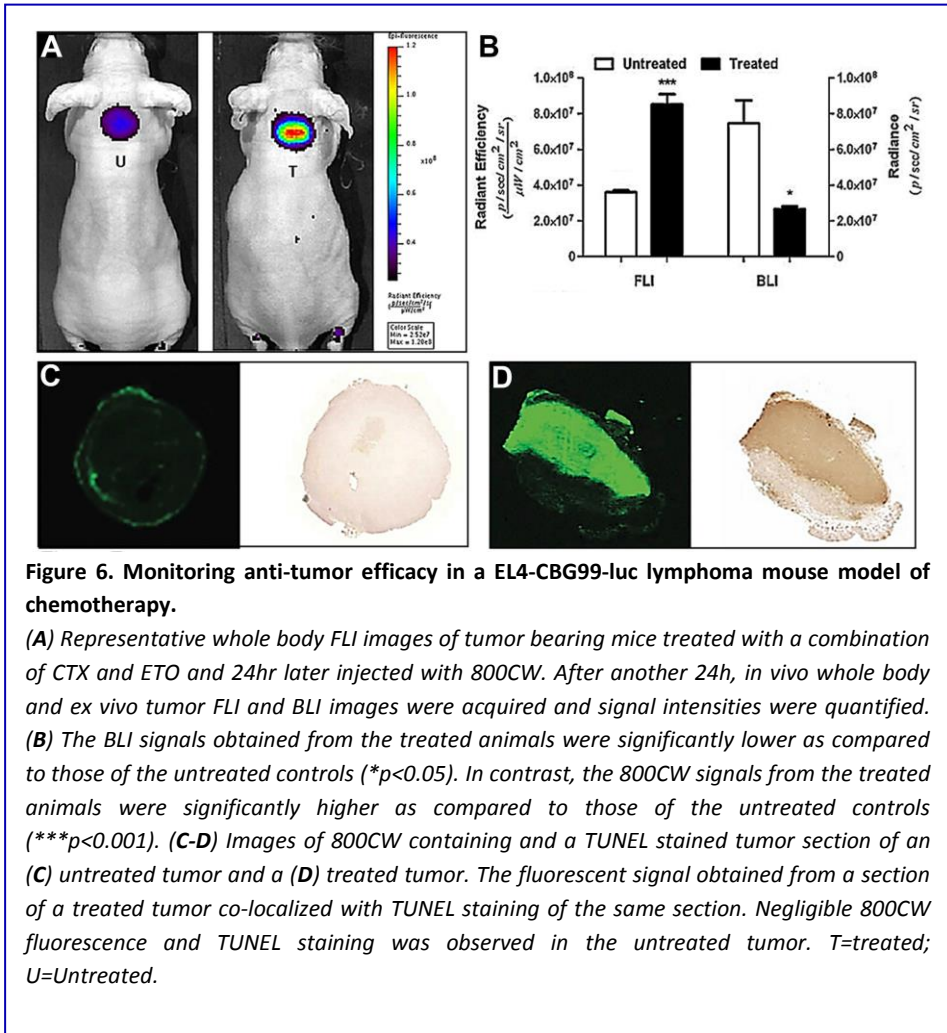




Monitoring early therapeutic response in tumors

We investigated early therapeutic responses in tumors treated with a combination of the chemotherapeutic agents Cyclophosphamide (Cy) and Etoposide (Et) in EL4-CBG99-luc lymphoma bearing mice. For this, control tumor bearing mice and mice treated with Cy/Et were injected with 800CW 24h after chemotherapy.

After another 24h, fluorescence intensity of the tumors was measured. We observed a 2.4-fold higher fluorescence intensity in the tumors of chemo treated mice compared to those of untreated animals ($p < 0.001$). Vice versa, the mean BLI intensity of untreated tumors was 2.8-fold higher than that of chemo treated tumors ($p < 0.05$) (**Fig. 6A-B**). Histological examination of the tumors showed a large area of TUNEL positive tissue in the tumors treated (**Fig. 6C**) with chemotherapy which co localized with 800CW staining, whereas, no TUNEL or 800CW positive tissue was present in control tumors (**Fig. 6D**).



Discussion

Reagents that can monitor necrosis *in vivo* have potential diagnostic and prognostic value in staging of cancer as well as for monitoring early efficacy of anti-cancer therapies^{1,34}. Compared to apoptosis, relatively few studies have addressed the possible role of necrosis as a biomarker for clinical applications. As a result, clinical probes that specifically image or target necrosis are currently unavailable. Consequently, we present two near infrared fluorescent carboxylated cyanines that display necrosis avidity *in vitro* and *in vivo*. Our dry ice cell death assay showed a selective staining of dead cells using the carboxylated cyanines HQ5 and 800CW. However, no dead cell staining was observed with the macromolecule, 800CW-PEG (25-60kDa). Nevertheless, the smaller 800CW-conjugated probes, 800CW-EGF (6kDa) and 800CW-2DG (1kDa), also selectively stained dead cells. The results obtained in the dry-ice assay were confirmed by FACS analyses. The difference in necrosis avidity between 800CW and its PEG conjugated form might be due to the relatively large size of PEG which may cause steric hindrance, as 800CW is maximally 4% of the mass of the conjugate. In line, de Boer et. al. recently showed that macromolecule cetuximab-IRDye800CW was also unable to accumulate in tumor necrosis³⁵. The binding to dead cells of the carboxylate forms of 800CW and HQ5 might be unexpected since these compounds, in contrast to the NHS-ester and maleimide forms, do not contain a reactive group and mainly serve as “dye-only” control to examine potential retention of the compound. In addition, for 800CW it has been shown that after i.v. injection it does not retain in the body and is rapidly cleared via the kidneys³⁶.

Confocal microscopy showed no uptake of any stain in living cells. Nevertheless, after GA treatment we observed HQ5 staining coincided with PI but not with AVF staining. As PI selectively targets cells that have lost membrane integrity, this characteristic is most likely also involved in the dead cell targeting of HQ5. This indicates that HQ5 does not stain apoptotic cells but specifically targets necrotic cells. On a single cell level HQ5 staining showed not to co-localize with either AVF or PI staining and the granular HQ5 staining pattern appeared to be cytoplasmic. The cellular localization of 800CW could not be examined due to the absence of specific 800nm microscope settings. We confirmed the cytoplasmatic protein binding of our cyanines by SDS-PAGE analyses using isolated cell membrane and cytoplasmatic protein fractions of 4T1-luc2 cells. These fractions were incubated with each dye and we observed

that both bound to cytoplasmic and not to the membrane protein fractions. The pattern of protein binding of HQ5 and 800CW to cytoplasmic proteins partly overlapped and also showed preference for a different subset of proteins. This is most likely due to the different physical-chemical properties of these compounds.

Using a QSAR model^{26,27}, which is based on the chemical characteristics of HQ5 and 800CW, the expected cellular localization was further explored. The selective accumulation of these dyes in dead cells requires consideration of both dye and cell properties; the former being summarized in Table 1. The major species of both HQ5 and 800CW under physiological conditions are anionic (Z values of 1- and 4- respectively). Moreover, both dyes have conjugated systems of moderate size (CBN values of 34 and 31). Consequently, the QSAR model predicts both dyes will bind to proteins, albeit not extremely strongly, affinity being due both to ionic attractions with cationic protonated amines and to various non-ionic interactions (van der Waals forces). However, in other respects the dyes differ markedly. Whilst 800CW is extremely hydrophilic ($\log P = -9.4$) and lacks amphiphilicity ($AI = 0$), HQ5 is lipophilic and extremely amphiphilic ($\log P = 5.0$ and $AI = 12.5$). Necrotic cells have two characteristic features, which are significant in this context. Their membranes, including those of the plasmalemma and mitochondria, are permeabilized, permitting the passage of impermeable dyes^{37,38}. As a result, the mitochondrial hydrophobic proteins are more easily accessed by dyes entering the necrotic cell. Moreover, protein denaturation will have increased the number of protein molecules with surface hydrophobic domains³⁹.

The hydrophilic character of 800CW renders it membrane impermeable²⁷ and so it can only enter permeabilised cells. Once within them, its accumulation will be favored by the enhanced dye-binding commonly found with denatured proteins⁴⁰. As this dye is not amphiphilic, it does not bind significantly to serum albumin. HQ5, however, is a lipophilic dye which based on our calculations could possibly enter cells by passive diffusion²⁷. The reason that we do not find this in our *in vitro* assay and confocal analyses is most probably due to the fact that HQ5 is very amphiphilic and will bind to serum albumin. It has been shown that amphiphilicity is correlated with serum albumin affinity^{27,41}. Binding to serum albumin of HQ5 was confirmed by us using SDS-PAGE analysis. Once the cells have lost membrane integrity, HQ5 bound to albumin will enter the cells and will bind to proteins with hydrophobic domains, such as those common in mitochondria, or those which are denatured⁴². This is in line with the confocal microscopy data showing that HQ5 for a large part co-

localizes with Mitotracker. From the QSAR model it is clear that, although HQ5 and 800CW have different chemical characteristics, both can bind to proteins but probably using different mechanisms. This is also reflected in the difference in binding patterns of the two dyes on SDS-PAGE, showing that they target similar and partly different cytoplasmic proteins. Further detailed studies are needed to elucidate the exact mechanism of binding of the dyes to necrotic cells.

Dyes with large conjugated systems (CBN>40), but lacking amphiphilicity, such as Coomassie Blue and Evans Blue, are predicted by the QSAR model to bind strongly to all proteins²⁷. Such dyes are therefore not expected to show selective uptake into necrotic cells, but will bind to whatever proteins are first contacted.

The question that remains is if, *in vivo*, 800CW and HQ5 specifically target necrotic tissues or that these compounds non-specifically localize in and around necrotic sites because they comprise blood pool characteristics? For example, previous studies indicated that blood pool contrast agents can be employed to indicate tissue injury, due to their passive leakage from blood vessels at sites of tissue damage. In addition, blood pool agents are employed to detect tumors because of their ability to accumulate in tumor tissue, as a result of a process known as the enhanced permeability and retention (EPR) effect⁴³. This process is characterized by the ability of macromolecules (>20 kDa), or small molecules bound to serum albumin, to accumulate in tumors as a result of their passive leakage from abnormal tumor vasculature. In contrast, small molecules (<20 kDa), which possess no affinity for blood proteins, do not retain and rapidly penetrate the interstitial space of tumors and subsequently diffuse freely back into the blood pool or the lymphatic system. Therefore, the increased retention of blood pool agents at or in the vicinity of tissue damage sites or in tumors is not due to a specific interaction with necrotic tissue, but is merely the result of reduced diffusion velocity of large molecules out of the tissue compartment.

Previous studies and our study show that 800CW possesses very low affinity for blood proteins and consequently rapidly extravasates after *i.v.* injection⁴⁴. This indicates that the small molecule 800CW is not a blood pool agent and, therefore, will retain in tissue because of a specific binding to intracellular proteins of necrotic cells. The *in vivo* specificity of 800CW for necrotic tissues is strengthened by the observation that this compound strongly co-localizes with TUNEL staining, a feature that is not observed with the blood pool agent

800CW-PEG. Similar to 800CW, HQ5 also shows a strong co-localization with TUNEL staining in necrotic areas in tumors. However, in contrast to 800CW, HQ5 can bind to serum albumin and thus potentially serves as blood pool agent. Similarly, the photosensitizer Hypericin, which is currently under pre-clinical investigation because of its necrosis avid properties, also possesses affinity for albumin⁴⁵. In contrast, the well-known blood pool agent Evans Blue, which also strongly binds to serum albumin, has been shown to target the viable rim of tumors rather than the necrotic core⁴⁶. Moreover, based on the observation that of the albumin binding compounds Gadophrin-2 and MP2269, only the first possessed NACA properties Ni et al.²³ stated that necrosis-avidity is an outstanding feature beyond the general pharmacological process of albumin-binding mediated drug transportation. Combined, it might be concluded that the role of blood protein binding in the mode of action of this particular group of NACAs needs, to be established.

In our 4T1-luc2 tumor necrosis model, HQ5 and 800CW showed co-localization with TUNEL staining, and the same was true for the 800CW-EGF and 800CW-2DG conjugated probes and not for 800CW-PEG. Therefore, it is important to note that 800CW-EGF and 800CW-2DG, that are specifically designed and have been extensively used to target the EGF receptor (EGFR) and the Glucose receptor-1 (GLUT)^{47,48}, also have strong necrosis avidity due to the presence of CW800 which can direct these probes towards necrotic cells. This new finding has to be taken into consideration when interpreting experimental results obtained with 800CW-EGF and 800CW-2DG^{36,49-51}.

The necrosis avidity of HQ5 and 800CW was further investigated in a well-known model of chemotherapy. We showed that 800CW could be used to monitor early treatment efficacy. This feature is of great significance since in current clinical practice the efficacy of anti-cancer treatment can only reliable be established late during treatment or after completion of the treatment. Therefore, currently non-responding patients receive an expensive treatment and are unnecessarily exposed to side effects^{1,2}. Finally, it is worth mentioning some of the limitations of the present study, which include the use of athymic mice, the use of transplanted and not spontaneous tumors and the usage of only one type of anti-cancer treatment, namely chemotherapy.

Future perspectives and clinical relevance

Opto-acoustic imaging, a technique in which a pulsating light signal is transformed into an ultrasound wave, provides much deeper tissue penetration (approximately 5 cm) and higher resolution than other–optical imaging modalities currently available. This technology can revolutionize medical imaging in clinical practice. With the development of a handheld MSOT scanner, with applications in breast and melanoma imaging, the clinical translation of opto-acoustic imaging is already materialized and may also ease the translation of our necrosis probes to the clinic especially since we have shown that HQ5 can be detected using MSOT⁵²⁻⁵⁵.

However, for detection of tumors deep within the body, when measurements beyond the maximal optical or Opto-acoustic penetration depth are required, the dyes have to be radiolabeled in order to allow their visualization with standard clinical imaging modalities like SPECT or PET. Our preliminary results show that radiolabeling of a structural analogue of HQ5 with Indium-111, using the chelate DTPA is feasible and that this probe still specifically accumulates in necrotic cells *in vitro* and in necrotic cores of tumors (unpublished data). Moreover, from an economical point of view it is worth to mention that the production costs of the cyanines, especially when synthesized in bulk amounts are low and that the rates for radio labeling and subsequent SPECT/PET scanning will be comparable to those of other clinically used SPECT/PET probes.

The concept of employing tissue necrosis, as a biomarker for diagnostic and prognostic purposes of disease, is not new. With the objective to target and image necrotic tissue, already back in 1988 Epstein and colleagues developed several so called TNT antibodies²⁰ and more recently Ni and colleagues^{22,45,56,57} reported on the specific necrosis avid properties of the photosensitizer Hypericin in small animals. However, both compounds were examined not just for their potential as contrast agents, but also for their possible usage in cancer treatment by coupling of Iodine-131 used for local radiation therapy. In this way, when the necrosis avid agent has accumulated in the necrotic core of the tumor, the cancer is selectively irradiated and killed from the inside. After showing proof of concept, in animal studies⁵⁸, the TNT antibodies even reached clinical phase I and II studies⁵⁹. However, for both TNT antibodies and Hypericin, full clinical translation is hampered because of increased concern about adverse effects and other drawbacks based on their

physical-chemical properties^{59,60}. No such concerns are expected with the employment of the NIRF cyanines examined in this study. NIRF cyanines are successfully used already for more than a decennium for experimental and clinical experimental purposes including fluorescence image guided surgery without serious side effects⁶¹. In addition, toxicity studies by Marshall and colleagues, showed that 800CW carboxylate administrated as a single intravenous or intradermal dose of 20mg/kg, which is about 100-fold above the maximum dose utilized in our experiments, did not result in any pathological evidence of toxicity in rats³⁶. Therefore, our necrosis avid carboxylated NIRF dyes can potentially be used clinically to image necrotic tissue for diagnostic and prognostic purposes, to detect treatment response in tumors and for drug delivery.

In conclusion, we have demonstrated that the carboxylated cyanines 800CW and HQ5, as well as 800CW-2DG and 800CW-EGF, possess strong necrosis avid properties. The molecular mechanism of necrosis avidity involves targeting of cytoplasmic proteins after loss of cell membrane integrity. Using NIRF imaging in different mouse models of cancer, we showed that these dyes can be applied to detect spontaneous tumor necrosis, which is of diagnostic and prognostic value. Moreover, we showed that they can be utilized to monitor early treatment responses in tumors after anti-cancer therapy and potentially they can also be used for drug delivery. Therefore, when translated to the clinic, these compounds might become of great value in cancer diagnostics and treatment.

Acknowledgments

We acknowledge the technical assistance of Henny Bloys-de Groot in preparing the immunohistochemistry sections. RWH thanks Dr. R. Aitken, School of Life Sciences, College of Medical, Veterinary and Life Sciences, University of Glasgow, for providing facilities.

This work was supported by project grants from TI Pharma (Project D4-603) and the EU Seventh Framework Programme: FP7-PEOPLE-2013-IAPP (612360 – BRAINPATH). HQ™ compounds are a trade mark of Ilumicare BV, Rotterdam, The Netherlands who also financially supported part of the studies.

References

1. de Bruin EC, Medema JP. Apoptosis and non-apoptotic deaths in cancer development and treatment response. *Cancer Treat Rev.* 2008;34(8):737-749.
2. Venkatramani R, Wang L, Malvar J, et al. Tumor necrosis predicts survival following neo-adjuvant chemotherapy for hepatoblastoma. *Pediatr Blood Cancer.* 2012;59(3):493-498.
3. Hiraoka N, Ino Y, Sekine S, et al. Tumour necrosis is a postoperative prognostic marker for pancreatic cancer patients with a high interobserver reproducibility in histological evaluation. *British journal of cancer.* 2010;103(7):1057-1065.
4. Kato T, Kameoka S, Kimura T, Tanaka S, Nishikawa T, Kobayashi M. p53, mitosis, apoptosis and necrosis as prognostic indicators of long-term survival in breast cancer. *Anticancer Res.* 2002;22(2B):1105-1112.
5. Maiorano E, Regan MM, Viale G, et al. Prognostic and predictive impact of central necrosis and fibrosis in early breast cancer: results from two International Breast Cancer Study Group randomized trials of chemoendocrine adjuvant therapy. *Breast cancer research and treatment.* 2010;121(1):211-218.
6. Park SY, Lee HS, Jang HJ, Lee GK, Chung KY, Zo JI. Tumor necrosis as a prognostic factor for stage IA non-small cell lung cancer. *The Annals of thoracic surgery.* 2011;91(6):1668-1673.
7. Pichler M, Hutterer GC, Chromecki TF, et al. Histologic tumor necrosis is an independent prognostic indicator for clear cell and papillary renal cell carcinoma. *American journal of clinical pathology.* 2012;137(2):283-289.
8. Pollheimer MJ, Kornprat P, Lindtner RA, et al. Tumor necrosis is a new promising prognostic factor in colorectal cancer. *Human pathology.* 2010;41(12):1749-1757.
9. Richards CH, Roxburgh CS, Anderson JH, et al. Prognostic value of tumour necrosis and host inflammatory responses in colorectal cancer. *The British journal of surgery.* 2012;99(2):287-294.
10. Uhl M, Saueressig U, Koehler G, et al. Evaluation of tumour necrosis during chemotherapy with diffusion-weighted MR imaging: preliminary results in osteosarcomas. *Pediatric radiology.* 2006;36(12):1306-1311.
11. Silva MT. Secondary necrosis: the natural outcome of the complete apoptotic program. *FEBS Lett.* 2010;584(22):4491-4499.
12. Kinahan PE, Fletcher JW. Positron emission tomography-computed tomography standardized uptake values in clinical practice and assessing response to therapy. *Semin Ultrasound CT MR.* 2010;31(6):496-505.
13. Mehta S, Shelling A, Muthukaruppan A, et al. Predictive and prognostic molecular markers for cancer medicine. *Ther Adv Med Oncol.* 2010;2(2):125-148.
14. Doornbos RM, De Grooth BG, Kraan YM, Van Der Poel CJ, Greve J. Visible diode lasers can be used for flow cytometric immunofluorescence and DNA analysis. *Cytometry.* 1994;15(3):267-271.
15. Schmid I, Hausner MA, Cole SW, Uittenbogaart CH, Giorgi JV, Jamieson BD. Simultaneous flow cytometric measurement of viability and lymphocyte subset proliferation. *Journal of immunological methods.* 2001;247(1-2):175-186.

16. Van Hooijdonk CA, Glade CP, Van Erp PE. TO-PRO-3 iodide: a novel HeNe laser-excitable DNA stain as an alternative for propidium iodide in multiparameter flow cytometry. *Cytometry*. 1994;17(2):185-189.
17. Peretto SP, Chattopadhyay PK, Lamoreaux L, et al. Amine-reactive dyes for dead cell discrimination in fixed samples. *Current protocols in cytometry / editorial board, J Paul Robinson, managing editor [et al]*. 2010;Chapter 9:Unit 9 34.
18. Peretto SP, Chattopadhyay PK, Lamoreaux L, et al. Amine reactive dyes: an effective tool to discriminate live and dead cells in polychromatic flow cytometry. *Journal of immunological methods*. 2006;313(1-2):199-208.
19. Verma N, Cowperthwaite MC, Burnett MG, Markey MK. Differentiating tumor recurrence from treatment necrosis: a review of neuro-oncologic imaging strategies. *Neuro-oncology*. 2013;15(5):515-534.
20. Epstein AL, Chen FM, Taylor CR. A novel method for the detection of necrotic lesions in human cancers. *Cancer research*. 1988;48(20):5842-5848.
21. Wang H, Cao C, Li B, et al. Immunogenicity of Iodine 131 chimeric tumor necrosis therapy monoclonal antibody in advanced lung cancer patients. *Cancer immunology, immunotherapy : CII*. 2008;57(5):677-684.
22. Jiang B, Wang J, Ni Y, Chen F. Necrosis avidity: a newly discovered feature of hypericin and its preclinical applications in necrosis imaging. *Theranostics*. 2013;3(9):667-676.
23. Ni Y, Bormans G, Chen F, Verbruggen A, Marchal G. Necrosis avid contrast agents: functional similarity versus structural diversity. *Investigative radiology*. 2005;40(8):526-535.
24. Cona MM, Wang H, Li J, et al. Continuing pursuit for ideal systemic anticancer radiotherapeutics. *Investigational new drugs*. 2012;30(5):2050-2065.
25. Keereweer S, Van Driel PB, Snoeks TJ, et al. Optical image-guided cancer surgery: challenges and limitations. *Clin Cancer Res*. 2013;19(14):3745-3754.
26. Horobin RW, Rashid-Doubell F. Predicting small molecule fluorescent probe localization in living cells using QSAR modeling. 2. Specifying probe, protocol and cell factors; selecting QSAR models; predicting entry and localization. *Biotechnic & histochemistry : official publication of the Biological Stain Commission*. 2013;88(8):461-476.
27. Horobin RW, Rashid-Doubell F, Pediani JD, Milligan G. Predicting small molecule fluorescent probe localization in living cells using QSAR modeling. 1. Overview and models for probes of structure, properties and function in single cells. *Biotechnic & histochemistry : official publication of the Biological Stain Commission*. 2013;88(8):440-460.
28. Mezzanotte L, An N, Mol IM, Lowik CW, Kaijzel EL. A new multicolor bioluminescence imaging platform to investigate NF-kappaB activity and apoptosis in human breast cancer cells. *PLoS one*. 2014;9(1):e85550.
29. Xie BW, Park D, Van Beek ER, et al. Optical imaging of cell death in traumatic brain injury using a heat shock protein-90 alkylator. *Cell death & disease*. 2013;4:e473.
30. van Horsen P, Siebes M, Hofer I, Spaan JA, van den Wijngaard JP. Improved detection of fluorescently labeled microspheres and vessel architecture with an imaging cryomicrotome. *Medical & biological engineering & computing*. 2010;48(8):735-744.
31. Razansky D, Buehler A, Ntziachristos V. Volumetric real-time multispectral optoacoustic tomography of biomarkers. *Nature protocols*. 2011;6(8):1121-1129.

32. Herzog E, Taruttis A, Beziere N, Lutich AA, Razansky D, Ntziachristos V. Optical imaging of cancer heterogeneity with multispectral optoacoustic tomography. *Radiology*. 2012;263(2):461-468.
33. Razansky D, Distel M, Vinegoni C, et al. Multispectral opto-acoustic tomography of deep-seated fluorescent proteins in vivo. *Nat Photonics*. 2009;3(7):412-417.
34. Kepp O, Galluzzi L, Lipinski M, Yuan J, Kroemer G. Cell death assays for drug discovery. *Nature reviews Drug discovery*. 2011;10(3):221-237.
35. de Boer E, Warram JM, Tucker MD, et al. In Vivo Fluorescence Immunohistochemistry: Localization of Fluorescently Labeled Cetuximab in Squamous Cell Carcinomas. *Scientific reports*. 2015;5:10169.
36. Marshall MV, Draney D, Sevick-Muraca EM, Olive DM. Single-dose intravenous toxicity study of IRDye 800CW in Sprague-Dawley rats. *Molecular imaging and biology : MIB : the official publication of the Academy of Molecular Imaging*. 2010;12(6):583-594.
37. Kroemer G, Galluzzi L, Brenner C. Mitochondrial membrane permeabilization in cell death. *Physiological reviews*. 2007;87(1):99-163.
38. Proskuryakov SY, Konoplyannikov AG, Gabai VL. Necrosis: a specific form of programmed cell death? *Experimental cell research*. 2003;283(1):1-16.
39. Majno G, Joris I. Apoptosis, oncosis, and necrosis. An overview of cell death. *The American journal of pathology*. 1995;146(1):3-15.
40. Haq SK, Rasheedi S, Khan RH. Characterization of a partially folded intermediate of stem bromelain at low pH. *European journal of biochemistry / FEBS*. 2002;269(1):47-52.
41. Steinhardt JR, J.A. Multiple equilibria in proteins. *Academic Press*. 1969:385.
42. Steinhardt J, Polet H, Moezie F. Acid denaturation of horse carboxylhemoglobin in the absence of oxygen. *The Journal of biological chemistry*. 1966;241(17):3988-3996.
43. Becker A, Riefke B, Ebert B, et al. Macromolecular contrast agents for optical imaging of tumors: comparison of indotricarbocyanine-labeled human serum albumin and transferrin. *Photochemistry and photobiology*. 2000;72(2):234-241.
44. Berezin MY, Guo K, Akers W, et al. Rational approach to select small peptide molecular probes labeled with fluorescent cyanine dyes for in vivo optical imaging. *Biochemistry*. 2011;50(13):2691-2700.
45. Miskovsky P. Hypericin--a new antiviral and antitumor photosensitizer: mechanism of action and interaction with biological macromolecules. *Current drug targets*. 2002;3(1):55-84.
46. Maeda H. Vascular permeability in cancer and infection as related to macromolecular drug delivery, with emphasis on the EPR effect for tumor-selective drug targeting. *Proceedings of the Japan Academy Series B, Physical and biological sciences*. 2012;88(3):53-71.
47. Keereweer S, Kerrebijn JD, Mol IM, et al. Optical imaging of oral squamous cell carcinoma and cervical lymph node metastasis. *Head & neck*. 2012;34(7):1002-1008.
48. Kovar JL, Volcheck W, Sevick-Muraca E, Simpson MA, Olive DM. Characterization and performance of a near-infrared 2-deoxyglucose optical imaging agent for mouse cancer models. *Analytical biochemistry*. 2009;384(2):254-262.
49. Terwisscha van Scheltinga AG, van Dam GM, Nagengast WB, et al. Intraoperative near-infrared fluorescence tumor imaging with vascular endothelial growth factor and human epidermal growth factor receptor 2

- targeting antibodies. *Journal of nuclear medicine : official publication, Society of Nuclear Medicine*. 2011;52(11):1778-1785.
50. Day KE, Beck LN, Deep NL, Kovar J, Zinn KR, Rosenthal EL. Fluorescently labeled therapeutic antibodies for detection of microscopic melanoma. *The Laryngoscope*. 2013;123(11):2681-2689.
 51. Huang R, Vider J, Kovar JL, et al. Integrin alphavbeta3-targeted IRDye 800CW near-infrared imaging of glioblastoma. *Clinical cancer research : an official journal of the American Association for Cancer Research*. 2012;18(20):5731-5740.
 52. Taruttis A, van Dam GM, Ntziachristos V. Mesoscopic and Macroscopic Optoacoustic Imaging of Cancer. *Cancer research*. 2015;75(8):1548-1559.
 53. Taruttis A, Ntziachristos V. Advances in real-time multispectral optoacoustic imaging and its applications. *Nat Photonics*. 2015;9(4):219-227.
 54. Dean-Ben XL, Fehm TF, Gostic M, Razansky D. Volumetric hand-held optoacoustic angiography as a tool for real-time screening of dense breast. *Journal of biophotonics*. 2015.
 55. Dean-Ben X, Fehm TF, Razansky D. Universal hand-held three-dimensional optoacoustic imaging probe for deep tissue human angiography and functional preclinical studies in real time. *Journal of visualized experiments : JoVE*. 2014(93):e51864.
 56. Van de Putte M, Wang H, Chen F, De Witte PA, Ni Y. Hypericin as a marker for determination of tissue viability after radiofrequency ablation in a murine liver tumor model. *Oncology reports*. 2008;19(4):927-932.
 57. Van de Putte M, Ni Y, De Witte PA. Exploration of the mechanism underlying the tumor necrosis avidity of hypericin. *Oncology reports*. 2008;19(4):921-926.
 58. Van Walleghen DM, Parseghian MH. Toxicity and biodistribution of an iodine-131-radiolabelled tumour necrosis-targeting antibody in non-tumour-bearing domestic felines. *Veterinary and comparative oncology*. 2006;4(1):9-20.
 59. Hdeib A, Sloan A. Targeted radioimmunotherapy: the role of (1)(3)(1)-chTNT-1/B mAb (Cotara) for treatment of high-grade gliomas. *Future oncology*. 2012;8(6):659-669.
 60. Cona MM, de Witte P, Verbruggen A, Ni Y. An overview of translational (radio)pharmaceutical research related to certain oncological and non-oncological applications. *World journal of methodology*. 2013;3(4):45-64.
 61. Vahrmeijer AL, Hutteman M, van der Vorst JR, van de Velde CJ, Frangioni JV. Image-guided cancer surgery using near-infrared fluorescence. *Nat Rev Clin Oncol*. 2013;10(9):507-518.



Chapter 6

Pre-clinical evaluation of a cyanine based SPECT probe for multimodal tumor necrosis imaging

Marieke A. Stammes, Vicky T. Knol-Blankevoort, Luis J. Cruz, Hans R.I.J. Feitsma, Laura Mezzanotte, Robert A. Cordfunke, Riccardo Sinisi, Elena A. Dubikovskaya, Azusa Maeda, Ralph S. DaCosta, Katja Bierau, Alan B. Chan, Eric L. Kaijzel, Thomas J.A. Snoeks, Ermond R. van Beek, Clemens W.G.M. Löwik.

Adapted from: Pre-clinical evaluation of a cyanine based SPECT probe for multimodal tumor necrosis imaging, *Mol Imaging Biol.* 2016 Dec; 18(6): 905-915

Abstract

Purpose

Recently we showed that a number of carboxylated near infra-red fluorescent (NIRF) cyanine dyes possess strong necrosis avid properties *in vitro* as well as in different mouse models of spontaneous and treatment induced tumor necrosis, indicating their potential use for cancer diagnostic- and prognostic purposes. In the previous study, the detection of the cyanines was achieved by whole body optical imaging, a technique that, due to the limited penetration of near-infra red light, is not suitable for investigations deeper than one centimeter within the human body. Therefore, in order to facilitate clinical translation, the purpose of the present study was to generate a necrosis avid cyanine based probe that could be used for Single Photon Emission Computed Tomography. For this, the necrosis avid NIRF cyanine HQ4 was radiolabeled with ¹¹¹Indium, via the chelate diethylene triamine pentaacetic acid (DTPA).

Procedures

The necrosis avid properties of the radiotracer [¹¹¹In]DTPA-HQ4 were examined *in vitro* and *in vivo* in different breast tumor models in mice using SPECT and optical imaging. Moreover, biodistribution studies were performed to examine the pharmacokinetics of the probe *in vivo*.

Results

Using optical imaging and radioactivity measurements, *in vitro*, we showed selective accumulation of [¹¹¹In]DTPA-HQ4 in dead cells. Using SPECT and in biodistribution studies, the necrosis avidity of the radiotracer was confirmed in a 4T1 mouse breast cancer model of spontaneous tumor necrosis and in a MCF-7 human breast cancer model of chemotherapy-induced tumor necrosis.

Conclusions

The radiotracer [¹¹¹In]DTPA-HQ4 possessed strong and selective necrosis avidity *in vitro* and in various mouse models of tumor necrosis, indicating its potential to be clinically applied for diagnostic purposes and to monitor anti-cancer treatment efficacy.

Introduction

Necrosis is a form of cell death characterized by severe cell swelling, denaturation and coagulation of cytoplasmic proteins and disruption of the cell membrane, causing the release of its intracellular content. Necrotic cell death is irreversible and is induced by external factors or disease, such as radiation, trauma and loss of blood supply, and is also involved in cancer development and treatment^{1,2}. In the center of most solid tumors, an area of ischemia and subsequent necrosis develops, as vascularization cannot keep up with the rapidly growing tumor mass. The size and growth rate of this necrotic area is positively correlated with the aggressiveness of cancer and can, therefore, be used as a diagnostic biomarker of cancer staging³⁻⁸. Moreover, anti-cancer treatments like chemotherapy are utilized to induce cell death, increasing the total amount of tumor necrosis⁹⁻¹¹. Thus, agents that specifically bind to necrotic tumor tissue can contribute to a more accurate disease diagnosis and can be exploited to predict early treatment outcome of anti-cancer treatments¹². To this end, back in 1988, Epstein and colleagues¹³ developed so called Tumor Necrosis Targeting (TNT) antibodies, that are directed towards nuclear proteins, and labeled with radioactive Iodine for imaging and anti-cancer treatment purposes. Likewise, the photosensitizing agent Hypericin has also been shown to possess necrosis avidity and is currently under investigation for cancer imaging and treatment purposes¹⁴⁻¹⁷. However, there are several drawbacks for the existing agents. Antibodies are relatively large in size, have long circulation time, could induce immune response and expensive to develop in Good Manufacturing Practices (GMP) quality, and the photosensitizer Hypericin is phototoxic, poorly soluble and tend to aggregate rapidly^{16,18,19}. All these issues hamper the clinical translation of these compounds^{14,20-22}.

Recently, we reported on two near infrared fluorescent (NIRF) carboxylated cyanine dyes, HQ5 and IRDye 800CW (800CW) that also possess strong necrosis avid properties²³. Cyanines are, amongst other dyes, widely used as fluorescent tags for protein labeling to enable whole body optical imaging in small animals²⁴⁻²⁸. Although the mechanism of necrosis avidity is not fully understood, it is independent on the Enhanced Permeability and Retention (EPR) effect^{23,29}. On a cellular level, increased retention of the dye may involve augmented accessibility to cells that have lost membrane integrity along with an increased affinity to denatured cytoplasmic proteins³⁰⁻³². Using whole body optical imaging in mice, we showed that these cyanines can

be employed to image areas of spontaneous necrosis in solid tumors and to determine the efficacy of chemotherapy by monitoring therapy-induced tumor necrosis²³.

Optical imaging is successfully applied in whole body imaging for small animals and in imaging of superficial tissues in humans. Optical imaging is based on the detection of light emitted from agents and/or tags coupled to biomolecules in living systems. In order to obtain better tissue penetration, optical imaging often makes use of agents and tags that emit light in the near infrared range. However, even with these compounds, the maximal penetration depth is limited to a few cm^{33,34}. Although, this relatively small measuring range is sufficient for the detection of light in small animals, it is not sufficient for the detection of light in deep tissues such as tumors situated deep within the human body. Alternatively, nuclear imaging modalities such as Single Photon Emission Computed Tomography (SPECT) and Positron Emission Tomography (PET) are used clinically to image deep tissues. To enable SPECT and/or PET imaging for clinical translation, our previously described necrosis avid NIRF cyanines must be radiolabeled. Generally, this is achieved by conjugating a targeting moiety to a chelate that is subsequently labeled with a metal radionuclide³⁵⁻³⁸. In the present study we employed this principle to the necrosis avid cyanine HQ4, a close structural analogue of the recently studied necrosis avid cyanine HQ5²³. As HQ5 has two moieties which can be functionalized by the chelate diethylene triamine pentaacetic acid (DTPA) we used HQ4, a mono-derived analogue, to avoid scrambling of the DTPA molecules or steric hindrance³⁹. HQ4 was conjugated to the chelate (DTPA) and subsequently labeling with ¹¹¹Indium-chloride (¹¹¹In-Cl₃) was performed. In this study we investigated the necrosis avidity of [¹¹¹In]DTPA-HQ4 *in vitro* and in mouse tumor models of spontaneous and chemotherapy induced tumor necrosis using optical imaging and SPECT.

Material and methods

Compounds

The cyanine dyes; HQ4 carboxylate and HQ4-NHS ester were obtained from Ilumicare BV (Rotterdam, The Netherlands).

Synthesis of HQ4-DTPA

Synthesis of diethylene triamine pentaacetic acid (DTPA)- Polyethylene Glycol (PEG) –NH₂, DTPA containing PEG amine link (4,7,10-trioxa-1,13-tridecanediamine, indicated as PEG-NH₂ in the formula (DTPA-PEG-NH₂) was synthesised on Chloride-Trityl Chloride (Cl-TrtCl) resin. Thus, Fluorenylmethoxycarbonyl (Fmoc)-PEG amine was incorporated on Cl-TrtCl resin (CTC resin) by reacting 3eq. Fmoc-PEG amine in presence of 6eq. N,N-Diisopropylethylamine (DIEA) in Dichloromethane (DCM) overnight at room temperature (RT). Final loading was measured by Fmoc quantification and the value obtained was around 0.8 mmol/g. Fmoc group removal was carried out with piperidine— Dimethylformamide (DMF) (1:5)(1 x 1min, 2 x 10min). Next, the DTPA-(*tert*-tBu ester)-COOH (2eq.) was coupled using N,N'-dipropan-2-ylmethanediiimine (DIPCDI) (2eq.) and Hydroxybenzotriazole (HOBt) (2eq.) in DMF overnight. After coupling overnight the ninhydrin test was negative. Later on, DTPA-(*tert*-tBu ester)-CO-NH-PEG-CTC-resin cleavage and deprotection was performed in two steps. DTPA-(*tert*-tBu ester)-CO-NH-PEG-CTC-resin was treated with 1% Trifluoroacetic acid (TFA) in DCM 10 times for 1min each time. Excess DCM was removed using vacuum and side chain protecting groups were removed using 95% TFA, 2.5% Triisopropylsilane (TIS) and 2.5% water. DTPA-CO-NH-PEG-NH₂ was precipitated with cold Methyl-*tert*-butylether (MTBE) after TFA removal under a N₂ stream. The DTPA-CO-NH-PEG-NH₂ was dissolved in water and lyophilized to obtain the final product. The desired DTPA-CO-NH-PEG-NH₂ was 85.0% in yield with a purity of 90.6% as analyzed by High-performance liquid chromatography (HPLC) (retention time 2.28min). HPLC- mass spectrometry (MS), m/z calc.: 523.25 for C₂₀H₃₇N₅O₁₁, Found: 524.5.28 [M+1]⁺ and matrix assisted laser desorption/ionisation time-of-flight (MALDI-TOF) analysis found 524.2 [M+1]⁺ 546.3 [M+Na].

Synthesis of DTPA-CO-NH-PEG-NH₂-HQ4: HQ4-NHS (8.3x10⁻⁴mmol, 1 mg) dissolved in 50μL of Dimethyl sulfoxide (DMSO) was added to DTPA-CO-NH-PEG-NH₂ (2.8 x 10⁻³mmol, 2mg) dissolved in 200 μL of DMSO containing 5μL DIEA and stirred overnight at room temperature. Later on, the complex DTPA-CO-NH-PEG-HQ4 was purified by reversed phase (RP)-HPLC. The desired DTPA-

PEG-HQ4 was 50.5% in yield with a purity of 98% as analyzed by HPLC (tR 5.34). HPLC-MS, m/z calc.: 1331.59 for C₆₆H₉₀N₈O₁₇S₂, Found: 1332.0[M+1]⁺ and MALDI-TOF Found 1331.9 [M+1]⁺ 1353.9 [M+Na].

Cells and culture conditions

4T1-luc2 mouse mammary cancer cells (PerkinElmer, Waltham, MA, USA) and, MCF-7 human mammary cancer cells were all cultured in RPMI-1640 medium (Life Technologies Inc., Carlsbad, CA, USA) supplemented with 10% fetal calf serum (FCS; Lonza, Basel Switzerland), 100 units/ml penicillin and 50 µg/ml Streptomycin (Life Technologies Inc.). All cell lines were cultured in a humidified incubator at 37°C and 5% CO₂, monthly checked for Mycoplasma infection by polymerase chain reaction (PCR) and checked routinely for morphologic changes.

Dry ice dead cell assay

In vitro, cell death was studied using a cryo-induced cell death assay as previously described⁴⁰. In short, 4T1-luc2 cells were seeded onto 24-well tissue culture plates (Sigma-Aldrich) and grown until confluent. After discarding the medium, a bar of dry ice 3-5mm in diameter was applied to the underside of the culture well for 20sec. Subsequently, the cells were incubated in the dark for 15min. at RT with HQ4 at a concentration of 100 nM. After incubation, the samples were gently washed with phosphate buffered saline (PBS) and subsequently scanned for fluorescence using the Odyssey Infrared Imager 9120 (LI-COR) and for radioactivity via phosphor imaging on the Typhoon 9410 imager (GE Healthcare).

***In vitro* viability assay**

4T1-luc2 cells were plated in a 96-well plate (Costar) in 100 µl medium at a density of 10.000 cells per well and left over night to adhere. The next day the medium was replaced with medium containing the experimental compounds: HQ4, HQ4-DTPA, HQ5 and Gambogic acid (GA), 3 wells per condition. After 24h, cell viability was measured using a nonradioactive colorimetric MTS viability assay (Promega Benelux) according to the manufacturer's protocol. Optical absorption was measured at 490 nm with a Versamax absorbance microplate reader (Molecular Devices).

Animals

Female athymic mice (BALB/c nu/nu, 6 weeks old) were purchased from Charles River Laboratories (L'Arbresle Cedex, France). Animals were housed at 22°C and 50% humidity with free access to food and water and maintained under standard 12 h light/12 h dark cycles. All surgical and analytical procedures were performed under isoflurane gas anesthesia (3% induction, 1.5-2% maintenance) in 70% pressurized air and 30% O₂. Animals were sacrificed by cervical dislocation at the end of the experimental period. The animals were housed per 4-5 animals in individually ventilated cages with ad libitum access to food and water.

All animal experiments were assessed for animal health, ethics, and research and approved by the Animal Welfare Committee of Leiden University Medical Center, the Netherlands. All mice received humane care and were kept in compliance with the Code of Practice Use of Laboratory Animals in Cancer Research (Inspectie W&V, July 1999).

Subcutaneous Tumor Model

Approximately 1×10^5 4T1-luc2 cells, suspended in 15 μ l PBS, were implanted bilateral and subcutaneously onto the upper back of nude mice. Tumors were grown until they reached a size of 6-7 mm in diameter which developed roughly after 1.5-2 weeks of tumor implantation.

Similarly, 2×10^6 MCF-7 cells, suspended in 15 μ l PBS in a 1:1 mixture with 15 μ l of Matrigel (BD biosciences, San Jose, CA, USA) were injected bilateral and subcutaneously onto the upper back. Tumors were grown until they reached 6-7 mm diameter, which developed after approximately 2-3 weeks.

Whole body FLI measurements were performed using the Pearl Impulse *in vivo* fluorescence imager (LI-COR) and/or IVIS Spectrum *in vivo* imaging system (PerkinElmer) several time points after injection. On the IVIS, an excitation and emission wavelength of 675nm and 720 nm was used for HQ4.

Radiolabeling of HQ4-DTPA and SPECT

To label HQ4-DTPA with $^{111}\text{In-Cl}_3$, it was dissolved in 0.1M Hepes (10 μ g/100 μ l) and $^{111}\text{In-Cl}_3$ (35MBq; Covidien-Mallinckrodt, Dublin, Ireland) was added. After 30min. of incubation on the shaker, labeling was validated with high-pressure liquid chromatography (HPLC) (Jasco Inc., Easton, MD, USA) or thin layer chromatography (TLC). In all cases, labeling efficacy was >90%.

To study the specificity of the radiolabeled HQ4-DTPA versus radiolabeled DTPA *in vivo*, 10 μ g [^{111}In]DTPA-HQ4 (=10 nmole per mouse) or 10 μ g

[¹¹¹In]DTPA was injected i.v. into mice bearing 4T1-luc2 tumors (n=3 and 4, respectively). The total injected dose (ID) in each mouse was determined in a dose-calibrator (VDC101, Veenstra Instruments, Joure, the Netherlands).

SPECT scans were conducted at several time points post injection on a 3-headed U-SPECT-II gamma camera (MILabs, Utrecht, The Netherlands) under isoflurane anesthesia for 40 minutes. Radioactivity counts from total body scans were acquired using a 0.6mm mouse pinhole collimator with energy settings at 171 and 245keV with a window of 20% and background energy settings of respectively 4.5% and 3.5% around the tails of the energy window⁴². Subsequently, the image was reconstructed using 20 POSEM iterations with 4 subsets, 3D gauss 1 mm (FWHM) filtering, a 0.2mm voxel size, and with decay and scatter corrections integrated into the reconstruction⁴³. Images were generated and analyzed using PMOD software. *In vivo* SPECT scanning was followed by *in vivo* fluorescence imaging on the Pearl Impulse Small Animal Imaging System (LI-COR).

After the last imaging time point mice were sacrificed and several tissues were excised, weighed, and counted for radioactivity (Wizard2 2470 automatic gamma scintillation counter, Perkin Elmer, USA) to determine the percentage of the injected dose per gram (%ID/g). The %ID/g was calculated as follows: ((MBq measured in tissue/injected dose) *100%) /weight of tissue).

Chemotherapy of MCF-7 tumors

In two groups of mice (n=5), two weeks after tumor implantation the mice received either an i.p. injection of cyclophosphamide (265 mg/kg; Baxter BV, Utrecht, The Netherlands)⁴⁴ or remained untreated. After 72hr, all animals received an i.v. injection of radiolabeled HQ4-DTPA. SPECT scans were conducted 24hr later, followed by whole body FLI. After the last imaging time point mice were sacrificed, several tissues were excised, weighted, and counted for radioactivity.

***Ex vivo* tumor imaging**

Ex vivo tumor imaging was performed to visualize the distribution of the probe in the tumor. Images were obtained for FLI (Odyssey Infrared Imager 9120 (LI-COR)) and for radioactivity via phosphor imaging (Typhoon 9410 imager (GE Healthcare) and ImageQuant TL software). For phosphor imaging the tumors were manually sliced in sagittal sections and placed o/n on a phosphorscreen.

Histological procedures

The tumors collected for histological analysis were fixed in 4% formaldehyde and embedded in paraffin. 5µm sections were prepared and FLI was performed using the Odyssey Infrared Imager (LI-COR). Afterwards, the sections were subjected to TdT-mediated dUTP Nick-End Labeling (TUNEL) staining (Promega, Madison, WI, USA) to validate accumulation of the NIRF probes in necrotic cells.

Statistical Analysis

All statistical analyses was performed using Prism software (GraphPad). For repeated measures a student's t-test was used in all cases. $P < 0.05$ was considered significant, and all error bars represent mean \pm SEM.

Results

We selected the necrosis avid cyanine HQ4, instead of HQ5, to perform radiolabeling and further *in vitro* and *in vivo* investigations to demonstrate its potential clinical translation. The choice for HQ4 was based on the number of functionalized moieties present in the cyanine molecules, which is one in the case of HQ4 and two in the case of HQ5 (see **Fig. 1A**). Furthermore, as shown in **Figure 1B**, HQ4 showed slightly higher necrosis avid properties in our dry ice dead cell assay than HQ5. The fluorescent signal intensity, obtained from the area of cell death caused by freezing, was over the whole dose range (1 -100 nM) 2.8 (+/- 1.0) -fold higher for HQ4 as compared to HQ5. A HQ4-DTPA hybrid complex was synthesized by covalent coupling via conjugation with a polyethylene glycol (PEG) linker (**Fig. 2**).

Reversed-phase chromatography showed a clear peak indicating the high grade of purity (98%) of this conjugate. Mass spectrometric analysis of HQ4-DTPA further showed the expected molecular weight (calc.: 1331.59 for $C_{66}H_{90}N_8O_{17}S_2$ and MALDI-TOF found 1332.4 [M+1]⁺ 1354.6 [M+Na]), indicating the high grade of purity of this conjugate (see **Fig. 3**). Lastly, the HQ4-DTPA conjugate was labeled with $^{111}\text{In-Cl}_3$ with a labeling efficiency of >90% (data not shown).

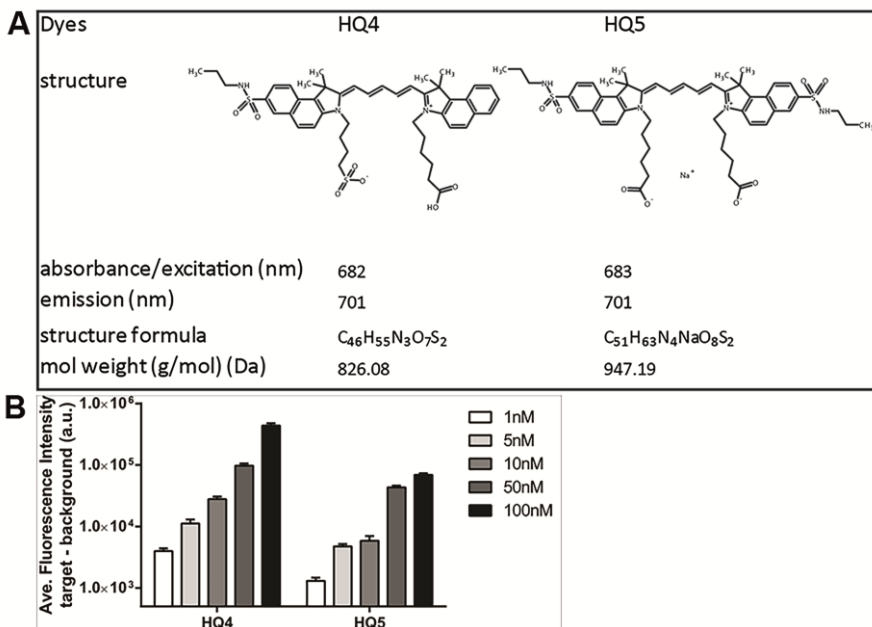


Figure 1. Structural characteristics and *in vitro* necrosis avid properties of HQ4 vs HQ5.

(A) Chemical and structural characteristics of the carboxylated cyanine dyes HQ4 and HQ5.

(B) *In vitro* necrosis targeting properties of HQ4 and HQ5 utilizing the dry ice assay. Fluorescent signal intensity was obtained from the area of dead cells in the center of a culture well after incubation with different concentrations of HQ4 or HQ5 (1-100 nM) and is subtracted by the background signal from the area of the living cells.

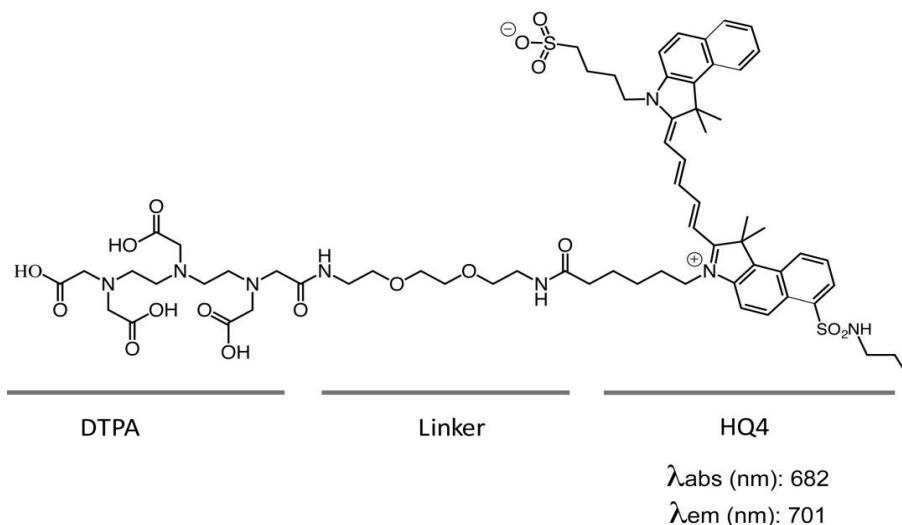


Figure 2. Chemical and structural characteristics of HQ4-DTPA.

Chemical structure of HQ4-DTPA. λ_{obs} =absorbance wavelength; λ_{em} =emission wavelength.

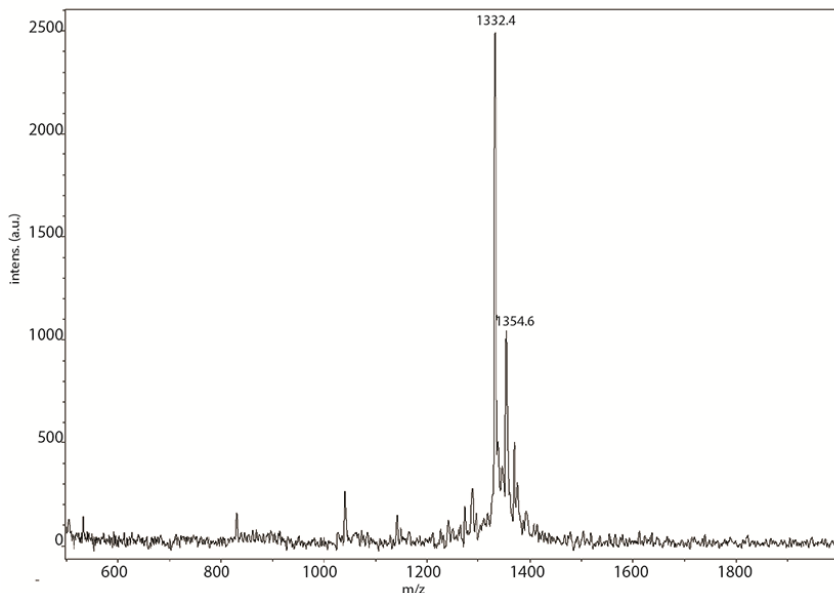


Figure 3. Reversed-phase mass spectrometry of HQ4-DTPA.

Reversed-phase chromatography showed a clear peak indicating the high grade of purity (98%) of this conjugate. Mass spectrometric analysis of HQ4-DTPA further showed the expected molecular weight (calc.: 1331.59 for $C_{66}H_{90}N_8O_{17}S_2$ and MALDI-TOF found 1332.4 $[M+1]^+$ 1354.6 $[M+Na]^+$), indicating the high grade of purity of this conjugate.

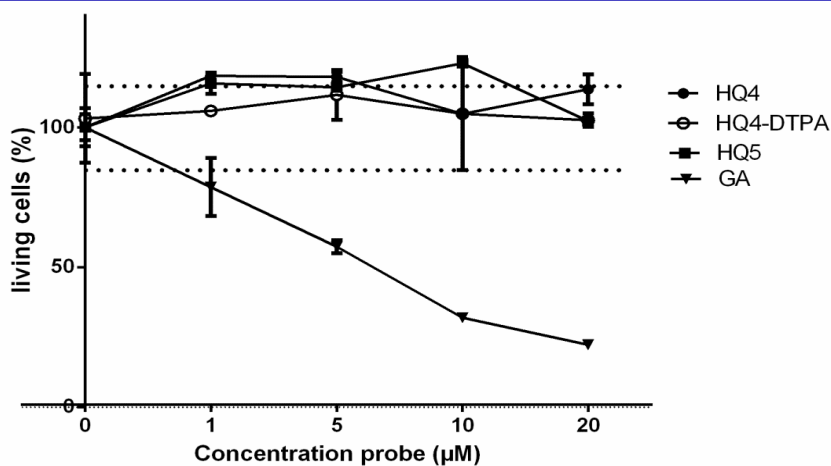


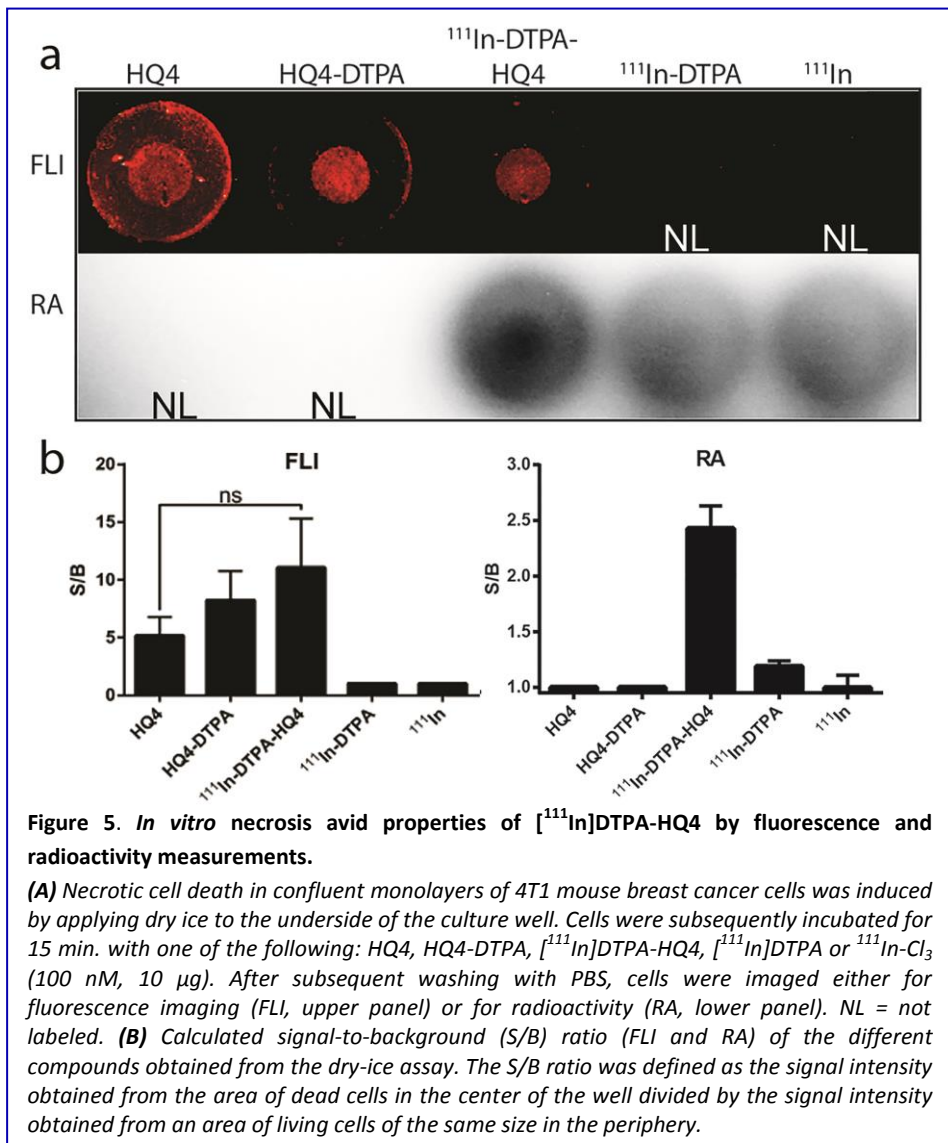
Figure 4. MTS cell viability assay of various agents.

Confluent cultures of 4T1 cells were incubated for 24hr with various concentrations HQ4, HQ4-DTPA, HQ5 or the natural anti-cancer compound Gambogic Acid (GA). Relative cell viability (%) was expressed as a percentage relative to the untreated control. HQ4, HQ4-DTPA and HQ5 did not affect cell viability, whereas, GA induced cell death with an IC50 of around 6µM.

HQ4, HQ4-DTPA and HQ5 were examined in 24h cultures of 4T1 breast cancer cell and compared with the cytotoxic compound Gambogic acid (GA). In the dose range of 0 - 20 μM , none of the cyanine compounds affected cell viability. GA, however, dose dependently induced cell death with an IC50 of around 6 μM (see Fig. 4).

In vitro necrosis targeting properties of [^{111}In]DTPA-HQ4

The dry ice dead cell assay was performed to examine the necrosis avid properties of the entire conjugate [^{111}In]DTPA-HQ4 and the individual



components, HQ4 and HQ4-DTPA, respectively, *in vitro*. HQ4, HQ4-DTPA and [^{111}In]DTPA-HQ4 all strongly accumulated in the area of dead cells, as shown by fluorescence imaging (**Fig. 5A**). In addition, radioactive signal was obtained in areas of dead cells only when incubated with [^{111}In]DTPA-HQ4. In contrast, neither [^{111}In]DTPA nor free $^{111}\text{In-Cl}_3$ accumulated in the dead cells area, as indicated by RA measurements. **Figure 5B** shows quantifications of the fluorescent and radioactive signal-to-background (S/B) (dead cells vs living cells area) ratios for the five different compounds tested confirming that [^{111}In]DTPA-HQ4 retains fluorescence and radioactivity, as well as necrosis avidity with a S/B ratio of 11.1 and 2.4 respectively.

Necrosis targeting properties of [^{111}In]-DTPA-HQ4 in a 4T1 mouse tumor model of spontaneous necrosis

The necrosis targeting properties of [^{111}In]DTPA-HQ4 were evaluated in subcutaneous 4T1 breast tumor bearing mice, using SPECT and optical imaging. [^{111}In]DTPA-HQ4 (10 nmole, 30-35MBq) was injected intravenously (i.v.) into the tumor bearing mice, and *in vivo* SPECT and optical images were obtained 6, 24h, 48 and 72h, post injection (**Fig. 6A and B**). An increased retention of [^{111}In]DTPA-HQ4 in the tumors and in the metabolizing organs was observed over time with both optical imaging and SPECT.

To further assess the biodistribution of [^{111}In]DTPA-HQ4 in different organs, mice (n=3) were sacrificed at each time-point. Subsequently, radioactivity in various organs and body fluids was quantified (**Fig. 6C**). The measured radioactivity across different time points confirmed accumulation of radioactivity in the tumors (4.8 %ID/w), liver (3.3 %ID/w) and the kidneys (7.6 %ID/w) at 72hrs post injection. Finally, histological examination of the 4T1 tumors confirmed the presence of a large necrotic core, see **Figure 6D**.

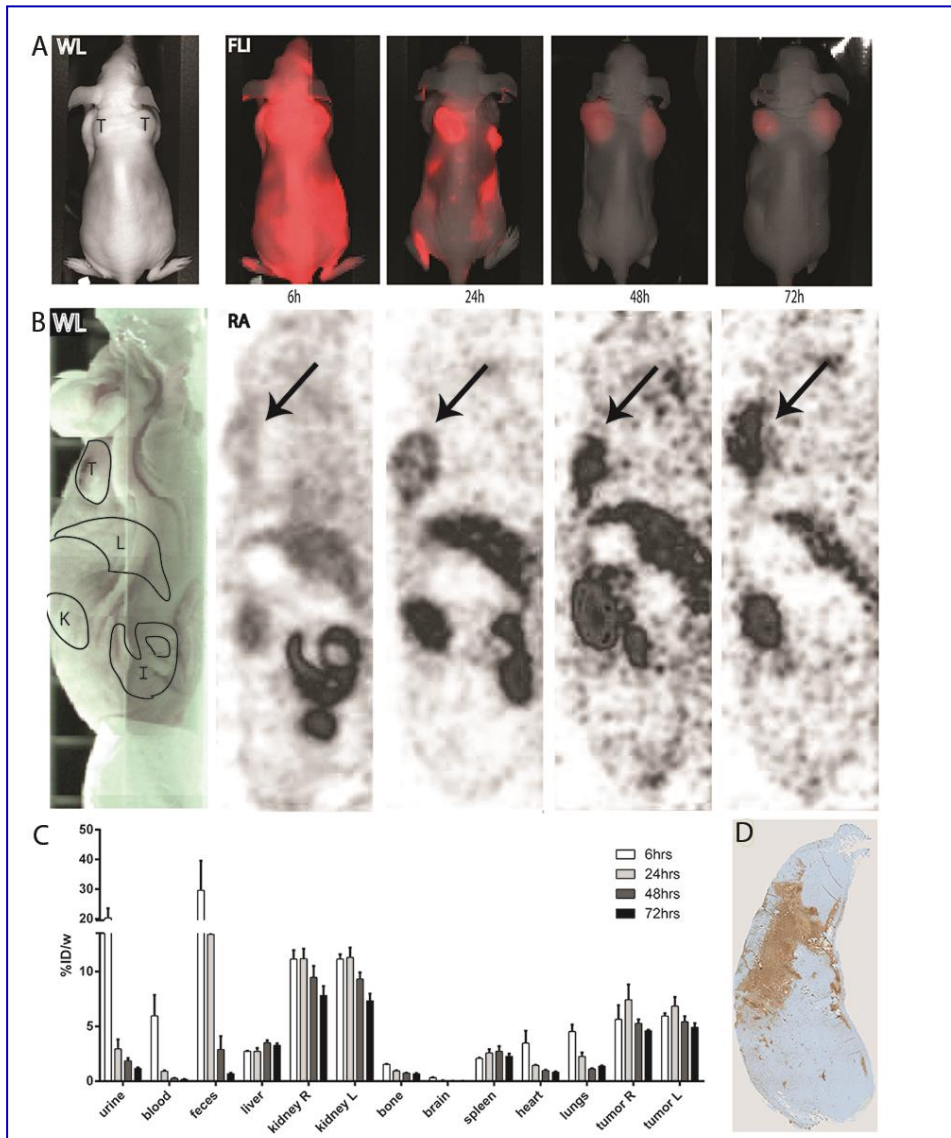


Figure 6. Optical imaging, SPECT and biodistribution of $[^{111}\text{In}]\text{DTPA-HQ4}$ in 4T1 breast tumor bearing mice.

(A) Whole body FLI (coronal view) obtained 6-72h after tail vein injection of $[^{111}\text{In}]\text{DTPA-HQ4}$ (10 nmole, 30-35 MBq). The white light image (WL) indicates the position of the mouse in the Pearl imager, from a dorsal point of view (T=tumor). The same device settings were applied to all FLI, rendering comparison between the different images possible. **(B)** Whole body SPECT images (sagittal view) obtained 6h-72h after tail vein injection of $[^{111}\text{In}]\text{DTPA-HQ4}$ (10 nmole, 30-35 MBq). The white light image (WL) indicates the position of the mouse from a sagittal point of view, in the μSPECT (RA); T=tumor, L=liver, K=kidney and I=intestine. Arrows indicate the tumor.

(C) Biodistribution of $[^{111}\text{In}]\text{DTPA-HQ4}$ in 4T1 tumor bearing mice. 6h, 24h, 48h and 72h after probe injection, mice ($n=3$ per time point) were sacrificed and the organs, body fluids and tumors were dissected, weighed and measured for radioactivity in a gamma counter. At each time point, the amount of radioactivity in the organs is expressed as percentage of the injected dose divided by body weight (%ID/w). **(D)** TUNEL stained histological section of a representative 4T1 mouse breast tumor showing a large area of necrosis (brown).

Similarly, the biodistribution of the radiolabeled chelate [^{111}In]DTPA was examined in 4T1 tumor bearing mice 24h after i.v. injection of [^{111}In]DTPA (10 μg , 30-35 MBq). Mice (n=4) were euthanized and the internal organs and body fluids were removed to quantify remaining radioactivity (see **Fig. 7A**). Greatest accumulation of radioactivity was observed in the kidneys (5.0 %ID/w) and only relatively low values of radioactivity could be measured in other organs, body fluids and tumors (tumors; 0.5 %ID/w, liver 0.6 %ID/w).

Figure 7B, shows the measured amount of radioactivity in the mouse corpus at different time points after injection of [^{111}In]DTPA-HQ4 or [^{111}In]DTPA, expressed as the percentage of the total injected doses (%ID). It was found that 24h and 48h after injection of [^{111}In]DTPA-HQ4, respectively 38% and 35% of total injected dose was retained in the body, whereas, this was only 10% and 8%, for [^{111}In]DTPA.

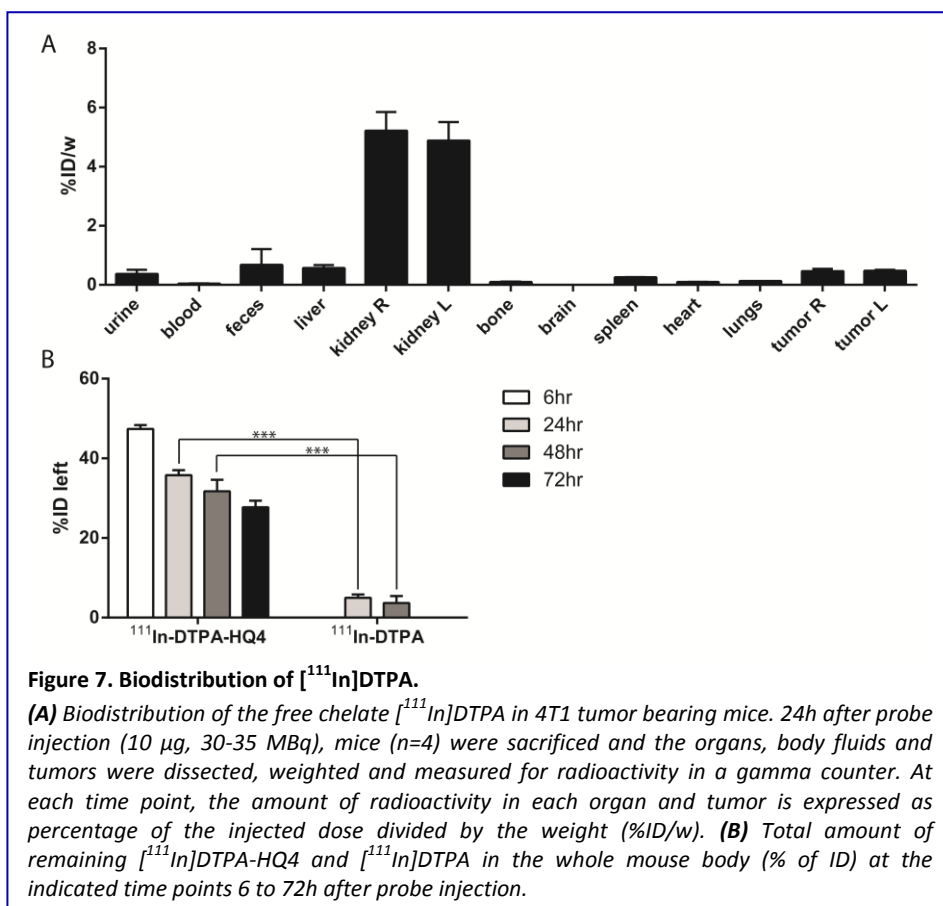
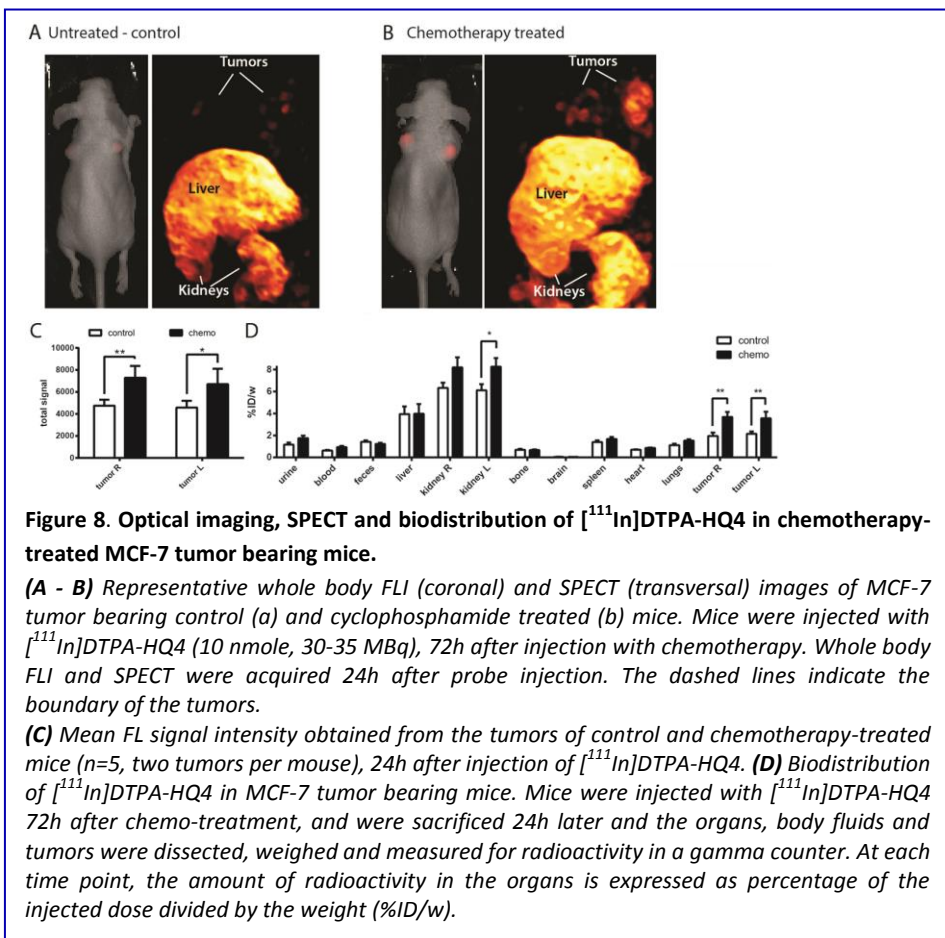


Figure 7. Biodistribution of [^{111}In]DTPA.

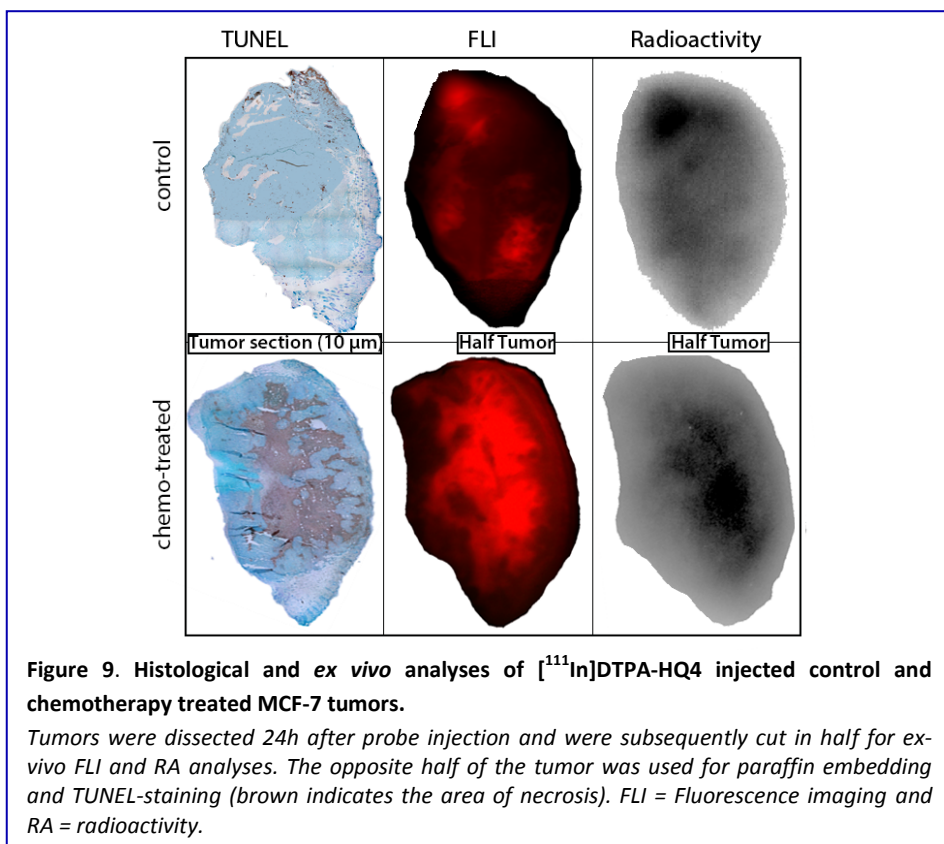
(A) Biodistribution of the free chelate [^{111}In]DTPA in 4T1 tumor bearing mice. 24h after probe injection (10 μg , 30-35 MBq), mice (n=4) were sacrificed and the organs, body fluids and tumors were dissected, weighted and measured for radioactivity in a gamma counter. At each time point, the amount of radioactivity in each organ and tumor is expressed as percentage of the injected dose divided by the weight (%ID/w). **(B)** Total amount of remaining [^{111}In]DTPA-HQ4 and [^{111}In]DTPA in the whole mouse body (% of ID) at the indicated time points 6 to 72h after probe injection.

SPECT and optical imaging of [¹¹¹In]DTPA-HQ4 in a MCF-7 mouse model of chemotherapy induced tumor necrosis

Using SPECT and optical imaging, we examined whether [¹¹¹In]DTPA-HQ4 could be employed to monitor chemotherapy induced tumor necrosis. For this, MCF-7 tumor bearing mice were treated with a single intraperitoneal (i.p.) injection of cyclophosphamide (265mg/kg)⁴⁴, followed by an i.v. injection of [¹¹¹In]DTPA-HQ4 (10 nmole, 30-35MBq) 72h later. 24h after injection of [¹¹¹In]DTPA-HQ4, whole body optical images and SPECT were obtained to assess its biodistribution. Both optical imaging and SPECT showed accumulation of [¹¹¹In]DTPA-HQ4 in cyclophosphamide treated tumors as compared to untreated tumors (**Fig. 8A and B**). **Figure 8C** shows quantification of the fluorescent signals obtained from the tumors, 24h after probe injection. A significant increase in tumor fluorescent signal intensity was observed in mice that were treated with chemotherapy as compared to untreated controls (ratio = 1.8:1.0, p= 0.0011).



Biodistribution study based on quantification of radioactivity in various organs further demonstrated higher amount of radioactivity in chemotherapy treated tumors compared to untreated controls. The average %ID/w was 1.85 for the control tumors vs 4.02 for the chemo-treated tumors (**Fig. 8D**). In addition, a significantly higher amount (1.4-fold) of radioactivity was observed in left kidneys of the chemotherapy-treated mice as compared to controls. Finally, tumors of chemotherapy-treated and control mice, which were injected with [^{111}In]DTPA-HQ4 (10 nmole, 30-35 MBq), were dissected and cut in half to perform *ex-vivo* fluorescence and radioactivity analysis. In addition, the opposite half of the tumor was processed for paraffin embedding and histological analysis. As shown in **Figure 9**, the TUNEL stained section of the untreated control tumor showed very little necrotic tissue, whereas the chemotherapy-treated tumor contained a large area of necrotic tissue (brown staining). Notably, the TUNEL staining showed co-localization with both fluorescence and radioactivity signals in tumors, confirming the specific increased necrosis retention property of [^{111}In]DTPA-HQ4. For comparison all the settings used for the different images are similar.



Discussion

Over the last two decades, several attempts have been made to exploit disease and/or therapy induced tumor necrosis as a diagnostic and/or prognostic biomarker of disease and to utilize necrotic tissue as a target for drug delivery. The existing necrosis imaging agents can be divided in two different groups; (non-) specific CT and MR contrast agents to enhance the natural signal and the other group consists out of mostly radiolabeled necrosis avid contrast agents (NACAs) that specifically target necrotic tissue. The latter can also be employed for therapeutic purposes e.g. when radiolabeled with ^{131}I iodine^{2-10,13,15,23,45-49}. It is expected that the non-specific necrosis contrast agents will fall into abeyance when compounds with high necrosis specificity become clinically available. However, thus far, only the ^{131}I iodine conjugated Tumor Necrosis Targeting Therapy monoclonal antibody (TNT-3), licensed by Peregrine Pharmaceuticals, reached the clinical trials for therapeutic use^{13,21}. This antibody, under the brand name CotaraTM, has been examined in clinical trials for treatment of Glioblastoma Multiforma. However, although encouraging results have been published on the website of the manufacturer in December 2012, no follow-up studies have been reported since⁵⁰. In addition, the necrosis avid photosensitizer Hypericin, under the brand name Oncocidia, is also under investigation to enter clinical trials^{14,51,52}. Although proof of concept has been shown for both approaches, both compounds, as mentioned earlier, suffer from major drawbacks which hampers their clinical translation.

To overcome the limitations associated with the size and possible immunogenicity of antibodies, the photo-toxicity, problems with solubility and ability to aggregate, a simple, injectable and non-toxic agent that displays specific necrosis avidity is required. Recently, we demonstrated that two non-toxic constituents of the group of NIRF cyanine dyes, IRDye800CW and HQ5 carboxylate, the former being commonly used as an optical probe for biomolecular labeling^{53,54}, display strong and specific necrosis avid properties *in vitro* as well as in tumor bearing mice²³. In this study, the increased retention of NIRF cyanine dyes in tumor necrosis was examined using whole body fluorescence imaging. Although whole body optical imaging is suitable for use in small animals, it is often insufficient for assessments of deep tissues in the human body, due to the limited tissue penetration depth of NIRF light. In order to seek for potential clinical applications for our newly discovered necrosis avid cyanines, we examined the possibility to radiolabel it for *in vivo*

nuclear imaging by conjugating to a chelator^{55,56}. To render HQ4 applicable for SPECT we first conjugated HQ4 to the chelate DTPA with a linker molecule, and subsequently radiolabeled with $^{111}\text{In-Cl}_3$. Following the synthesis and purification procedures, purity of 98% was achieved. Thus, we created a molecule that targets necrosis and can be imaged using both NIRF and SPECT.

We demonstrated *in vitro* that [^{111}In]DTPA-HQ4, like unconjugated HQ4, appears to specifically bound to dead cells after washing. Our findings, in the dry ice assay, show that the specificity of [^{111}In]DTPA-HQ4 for necrotic cells was solely due to the presence of the HQ4 molecule, as the radiolabeled chelate [^{111}In]DTPA alone and free $^{111}\text{In-Cl}_3$ did not show to bind to the dead cells. Although DTPA conjugation is likely to change the chemical and physico-chemical properties of HQ4, for example by increasing its overall hydrophilicity⁵⁷, it retained its necrosis avid- and fluorescent properties. We observed a clear difference in the signal-to-background (S/B) ratio of [^{111}In]DTPA-HQ4 between fluorescence- and radioactivity measurements. The reason for this discrepancy is unclear, but may involve environmental conditions that specifically affect the fluorescent properties of the molecule. Previously, Jiskoot et. al⁵⁸ reviewed the fluorescence properties of extrinsic dyes, which are strongly influenced by their environment (hydrophilic/hydrophobic or differences in pH) and/or by interactions with proteins. Such factors may also influence fluorescence signal intensity of HQ4 in an environment of living cells compared to in an environment of dead cells. However, such environmental dependent signal intensity influences will not occur when a radiolabel, offering a quantitative readout, is utilized. Nevertheless, the observed S/B ratio of 2.5, obtained with radioactivity measurements, is theoretically sufficient for clinical translation⁵⁹. Additional studies that determine the relationship between time, probe concentration, and S/B ratio could help to optimize the sensitivity of the measurements. Furthermore, none of the cyanine dyes, including HQ4-DTPA, showed any acute *in vitro* toxicity in cultures of 4T1 cells. Even at the highest concentration of 20uM (during 24h), which is 200-fold higher compared to the concentration used to image dead cells *in vitro*, cell viability remained unaffected. Collectively, our *in vitro* study revealed that DTPA conjugation is not deleterious to the necrosis avid properties of HQ4 and the lack of toxicity encouraging further studies with the aim of its clinical translation. Further investigations are warranted concerning the mechanism of interaction of the DTPA conjugated cyanine to specific proteins in necrotic cells. In the paper of

Xie et. al.²³ we showed that HQ5, a close cyanine analogue of HQ4, specifically accumulated in necrotic cells and not in apoptotic cells. Moreover we have shown that HQ5 does not co-localize with F4/80 macrophage staining in an around the tumor, indicative of inflammation. Nevertheless, we did not yet examine these specific mechanistic properties for HQ4..

Using *in vivo* whole body optical imaging, SPECT, and *ex vivo* analysis, we confirmed the observed *in vitro* necrosis avid properties of [¹¹¹In]DTPA-HQ4 in two tumor models: 4T1 mouse breast cancer tumor model of spontaneous necrosis and MCF-7 human breast cancer tumor model of chemotherapy induced tumor necrosis. MCF-7 tumor model was selected to assess chemotherapy-induced necrosis due to its slow growth kinetics. MCF-7 tumor cells have a population doubling time (PDT) of approximately 38h *in vitro*⁶⁰, thus representing a slow-growing tumor. This is in contrast to 4T1-cells, PDT +/- 12h⁶¹, which develop necrotic cores spontaneously, and to EL4-cells, PDT +/- 17h⁶², used in the previous paper²³. Since MCF-7 cells hardly develop spontaneous necrosis during their growth, necrosis induced by chemotherapy is more evident and can be determined with higher accuracy. Moreover, MCF-7 cells are of human origin, which may also more accurately mimic the clinical situation⁶³.

In both mouse tumor models, the acquired optical imaging and SPECT results over time, provided information on the pharmacokinetic profile of [¹¹¹In]DTPA-HQ4. In the model of spontaneous tumor necrosis, necrotic areas in the tumor were clearly delineated using optical imaging and SPECT. No clear specific tissue interactions could be detected 6h after injection, probably due to high quantities of unbound circulating probe in the blood at this early time point. The amount of radioactivity that retained in the 4T1 tumors remained approximately equal over time, while, it declined in most organs and body fluids, resulting in a relative increase in tumor signal intensity inside the tumor at later time points. In the chemotherapy-induced tumor necrosis model, the specific targeting of [¹¹¹In]DTPA-HQ4 to necrotic areas of MCF-7 tumors was confirmed histologically using TUNEL staining. In this model we also observed that the kidneys of the chemotherapy-treated mice retained more radioactivity than in untreated mice. The reason for this is unknown, but it might be speculated that some necrosis may develop due to cyclophosphamide induced renal oxidative stress which leads to peroxidative damage to the kidneys⁶⁴.

Finally, we compared the biodistribution and clearance rate of [¹¹¹In]DTPA-HQ4 with that of the free labeled chelate ([¹¹¹In]DTPA). We observed that both

the biodistribution and the excretion rate of the two compounds were vastly different. 24h after probe injection, [^{111}In]DTPA was mainly retained in the kidneys and could hardly be detected in other organs or in the tumors, confirming our *in vitro* findings of a lack of tumor necrosis specificity. The observed accumulation of [^{111}In]DTPA in the kidneys confirms findings of Boswell and colleagues⁶⁵ who also reported predominant clearance of this hydrophilic compound via this excretion route. Moreover, not only the organ distribution of these two compounds was dissimilar, the clearance rate of [^{111}In]DTPA was about 8-fold faster than that of [^{111}In]DTPA-HQ4. Combined, these findings indicate that both the pharmacokinetics and the tissue targeting properties of [^{111}In]DTPA-HQ4 and [^{111}In]DTPA are largely different and strengthen the notion that the cyanine HQ4 governs the overall necrosis avid properties of the [^{111}In]DTPA-HQ4 molecule.

In summary, we successfully yielded a new necrosis avid SPECT radiotracer by conjugating the necrosis avid cyanine HQ4 to DTPA, followed by radiolabeling with $^{111}\text{In-Cl}_3$. We showed that, after DTPA conjugation, this newly synthesized radiotracer retained its specific necrosis targeting properties *in vitro* and *in vivo* in mouse models of spontaneous and therapy induced tumor necrosis. The advantages of the small molecule [^{111}In]DTPA-HQ4 include; high water solubility, NIR property that enables deep penetration into tissues, lack of photo-toxicity, and low production costs. Therefore, the necrosis avid radiotracer [^{111}In]DTPA-HQ4 has the potential to be clinically translated for diagnostic-prognostic purposes and to predict early treatment outcome of anti-cancer treatments.

Acknowledgments

This work was supported by project grants from TI Pharma (Project D4-603), the EU Seventh Framework Program: FP7-PEOPLE-2013-IAPP (612360 – BRAINPATH), H2020-MSCA-RISE grant number 644373 – PRISAR. K.B. is supported by a FP7-PEOPLE-2013-IEF grant (625798 Image-Guided Surgery). HQTM compounds are a trade mark of Ilumicare BV, Rotterdam, The Netherlands who also financially supported part of the studies. We acknowledge the technical assistance of Henny Bloys-de Groot in preparing the immunohistochemistry sections. We would further like to acknowledge the generous gift of Π.pmod Biomedical Image Quantification to be able to use their software to reconstruct our μSPECT scans.

References

1. de Bruin EC, Medema JP. Apoptosis and non-apoptotic deaths in cancer development and treatment response. *Cancer Treat Rev.* 2008;34(8):737-749.
2. Venkatramani R, Wang L, Malvar J, et al. Tumor necrosis predicts survival following neo-adjuvant chemotherapy for hepatoblastoma. *Pediatr Blood Cancer.* 2012;59(3):493-498.
3. Hiraoka N, Ino Y, Sekine S, et al. Tumour necrosis is a postoperative prognostic marker for pancreatic cancer patients with a high interobserver reproducibility in histological evaluation. *British journal of cancer.* 2010;103(7):1057-1065.
4. Kato T, Kameoka S, Kimura T, Tanaka S, Nishikawa T, Kobayashi M. p53, mitosis, apoptosis and necrosis as prognostic indicators of long-term survival in breast cancer. *Anticancer Res.* 2002;22(2B):1105-1112.
5. Maiorano E, Regan MM, Viale G, et al. Prognostic and predictive impact of central necrosis and fibrosis in early breast cancer: results from two International Breast Cancer Study Group randomized trials of chemoendocrine adjuvant therapy. *Breast cancer research and treatment.* 2010;121(1):211-218.
6. Park SY, Lee HS, Jang HJ, Lee GK, Chung KY, Zo JI. Tumor necrosis as a prognostic factor for stage IA non-small cell lung cancer. *The Annals of thoracic surgery.* 2011;91(6):1668-1673.
7. Pichler M, Hutterer GC, Chromecki TF, et al. Histologic tumor necrosis is an independent prognostic indicator for clear cell and papillary renal cell carcinoma. *American journal of clinical pathology.* 2012;137(2):283-289.
8. Pollheimer MJ, Kornprat P, Lindtner RA, et al. Tumor necrosis is a new promising prognostic factor in colorectal cancer. *Human pathology.* 2010;41(12):1749-1757.
9. Richards CH, Roxburgh CS, Anderson JH, et al. Prognostic value of tumour necrosis and host inflammatory responses in colorectal cancer. *The British journal of surgery.* 2012;99(2):287-294.
10. Uhl M, Saueressig U, Koehler G, et al. Evaluation of tumour necrosis during chemotherapy with diffusion-weighted MR imaging: preliminary results in osteosarcomas. *Pediatric radiology.* 2006;36(12):1306-1311.
11. Silva MT. Secondary necrosis: the natural outcome of the complete apoptotic program. *FEBS Lett.* 2010;584(22):4491-4499.
12. Kepp O, Galluzzi L, Lipinski M, Yuan J, Kroemer G. Cell death assays for drug discovery. *Nature reviews Drug discovery.* 2011;10(3):221-237.
13. Epstein AL, Chen FM, Taylor CR. A novel method for the detection of necrotic lesions in human cancers. *Cancer research.* 1988;48(20):5842-5848.
14. Cona MM, de Witte P, Verbruggen A, Ni Y. An overview of translational (radio)pharmaceutical research related to certain oncological and non-oncological applications. *World journal of methodology.* 2013;3(4):45-64.
15. Jiang B, Wang J, Ni Y, Chen F. Necrosis avidity: a newly discovered feature of hypericin and its preclinical applications in necrosis imaging. *Theranostics.* 2013;3(9):667-676.
16. Hritz J, Kascakova S, Ulicny J, Miskovsky P. Influence of structure of human, rat, and bovine serum albumins on binding properties of photoactive drug hypericin. *Biopolymers.* 2002;67(4-5):251-254.

17. Miskovsky P. Hypericin--a new antiviral and antitumor photosensitizer: mechanism of action and interaction with biological macromolecules. *Current drug targets*. 2002;3(1):55-84.
18. Solar P, Cavarga I, Hofmanova J, et al. Effect of acetazolamide on hypericin photocytotoxicity. *Planta medica*. 2002;68(7):658-660.
19. Wang H, Cao C, Li B, et al. Immunogenicity of Iodine 131 chimeric tumor necrosis therapy monoclonal antibody in advanced lung cancer patients. *Cancer immunology, immunotherapy : CII*. 2008;57(5):677-684.
20. Ni Y, Bormans G, Chen F, Verbruggen A, Marchal G. Necrosis avid contrast agents: functional similarity versus structural diversity. *Investigative radiology*. 2005;40(8):526-535.
21. Hdeib A, Sloan A. Targeted radioimmunotherapy: the role of (1)(3)(1)I-chTNT-1/B mAb (Cotara) for treatment of high-grade gliomas. *Future oncology*. 2012;8(6):659-669.
22. Cona MM, Alpizar YA, Li J, et al. Radioiodinated hypericin: its biodistribution, necrosis avidity and therapeutic efficacy are influenced by formulation. *Pharmaceutical research*. 2014;31(2):278-290.
23. Xie B, Stammes MA, van Driel PB, et al. Necrosis avid near infrared fluorescent cyanines for imaging cell death and their use to monitor therapeutic efficacy in mouse tumor models. *Oncotarget*. 2015.
24. Boonstra MC, van Driel PB, van Willigen DM, et al. uPAR-targeted multimodal tracer for pre- and intraoperative imaging in cancer surgery. *Oncotarget*. 2015;6(16):14260-14273.
25. He H, Tu X, Zhang J, et al. A novel antibody targeting CD24 and hepatocellular carcinoma in vivo by near-infrared fluorescence imaging. *Immunobiology*. 2015;220(12):1328-1336.
26. Verbeek FP, van der Vorst JR, Tummers QR, et al. Near-infrared fluorescence imaging of both colorectal cancer and ureters using a low-dose integrin targeted probe. *Annals of surgical oncology*. 2014;21 Suppl 4:S528-537.
27. Warram JM, de Boer E, Sorace AG, et al. Antibody-based imaging strategies for cancer. *Cancer metastasis reviews*. 2014;33(2-3):809-822.
28. Sato K, Gorka AP, Nagaya T, et al. Role of Fluorophore Charge on the In Vivo Optical Imaging Properties of Near-Infrared Cyanine Dye/Monoclonal Antibody Conjugates. *Bioconjugate chemistry*. 2015.
29. Berezin MY, Guo K, Akers W, et al. Rational approach to select small peptide molecular probes labeled with fluorescent cyanine dyes for in vivo optical imaging. *Biochemistry*. 2011;50(13):2691-2700.
30. Kroemer G, Galluzzi L, Brenner C. Mitochondrial membrane permeabilization in cell death. *Physiological reviews*. 2007;87(1):99-163.
31. Proskuryakov SY, Konoplyannikov AG, Gabai VL. Necrosis: a specific form of programmed cell death? *Experimental cell research*. 2003;283(1):1-16.
32. Majno G, Joris I. Apoptosis, oncosis, and necrosis. An overview of cell death. *The American journal of pathology*. 1995;146(1):3-15.
33. Keereweer S, Van Driel PB, Snoeks TJ, et al. Optical image-guided cancer surgery: challenges and limitations. *Clin Cancer Res*. 2013;19(14):3745-3754.
34. Pleijhuis R, Timmermans A, De Jong J, De Boer E, Ntziachristos V, Van Dam G. Tissue-simulating phantoms for assessing potential near-infrared fluorescence

- imaging applications in breast cancer surgery. *Journal of visualized experiments : JoVE*. 2014(91):51776.
35. Paulus A, Desai P, Carney B, et al. Development of a clickable bimodal fluorescent/PET probe for in vivo imaging. *EJNMMI research*. 2015;5(1):120.
 36. Seibold U, Wangler B, Schirmmacher R, Wangler C. Bimodal imaging probes for combined PET and OI: recent developments and future directions for hybrid agent development. *BioMed research international*. 2014;2014:153741.
 37. Morais M, Campello MP, Xavier C, et al. Radiolabeled mannosylated dextran derivatives bearing an NIR-fluorophore for sentinel lymph node imaging. *Bioconjugate chemistry*. 2014;25(11):1963-1970.
 38. Zhu H, Zhao J, Lin X, Hong Y, Li C, Yang Z. Design, synthesis and evaluation of dual-modality glyco-nanoparticles for tumor imaging. *Molecules*. 2013;18(6):6425-6438.
 39. Majonis D, Ornatsky O, Weinrich D, Winnik MA. Dual-purpose polymer labels for fluorescent and mass cytometric affinity bioassays. *Biomacromolecules*. 2013;14(5):1503-1513.
 40. Xie BW, Park D, Van Beek ER, et al. Optical imaging of cell death in traumatic brain injury using a heat shock protein-90 alkylator. *Cell death & disease*. 2013;4:e473.
 41. Brom M, Joosten L, Oyen WJ, Gotthardt M, Boerman OC. Improved labelling of DTPA- and DOTA-conjugated peptides and antibodies with ¹¹¹In in HEPES and MES buffer. *EJNMMI research*. 2012;2:4.
 42. Goorden MC, Beekman FJ. High-resolution tomography of positron emitters with clustered pinhole SPECT. *Physics in medicine and biology*. 2010;55(5):1265-1277.
 43. Branderhorst W, Vastenhouw B, Beekman FJ. Pixel-based subsets for rapid multi-pinhole SPECT reconstruction. *Physics in medicine and biology*. 2010;55(7):2023-2034.
 44. Paine-Murrieta GD, Taylor CW, Curtis RA, et al. Human tumor models in the severe combined immune deficient (scid) mouse. *Cancer chemotherapy and pharmacology*. 1997;40(3):209-214.
 45. Prinsen K, Jin L, Vunckx K, et al. Radiolabeling and preliminary biological evaluation of a (99m)Tc(CO)(3) labeled 3,3'-(benzylidene)-bis-(1H-indole-2-carbohydrazide) derivative as a potential SPECT tracer for in vivo visualization of necrosis. *Bioorganic & medicinal chemistry letters*. 2011;21(1):502-505.
 46. Van Walleghe DM, Parseghian MH. Toxicity and biodistribution of an iodine-131-radiolabelled tumour necrosis-targeting antibody in non-tumour-bearing domestic felines. *Veterinary and comparative oncology*. 2006;4(1):9-20.
 47. Verma N, Cowperthwaite MC, Burnett MG, Markey MK. Differentiating tumor recurrence from treatment necrosis: a review of neuro-oncologic imaging strategies. *Neuro-oncology*. 2013;15(5):515-534.
 48. Murphy KP, O'Connor OJ, Maher MM. Updated imaging nomenclature for acute pancreatitis. *AJR American journal of roentgenology*. 2014;203(5):W464-469.
 49. Carlsson M, Arheden H, Higgins CB, Saeed M. Magnetic resonance imaging as a potential gold standard for infarct quantification. *Journal of electrocardiology*. 2008;41(6):614-620.
 50. Pharmaceuticals P. Cotara Oncology. Accessed October 26, 2015.

51. Ni Y. Abstract 1767: Oncocidia: a small molecule dual targeting pan-anticancer theragnostic strategy. abstract presented at Proceedings of the 105th Annual Meeting of the American Association for Cancer Research; 2014 Apr 5-9, 2014; San Diego, CA. Philadelphia (PA).
52. Cona MM, Li J, Feng Y, et al. Targetability and biodistribution of radioiodinated hypericin: comparison between microdosing and carrier-added preparations. *Anti-cancer agents in medicinal chemistry*. 2014;14(6):852-861.
53. Krabbendam R, Pool M, de Vries LG, Offerhaus HL, Herek JL, Otto C. Hybrid imaging of fluorescently labeled cancer drugs and label-free four-wave mixing microscopy of cancer cells and tissues. *Journal of biomedical optics*. 2015;20(8):86006.
54. Rijpkema M, Bos DL, Cornelissen AS, et al. Optimization of Dual-Labeled Antibodies for Targeted Intraoperative Imaging of Tumors. *Molecular imaging*. 2015;14:348-355.
55. Sosabowski JK, Mather SJ. Conjugation of DOTA-like chelating agents to peptides and radiolabeling with trivalent metallic isotopes. *Nature protocols*. 2006;1(2):972-976.
56. Cooper MS, Sabbah E, Mather SJ. Conjugation of chelating agents to proteins and radiolabeling with trivalent metallic isotopes. *Nature protocols*. 2006;1(1):314-317.
57. Adams PC, Lin E, Barber KR, Grant CW. Enhanced biliary iron excretion with amphiphilic diethylenetriaminepentaacetic acid. *Hepatology*. 1991;14(6):1230-1234.
58. Hawe A, Sutter M, Jiskoot W. Extrinsic fluorescent dyes as tools for protein characterization. *Pharmaceutical research*. 2008;25(7):1487-1499.
59. Frangioni JV. New technologies for human cancer imaging. *Journal of clinical oncology : official journal of the American Society of Clinical Oncology*. 2008;26(24):4012-4021.
60. ATCC. SOP: Thawing, Propagating and Cryopreserving of NCI-PBCF-HTB22 (MCF-7). 2012.
61. Kim JB, Urban K, Cochran E, et al. Non-invasive detection of a small number of bioluminescent cancer cells in vivo. *PloS one*. 2010;5(2):e9364.
62. Koo GC, Huang C, Camacho R, et al. Immune enhancing effect of a growth hormone secretagogue. *Journal of immunology*. 2001;166(6):4195-4201.
63. Friberg S, Mattson S. On the growth rates of human malignant tumors: implications for medical decision making. *Journal of surgical oncology*. 1997;65(4):284-297.
64. Rehman MU, Tahir M, Ali F, et al. Cyclophosphamide-induced nephrotoxicity, genotoxicity, and damage in kidney genomic DNA of Swiss albino mice: the protective effect of Ellagic acid. *Molecular and cellular biochemistry*. 2012;365(1-2):119-127.
65. Boswell CA, Ferl GZ, Mundo EE, et al. Effects of anti-VEGF on predicted antibody biodistribution: roles of vascular volume, interstitial volume, and blood flow. *PloS one*. 2011;6(3):e17874.



Chapter 7

The necrosis-avid small molecule HQ4-DTPA as a multimodal imaging agent for monitoring radiation therapy-induced tumor cell death

Marieke A. Stammes*, Azusa Maeda*, Jiachuan Bu, Deborah A. Scollard, Iris Kulbatski, Philip J. Medeiros, Riccardo Sinisi, Elena A. Dubikovskaya, Thomas J.A. Snoeks, Ermond R. van Beek, Alan B. Chan, Clemens W.G.M. Löwik, Ralph S. DaCosta

* contributed equally to this work

Adapted from: the necrosis-avid small molecule HQ4-DTPA as a multimodal imaging agent for monitoring radiation therapy-induced tumor cell death, *Front Oncol.* 2016 Oct 21;6:221

Abstract

Purpose

Most effective antitumor therapies induce tumor cell death. Non-invasive, rapid and accurate quantitative imaging of cell death is essential for monitoring early response to antitumor therapies. To facilitate this, we previously developed a biocompatible necrosis-avid near-infrared fluorescence (NIRF) imaging probe, HQ4, which was radiolabeled with ¹¹¹Indium-chloride (¹¹¹In-Cl₃) via the chelate diethylene triamine pentaacetic acid (DTPA), to enable clinical translation. The aim of the present study was to evaluate the application of HQ4-DTPA for monitoring tumor cell death induced by radiation therapy. Apart from its NIRF and radioactive properties, HQ4-DTPA was also tested as a photoacoustic imaging probe to evaluate its performance as a multimodal contrast agent for superficial and deep tissue imaging.

Procedures

Radiation-induced tumor cell death was examined in a xenograft mouse model of human breast cancer (MCF-7). Tumors were irradiated with three fractions of 9 Gy each. HQ4-DTPA was injected intravenously after the last irradiation, NIRF and photoacoustic imaging of the tumors were performed at 12, 20 and 40 h after injection. Changes in probe accumulation in the tumors were measured *in vivo*, and *ex vivo* histological analysis of excised tumors was performed at experimental endpoints. In addition, biodistribution of radiolabeled [¹¹¹In]DTPA-HQ4 was assessed using hybrid single-photon emission computed tomography-computed tomography (SPECT-CT) at the same time points.

Results

In vivo NIRF imaging demonstrated a significant difference in probe accumulation between control and irradiated tumors at all time points after injection. A similar trend was observed using *in vivo* photoacoustic imaging, which was validated by *ex vivo* tissue fluorescence and photoacoustic imaging. Serial quantitative radioactivity measurements of probe biodistribution further demonstrated increased probe accumulation in irradiated tumors.

Conclusions

HQ4-DTPA has high specificity for dead cells *in vivo*, potentiating its use as a contrast agent for determining the relative level of tumor cell death following radiation therapy using NIRF, photoacoustic imaging and SPECT *in vivo*. Initial preclinical results are promising and indicate the need for further evaluation in larger cohorts. If successful, such studies may help develop a new multimodal method for non-invasive and dynamic deep-tissue imaging of treatment-induced cell death to quantitatively assess therapeutic response in patients.

Introduction

The International Agency for Research on Cancer estimated that globally in 2012, 14.1 million new patients were diagnosed with cancer and that this number will increase to more than 20 million in 2025¹. After diagnosis, most patients with solid tumors undergo surgery, radiotherapy and/or chemotherapy, and may be followed up with alternative treatments. Conventional methods for monitoring antitumor treatment response are based on anatomical imaging, e.g. X-ray, magnetic resonance imaging (MRI) and computed tomography (CT) every 6-8 weeks during the course of treatment as described in the Response Evaluation Criteria In Solid Tumors (RECIST)². Although RECIST provides a standardized guideline, assessment of treatment efficacy based on gross tumor size alone may be insufficient for certain organs and treatments³. Moreover, volumetric change in tumor size based on conventional imaging may be a delayed indicator of treatment effectiveness⁴, unnecessarily exposing patients to the side effects of additional ineffective treatments, and postponing treatment adjustment. Thus, there is a need for novel imaging methods to assess tumor response early and at a cellular/molecular level in order to determine treatment efficacy accurately and adjust the therapy based on tumor response^{5,6}. Ideally, such methods would be non-invasive, clinically practical, and have sufficient sensitivity and specificity for tumor cell death in real time.

Imaging of treatment-induced tumor necrosis may facilitate quantitation of early treatment response in solid tumors as an alternative to the conventional radiological volumetric imaging. Firstly, antitumor therapies such as radiation therapy are known to induce several forms of tumor cell death which will often lead to secondary necrosis⁷⁻⁹. Secondly, necrosis is primarily induced by external factors that cause physiochemical damage compared to apoptosis which can occur in any tissues during normal development and cell turnover^{10,11}, making necrosis-based imaging method suitable to distinguish cell death induced by antitumor therapies. Lastly, tumor necrosis, secondary to ischemia and insufficient vascularization to support a rapidly proliferating tumor mass¹², has been positively correlated with the aggressiveness of cancer, and, therefore, has been used as a diagnostic biomarker for cancer staging¹³⁻¹⁸. Thus, exogenous imaging contrast agents that specifically bind to necrotic tumor cells *in vivo* could enable accurate determination of treatment effects

and disease staging, as well as earlier prediction of treatment outcomes for solid tumors¹⁹.

Accurate quantification of tissue necrosis may have wide clinical relevance compared to conventional practice, especially in monitoring the efficacy of antitumor therapies at earlier stages. Existing necrosis-based imaging agents can be divided in two general groups: 1) MRI and CT contrast agents that enhance endogenous tissue necrosis contrast non-specifically by enabling visualization of the presence of an avascular necrotic core, and 2) positron emission tomography (PET) and single-photon emission computed tomography (SPECT) contrast agents that are specifically targeted to endogenous necrotic tissue^{8,13-18,20-29}. Non-specific tissue necrosis imaging agents will likely fall into abeyance when affordable necrosis-specific agents become clinically available. Thus far, only a few agents have been considered clinically applicable, including necrosis-avid photosensitizer Hypericin (OncocidiaTM)³⁰⁻³² and ¹³¹Iodine-conjugated Tumor Necrosis Targeting monoclonal antibody (TNT-3, Peregrine Pharmaceuticals, California, USA)^{24,33}. While clinical feasibility has been shown for both agents³⁴, several drawbacks may hinder their widespread clinical adoption^{27, 30, 35-37}. For example, Hypericin is phototoxic, poorly soluble and aggregates rapidly. Monoclonal antibodies are relatively large in size, have long circulation times, may induce host immune response, and are expensive to develop using Good Manufacturing Practices (GMP)³⁵⁻³⁸.

Recognizing the biological significance of tumor necrosis as a hallmark of tumor response to treatment and the need for alternative imaging methods to measure treatment-induced solid tumor necrosis, we previously developed a biocompatible near-infrared fluorescent (NIRF), water-soluble imaging probe called HQ4. HQ4 is economical to produce, is non-phototoxic, and binds specifically to cells with compromised cell membrane integrity³⁸. We validated HQ4-DTPA as a necrosis-avid contrast agent histologically by demonstrating localization of HQ4-DTPA in necrotic tumors, and indicated that HQ4-DTPA could be made more clinically practical by addition of a radioactive moiety³⁸. Building on these results, in the current study, we investigated the utility of HQ4-DTPA as a necrosis-imaging agent *in vivo* to measure tumor response to radiation therapy. Radiotherapy is used to treat over 50% of cancer patients³⁹, making the translational value of HQ4-DTPA universally significant.

In this study, we examined a relatively high dose-per-fraction treatment scheme (3 x 9 Gy) to induce tumor cell death based on a biological equivalent dose (BED) that is clinically relevant to 60 Gy for 2 Gy fractions. We investigated a trimodal HQ4-DTPA imaging (photoacoustic, NIRF, SPECT) approach to measure tumor response to radiation therapy in a MCF-7 human breast cancer mouse xenograft model. We reasoned that the addition of photoacoustic imaging would overcome some of the disadvantages associated with SPECT and NIRF, such as the exposure to ionizing radiation emitted from radionuclides and the limited penetration depth⁴⁰, respectively. Photoacoustic imaging may also be ideal for routine clinical use as it is easily accessible, minimally invasive, and technologically inexpensive compared to conventional imaging methods (CT, MRI). The results of this work demonstrate the feasibility of using the multimodal (NIRF, photoacoustic, SPECT) HQ4-DTPA probe *in vivo* for longitudinal measurement of solid tumor necrosis in response to clinically relevant high-dose radiotherapy.

Materials and Methods

HQ preparation

HQ4-DTPA was obtained from Ilumicare BV (Rotterdam, The Netherlands). HQ4-DTPA was synthesized as previously described³⁸. For phantom studies, dilutions of HQ4-DTPA were prepared in phosphate buffered saline (PBS) at various concentrations (12.5, 25, 50, and 100 μM). For *in vivo* mouse studies, 100 μl which represents 10 nmol HQ4-DTPA was injected via the tail vein. To label HQ4-DTPA with $^{111}\text{InCl}_3$, HQ4-DTPA was dissolved in 0.1 M HEPES (10 $\mu\text{g}/100 \mu\text{L}$)⁴¹ and incubated with $^{111}\text{InCl}_3$ (35 MBq; Nordion, Vancouver, BC). After 30 minutes of incubation on a shaker, labeling was validated with instant thin layer chromatography (ITLC). In all cases, labeling efficacy was greater than 90%.

Cell Culture

GFP-fluorescent MCF-7 human breast cancer cells (kindly provided by Dr. Shirley Wu, Leslie Dan Faculty of Pharmacy, University of Toronto) were grown in D-MEM Medium supplemented with 10% fetal bovine serum and 1% Pen-Strep in a humidified incubator at 37°C and 5% CO_2 . Cells were trypsinized, counted and suspended in 10% PBS before further use.

Animal Studies

All animal procedures were conducted in accordance with appropriate regulatory standards under protocols AUP#2407 and #3004 approved by the University Health Network Institutional Animal Care Committee, and conform to the institutional guidelines for the proper and humane use of animals in research. Eight to 10-week-old female athymic nude mice (NCRNU-F strain) were obtained from Taconic Biosciences (Hudson, NY). 2×10^6 MCF-7-GFP cells were injected subcutaneously in both sides of the mouse scapularis region and were allowed to grow for 3-4 weeks until they reached approximately 5 mm in diameter, as measured using a caliper. All experimental procedures were

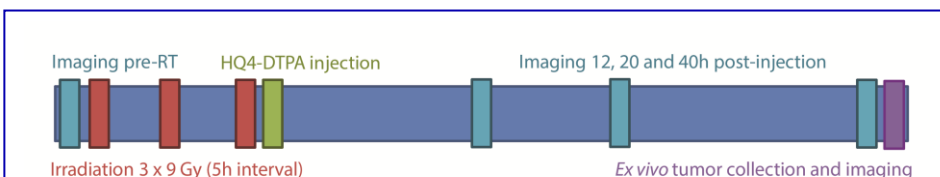


Figure 1. Experimental schedule.

Three fractions of 9 Gy irradiation were delivered with a 5-hour interval and HQ4-DTPA was injected at the end of the irradiation schedule. *In vivo* photoacoustic and fluorescence imaging were performed at 12, 20 and 40 h following the injection.

conducted under isoflurane gas anesthesia (2-3%, 0.8 l/min). All animal experiments were performed following the treatment schedule shown in **Figure 1**.

Briefly, pre-treatment images were obtained prior to irradiation to determine the size of the tumors based on bulk tumor GFP fluorescence. Tumor GFP fluorescence intensity is a delayed indicator of tumor response to irradiation since the GFP protein has a half-life of ~ 26 h⁴², ergo, GFP fluorescence intensity was not used to quantify tumor response following irradiation.

Radiation Treatment and HQ4-DTPA Administration

All irradiation procedures were performed using a small animal irradiation system (XRad 225Cx, Precision X-Ray Inc., North Branford, CT) at a photon energy of 225 kVp and a tube current of 13 mA. Tumors were localized using x-ray fluoroscopy prior to irradiation. A 1.5 cm circular collimator was used to irradiate tumors at a dose rate of 2.9 Gy/min. The dose rate was measured using radiochromic films and a solid water phantom, as described previously⁴³. After delivery of the last radiation fraction, HQ4-DTPA was injected via the tail vein and anesthetized mice were imaged with each modality at 12, 20 and 40 h following injection (**Fig. 1**).

Fluorescence Imaging

In vivo and *ex vivo* fluorescence images of GFP and HQ4-DTPA signals in MCF-7 tumors were obtained using the IVIS Spectrum imaging system (Perkin Elmer Inc., Waltham, MA). GFP fluorescence signal was collected with an excitation wavelength of 465 nm and an emission wavelength of 500 nm (+/- 20 nm). HQ4-DTPA NIRF signal was collected with an excitation wavelength of 675 nm and an emission wavelength of 720 nm (+/- 20 nm).

Photoacoustic Imaging

Tissue phantom, *in vivo* and *ex vivo* photoacoustic imaging of MCF-7 tumors was performed using the Vevo LAZR system (FujiFilm VisualSonics Inc., Toronto, ON) with a 21 MHz center-frequency transducer. To prepare the phantom, HQ4-DTPA samples prepared at different concentrations (12.5, 25, 50, and 100 μ M) were passed through polyethylene tubes that were placed on a piece of sliced turkey breast, having an approximate thickness of 2.5 mm. Additional layers of meat were added to simulate various thicknesses of tissues. Photoacoustic images were obtained after the addition of each layer. For all experiments, 3D photoacoustic and ultrasound images were acquired

simultaneously with a single wavelength of 700 nm for HQ4-DTPA, and the built-in Spectro mode was used to obtain the absorption spectrum from 680 nm to 900 nm.

SPECT-CT

Mice were imaged at 12, 20 and 40 h after intravenous injection of [¹¹¹In]DTPA-HQ4. Mice were anesthetized by inhalation of 2% isoflurane in medical grade air. Imaging was performed on a nanoSPECT/CT system (Bioscan Inc., Washington, DC) with four NaI(Tl) detectors fitted with 1.4 mm multi-pinhole collimators (resolution <1.2 mm at full-width-half-maximum). Cone beam CT images were acquired first (180 projections, 45 kVp), followed by the SPECT images. Photons were accepted from the 10% window centered on both the 245 keV and 171 keV photopeaks of ¹¹¹In. A total of 24 projections were obtained in a 256 x 256 matrix for a total of 45 minutes. The CT slices were reconstructed using a filtered back-projection algorithm, whereas the SPECT slices were reconstructed using an ordered subset expectation maximization (OSEM) algorithm with four subsets and nine iterations. CT and SPECT images were anatomically co-registered using the InVivoScope software (Bioscan, Boston, MA).

Three mice were sacrificed after each experimental time point. Tissues were excised, weighed, and counted for radioactivity (PerkinElmer Wallac 1480 Wizard 3" gamma-counter, Waltham, MA) along with a standard of the injected dose, so that the decay-corrected uptakes of HQ4-DTPA were determined as the percentage of the injected dose per gram (% ID/g). The % ID/g was calculated as follows: [(MBq measured in tissue/injected dose) * 100%]/weight of tissue]. The total injected dose per mouse was equal to the difference between the pre- and post-injection syringe radioactivity, as measured by a CRC-15R dose calibrator (Capintec, Ramsay, NJ).

***Ex vivo* Fluorescence Imaging and Autoradiography**

Tumors were resected at the experimental endpoints, and were either embedded in OCT compound and snap frozen in liquid nitrogen, or fixed in formalin. Frozen sections were imaged using a phosphor imager (Cyclone Plus, Perkin Elmer) to detect ¹¹¹In radioactivity. The same sections were subsequently imaged to measure HQ4-DTPA fluorescence with an excitation wavelength of 650 nm using TissueScope system (Huron Technologies). Formalin-fixed tissue sections were subjected to Haemotoxylin and Eosin

(H&E) staining and TdT-mediated dUTP Nick-End Labeling (TUNEL) staining (Promega, Madison, WI) to detect radiation-induced tumor cell death including necrosis^{44,45}.

Statistical Analysis

All statistical analysis was performed using GraphPad Prism® software (GraphPad Software, San Diego, CA). Student's t-test was used to compare two sets of data, and two-way repeated measures ANOVA with Bonferroni post-test was used for serial imaging data. $P < 0.05$ was considered significant, and error bars represent the mean \pm SEM.

Results

HQ4-DTPA as a photoacoustic contrast agent

To evaluate the application of HQ4-DTPA in addition to the NIRF property that was described previously³⁸, the photoacoustic property of carboxylated cyanine HQ4-DTPA was tested in a phantom composed of transparent plastic tubes. As seen in **Figure 2A-B**, HQ4-DTPA absorption increased with increasing concentration, demonstrating a peak at around 710 nm excitation. The photoacoustic absorption spectrum was similar to its known fluorescence spectrum³⁸, supporting its use as an extrinsic photoacoustic contrast agent.

To further characterize its performance as a photoacoustic contrast agent, multiple layers of meat were added over top of the tube phantoms to simulate a tissue thickness of up to 1 cm. After the addition of each layer of meat, fluorescence and photoacoustic images, as well as photoacoustic absorption spectra, were acquired. In this way, we represented similar scattering and absorption patterns to those found in the human body. The fluorescence signals derived from the different concentrations were indistinguishable by the addition of the first layer of turkey breast tissue (2.5 mm thick) (data not shown). The photoacoustic intensity of the agent in the tubes was, however, detectable with layers up to 10 mm in total thickness at the highest concentration of HQ4-DTPA (100 μ M) (**Fig. 2C**). **Figure 2D** shows the PA absorption spectra of 100 μ M HQ4-DTPA with the addition of 2.5 mm thick tissue layers.

***In vivo* serial photoacoustic and fluorescence imaging of HQ4-DTPA accumulation in irradiated tumors**

TdT-mediated dUTP nick-end labeling (TUNEL) staining of irradiated tumor demonstrated over a two-fold difference in tumor cell death in tumors irradiated with 3 fractions of 9 Gy (27 Gy total), compared to non-irradiated control tumors (**Fig. 3A-B**). H&E staining was performed to confirm the TUNEL positive area as necrotic. The arrowheads in the image mark the difference in H&E staining between healthy and necrotic tissue. Based on those results, the same irradiation treatment regimen was used for all subsequent experiments.

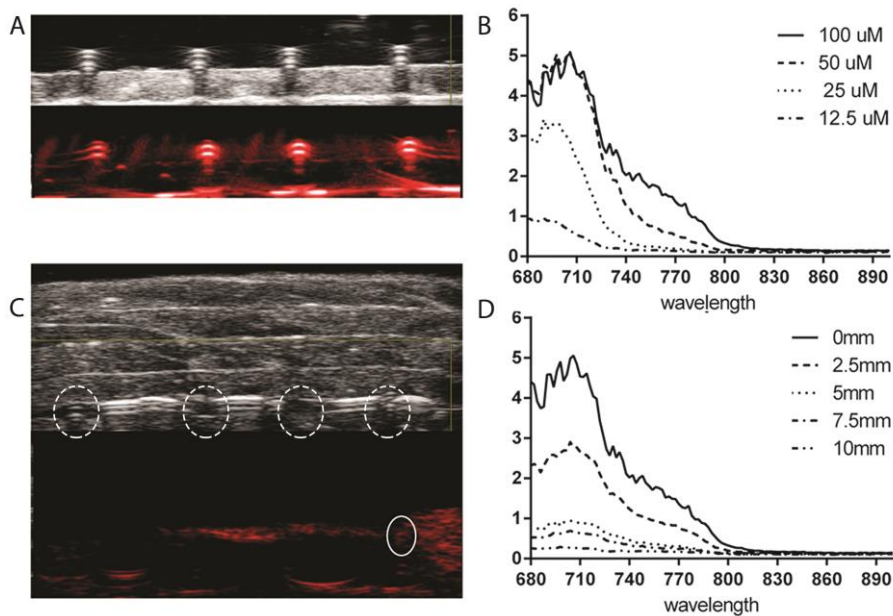
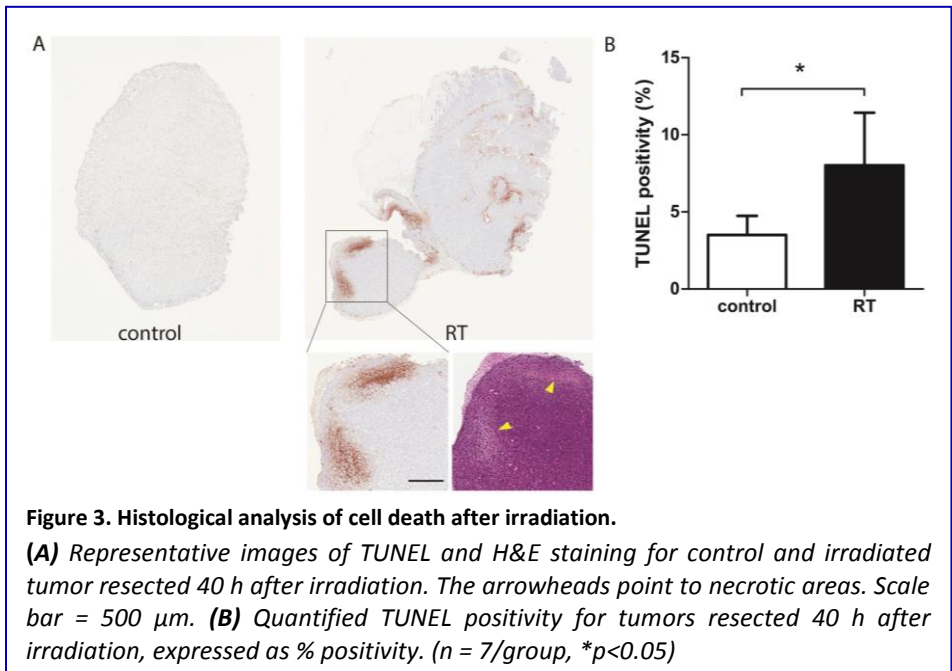


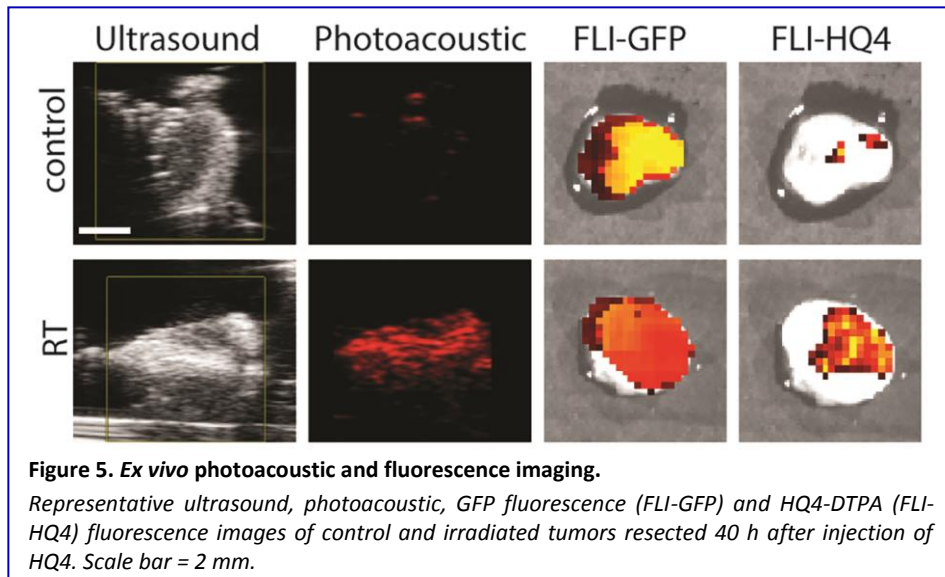
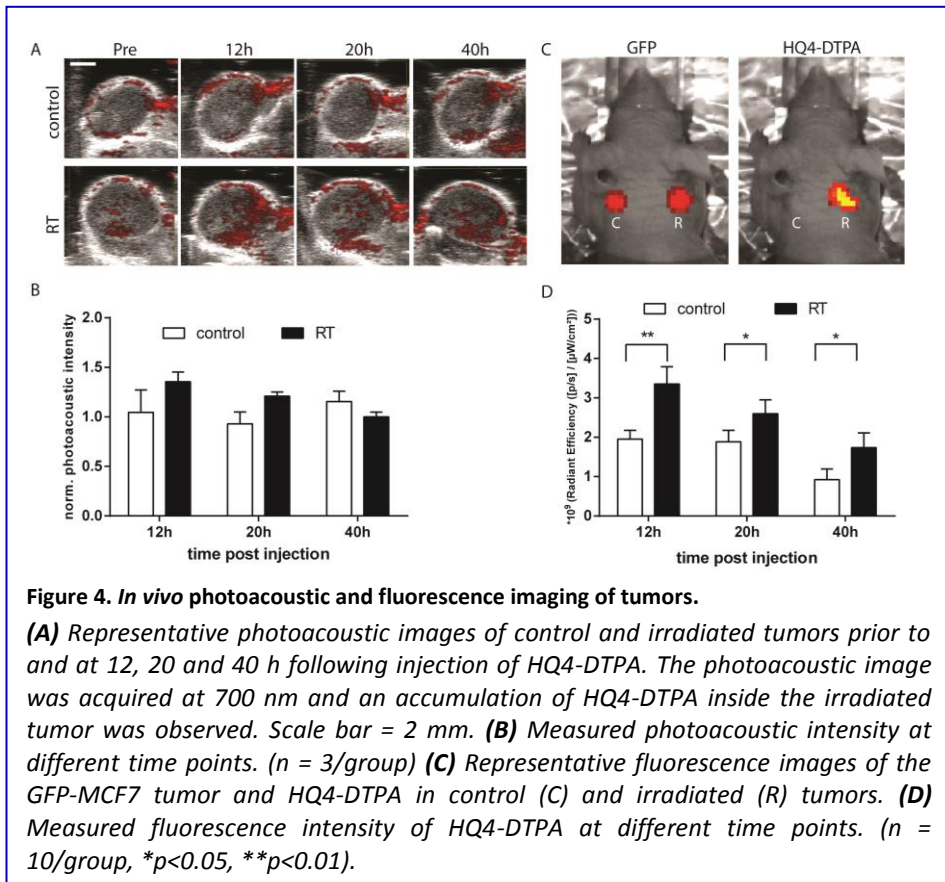
Figure 2. Photoacoustic property of HQ4-DTPA.

(A) Representative ultrasound (top) and photoacoustic (bottom) images of HQ4-DTPA in a tube phantom at different concentrations (from left to right: 12.5, 25, 50, and 100 μM). The photoacoustic image was acquired at 700 nm. **(B)** Corresponding absorption spectra of HQ4-DTPA for the different concentrations. **(C)** Representative ultrasound (top) and photoacoustic (bottom) images of HQ4-DTPA in the same tube phantom as in (A), covered with 10 mm-thick meat. The yellow circles indicate the location of tubes, and the white circle indicates the photoacoustic absorption of the tube containing 100 μM HQ4-DTPA. **(D)** The corresponding absorption spectra of 100 μM HQ4-DTPA with various thicknesses of meat covering the tube.

As demonstrated in **Figure 4A**, the photoacoustic images demonstrated accumulation of HQ4-DTPA inside the treated tumor mass, while some endogenous photoacoustic signals were observed in the outer rim of the

tumor in both control and irradiated tumors. **Figure 4B** demonstrated a trend for increased accumulation of HQ4-DTPA in irradiated tumors compares to control tumors, although the difference was not statistically significant. The fluorescence images (**Fig. 4C-D**) showed an approximate 1.8-fold increase in HQ4-DTPA accumulation in the irradiated subcutaneous tumors compared to non-irradiated controls, most notably at 12 h post-radiotherapy.



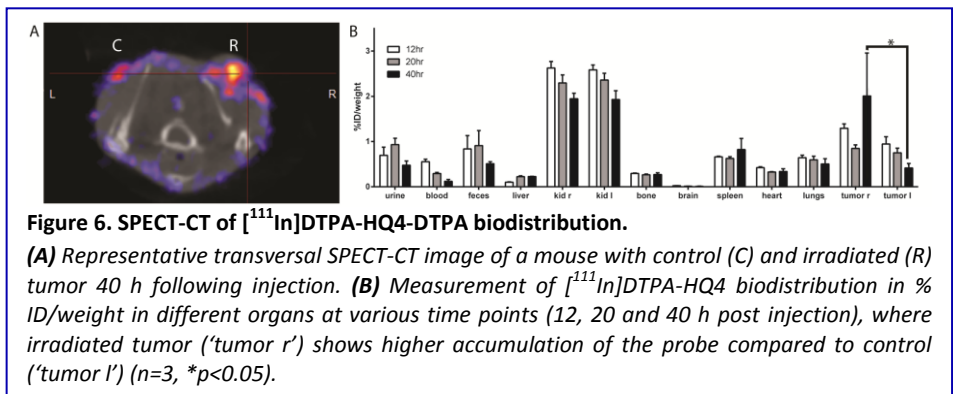


Validation of photoacoustic and fluorescence imaging of HQ4-DTPA in *ex vivo* tissues

40 h following injection of HQ4-DTPA and subsequently imaged by photoacoustic and fluorescence systems. The resected masses were confirmed to be tumors based on the GFP fluorescence signal. As seen in **Figure 5**, increased HQ4-DTPA accumulation in an irradiated tumor was observed based on photoacoustic and fluorescence images. This indicated that the increased accumulation of HQ4-DTPA was specific to radiation-induced tumor cell necrosis in tumors. Since the skin covering the xenografted tumor was removed during resection, there was less interference from the intrinsic hemoglobin signal from blood vessels in the skin.

In vivo biodistribution and *ex vivo* validation of ^{111}In radiolabeled HQ4-DTPA

SPECT-CT was performed to quantify whole-body biodistribution of [^{111}In]DTPA-HQ4 in MCF-7 tumor-bearing mice following the experimental treatment schedule shown in **Figure 1**. Radiolabeling efficiency of HQ4-DTPA was determined to be greater than 90%. Significantly higher accumulation of [^{111}In]DTPA-HQ4 in irradiated tumors was observed compared to controls in the same mice 40 h after probe injection (tumor-to-background ratio (TBR)=1.8, $P_{40\text{h}}=0.03$) (**Fig. 6A**), thus confirming HQ4's specificity for necrotic tissues and suggesting the kinetics of HQ4-DTPA accumulation. Measurements



of radioactivity in various resected organs demonstrated that [^{111}In]DTPA-HQ4 was concentrated in the excreting organs with a peak in the kidneys, suggesting that the renal system was the main excreting route (**Figure 6B**).

Lastly, the tumors were resected and imaged for [^{111}In]DTPA-HQ4 using autoradiography and fluorescence. The autoradiographic images revealed a clear difference in structural characteristics between the irradiated and control tumors (**Fig. 7A-B**). The internal tissue organization of the non-irradiated tumor was cohesive and showed a clear cellular pattern with a homogeneous color. In contrast, the irradiated tumor showed a high level of disorganization. Furthermore, the overlay (C3) of fluorescence (C1-red) and autoradiography (C2-green) images showed a high degree of co-localization of ^{111}In radioactive signal and HQ4-DTPA fluorescence signal (**Fig. 7C**).

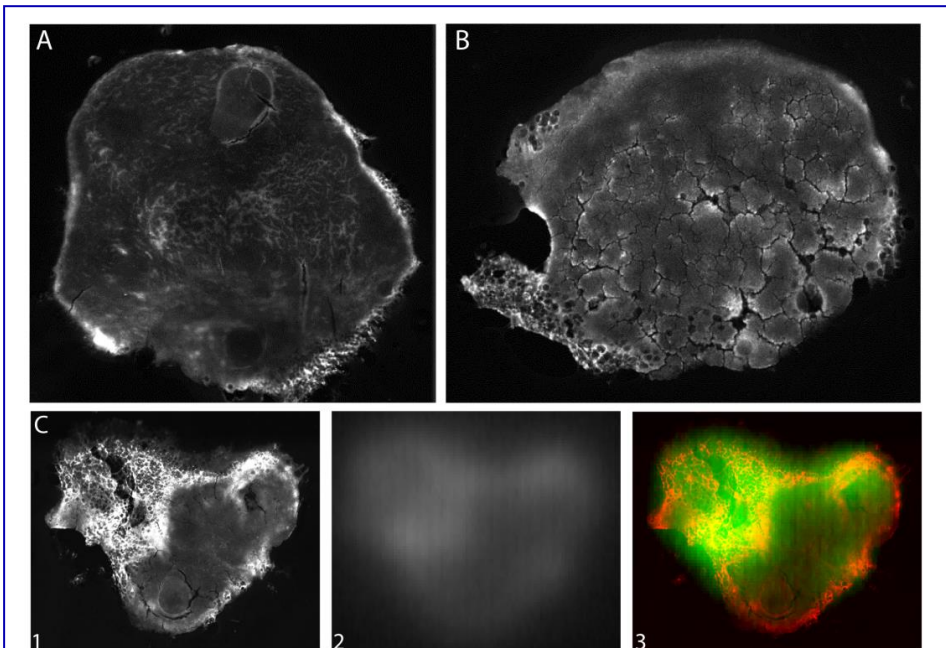


Figure 7. *Ex vivo* fluorescence and autoradiography images of tumors.

Representative images of **(A)** control and **(B)** irradiated tumor resected 40 h following injection of [^{111}In]DTPA-HQ4. The tumors were imaged for HQ4-DTPA fluorescence. **(C)** Overlay (C3) of HQ4-DTPA fluorescence (C1/red) and $^{111}\text{In-Cl}_3$ radioactivity (C2/green) in a tumor, illustrating co-localization of the two signals.

Discussion

In the current study, we evaluated HQ4-DTPA as a multimodal necrosis-avid imaging agent to assess tumor response to a clinically relevant radiotherapy dose using a MCF-7 human breast cancer mouse xenograft model. The necrosis-avid property of HQ4-DTPA for detection of chemotherapy-induced tumor cell necrosis was previously demonstrated using NIRF imaging and SPECT³⁸. To extend the applicability of HQ4-DTPA to another imaging modality, we first assessed its photoacoustic property and demonstrated its distinct optical absorption peak at approximately 700 nm. Based on this result, multimodal imaging was performed to quantitatively evaluate the *in vivo* use of HQ4-DTPA to detect tumor response to radiotherapy using a fractionated irradiation scheme (3 x 9 Gy). Our *in vivo* fluorescence results demonstrated an increase in HQ4-DTPA signal in irradiated tumors compared to non-irradiated tumors *in vivo* for up to 40 h after treatment, indicating specific and sustained accumulation of HQ4-DTPA in irradiated tumors. These data were supported by *ex vivo* NIRF and photoacoustic imaging of control and irradiated tumors. Lastly, we used SPECT-CT to quantitate the biodistribution of HQ4-DTPA, demonstrating HQ4-DTPA accumulation in irradiated tumors and clearance of unbound HQ4-DTPA mostly via kidneys, which was visualised at all time points. Collectively, our data indicated that HQ4-DTPA may be used as a multimodal necrosis-specific imaging agent. The data also suggested that HQ4-DTPA may be used clinically in the future to monitor solid tumor response to radiation therapy in a practical time frame.

Radiation therapy was selected as the treatment modality for the breast cancer model in the present study because of its wide-spread clinical usage. Breast conserving surgery is the standard treatment for localized breast cancer in combination with

(neo-) adjuvant therapies⁴⁶, such as radiation therapy, which has been shown to reduce local recurrence⁴⁷. Radiation therapy is commonly administered in a conventional fractionated schedule (25 fractions of 2 Gy) on the breast with an additional boost of up to 10 Gy on the lumpectomy cavity⁴⁷. Since such treatment schemes cannot be easily replicated in a relevant manner in animal models, we selected a radiation regimen that is isoeffective to a clinically-relevant fractionated irradiation regimen based on a BED of 60 Gy in 2 Gy fractions^{48,49}. Thus the rationale for 3 fractions of 9 Gy with a 5 h interval was based on the BED for 60 Gy, calculated using the α/β ratio of MCF-7 cells

(4.62)^{50,51} and by taking into account the incomplete repair model based on the half-time of recovery from radiation damage in murine skin. Although the radiation regimen used in our study may not be used routinely or be clinically practical, we assumed that the regimen was appropriate to mimic the total radiation dose given in cancer patients as the BED is used to compare the relative effectiveness of different radiation protocols that vary in fraction size.

The NIRF properties of carboxylated cyanine HQ4-DTPA and its radioactive labeled variant [¹¹¹In]DTPA-HQ4 have been previously demonstrated by our group³⁸. Although nuclear imaging overcomes the limited tissue penetration depth of NIRF imaging^{40,52}, it has its drawbacks including radiation safety, cost of radioactive materials, limited temporal sensitivity, and the lack of anatomical detail⁵³. Photoacoustic imaging overcomes such limitations and offers a novel and clinically relevant means of imaging HQ4-DTPA *in vivo*. Since photoacoustic imaging includes ultrasound imaging, both anatomical and functional information can be obtained simultaneously in real-time. Photoacoustic imaging can image beyond the depth limitation of fluorescence imaging to more than 5 cm⁵⁴, making it suitable for imaging deeper tumors. In the current *in vitro* experiments, we distinguished a specific photoacoustic signal at a maximum depth of 1 cm, achieving 5 times the tissue depth of NIRF imaging. However, depth imaging beyond 1 cm could not be performed due to the inherent property of the high-frequency ultrasound transducer (21 MHz) used in our study. Photoacoustic imaging depth may be increased by using a lower frequency transducer, but at the expense of reduced detection sensitivity⁵⁵. Alternatively, a higher concentration of the probe may facilitate detection in deeper tissue.

Despite the advantages of photoacoustic imaging, there are some technical limitations. Firstly, photoacoustic imaging may not be a suitable method for certain organs, such as lung and brain, where acoustic impedance is different between tissue interfaces⁵⁶. However, several preclinical studies demonstrated the use of photoacoustic imaging in these organs, suggesting future use of photoacoustic imaging in a variety of organs⁵⁷⁻⁵⁹. Secondly, the clinical use of photoacoustic contrast must be approached cautiously, since photoacoustic imaging visualizes any tissue-based optical absorber at a given wavelength. As such, this method detects the presence of endogenous hemoglobin, a primary optical absorber in tissues, across a broad spectral range that includes 700-750 nm, corresponding to the peak absorption of

HQ4. Our photoacoustic imaging results indicated the presence of an endogenous optical absorber mostly in the periphery of control and irradiated tumors, suggesting the presence of vasculature around the tumor. The endogenous absorption limited our ability to detect HQ4-DTPA in a highly-specific manner. To distinguish absorption by any contrast agent from that of endogenous absorbers, photoacoustic spectral unmixing techniques can be performed to obtain a clear overview of the contrast agent signal based on its known spectrum⁶⁰. Such techniques can be applied in future studies to visualize the accumulation of HQ4-DTPA inside the irradiated tumors in a specific manner. In addition, the imaging probe may accumulate inside tumors due to intrinsic tumor necrosis resulting in the presence of background signal in both fluorescence and photoacoustic imaging. In such cases, baseline imaging needs to be performed with the injection of HQ4-DTPA prior to initiation of an anticancer treatment.

Although NIRF imaging is widely clinically applicable, its use as a singular imaging modality to assess biological activities may be suboptimal. For example, fluorescence properties of exogenous dyes used *in vivo* are strongly influenced by the tissue microenvironment, such as hydrophobicity and pH, as well as by interactions with various proteins^{61,62}. Such interactions will influence HQ4-DTPA fluorescence intensity differently in an *in vivo* environment of living cells, which may hamper quantification of probe accumulation inside necrotic tumors. These same interactions may have contributed to the differences in the time point of highest signal accumulation observed using the different imaging methods in our model, although it was not explicitly addressed in this study. To achieve absolute quantification of a probe, gamma spectroscopy or mass spectrometry should be considered^{61,62}. In our study, quantification of HQ4-DTPA was achieved by measurement of radioactivity in various organs, supporting the *in vivo* imaging data in a quantitative manner.

Irradiation causes direct DNA damage and the production of reactive oxygen species (ROS), both leading to cell death. The amount and the type of cell death depends on the tumor type and the irradiation dose per fraction. For MCF-7 cells, the α/β ratio, a model of radiation effect, is relatively low compared to the higher α/β ratios for other tumors such as Tara-1/2 (teratoma), DU145 (bladder), TSU and UNCap (prostate) (e.g. 7-20 Gy)⁵¹, suggesting that the treatment response may be delayed in MCF-7 tumor-

bearing animals. This delayed response can be seen by our *in vivo* radioactivity-based biodistribution results demonstrating significant differences of HQ4-DTPA accumulation between the treated and control tumor 40 h after irradiation. This discrepancy may increase even more over time, requiring re-injection of the probe at a later time point or at multiple time points following radiotherapy. In addition, radiation-induced damage may be more severe when high dose of radiation is used per fraction, leading to direct tumor cell destruction as well as secondary tumor cell death^{63,64}. Therefore, future studies may focus on multi-fractionated scheme with a lower fraction dose to assess whether the proposed necrosis-imaging technique is still applicable. In testing multi-fractionation schemes, the imaging technique could be initially tested in the same way so immediately after the end of the complete treatment, and later on even during the treatment process to assess its utility in adapting therapeutic regimen. In the current study, we chose to inject HQ4-DTPA immediately after the final tumor irradiation to detect early treatment response since the goal of this study was to investigate HQ4-DTPA imaging as an early indicator of radiation induced necrosis. Collectively, future studies are warranted with multi-fractionation scheme and/or injections at multiple time points to evaluate its utility in treatment monitoring and adaptive treatment.

Overall, we have demonstrated that HQ4-DTPA can be used to objectively assess tumor response to radiation therapy. HQ4-DTPA is distinct from current clinically-available necrosis-avid agents given its unique *in vivo* specificity and multimodal imaging capability. The added benefit of multimodal imaging potentially broadens its applicability in a variety of clinical settings, where tissue necrosis serves as a surrogate marker of diseases as well as response to necrosis-inducing treatments. The advantages of the small molecule [¹¹¹In]DTPA-HQ4 include high water solubility, the photoacoustic property that enables deep tissue penetration into tissues, lack of phototoxicity, and low production costs. Unlike fluorescence imaging and SPECT, photoacoustic imaging combines the anatomical and functional properties of tissue in a 3D image. Therefore, the necrosis avid radiotracer [¹¹¹In]DTPA-HQ4 has the potential to be clinically translated for diagnostic and prognostic purposes, as well as to predict early treatment outcome of antitumor treatments such as radiation therapy. Additional preclinical and clinical studies are required to demonstrate the advantages of this novel imaging approach to assess early

treatment efficacy and inform adaptive therapy decisions for individual patients.

Acknowledgments

This work was supported by funding provided to R. DaCosta by the Canadian Institutes of Health Research, Terry Fox Research Institute and by the International Collaboration R&D Program, South Korean Ministry of Knowledge Economy. The authors would like to acknowledge the Spatio-Temporal Targeting and Amplification of Radiation Response (STTARR) program and its affiliated funding agencies. Additionally, this work was supported by project grants from the EU Program: FP7-PEOPLE-2013-IAPP (612360 – BRAINPATH) and H2020-MSCA-RISE grant number 644373 - PRISAR.

References

1. Ferlay J, Soerjomataram I, Dikshit R, et al. Cancer incidence and mortality worldwide: Sources, methods and major patterns in GLOBOCAN 2012. *International Journal of Cancer*. 2015;136(5):E359-E386.
2. Eisenhauer EA, Therasse P, Bogaerts J, et al. New response evaluation criteria in solid tumours: revised RECIST guideline (version 1.1). *Eur J Cancer*. 2009;45(2):228-247.
3. Fournier L, Ammari S, Thiam R, Cuénod CA. Imaging criteria for assessing tumour response: RECIST, mRECIST, Cheson. *Diagnostic and Interventional Imaging*. 2014;95(7-8):689-703.
4. Han Z, Fu A, Wang H, et al. Noninvasive assessment of cancer response to therapy. *Nat Med*. 2008;14(3):343-349.
5. Nishino M, Jagannathan JP, Krajewski KM, et al. Personalized Tumor Response Assessment in the Era of Molecular Medicine: Cancer-Specific and Therapy-Specific Response Criteria to Complement Pitfalls of RECIST. *American Journal of Roentgenology*. 2012;198(4):737-745.
6. Zhao B, Schwartz LH, Larson SM. Imaging Surrogates of Tumor Response to Therapy: Anatomic and Functional Biomarkers. *Journal of Nuclear Medicine*. 2009;50(2):239-249.
7. Silva MT. Secondary necrosis: The natural outcome of the complete apoptotic program. *FEBS Letters*. 2010;584(22):4491-4499.
8. Uhl M, Saueressig U, Koehler G, et al. Evaluation of tumour necrosis during chemotherapy with diffusion-weighted MR imaging: preliminary results in osteosarcomas. *Pediatric radiology*. 2006;36(12):1306-1311.
9. Eriksson D, Stigbrand T. Radiation-induced cell death mechanisms. *Tumor Biology*. 2010;31(4):363-372.
10. Fink SL, Cookson BT. Apoptosis, Pyroptosis, and Necrosis: Mechanistic Description of Dead and Dying Eukaryotic Cells. *Infection and Immunity*. 2005;73(4):1907-1916.
11. Nikolettou V, Markaki M, Palikaras K, Tavernarakis N. Crosstalk between apoptosis, necrosis and autophagy. *Biochimica et Biophysica Acta (BBA) - Molecular Cell Research*. 2013;1833(12):3448-3459.
12. Herman AB, Savage VM, West GB. A quantitative theory of solid tumor growth, metabolic rate and vascularization. *PloS one*. 2011;6(9):e22973.
13. Hiraoka N, Ino Y, Sekine S, et al. Tumour necrosis is a postoperative prognostic marker for pancreatic cancer patients with a high interobserver reproducibility in histological evaluation. *British journal of cancer*. 2010;103(7):1057-1065.
14. Kato T, Kameoka S, Kimura T, Tanaka S, Nishikawa T, Kobayashi M. p53, mitosis, apoptosis and necrosis as prognostic indicators of long-term survival in breast cancer. *Anticancer Res*. 2002;22(2B):1105-1112.
15. Maiorano E, Regan MM, Viale G, et al. Prognostic and predictive impact of central necrosis and fibrosis in early breast cancer: results from two International Breast Cancer Study Group randomized trials of chemoendocrine adjuvant therapy. *Breast cancer research and treatment*. 2010;121(1):211-218.
16. Park SY, Lee HS, Jang HJ, Lee GK, Chung KY, Zo JI. Tumor necrosis as a prognostic factor for stage IA non-small cell lung cancer. *The Annals of thoracic surgery*. 2011;91(6):1668-1673.
17. Pichler M, Hutterer GC, Chromecki TF, et al. Histologic tumor necrosis is an independent prognostic indicator for clear cell and papillary renal cell carcinoma. *American journal of clinical pathology*. 2012;137(2):283-289.

18. Pollheimer MJ, Kornprat P, Lindtner RA, et al. Tumor necrosis is a new promising prognostic factor in colorectal cancer. *Human pathology*. 2010;41(12):1749-1757.
19. Kepp O, Galluzzi L, Lipinski M, Yuan J, Kroemer G. Cell death assays for drug discovery. *Nature reviews Drug discovery*. 2011;10(3):221-237.
20. Prinsen K, Jin L, Vunckx K, et al. Radiolabeling and preliminary biological evaluation of a (99m)Tc(CO)(3) labeled 3,3'-(benzylidene)-bis-(1H-indole-2-carbohydrazide) derivative as a potential SPECT tracer for in vivo visualization of necrosis. *Bioorganic & medicinal chemistry letters*. 2011;21(1):502-505.
21. Venkatramani R, Wang L, Malvar J, et al. Tumor necrosis predicts survival following neo-adjuvant chemotherapy for hepatoblastoma. *Pediatr Blood Cancer*. 2012;59(3):493-498.
22. Van Walleghe DM, Parseghian MH. Toxicity and biodistribution of an iodine-131-radiolabelled tumour necrosis-targeting antibody in non-tumour-bearing domestic felines. *Veterinary and comparative oncology*. 2006;4(1):9-20.
23. Richards CH, Roxburgh CS, Anderson JH, et al. Prognostic value of tumour necrosis and host inflammatory responses in colorectal cancer. *The British journal of surgery*. 2012;99(2):287-294.
24. Epstein AL, Chen FM, Taylor CR. A novel method for the detection of necrotic lesions in human cancers. *Cancer research*. 1988;48(20):5842-5848.
25. Jiang B, Wang J, Ni Y, Chen F. Necrosis avidity: a newly discovered feature of hypericin and its preclinical applications in necrosis imaging. *Theranostics*. 2013;3(9):667-676.
26. Xie B, Stammes MA, van Driel PB, et al. Necrosis avid near infrared fluorescent cyanines for imaging cell death and their use to monitor therapeutic efficacy in mouse tumor models. *Oncotarget*. 2015.
27. Verma N, Cowperthwaite MC, Burnett MG, Markey MK. Differentiating tumor recurrence from treatment necrosis: a review of neuro-oncologic imaging strategies. *Neuro-oncology*. 2013;15(5):515-534.
28. Murphy KP, O'Connor OJ, Maher MM. Updated imaging nomenclature for acute pancreatitis. *AJR American journal of roentgenology*. 2014;203(5):W464-469.
29. Carlsson M, Arheden H, Higgins CB, Saeed M. Magnetic resonance imaging as a potential gold standard for infarct quantification. *Journal of electrocardiology*. 2008;41(6):614-620.
30. Cona MM, de Witte P, Verbruggen A, Ni Y. An overview of translational (radio)pharmaceutical research related to certain oncological and non-oncological applications. *World journal of methodology*. 2013;3(4):45-64.
31. Ni Y. Abstract 1767: Oncocidia: a small molecule dual targeting pan-anticancer theragnostic strategy. abstract presented at Proceedings of the 105th Annual Meeting of the American Association for Cancer Research; 2014 Apr 5-9, 2014; San Diego, CA. Philadelphia (PA).
32. Cona MM, Li J, Feng Y, et al. Targetability and biodistribution of radioiodinated hypericin: comparison between microdosing and carrier-added preparations. *Anti-cancer agents in medicinal chemistry*. 2014;14(6):852-861.
33. Hdeib A, Sloan A. Targeted radioimmunotherapy: the role of (1)(3)(1)I-chTNT-1/B mAb (Cotara) for treatment of high-grade gliomas. *Future oncology*. 2012;8(6):659-669.
34. Pharmaceuticals P. Cotara Oncology. Accessed October 26, 2015.
35. Hritz J, Kascakova S, Ulicny J, Miskovsky P. Influence of structure of human, rat, and bovine serum albumins on binding properties of photoactive drug hypericin. *Biopolymers*. 2002;67(4-5):251-254.
36. Solar P, Cavarga I, Hofmanova J, et al. Effect of acetazolamide on hypericin photocytotoxicity. *Planta medica*. 2002;68(7):658-660.

37. Wang H, Cao C, Li B, et al. Immunogenicity of Iodine 131 chimeric tumor necrosis therapy monoclonal antibody in advanced lung cancer patients. *Cancer immunology, immunotherapy : CII*. 2008;57(5):677-684.
38. Stammes MA, Knol-Blanckevoort VT, Cruz LJ, et al. Pre-clinical Evaluation of a Cyanine-Based SPECT Probe for Multimodal Tumor Necrosis Imaging. *Molecular imaging and biology : MIB : the official publication of the Academy of Molecular Imaging*. 2016.
39. Delaney G, Jacob S, Featherstone C, Barton M. The role of radiotherapy in cancer treatment. *Cancer*. 2005;104(6):1129-1137.
40. Smith AM, Mancini MC, Nie S. Second window for in vivo imaging. *Nature nanotechnology*. 2009;4(11):710-711.
41. Brom M, Joosten L, Oyen WJ, Gotthardt M, Boerman OC. Improved labelling of DTPA- and DOTA-conjugated peptides and antibodies with ¹¹¹In in HEPES and MES buffer. *EJNMMI research*. 2012;2:4.
42. Corish P, Tyler-Smith C. Attenuation of green fluorescent protein half-life in mammalian cells. *Protein Engineering*. 1999;12(12):1035-1040.
43. Stewart JMP, Lindsay PE, Jaffray DA. Two-dimensional inverse planning and delivery with a preclinical image guided microirradiator. *Medical Physics*. 2013;40(10):101709.
44. de Torres C, Munell F, Ferrer I, Reventós J, Macaya A. Identification of necrotic cell death by the TUNEL assay in the hypoxic-ischemic neonatal rat brain. *Neuroscience Letters*. 1997;230(1):1-4.
45. Loo DT. In Situ Detection of Apoptosis by the TUNEL Assay: An Overview of Techniques. In: Didenko VV, ed. *DNA Damage Detection In Situ, Ex Vivo, and In Vivo: Methods and Protocols*. Totowa, NJ: Humana Press; 2011:3-13.
46. Nounou MI, ElAmrawy F, Ahmed N, Abdelraouf K, Goda S, Syed-Sha-Qhattal H. Breast Cancer: Conventional Diagnosis and Treatment Modalities and Recent Patents and Technologies. *Breast Cancer : Basic and Clinical Research*. 2015;9(Suppl 2):17-34.
47. Lee E, Takita C, Wright JL, et al. Characterization of risk factors for adjuvant radiotherapy-associated pain in a tri-racial/ethnic breast cancer population. *Pain*. 2016;157(5):1122-1131.
48. Kyrgias G, Zygogianni A, Theodorou K, et al. Accelerated Hypofractionated Whole-Breast Irradiation With Concomitant Daily Boost in Early Breast Cancer. *American Journal of Clinical Oncology*. 2015;38(4):358-363.
49. Zygogianni A, Kouloulis V, Antypas C, Armpilia C, Kyrgias G, Kouvaris J. The Impact of Intermediate Time between Chemotherapy and Hypofractionated Radiotherapy to the Radiation Induced Skin Toxicity for Breast Adjuvant Treatment. *The Breast Journal*. 2014;20(1):74-78.
50. Williams JR, Zhang Y, Zhou H, et al. A quantitative overview of radiosensitivity of human tumor cells across histological type and TP53 status. *International Journal of Radiation Biology*. 2008;84(4):253-264.
51. Joiner M, van der Kogel A. *Basic Clinical Radiobiology*. Hodder Arnold.
52. Xie B, Stammes MA, van Driel PBAA, et al. Necrosis avid near infrared fluorescent cyanines for imaging cell death and their use to monitor therapeutic efficacy in mouse tumor models. *Oncotarget*. 2015;6(36):39036-39049.
53. Erdi YE. Limits of Tumor Detectability in Nuclear Medicine and PET. *Molecular Imaging and Radionuclide Therapy*. 2012;21(1):23-28.
54. Kim C, Erpelding TN, Jankovic L, Pashley MD, Wang LV. Deeply penetrating in vivo photoacoustic imaging using a clinical ultrasound array system. *Biomedical Optics Express*. 2010;1(1):278-284.
55. Yao J, Wang LV. Photoacoustic Microscopy. *Laser & photonics reviews*. 2013;7(5):10.1002/lpor.201200060.

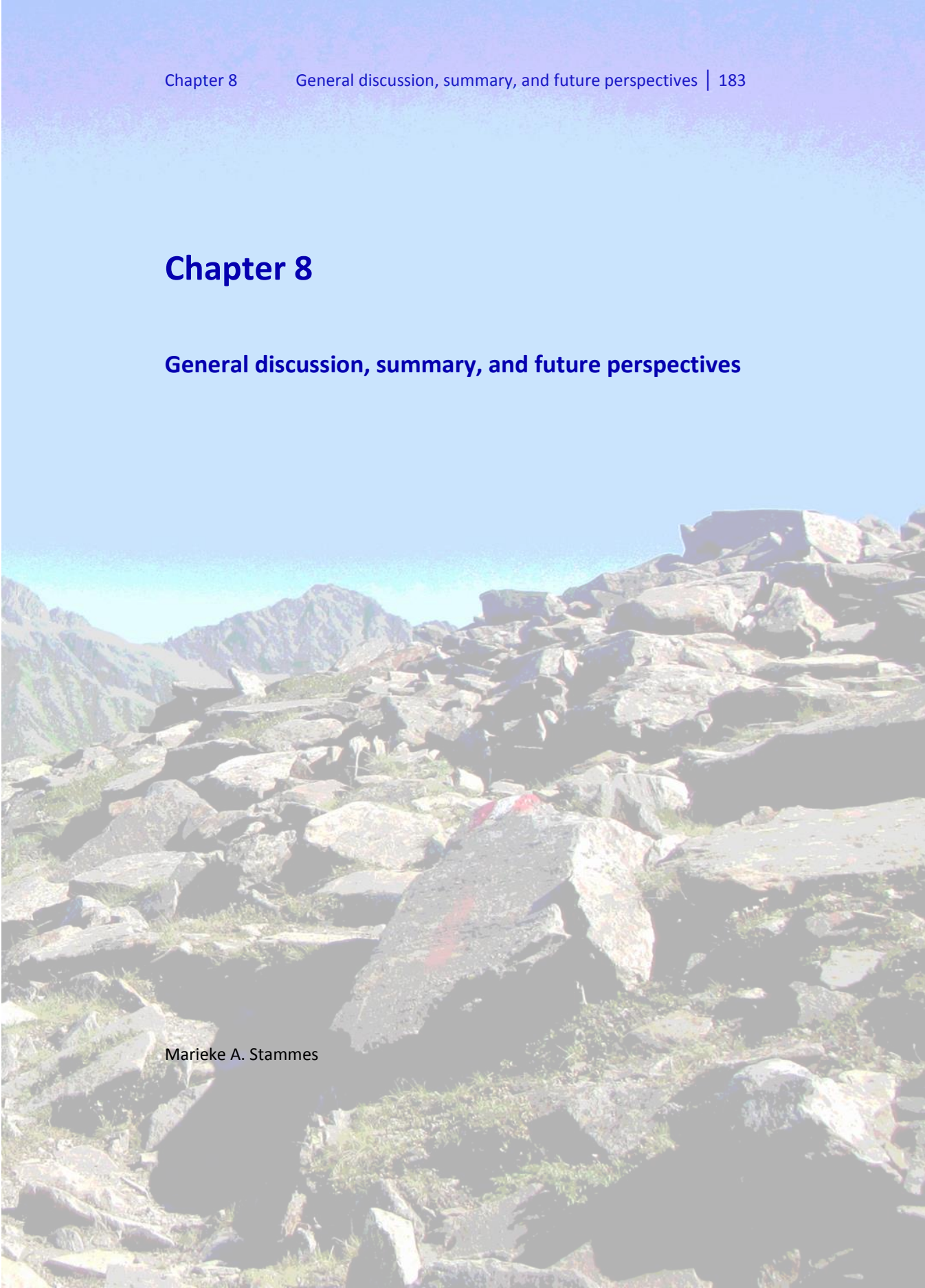
56. Beard P. Biomedical photoacoustic imaging. *Interface Focus*. 2011;1(4):602-631.
57. Raes F, Sobilo J, Le Mée M, et al. High Resolution Ultrasound and Photoacoustic Imaging of Orthotopic Lung Cancer in Mice: New Perspectives for Onco-Pharmacology. *PloS one*. 2016;11(4):e0153532.
58. Wang D, Wu Y, Xia J. Review on photoacoustic imaging of the brain using nanoprobes. *Neurophotonics*. 2016;3(1):010901-010901.
59. Yao J, Wang LV. Photoacoustic brain imaging: from microscopic to macroscopic scales. *Neurophotonics*. 2014;1(1):011003.
60. Luke GP, Nam SY, Emelianov SY. Optical wavelength selection for improved spectroscopic photoacoustic imaging. *Photoacoustics*. 2013;1(2):36-42.
61. Liu Y, Tseng Y-c, Huang L. Biodistribution Studies of Nanoparticles Using Fluorescence Imaging: A Qualitative or Quantitative Method? *Pharmaceutical research*. 2012;29(12):3273-3277.
62. Hawe A, Sutter M, Jiskoot W. Extrinsic Fluorescent Dyes as Tools for Protein Characterization. *Pharmaceutical research*. 2008;25(7):1487-1499.
63. Hellevik T, Martinez-Zubiaurre I. Radiotherapy and the Tumor Stroma: The Importance of Dose and Fractionation. *Frontiers in Oncology*. 2014;4:1.
64. Song CW, Cho LC, Yuan J, Dusenbery KE, Griffin RJ, Levitt SH. Radiobiology of Stereotactic Body Radiation Therapy/Stereotactic Radiosurgery and the Linear-Quadratic Model. *International Journal of Radiation Oncology*Biography*Physics*. 2013;87(1):18-19.



Chapter 8

General discussion, summary, and future perspectives

Marieke A. Stammes



This thesis consists of two parts addressing novel imaging technologies to improve the treatment of cancer patients. In part I, the additional value of real time image guidance during surgery is discussed and the research described in this part of the thesis showed that imaging performed during surgery can be of great value. Nevertheless, the success rate is highly dependent on the choice of imaging modality and biomarker to be targeted. In part II, a necrosis avid probe was successfully evaluated as novel method for early neoadjuvant treatment response monitoring.

Part I: Image-guided Surgery

For patients with a solid tumor, extensive diagnostic procedures are performed before the start of treatment as baseline and to determine the cancer stage^{1,2}. However, during surgery, the tissue is deformed and margin assessment is only accessible by visual inspection and palpation³. In surgical oncology, clear demarcation of the tumor boundaries is of course essential. Nevertheless, the final conformation whether visual tumor resection indeed resulted in a complete tumor resection, can only be determined by final pathology assessment of which the results become available approximately one week after surgery³. The main advantage of using (molecular) image-guidance during surgery is to enhance the visualization during the surgical procedure and to provide direct feedback.

In **Chapter 2**, conventional imaging modalities and a variety of state-of-the-art image- and molecular guided surgery modalities are described and compared. The modalities are divided in four groups: conventional, fluorescence, radioactive, and endogenous reflectance. The majority of these techniques encountered a challenge, such as lack of functional information, limited penetration depth or the need for a specifically targeted contrast agent. Unfortunately, there is not a single modality which is able to cover all our clinical needs. Therefore, it is necessary to combine imaging modalities to obtain the best surgical outcome.

Creating sufficient tumor-to-background contrast is one of the main challenges for advanced imaging. In general, imaging contrast is based on endogenous tissue contrast which is not sufficient to detect microscopic involvement of the tumor. The amount of contrast generated in an image can be increased with the use of an exogenous contrast agent. Non-specific exogenous contrast agents, such as gadolinium for MRI or iodine for CT, are

widely available, however, only specifically increase the visibility of the vasculature. As these contrast agents are not tumor-specific, they are only helpful to a certain extent⁴⁻⁷. Therefore, there is a need for targeted exogenous contrast agents, which are more specific for imaging of cancer. Nevertheless, the difficulty will be to characterize an appropriate target which is suitable for a defined group of cancer patients⁸.

In general, every specifically activated, expressed or upregulated marker on the surface of a tumor could serve as a target for image guided surgery (IGS)^{4,9}. Many markers are in different phases of clinical development, of which several show positive results in preclinical investigations. However, the next step, the actual translation from bench to bedside is demanding. Therefore, most probes are not able to pass the early stages of clinical translation, often due to lack of efficacy by detecting a high rate of unspecific binding^{7,10-12}.

In **Chapter 3** the molecular expression of a target was determined in a human tissue microarray (TMA) to determine whether this would be an interesting target for IGS or not. Using this approach, EphB4, a tyrosine kinase receptor binding the transmembrane ephrin-B2, was identified which is overexpressed in the majority of colorectal cancer patients. Eph receptors and their ephrin ligands play an essential role in cell communication and EphB4 upregulation is associated with cancer progression¹³. To (semi-)quantify the expression of EphA2 and EphB4 in tumor tissue, compared to the expression in adjacent healthy tissue, a normal-to-tumor scorings diagram was developed. This shows that both EphA2 and EphB4 were overexpressed in the majority of colorectal cancer patients. Only EphB4, demonstrated a clear difference between tumor and normal adjacent tissue. Although EphA2 is currently on the prioritization list of the national cancer institute (NCI) to be used as cancer vaccine target, it turned out to be an unsuitable target for the determination of tumor boundaries during surgery⁹.

To overcome the drawback of low specificity rates, it is essential that there is a clear difference between expression of the marker in the tumor, as visualized in the scorings diagram, compared to adjacent healthy tissue which will lead to a difference in uptake of the imaging agent. In general, during surgical procedures, a tumor-to-background ratio (TBR) of around 2 is determined as acceptable to provide sufficient diagnostic accuracy¹⁴.

The main aim of **Chapter 4** was to determine whether a combination of pre-operative multispectral optoacoustic tomography (MSOT) and fluorescence guided surgery (FGS) would be able to overcome the drawbacks of limited depth penetration of FGS. This combination provided detailed visualization of an integrin targeting near infrared fluorescent (NIRF) contrast agent, which resulted in a complete and specific overview, both before and during surgery, of the distribution and localization of a pancreatic ductal adenocarcinoma (PDAC) in an orthotopic mouse model. Overall, this chapter clearly showed the additional value of 3D imaging over 2D imaging, independent of the technique used, and showed that MSOT might be a suitable addition or alternative for FGS to improve visualization at a penetration depth over 1 cm.

Part I of this thesis addressed the advantages of IGS. There are, however, also some drawbacks. The disadvantages are related to the use of certain imaging modalities during surgery. The use of a nuclear imaging modality, for instance PET and SPECT, requires the use of radioactivity or, when using tracers with a short half-life, the availability of an on-site cyclotron facility¹⁵. Also, the magnetic field associated with the use of an MRI requires additional safety and logistic planning requirements, which makes these techniques less attractive and expensive to be used during surgery¹⁶.

Part II: Necrosis Imaging

Cell death is a universal process in the human body and tumor cell death is in general an effect of anti-cancer treatment, which is necessary to cure cancer patients¹⁷. Cell death is related to the cancer hallmark “resisting cell death” which makes visualizing the amount of cell death via a molecular pathway an interesting concept instead of focusing on morphology¹⁸. In general, morphological imaging is suitable when the tumor is clearly responding (e.g. shows a reduction in tumor size). However, when this is not the case, anatomical imaging modalities have limited value in differentiating tumor progression from pseudo-progression, which some neoadjuvant therapies can initiate^{19,20}. Patients are, in general, only selected to undergo (organ preserving) surgery, after neoadjuvant therapy, when the tumor is responding. When the surgeon is not able to distinguish non-responders from responders it is impossible to select the appropriate patients for surgery²¹.

In the second part of this thesis the hypothesis is being explored that an increase in tumor cell death is a sign that a patient does respond to neoadjuvant therapy. Nevertheless, it is also possible that due to the therapy, the biological systems around a tumor are activated to release tumor promoting factors instead of suppressive by which the tumor can grow even faster²². In fast growing tumors, angiogenesis cannot keep up with the size of the tumor which will also create an increase in cell death in the core of the tumor. Next to this, it is highly likely that the cell death which occurs after cancer treatment is a combination of several types of cell death and is not solely based on a form of apoptosis or necrosis^{23,24}.

Imaging cell death

Imaging of cell death nowadays can roughly be divided into apoptotic imaging and necrosis imaging. Apoptosis is a controlled type of cell death, visualizing apoptosis is based on targeting a marker in the apoptotic pathway. Caspases are potential targets nonetheless often difficult to reach as they reside inside the cell²⁵. The most well-known apoptosis targeting agent is Annexin V, which selectively binds, with a high affinity, to Phosphatidylserine (PS). Annexin V, labeled with Technetium-99m, was used in clinical trials, though facing some drawbacks. Suboptimal biodistribution patterns have been found with a high background uptake in the abdomen. Another disadvantage is that PS as target is only available for a limited amount of time in the process of apoptosis. An alternative target is phosphatidylethanolamine (PE) targeted via duramycin. The major advantage of PE over PS is the higher availability of PE on the cell membrane. Duramycin as probe is stable with a high binding affinity and specificity, radiolabeled with Technetium-99m makes it a promising probe, currently available for preclinical studies^{25,26}. Although apoptosis imaging will probably be able to reflect treatment response as the amount of apoptosis is relative high, it is not tumor specific as it targets a process which also is required to occur in a healthy multicellular environment to maintain homeostasis¹⁷. Therefore, the accuracy to identify tumors with a marginal treatment response might be limited.

Necrosis imaging is also not tumor specific. The chance of coexistence of a simultaneously ongoing pathological process of cell death in the neighborhood of the tumor is quite unlikely. This makes necrosis an interesting target for tumor treatment response evaluation. Probes targeting necrosis can be

divided in three groups: porphyrins, antibodies and dianthrone. The first group consists of gadolinium-diethylenetriaminepentaacetic acid (Gd-DTPA) derivatives which accumulate in nonviable tissue. Unfortunately, porphyrins are hampered for clinical use mostly due to their phototoxicity, limited effectiveness and difficult synthesizing procedure²⁷⁻²⁹. Antibodies, the second group, are in general more specific. One of the antibodies, Cotara, is directed against the DNA histone complex which is present in dead and dying cells in the center of solid tumors^{30,31}. Another antibody, Myoscint, targets the intracellular heavy chain of myosin. In general, the clinical translation of antibodies is challenging due to several reasons including their size which results in a limited tissue penetration due to disturbed architecture of the vasculature³².

The last groups are dianthrone, Hypericin, is a natural occurring photosensitizer, proved to be a potent agent for photodynamic therapy in cancer treatment and also shows necrosis avidity. Hypericin and its derivatives Sennidin A and Sennoside b are labeled with Iodine for both diagnostics and therapeutic approaches. The main drawback of these agents is that they are phototoxic and difficult to dissolve^{25,33-35}.

The carboxylated cyanine dyes tested in this thesis do not suffer from the drawbacks of the above-mentioned agents, as they are non-toxic small molecules which are easy to dissolve.

Therapeutic cell death

The most prominent process of cell death, initiated by chemotherapy and radiotherapy, was investigated to prove the value of our necrosis avid contrast agent. Chemotherapy and radiotherapy were chosen as they are the two most frequently used approaches of neoadjuvant therapy^{36,37}.

Chemotherapy induces alterations in Adenosine Triphosphate (ATP) levels, which is distinctive for dying cells: ATP decreases intracellularly and increases extracellularly. The level of decrease intracellularly will determine the switch between apoptotic or necrotic cell death. When cell death progresses and the membrane potential is completely disrupted, the intracellular ATP level is further decreased, finally leading to secondary necrosis. Based on this knowledge, apoptosis is the initial form of cell death after treatment with a chemotherapeutic agent, followed by (secondary) necrosis^{17,38}. However, some chemotherapeutic agents, such as cyclophosphamide, induces type I immunogenic cell death (ICD). Cyclophosphamide is used in the experiments

in **Chapter 5 & 6**, in an immunodeficient mouse model. ICD is a form of cell death which is closely related to the secretion and release of damage-associated molecular patterns (DAMPs)^{39,40}. This means that molecules inside the cell, which under normal circumstances are not associated with immunological functions, will be released, secreted or exposed on the cell surface of damaged or dying cells. In this way, they trigger an immune response in the absence of infection and they stimulate immunogenicity through endoplasmatic reticulum stress related effects⁴⁰. Extracellular ATP is seen as DAMP and as mentioned above the amount of extracellular ATP determines the cell death pathway³⁹.

Radiotherapy eliminate cancer cells by the use of ionizing radiation⁴¹. Ionizing radiation creates DNA damage which will have a direct and indirect effect on cells both leading to cell death. Irradiation with a high dose per fraction (>10 Gy) will cause, in general, more direct DNA double strand breaks and will result in lethal damage in a higher number of cells, as compared with irradiation using a lower fraction dose (<10 Gy). Nevertheless, this is compensated with fractionation which will cause a similar linear decrease in the number of surviving cells at the end of the treatment^{37,42,43}. In addition, fractions above 10 Gy will also cause severe vascular damage, leading to indirect cell death⁴². Vascular damage causes a reduction in blood perfusion and has a negative influence on the oxygenation status, severe ischemia will lead to necrotic cell death^{17,44}.

The results described in **Chapter 5** shows that the two identified NIRF carboxylated cyanine dyes, HQ5 and IRDye800CW, possess strong necrosis avidity. The exact molecular targeting mechanism is not clear; however, it involves avidity for probably a mixture of cytoplasmic proteins available after loss of cell membrane integrity.

In preclinical research, the advantages of using optical modalities over radionuclide imaging are clear as they require less safety requirements, are cheap and fast. The downside of limited tissue penetration and lack of quantification is relatively small in early stages of research. Research closer to clinical translation needs quantitative pharmacokinetic and distribution profiles which are demanding to provide with optical imaging only. In addition, the limited penetration depth of only 1 cm makes the technique not feasible for quantitative pharmacokinetic studies in humans.

To enable quantification and a possible clinical translation, in **Chapter 6** one of the members of the family of HQ5 cyanine dyes, HQ4, was conjugated with Indium-111 as radiolabel via the chelate DTPA. This chapter illustrates that also after radiolabeling the necrosis avidity was still intact and could be visualized both with the fluorescence- and the radiolabel. Moreover, due to radiolabeling, the specificity of the probe *in vivo* could be demonstrated. It was shown that the uptake was not solely due to the enhanced permeability and retention (EPR) effect. Latter could be caused by the positive charge of the HQ-compound, conceivably leading to binding to albumin. By comparing the radiolabel alone with radiolabeled HQ4, a significant difference in tumor uptake could be measured.

In **Chapter 7** another imaging modality, optoacoustic tomography, was validated. In this chapter, the performance of the probe was confirmed as a truly multimodal contrast agent for both superficial and deeply situated tumor imaging. Based on the obtained results, the necrosis avid contrast agent, HQ4, has the potential to be clinically translated for multiple purposes. One of those purposes is the evaluation of treatment (chemotherapy and or radiotherapy) response, which was already successfully tested in **Chapter 6**, by monitoring chemotherapy response, at clinically relevant dose levels. **Chapter 7** further elucidates its use in monitoring radiotherapy induced tumor cell death. Nowadays, measuring treatment response is mostly performed with ^{18}F -fluorodeoxyglucose (FDG), the most widely available PET-tracer⁴⁵. In several tumor types, FDG-PET showed a high predictive value to assess tumor response early after start of treatment. The disadvantage of FDG is that it is taken up by cells with an increased glucose metabolism. Macrophages, often involved in the removal of necrotic tumor cells, also accumulate FDG. In addition, it is challenging, during radiotherapy, to discriminate between FDG uptake in tumor cells or radiation-induced inflammation, inducing an underestimation of the treatment response. Nevertheless, it is already proved for both lung and rectal cancer patients treated with chemoradiotherapy that the alteration in glycolysis level or standard uptake value during therapy was predictive for progression-free survival. In addition, scans obtained 3 months post-treatment showed a clear positive correlation between FDG uptake and patient outcome^{25,46-50}. Another promising PET-tracer is ^{18}F -fluorothymidine (FLT) which detects cell proliferation; the uptake is positively correlated with cell growth. It has been found that, in preclinical research, FLT is superior to FDG and that it is a sensitive and early predictor of therapy response in various

cancer types⁵¹. In clinical practice, however, it is found that the sensitivity of FLT is lower compared to FDG and that a decrease in uptake during therapy is not associated with a longer overall survival which makes it less suitable to use for treatment evaluation and adaptive therapies⁴⁸. As mentioned above, there are a couple of other promising agents in several stages of clinical development which can also be used for the same purpose. Unfortunately, it is not possible to compare these probes with the results obtained with HQ4 (Chapter 6 & 7), since each of the probes visualizes another biological process. Necrosis is the only process which is in general not present in healthy tissue though also not solely linked to cancer.

For longitudinal monitoring of treatment responses most probes could be used as an increased cell metabolism, cell proliferation, apoptosis and necrosis are all taking place in the tumor environment. However, the use of HQ4 is in this form the least favorable, as it is coupled to the SPECT isotope Indium-111, which has a long half-life. SPECT has a lower intrinsic resolution and sensitivity as compared to PET. An isotope with a longer half-life, however, is necessary as it takes about 24h before HQ4 reaches its most optimal TBR. Indium-111 could be replaced by a PET isotope like Zirconium-89 to be able to image it with PET. However, DTPA is not the most optimal chelate to incorporate Zirconium-89, desferrioxamine (DFO) is a better alternative⁵². Nonetheless, HQ4 can be a suitable theranostic agent, since instead of Indium-111, also Yttrium-90 or Lutetium-177 can be incorporated.

Future Perspectives

Combining targets

Over the last years a lot of anticancer drugs have been developed. Unfortunately, only a small percentage reached the clinical market. The same is true for targeted contrast agents. Due to a high level of tumor heterogeneity in human cancer it will be difficult to find one suitable, personalized target which will target the whole tumor. Instead of using one target it is probably more favorable to use a variety of targets combined in one targeted contrast agent. In this way, one could create the potential to target and visualize multiple receptors at the same time. The question which markers to combine is difficult to answer and depends on two main points. The first point is related to the tumor to be imaged. Suggestions would be to combine markers towards targets directed to one of the biological processes mentioned in the “hallmarks of cancer” instead of combining highly specific markers downstream the cascade^{18,53}. Additionally, literature already showed that targeting multiple pathways is more effective compared to targeting multiple targets of one pathway, especially when the tumor is trying to bypass a certain pathway, in case of multidrug resistance^{10,54}. This also accounts for the development of a broadly applicable targeted contrast agent. Final suggestion would be to combine markers which are known to be upregulated in different phases of the disease development to increase sensitivity. The second point to take into account when combining targets is the chemical construction and pharmacological behavior of such probes: its physicochemical character. This character can be partly predicted by the use of quantitative structure activity relations (QSAR) modelling. Nevertheless, in general, an increase in size and alteration in charge will influence the clearance and biodistribution of a probe⁵⁵⁻⁵⁷. In addition, some combinations of targeting moieties or imaging agents can interact with each other by which they could block their function or lose their specificity leading to unwanted high background signals⁵⁸.

Combining imaging modalities

As already concluded above there is not a single imaging modality which could be used for all purposes. Combining imaging modalities is an option to circumvent this problem. Unfortunately, the generation of hybrid imaging modalities is only feasible with a limited number of machines. Nevertheless, fusing of the images obtained is always an option. Combining analysis data of different modalities instead of analyzing each modality separately will create a

high-dimensional dataset. New methods to analyze such data sets are under development, like t-distributed stochastic neighbor embedding (t-SNE). T-SNE will give more detailed information and will hopefully reveal new relationships which could be used to stratify patients before they start with their cancer treatment or during neoadjuvant treatment⁵⁹. However, it will be demanding, if ever possible, to use this during IGS, where analyses and feedback need to be performed fast and real-time.

In **Chapter 4** MSOT is introduced to overcome the limited penetration depth of FGS. In this chapter, the preclinical MSOT machine is used, showing promising results, however, it is still limited by relatively long acquisition and reconstruction times. These long acquisition times are necessary due to the limited sensitivity as compared to fluorescence only imaging systems. Nowadays, clinical MSOT systems, used in combination with ICG, are available and the time to capture single cross-sectional images is reduced to less than 1 ms⁶⁰. In addition, the concentration of ICG for SLN detection in melanoma using either MSOT or fluorescence is relatively similar with a dose of 0.5 mg ICG injected around the tumor^{60,61}. Hopefully, newer generations of this imaging system will reach higher sensitivity, which is of importance to further increase the resolution, to reduce the dose of the contrast agent and/or to decrease image acquisition time. In addition, as it is impossible to chemically link a targeting agent to ICG, ICG will be replaced in the future for another fluorophore, such as IRDye800CW combined with a targeting agent, which will hopefully improve detection sensitivity even further. The future perspective would then be that MSOT could be used both for image guided surgery and for diagnostic imaging purposes, for instance for treatment monitoring of not only superficially located melanoma but also for deeper-located tumors. Nowadays, for instance, human breast cancer is already visualized via a label-free method, reaching imaging depths of up to 2.5 cm⁶². Nevertheless, reaching an imaging depth of over 5 cm, at least necessary for full clinical usage, will not be reached with this technique so far. However, when MSOT would become available as endoscopic tool, this penetration depth would be sufficient in for example rectal cancer Watch & Wait strategies.

The Watch & Wait strategy offers a lot of opportunities for patients with a complete clinical response after neoadjuvant therapy for rectal cancer and oesophageal cancer patients. When those patients could be identified before

surgery, unnecessary procedures and subsequent postoperative morbidity could be avoided. However, for those patients it is essential to keep them under a strict follow-up regimen to detect possible local recurrences in an early stage^{63,64}. During the follow-up period the use of personalised imaging with targeted contrast agents is obligatory. For Watch & Wait PET-CT for total body imaging could be used in combination with an endoscopic modality by either fluorescence or MSOT.

Combining therapy and diagnostics

Theranostics combines diagnostics and therapeutics to eliminate multi-step procedures and increase efficacy by using the diagnostic agent to visualize whether the proposed treatment will arrive at the tumor site^{65,66}. By using click chemistry this efficacy can be even further improved as click chemistry combines the beneficial targeting properties of, in general, antibodies to reach high TBRs, with the fast pharmacokinetics of small molecules for therapeutic agents^{67,68}. The method relies on a two-step approach in which in the first step an antibody, labeled with a click label, is injected. After a couple of days, when the antibody is accumulated in the tumor and cleared from the blood, the second part is injected consisting out of a radionuclide combined with the opposite site of the click label. As the radiolabel is relative small it will be cleared fast from the blood and does not accumulate in other parts than the tumor⁶⁷. Such an approach is investigated for radioimmunotherapy, however, can also be used for IGS in combination with radionuclide therapy^{67,68}. Administer a patient a couple of days before surgery with the first agent, now additionally labelled with a NIR fluorophore to use during surgery. Afterwards the second part is injected to treat possible tumor residues with targeted radionuclide therapy based on the same probe.

To finish, as the Chinese philosopher Lao Tzu quoted; *“the journey of a thousand miles begins with one step”*, which means in the context of the present thesis: *“to beat a high variety of cancer types, all knowledge gained is a little step forward in unraveling the behavior of cancer. Each tiny little step will help in the fight against cancer and I hope that this thesis provided such tiny step forward in the right direction!”*

References

1. Orucevic A, Chen J, McLoughlin JM, Heidel RE, Panella T, Bell J. Is the TNM staging system for breast cancer still relevant in the era of biomarkers and emerging personalized medicine for breast cancer - an institution's 10-year experience. *Breast J.* 2015;21(2):147-154.
2. Seevaratnam R, Cardoso R, McGregor C, et al. How useful is preoperative imaging for tumor, node, metastasis (TNM) staging of gastric cancer? A meta-analysis. *Gastric Cancer.* 2012;15 Suppl 1:S3-18.
3. Tipirneni KE, Warram JM, Moore LS, et al. Oncologic Procedures Amenable to Fluorescence-guided Surgery. *Ann Surg.* 2016.
4. Pierce MC, Javier DJ, Richards-Kortum R. Optical contrast agents and imaging systems for detection and diagnosis of cancer. *Int J Cancer.* 2008;123(9):1979-1990.
5. Zhou Z, Lu ZR. Gadolinium-based contrast agents for magnetic resonance cancer imaging. *Wiley Interdiscip Rev Nanomed Nanobiotechnol.* 2013;5(1):1-18.
6. Lusic H, Grinstaff MW. X-ray-computed tomography contrast agents. *Chem Rev.* 2013;113(3):1641-1666.
7. Wong FC, Kim EE. A review of molecular imaging studies reaching the clinical stage. *Eur J Radiol.* 2009;70(2):205-211.
8. Rosenthal EL, Warram JM, Bland KI, Zinn KR. The status of contemporary image-guided modalities in oncologic surgery. *Ann Surg.* 2015;261(1):46-55.
9. Cheever MA, Allison JP, Ferris AS, et al. The prioritization of cancer antigens: a national cancer institute pilot project for the acceleration of translational research. *Clin Cancer Res.* 2009;15(17):5323-5337.
10. Liu Z, Delavan B, Roberts R, Tong W. Lessons Learned from Two Decades of Anticancer Drugs. *Trends Pharmacol Sci.* 2017.
11. van Dam GM, Themelis G, Crane LM, et al. Intraoperative tumor-specific fluorescence imaging in ovarian cancer by folate receptor- α targeting: first in-human results. *Nature medicine.* 2011;17(10):1315-1319.
12. Harlaar NJ, Koller M, de Jongh SJ, et al. Molecular fluorescence-guided surgery of peritoneal carcinomatosis of colorectal origin: a single-centre feasibility study. *Lancet Gastroenterol Hepatol.* 2016;1(4):283-290.
13. Pasquale EB. Eph receptors and ephrins in cancer: bidirectional signalling and beyond. *Nat Rev Cancer.* 2010;10(3):165-180.
14. Elbayoumi T TV. Use of radiolabeled liposomes for tumor imaging. In: Bulte J, Modo MMJ, ed. *Nanoparticles in biomedical imaging: emerging technologies and applications*: Springer Science & Business Media; 2008.
15. Keereweer S, Kerrebijn JD, van Driel PB, et al. Optical image-guided surgery--where do we stand? *Molecular imaging and biology : MIB : the official publication of the Academy of Molecular Imaging.* 2011;13(2):199-207.
16. Buchfelder M, Schlaffer SM. Intraoperative magnetic resonance imaging during surgery for pituitary adenomas: pros and cons. *Endocrine.* 2012;42(3):483-495.
17. Hotchkiss RS, Strasser A, McDunn JE, Swanson PE. Cell death. *N Engl J Med.* 2009;361(16):1570-1583.

18. Hanahan D, Weinberg RA. Hallmarks of cancer: the next generation. *Cell*. 2011;144(5):646-674.
19. Wiggenraad R, Bos P, Verbeek-de Kanter A, et al. Pseudo-progression after stereotactic radiotherapy of brain metastases: lesion analysis using MRI cine-loops. *J Neurooncol*. 2014;119(2):437-443.
20. Agarwal A, Kumar S, Narang J, et al. Morphologic MRI features, diffusion tensor imaging and radiation dosimetric analysis to differentiate pseudo-progression from early tumor progression. *J Neurooncol*. 2013;112(3):413-420.
21. Tantiwongkosi B, Yu F, Kanard A, Miller FR. Role of (18)F-FDG PET/CT in pre and post treatment evaluation in head and neck carcinoma. *World J Radiol*. 2014;6(5):177-191.
22. Hagemann T, Balkwill F, Lawrence T. Inflammation and cancer: a double-edged sword. *Cancer cell*. 2007;12(4):300-301.
23. Galluzzi L, Vitale I, Abrams JM, et al. Molecular definitions of cell death subroutines: recommendations of the Nomenclature Committee on Cell Death 2012. *Cell death and differentiation*. 2012;19(1):107-120.
24. Kroemer G, Galluzzi L, Vandenabeele P, et al. Classification of cell death: recommendations of the Nomenclature Committee on Cell Death 2009. *Cell death and differentiation*. 2009;16(1):3-11.
25. De Saint-Hubert M, Prinsen K, Mortelmans L, Verbruggen A, Mottaghy FM. Molecular imaging of cell death. *Methods*. 2009;48(2):178-187.
26. Elvas F, Stroobants S, Wyffels L. Phosphatidylethanolamine targeting for cell death imaging in early treatment response evaluation and disease diagnosis. *Apoptosis : an international journal on programmed cell death*. 2017;22(8):971-987.
27. Ni Y, Cresens E, Adriaens P, et al. Exploring multifunctional features of necrosis avid contrast agents. *Academic radiology*. 2002;9 Suppl 2:S488-490.
28. Ni Y, Cresens E, Adriaens P, et al. Necrosis-avid contrast agents: introducing nonporphyrin species. *Academic radiology*. 2002;9 Suppl 1:S98-101.
29. Ni Y, Bormans G, Chen F, Verbruggen A, Marchal G. Necrosis avid contrast agents: functional similarity versus structural diversity. *Investigative radiology*. 2005;40(8):526-535.
30. Epstein AL, Chen FM, Taylor CR. A novel method for the detection of necrotic lesions in human cancers. *Cancer research*. 1988;48(20):5842-5848.
31. Hdeib A, Sloan A. Targeted radioimmunotherapy: the role of (1)(3)(1)I-chTNT-1/B mAb (Cotara) for treatment of high-grade gliomas. *Future oncology*. 2012;8(6):659-669.
32. Wang H, Cao C, Li B, et al. Immunogenicity of Iodine 131 chimeric tumor necrosis therapy monoclonal antibody in advanced lung cancer patients. *Cancer immunology, immunotherapy : CII*. 2008;57(5):677-684.
33. Jiang B, Wang J, Ni Y, Chen F. Necrosis avidity: a newly discovered feature of hypericin and its preclinical applications in necrosis imaging. *Theranostics*. 2013;3(9):667-676.
34. Van de Putte M, Marysael T, Fonge H, et al. Radiolabeled iodohypericin as tumor necrosis avid tracer: diagnostic and therapeutic potential. *International journal of cancer Journal international du cancer*. 2012;131(2):E129-137.

35. Van de Putte M, Ni Y, De Witte PA. Exploration of the mechanism underlying the tumor necrosis avidity of hypericin. *Oncology reports*. 2008;19(4):921-926.
36. Padma VV. An overview of targeted cancer therapy. *Biomedicine (Taipei)*. 2015;5(4):19.
37. Baskar R, Lee KA, Yeo R, Yeoh KW. Cancer and radiation therapy: current advances and future directions. *Int J Med Sci*. 2012;9(3):193-199.
38. Martins I, Tesniere A, Kepp O, et al. Chemotherapy induces ATP release from tumor cells. *Cell cycle*. 2009;8(22):3723-3728.
39. Krysko O, Love Aaes T, Bachert C, Vandenabeele P, Krysko DV. Many faces of DAMPs in cancer therapy. *Cell death & disease*. 2013;4:e631.
40. Garg AD, Krysko DV, Verfaillie T, et al. A novel pathway combining calreticulin exposure and ATP secretion in immunogenic cancer cell death. *The EMBO journal*. 2012;31(5):1062-1079.
41. Aureli M, Murdica V, Loberto N, et al. Exploring the link between ceramide and ionizing radiation. *Glycoconjugate journal*. 2014;31(6-7):449-459.
42. Song CW, Park I, Cho LC, et al. Is indirect cell death involved in response of tumors to stereotactic radiosurgery and stereotactic body radiation therapy? *International journal of radiation oncology, biology, physics*. 2014;89(4):924-925.
43. *Basic Clinical Radiobiology*. Vol 4. London, Great Britain: Hodder Arnold; 2009.
44. Park HJ, Griffin RJ, Hui S, Levitt SH, Song CW. Radiation-induced vascular damage in tumors: implications of vascular damage in ablative hypofractionated radiotherapy (SBRT and SRS). *Radiat Res*. 2012;177(3):311-327.
45. Geus-Oei LF, Oyen WJ. Predictive and prognostic value of FDG-PET. *Cancer Imaging*. 2008;8:70-80.
46. Ferreira LM. Cancer metabolism: the Warburg effect today. *Exp Mol Pathol*. 2010;89(3):372-380.
47. Kaira K, Serizawa M, Koh Y, et al. Biological significance of 18F-FDG uptake on PET in patients with non-small-cell lung cancer. *Lung cancer*. 2014;83(2):197-204.
48. Everitt S, Ball D, Hicks RJ, et al. Prospective Study of Serial Imaging Comparing Fluorodeoxyglucose Positron Emission Tomography (PET) and Fluorothymidine PET During Radical Chemoradiation for Non-Small Cell Lung Cancer: Reduction of Detectable Proliferation Associated With Worse Survival. *International journal of radiation oncology, biology, physics*. 2017;99(4):947-955.
49. Usmanij EA, de Geus-Oei LF, Troost EG, et al. 18F-FDG PET early response evaluation of locally advanced non-small cell lung cancer treated with concomitant chemoradiotherapy. *Journal of nuclear medicine : official publication, Society of Nuclear Medicine*. 2013;54(9):1528-1534.
50. Koo PJ, Kim SJ, Chang S, Kwak JJ. Interim Fluorine-18 Fluorodeoxyglucose Positron Emission Tomography/Computed Tomography to Predict Pathologic Response to Preoperative Chemoradiotherapy and Prognosis in Patients With Locally Advanced Rectal Cancer. *Clin Colorectal Cancer*. 2016;15(4):e213-e219.

51. Mogensen MB, Loft A, Aznar M, et al. FLT-PET for early response evaluation of colorectal cancer patients with liver metastases: a prospective study. *EJNMMI Res.* 2017;7(1):56.
52. Deri MA, Zeglis BM, Francesconi LC, Lewis JS. PET imaging with (8)(9)Zr: from radiochemistry to the clinic. *Nucl Med Biol.* 2013;40(1):3-14.
53. Hanahan D, Weinberg RA. The hallmarks of cancer. *Cell.* 2000;100(1):57-70.
54. Ozben T. Mechanisms and strategies to overcome multiple drug resistance in cancer. *FEBS letters.* 2006;580(12):2903-2909.
55. Burke BP, Cawthorne C, Archibald SJ. Multimodal nanoparticle imaging agents: design and applications. *Philos Trans A Math Phys Eng Sci.* 2017;375(2107).
56. Horobin RW, Rashid-Doubell F. Predicting small molecule fluorescent probe localization in living cells using QSAR modeling. 2. Specifying probe, protocol and cell factors; selecting QSAR models; predicting entry and localization. *Biotech Histochem.* 2013;88(8):461-476.
57. Horobin RW, Rashid-Doubell F, Pediani JD, Milligan G. Predicting small molecule fluorescent probe localization in living cells using QSAR modeling. 1. Overview and models for probes of structure, properties and function in single cells. *Biotech Histochem.* 2013;88(8):440-460.
58. Zhang J, Li C, Zhang X, et al. In vivo tumor-targeted dual-modal fluorescence/CT imaging using a nanoprobe co-loaded with an aggregation-induced emission dye and gold nanoparticles. *Biomaterials.* 2015;42:103-111.
59. van der Maaten L, Hinton G. Visualizing Data using t-SNE. *J Mach Learn Res.* 2008;9:2579-2605.
60. Stoffels I, Morscher S, Helfrich I, et al. Metastatic status of sentinel lymph nodes in melanoma determined noninvasively with multispectral optoacoustic imaging. *Science translational medicine.* 2015;7(317):317ra199.
61. Goppner D, Nekwasil S, Jellestad A, Sachse A, Schonborn KH, Gollnick H. Indocyanine green-assisted sentinel lymph node biopsy in melanoma using the "FOVIS" system. *J Dtsch Dermatol Ges.* 2017;15(2):169-178.
62. Diot G, Metz S, Noske A, et al. Multi-Spectral Optoacoustic Tomography (MSOT) of human breast cancer. *Clinical cancer research : an official journal of the American Association for Cancer Research.* 2017.
63. Sao Juliao GP, Habr-Gama A, Vailati BB, Araujo SEA, Fernandez LM, Perez RO. New Strategies in Rectal Cancer. *Surg Clin North Am.* 2017;97(3):587-604.
64. Donohoe CL, Reynolds JV. Neoadjuvant treatment of locally advanced esophageal and junctional cancer: the evidence-base, current key questions and clinical trials. *J Thorac Dis.* 2017;9(Suppl 8):S697-S704.
65. Pene F, Courtine E, Cariou A, Mira JP. Toward theragnostics. *Critical care medicine.* 2009;37(1 Suppl):S50-58.
66. Srivastava SC. Paving the way to personalized medicine: production of some promising theragnostic radionuclides at Brookhaven National Laboratory. *Semin Nucl Med.* 2012;42(3):151-163.
67. Lappchen T, Rossin R, van Mourik TR, et al. DOTA-tetrazine probes with modified linkers for tumor pretargeting. *Nucl Med Biol.* 2017;55:19-26.
68. Rossin R, van Duijnhoven SM, Lappchen T, van den Bosch SM, Robillard MS. Trans-cyclooctene tag with improved properties for tumor pretargeting with the diels-alder reaction. *Molecular pharmaceuticals.* 2014;11(9):3090-3096.

Appendices

Nederlandse Samenvatting

List of Abbreviations

Curriculum Vitae

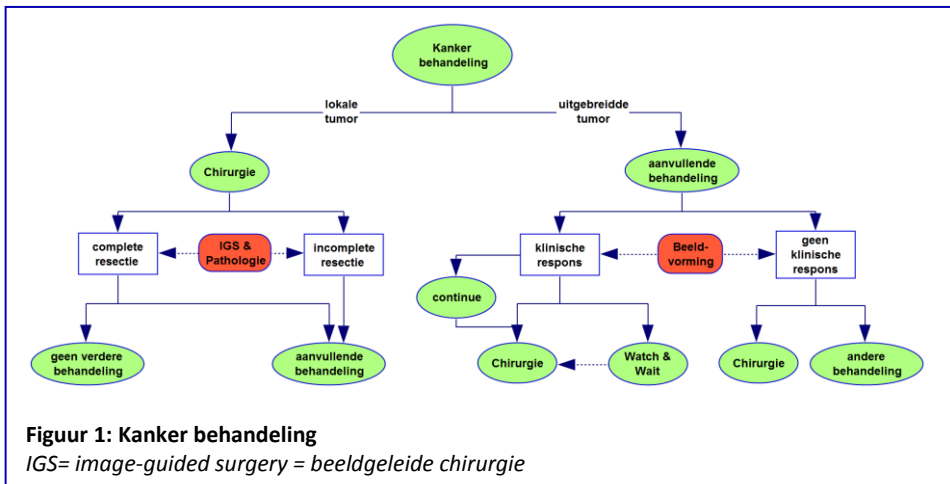
List of Publications & Conference Abstracts

Dankwoord

Marieke A. Stammes

Nederlandse Samenvatting

Op dit moment is kanker één van de belangrijkste doodsoorzaken in de wereld met circa 14 miljoen nieuw gediagnosticeerde gevallen in 2012 en rond de 20 miljoen in 2025. Dit betekent dat het risico dat iemand kanker krijgt nu al op 18.5% ligt en alleen nog maar verder gaat stijgen. Het doel van het onderzoek uitgevoerd in dit proefschrift is dan ook om een bijdrage te leveren aan zowel de diagnostiek als behandeling van kankerpatiënten. De meest gebruikte behandelingen voor kanker zijn: chirurgie, systemische therapie of radiotherapie. Vaak zal er voor een combinatie van deze behandelingen worden gekozen en wanneer mogelijk maakt chirurgie daar deel vanuit. Voor alle combinaties geldt dat het doel is om het kankergezwel in zijn geheel te verwijderen. Wanneer chirurgie in eerste instantie niet goed mogelijk is, dan is het soms mogelijk om eerst een andere behandeling te geven om de tumor te verkleinen. Indien dit succesvol blijkt, dan hoopt men in tweede instantie de tumor alsnog operatief te kunnen verwijderen (**Figuur 1**).



Tegenwoordig is één van de speerpunten in de behandeling van kankerpatiënten om deze meer patiënt- en doelgericht te maken. Op deze manier hopen we de nauwkeurigheid om kankercellen te vernietigen te verhogen en om daarnaast meer gezond weefsel te kunnen sparen. Er zijn meerdere manieren om dit aan te pakken en te verbeteren.

Dit proefschrift bestaat uit twee delen, in het eerste gedeelte wordt de mogelijke meerwaarde van beeldgeleide chirurgie besproken en bediscussieerd. Het onderzoek dat in dit gedeelte is uitgevoerd, toont aan dat beeldvorming van grote meerwaarde kan zijn tijdens de operatie. Het slagingspercentage hiervan is echter afhankelijk van de keuze van de beeldvormende modaliteit in combinatie met het target waartegen het contrastmiddel gericht is. In het tweede gedeelte van het proefschrift wordt een stof getest die necrose, onnatuurlijke celdood, aantoonst. In dit gedeelte wordt succesvol aangetoond dat deze stof gebruikt zou kunnen worden als biomarker voor een vroege evaluatie van de behandelrespons tijdens een kankerbehandeling.

Deel I: Beeldgeleide Chirurgie

Voor de start van een behandeling van een kankerpatiënt, met een solide tumor, worden er verschillende vormen van beeldvorming gedaan om een goed overzicht te krijgen van de conditie van de patiënt en voor de stadiëring van de tumor. Tijdens een operatie is het beeld echter veranderd doordat de anatomie van alle weefsels gewijzigd is. Het vaststellen van de rand van de tumor kan dan dus niet meer op basis van de voorafgaande beeldvorming adequaat gedaan worden maar moet gedaan worden door visuele inspectie en palpatie door de chirurg. Complete verwijdering van een tumor wordt dan bepaald op basis van palpabel en visueel afwezig tumorweefsel. De bevestiging of dit juist was wordt bepaald door histologische inspectie van het uitgenomen weefsel door de patholoog, echter de resultaten hiervan zijn ongeveer een week na de operatie bekend met alle consequenties van dien. Het grote voordeel van beeld- of moleculair geleide chirurgie is dat, door de toevoeging van deze nieuwe techniek, de chirurg een directe terugkoppeling krijgt over het weefsel wat hij uitgenomen heeft door een verbetering van het zicht.

Over het algemeen kan ieder element in een tumor dat specifiek geactiveerd, tot expressie gebracht of overgereguleerd wordt, dienen als doelwit voor beeldgeleide chirurgie. Op dit moment zijn een groot aantal van dit soort 'elementen' of biomarkers voor optische beeldvorming in verschillende fases van onderzoek, waarbij veelbelovende resultaten worden verkregen. Deze studies tonen aan dat de standaard chirurgische procedure niet negatief wordt beïnvloed door het gebruik van optische beeldvorming en dat de tumor

zonder vertraging “live” in beeld kan worden gebracht. De twee grootste problemen die gezien worden is het hoge aantal vals-positieve bevindingen en daarmee de overbehandeling van patiënten en de minimale penetratie diepte van optische beeldvorming. Voor de ontwikkeling van nieuwe beeldgeleide technieken zijn doelgerichte contrast middelen noodzakelijk die een hoge weefsel specificiteit hebben met daarbij een hoge tumor-achtergrond ratio voor een meer specifieke en gedetailleerde visualisatie van de tumor (**hoofdstuk 3**). Daarnaast is het zinvol om op zoek te gaan naar alternatieve beeldvormende modaliteiten of combinaties hiervan (**hoofdstuk 2 & 4**)

In **Hoofdstuk 2** worden tien verschillende innovatieve en beschikbare beeldvormende modaliteiten, die tijdens de operatie gebruikt zouden kunnen worden, met elkaar vergeleken vanuit een klinisch oogpunt. De conclusie die in dit hoofdstuk getrokken wordt, is dat geen enkele beeldvormende modaliteit op zichzelf in staat is om al het noodzakelijke weer te geven. Het gebruik van multimodale beeldvorming is vereist om op die manier de voordelen te laten prevaleren boven de nadelen. De betrouwbaarheid en beeldkwaliteit van de meeste van deze modaliteiten kan verbeterd worden door het gebruik van doelgerichte contrastmiddelen. Hierbij lijken specifieke “doelen”, die ruimschoots aanwezig zijn op het celoppervlak van tumorcellen en afwezig zijn bij gezonde cellen, de beste en meest kansrijke kandidaten voor beeldgeleide chirurgie.

In **Hoofdstuk 3** worden twee biomarkers; EphA2 en EphB4 met elkaar vergeleken. Beide worden tot over-expressie gebracht bij de meerderheid van patiënten met een colorectale tumor. Om de verschillen in expressie tussen tumor en nabijgelegen gezond weefsel in beeld te brengen werd een scoringsdiagram ontwikkeld. Dit gaf in één oogopslag weer dat hoewel beide biomarkers tot over expressie werden gebracht, alleen EphB4 een duidelijk verschil toonde in vergelijking met gezond weefsel.

In **Hoofdstuk 4** wordt de meerwaarde van multi-spectrale optoacoustische tomografie (MSOT) aangetoond. MSOT is vergelijkbaar aan optische fluorescente beeldvorming, alleen gebruikt MSOT licht als bron en geluid voor signaal detectie, waardoor de penetratie diepte groter is. Dit hoofdstuk toont de meerwaarde van 3D over 2D beeldvorming aan, onafhankelijk van de techniek die gebruikt wordt. Daarnaast wordt hard gemaakt dat een

combinatie van anatomische en functionele beeldvorming onontbeerlijk is voor het verkrijgen van een compleet overzicht van de tumor voor de operatie.

Deel II: Beeldvorming van Necrose

Celdood is een essentieel proces in het menselijke lichaam om in zijn geheel te kunnen overleven. Tumor celdood is meestal het effect van een kankerbehandeling en hoewel geïnduceerd van buiten het lichaam noodzakelijk om patiënten kanker te laten overleven. In dit gedeelte van het proefschrift doen we de aanname dat een verhoging van de hoeveelheid celdood in een tumor een teken is dat een patiënt reageert op de behandeling. Dit is een aanname, omdat het ook mogelijk is dat door de behandeling de biologische systemen rond een tumor geactiveerd worden en dat de tumor daardoor zelfs sneller gaat groeien. Ook dit proces zal celdood veroorzaken in de kern van de tumor, daar de bloedvaten niet zo snel mee kunnen groeien. Zowel respons op de behandeling als het sneller groeien van de tumor leidt tot celdood echter alleen een respons op de behandeling is een positief teken. De tweede aanname is dat necrose de belangrijkste vorm van celdood is, die plaatsvindt tijdens het behandelproces van kankerpatiënten. Deze aanname doen we omdat necrose geclassificeerd wordt als onnatuurlijk en veroorzaakt door directe onherstelbare schade aan de cel. Echter, volgens de internationale classificaties van celdood, zijn er 13 verschillende vormen van celdood te onderscheiden. Elke vorm heeft zijn eigen karakteristieken. Hoogstwaarschijnlijk vindt er dus een combinatie van verschillende vormen van celdood plaats na een behandeling.

In **Hoofdstuk 5** werd aangetoond dat de twee gecarboxyleerde cyanine kleurstoffen, HQ5 en IRDye800CW, een sterke aantrekkingskracht tot necrose hebben. Het exacte mechanisme waarmee ze binden op moleculair niveau is onduidelijk. We weten dat deze stoffen zich richten op cytoplasmatische eiwitten, die beschikbaar komen nadat de membraan integriteit verbroken is. Hiermee is de aanname uit bovenstaande alinea gerechtvaardigd, aangezien het eindpunt bij vele vormen van celdood het verlies van de membraan integriteit is.

Om deze stoffen in de toekomst klinisch bruikbaar te maken en om de hoeveelheid celdood te kunnen kwantificeren hebben we in **Hoofdstuk 6** één

van de leden van de HQ5 familie, HQ4, gekoppeld met een radioactief label. In dit hoofdstuk hebben we laten zien dat na deze koppeling er nog steeds binding aan necrose plaatsvindt en dat deze binding specifiek is. Hierdoor heeft HQ4 de potentie om gebruikt te gaan worden voor meerdere klinische toepassingen. Eén van de belangrijkste toepassingen is de evaluatie van behandelrespons. In **Hoofdstuk 6** laten we zien dat dit mogelijk is in met chemotherapie behandelde muizen, en in **Hoofdstuk 7**, door muizen te behandelen met radiotherapie.

Daarnaast testen we in **Hoofdstuk 7** ook een andere beeldvormende modaliteit, optoacoustische tomografie, voor de detectie van necrose met behulp van HQ4. In dit hoofdstuk is aangetoond dat HQ4 een multimodaal contrastmiddel is voor de beeldvorming van zowel oppervlakkig als dieper gelegen weefsels. De resultaten uit dit deel van het proefschrift laten zien dat contrastmiddelen gericht tegen necrose de potentie hebben om in de kliniek gebruikt te worden voor zowel diagnostische, prognostische als therapeutische doeleinden.

Toekomst Perspectief

Kort samengevat laten de onderzoeken in dit proefschrift zien dat er meerdere veelbelovende technieken in ontwikkeling zijn, die mogelijk van meerwaarde kunnen zijn bij beeldgeleide chirurgie en behandel evaluatie van kankerpatiënten. Dit proefschrift toont ook aan dat het noodzakelijk is om modaliteiten te combineren, om de behandeling van kankerpatiënten verder te kunnen verbeteren. In dit proefschrift werd gekozen voor een combinatie van beeldvormende technieken en biomarkers. Een andere mogelijkheid is het combineren van diagnostiek en therapie, theranostiek. Theranostiek kan een combinatie zijn van diagnostiek gevolgd door therapie waarbij de diagnostiek gebruikt wordt om te onderzoeken of de therapie aan gaat slaan. Daarnaast kan theranostiek ook therapie gevolgd door diagnostiek zijn om vroege behandel respons vast te leggen. De laatste mogelijkheid is dat diagnostiek en therapie tegelijkertijd worden uitgevoerd. Het doel van theranostiek is dat er gepersonaliseerde behandelingen gegeven worden. De juiste behandeling wordt dan aan de juiste patiënt gegeven. Het maakt de patiëntenzorg efficiënter en tevens (kosten) effectiever. Doordat patiënten minder belast

worden met onnodige bijwerkingen, zorgt dit tevens voor een verbetering van de kwaliteit van leven.

Ik zou willen afsluiten met een citaat van de Chinese filosoof Lao Tzu; *“een reis van duizend kilometer begint met één enkele stap”*. In de context van mijn proefschrift heeft dit voor mij de volgende betekenis: om een hoge variëteit aan kankersoorten te verslaan is iedere stap voorwaarts er één. Met elke stap kunnen we het gedrag van kanker en het complete biologische proces erachter iets verder ontrafelen, met als doel kanker in de toekomst nog beter te kunnen behandelen. Ik hoop dat dit proefschrift bijgedragen heeft met een kleine stap voorwaarts in de juiste richting!

List of Abbreviations

%ID/g	Percentage injected dose per gram
%ID/w	Percentage injected dose corrected for the weight
¹¹¹In-Cl₃	¹¹¹ indium-chloride
¹⁸F	¹⁸ fluor
2DG	2-Deoxyglucose
800CW	IRDye800CW
AI	Amphiphilicity index
5-ALA	5-aminolevulinic acid
ATM	Ataxia telangiectasia mutated
ATP	Adenosine triphosphate
AVF	Annexin V-FITC
BED	Biological effective dose
BF	Bright-field
BLI	Bioluminescent imaging
BSA	Bovine serum albumin
CA	Contrast agent
CBG99	Green click beetle luciferase
CBN	Conjugated bond number
CLI	Cherenkov luminescence imaging
cRGD	c[RGDyK], cyclo (Arginine- Glycine – Aspartic acid-Tyrosine- Lysine)
CT	Computed tomography
CTX	Cyclophosphamide
DAMP	Damage-associated molecular pattern
DNA	Deoxyribonucleic acid
DTPA	Diethylene triamine pentaacetic acid
EGF	Epidermal growth factor
EphA2	Erythropoietin-producing hepatocellular carcinoma receptor A2
EphB4	Erythropoietin-producing hepatocellular carcinoma receptor B4
EPR	Enhanced permeability and retention
ERC	European research council
ETO	Etoposide
FACS	Fluorescence-activated cell sorting
FDA	Food and Drug Administration
FDG	Fluorodeoxyglucose
FFPE	Formalin-fixed paraffin-embedded
FGD	Fluorescence-guided dissection
FGS	Fluorescence-guided surgery
FITC	Fluorescein isothiocyanate
FLI	Fluorescence imaging
FOV	Field of view
FP7	Seventh framework programme

FWHM	Full width half maximum
GA	Gambogic acid
GFP	Green fluorescent protein
GLUT	Glucose receptor-1
GMP	Good manufacturing practices
HIPEC	Hyperthermic intra-peritoneal chemotherapy
H&E	Hematoxylin and Eosin
H&N	Head and neck
H2020	Horizon 2020, funding programme
ICD	Immunogenic cell death
ICG	Indocyanine green
iCT	Intraoperative computed tomography
IGS	Image-guided surgery
IGOS	Image-guided oncologic surgery
IHC	immunohistochemistry
iMRI	Intraoperative magnetic resonance imaging
ioUS	Intraoperative ultrasound
logP	Log octanol-water partition coefficient, Lipophilicity
MALDI	Matrix assisted laser desorption/ionisation
MIP	Maximum intensity projection
MR	Magnetic resonance
MRI	Magnetic resonance imaging
mRNA	Messenger Ribonucleic Acid
MSCA	Marie Skłodowska-Curie actions
MSOT	Multispectral optoacoustic tomography
MTS	3-(4,5-dimethylthiazol-2-yl)-5-(3-carboxymethoxyphenyl)-2-(4-sulfophenyl)-2H-tetrazolium)
Mw	Molecular weight
N/T	Normal to tumor
NACA	Necrosis avid contrast agent
NCI	National Cancer Institute
NHS	N-Hydroxysuccinimide
NIH	National Institutes of Health
NIR (F)	Near- infrared fluorescence
NL	Not labeled
OA	Optoacoustic imaging
OCT (1)	Optical coherence tomography
OCT (2)	Optimum cutting temperature
OR	Operating room
OSEM	Ordered subset expectation maximization
PA	Photoacoustic
PBS	Phosphate-buffered saline
PCR	Polymerase chain reaction

PDAC	Pancreatic ductal adenocarcinoma
PDT (1)	Photodynamic therapy
PDT (2)	Population doubling time
PEG	Polyethylene glycol
PET	Positron emission tomography
PI	Propidium iodide
POSEM	Pixel-based ordered subset expectation maximization
PS	Phosphatidylserine
qPCR	Realtime PCR
QSAR	Quantitative Structure Activity Relations
R0 resection	Radical resection
R1 resection	Irradical resection
RA	Radioactivity
RECIST	Response Evaluation Criteria in Solid Tumors
REIMS	Rapid evaporative ionization mass spectrometry
REMARK	REporting recommendations for tumor MARKer prognostic studies
RIP-1	Receptor-Interacting Protein 1
ROI	Region of interest
ROS	Reactive oxygen species
RS	Raman spectroscopy
RT	Room temperature
RT	Radiation therapy
S/B	Signal-to-background
SDS-PAGE	Sodium dodecyl sulfate polyacrylamide gel electrophoresis
SEM	Standard error of the mean
SGC	Small gamma camera
SLN	Sentinel lymph node
SNR	Signal to noise ratio
SOP	Standard operating protocol
SPECT	Single-photon emission computed tomography
Sta	Staurosporine
SUV	Standard uptake value
TBR	Tumor to background ratio
TCO	Trans-Cyclooctene
TMA	Tissue microarray
TNM	Tumor node metastasis classification of malignant tumors
TNT	Tumor necrosis targeting
TOF	Time of flight
TUNEL	TdT-mediated dUTP Nick-end labelling
US	Ultrasound
Z	Electric charge
λ_{abs}	Absorbance wavelength
λ_{em}	Emission wavelength

Curriculum Vitae

Marieke Alice Stammes was born on January 25, 1986 in Alkmaar, the Netherlands. She graduated (VWO) from the Jac P Thijssen college in Castricum. In 2004, she started her bachelor study Medical Imaging and Radiation Technology (MBRT) at Inholland University of applied sciences in Haarlem. She followed a dual (work-study) program in which she worked at the Medical Centre of Alkmaar in Alkmaar on the department of Radiotherapy.

After obtaining her bachelor degree in 2008, Marieke continued with a premaster year at the Free University in Amsterdam before she could start in 2009 with the master Oncology that was also at the Free University in Amsterdam.

During her master study, she performed two internships. The first internship was performed at the Free University Medical Center in Amsterdam at the RadioNuclideCenter, under the main supervision of prof. dr. G.A.M.S. van Dongen. The title of the internship was: 'Development of antibody conjugates for photoimmunodetection'. The second internship was completed at Leiden University Medical Center at the departments of Anatomy and Embryology in combination with Radiology under the supervision of prof. dr. R.E. Poelmann and dr. L. van der Weerd. The title of this internship was; 'evaluation of different MR contrast agents for the detection of atherosclerotic plaques' and included a literature review addressing the problems to be faced in the transfer from 'bench to bedside' for MRI contrast agents. Marieke received her Master's degree in July 2011.

Until September 2012 Marieke combined her job as radiation technologist at the Free University Medical Center Amsterdam with a job as researcher at Leiden University Medical Center and Percuros. During this period she also joined the Venture Challenge organised by the Netherlands Genomics Initiative (NGI) with 'CancerVisuals'.

In October 2012, she started working fulltime on the PhD-project, which led to this thesis. From February 2015 on Marieke was also the project manager of a H2020 MSCA-RISE project called PRISAR.

Marieke started in March 2017 as Advanced Practitioner Pretreatment Imaging at the Radiotherapy department at Leiden University Medical Center. In her current job, Marieke is able to combine the knowledge she gained over the past 10 years.

List of Publications & Conference Abstracts

Publications

Inert coupling of IRDye800CW to monoclonal antibodies for clinical optical imaging of tumor targets.

Cohen R, [Stammes MA](#), de Roos IH, Stigter-van Walsum M, Visser GW, van Dongen GA. EJNMMI Res. 2011 Dec 1;1(1):31

uPAR-targeted multimodal tracer for pre- and intraoperative imaging in cancer surgery.

Boonstra MC*, van Driel PB*, van Willigen DM, [Stammes MA](#), Prevoo HA, Tummers QR, Mazar AP, Beekman FJ, Kuppen PJ, van de Velde CJ, Löwik CW, Frangioni JV, van Leeuwen FW, Sier CF, Vahrmeijer AL. Oncotarget. 2015 Jun 10;6(16):14260-73.

Necrosis avid near infrared fluorescent cyanines for imaging cell death and their use to monitor therapeutic efficacy in mouse tumor models

Xie B, [Stammes MA](#), van Driel PBAA, Cruz LJ, Knol-Blankevoort VT, Löwik MAM, Mezzanotte L, Que I, Chan A, van den Wijngaard JPHM, Siebes M, Gottschalk S, Razansky D, Ntziachristos V, Keereweer S, Horobin RW, Hoehn M, Kaijzel EL, van Beek ER, Snoeks TJA, Löwik CWGM. Oncotarget. 2015 Nov 17;6(36):39036-49.

Effect of PLGA NP Size on Efficiency to Target Traumatic Brain Injury Journal of Controlled Release

Cruz LJ, [Stammes MA](#), Que I, van Beek ER, Knol-Blankevoort VT, Snoeks TJA, Chan A, Kaijzel EL, Löwik CWGM. J Control Release. 2016 Feb 10;223:31-41.

EGFR targeted nanobody-photosensitizer conjugates for photodynamic therapy in pre-clinical head and neck cancer

van Driel PBAA*, Boonstra MC*, Slooter M, Heukers R, [Stammes MA](#), Snoeks TJA, de Bruijn HS, van Diest PJ, Vahrmeijer AL, van Bergen en Henegouwen PMP, van de Velde CJH, Löwik CWGM, Robinson DJ, Oliveira S. J Control Release. 2016 May 10;229:93-105.

Pre-clinical evaluation of a cyanine based SPECT probe for multimodal tumor necrosis imaging

[Stammes MA](#), Knol-Blankevoort VT, Cruz LJ, Feitsma HRIJ, Mezzanotte L, Cordfunke RA, Sinisi R, Dubikovskaya EA, Maeda A, DaCosta RS, Bierau K, Chan A, Kaijzel EL, Snoeks TJA, van Beek ER, Löwik CWGM. Mol Imaging Biol. 2016 Dec;18(6):905-915.

The Necrosis-Avid Small Molecule HQ4-DTPA as a Multimodal Imaging Agent for Monitoring Radiation Therapy-Induced Tumor Cell Death.

Stammes MA*, Maeda A*, Bu J, Scollard DA, Kulbatski I, Medeiros PJ, Sinisi R, Dubikovskaya EA, Snoeks TJA, van Beek ER, Chan A, Löwik CWGM and DaCosta RS. *Front Oncol.* 2016 Oct 21;6:221.

Traumatic Brain Injury: Preclinical imaging diagnostic(s) and therapeutic approaches

Kaijzel EL, van Beek ER, Stammes MA, Que I, Chan A, Löwik CWGM, Cruz LJ *Curr Pharm Des.* 2017;23(13):1909-1915.

Evaluation of EphA2 and EphB4 as targets for image-guided colorectal cancer surgery

Stammes MA, Prevoo HAJM, ter Horst MC, Groot SA, van de Velde CJH, Chan A, de Geus-Oei L-F, Kuppen PJK, Vahrmeijer AL, Pasquale EB, Sier CFM. *Int J Mol Sci.* 2017 Feb 3;18(2). pii: E307.

Preclinical uPAR-targeted multimodal imaging of locoregional oral cancer

Boonstra MC, van Driel PBAA, Keereweer S, Prevoo HAJM, Stammes MA, Baart VM, Löwik CWGM, Mazar AP, van de Velde CJH, Vahrmeijer AL, Sier CFM *Oral Oncol.* 2017 Mar;66:1-8.

Fluorescence- and multispectral optoacoustic imaging for an optimised detection of deeply located tumours in an orthotopic mouse model of pancreatic carcinoma

Napp J*, Stammes MA*, Claussen J, Prevoo HAJM, Sier CFM, Hoeben FJM, Robillard MS, Vahrmeijer AL, Devling T, Chan A, de Geus-Oei L-F, Alves F. *Int J Cancer* 2017 Dec; doi:10.1002/ijc.31236

Modalities for image- and molecular-guided cancer surgery

Stammes MA, Bugby SL, Porta T, Pierzchalski K, Devling T, Otto C, Dijkstra J, Vahrmeijer AL, de Geus-Oei L-F, Mieog JSD *Br J Surg.* 2018 Jan; 105(2):e69-e83.

* = shared authorship.

Conference Abstracts (presenting author)

- Small molecule HQ5 as a multimodal imaging agent for radiotherapy-induced tumor cell death.
ESTRO 2014, Vienna, Poster
- Necrosis avid near infrared fluorescent cyanines for imaging cell death and their use to monitor therapeutic efficacy in cancer.
EMIM 2015, Tübingen, Poster
- HQ4, a new necrosis avid cyanine utilized for multimodal imaging of chemotherapy and radiotherapy-induced tumor cell death.
EMIM 2015, Tübingen, Poster
- Necrosis avid near infrared fluorescent cyanines for the visualization of traumatic brain injury (TBI).
GlowBrain final conference 2015, Zagreb, Oral presentation
- Preclinical evaluation of a cyanine-based SPECT probe for multimodal tumor necrosis imaging.
MiLabs user meeting 2016, Utrecht, Oral presentation
- Two different approaches to treat tumor-positive resection margins using targeted radioactive imaging and fluorescence-guided surgery.
EANM 2016, Barcelona, Oral Presentation
- Molecular imaging of disseminated orthotopic pancreatic cancer using MSOT.
MSOT iThera usermeeting 2016, Londen, Oral presentation
- Image-guided fluorescence surgery directed by pre-operative 3D multispectral optoacoustic tomography (MSOT).
EMIM 2017, Cologne, Poster
- Imaging from Mice to Men.
EMIM 2017, Cologne, Oral presentation Science Slam (winner)

Dankwoord

Yes, de dag waarvan ik op een gegeven moment dacht, dat die nooit ging komen, is daar en ik mag dit dankwoord schrijven! Een berg beklimmen kost doorzettingsvermogen en datzelfde geldt voor promoveren. Daarnaast beklim je een berg nooit alleen, je hebt hulp en vooral mentale ondersteuning van de mensen om je heen nodig. Ook hiervoor geldt dat dit vergelijkbaar is met het doen van onderzoek en promoveren, er moeten nu eenmaal bergen werk verzet worden. Vaak wordt deze ondersteuning als normaal opgevat, alhoewel dat volstrekt niet vanzelfsprekend is. Dat ik figuurlijk de ene voet voor de andere ben blijven zetten, gestaag klimmend naar het einddoel toe, is te danken aan de mensen om me heen, mijn figuurlijke steenmannetjes, die me de weg hebben gewezen. Alleen had ik de top nooit gevonden. Over de jaren ben ik heel veel “steenmannetjes” tegengekomen, teveel om allemaal te kunnen bedanken in dit dankwoord. Tot enkelen van hen wil ik echter wel kort het woord richten.

Ten eerste wil ik Clemens en Alan bedanken voor de mogelijkheid om aan dit promotietraject te beginnen.

Lioe-Fee, ergens halverwege de rit ben je op mijn bergpad gekomen en ik ben je daar enorm dankbaar voor. Ik heb je meerdere malen gevraagd of je nog blij was dat ik op jouw pad ben verschenen, maar onder het motto; “we gaan dit gewoon samen aanpakken” hebben we de top gehaald.

Als ik de weg weer eens dreigde kwijt te raken of er een obstakel op de weg lag, dat ik niet zelf kon opruimen, kon ik altijd bij jullie langs: Alex, Boudewijn en Kees ontzettend bedankt voor jullie steun de afgelopen jaren!

Voor een bergbeklimming is niet alleen kracht maar ook techniek nodig. Wat betreft het onderzoek hebben Vicky, Marieke, Henny en Karien geprobeerd om hun laboratorium technieken gedeeltelijk op me over te brengen. Bedankt voor het altijd meedenken in oplossingen, in plaats van in problemen, zodat ik weer verder kon.

Annemieke en Marieke, wat fijn dat jullie me tijdens het laatste stukje van mijn bergbeklimming ondersteunen, hiervoor heb je mensen nodig die je volledig kunt vertrouwen. Dat kan ik zonder enige twijfel. Bedankt dat ik altijd bij jullie terecht kon en kan, tijdens mijn verdediging.

Mark en Hein, samen hebben we heel wat uurtjes op E0 doorgebracht. Ook al ben je daar nooit alleen vanwege onze kleine vriendjes, samen is het toch gezelliger en gaat het werk ook sneller. In dit kader wil ik ook Fred & Ben bedanken voor de goede zorgen voor mijn kleine vriendjes.

Pia, Judith and Jolijn, it was a pleasure guiding you with your first steps in a research environment. Besides, you gave me a fresh view on research and a lot of energy with your enthusiasm.

In the past years I have seen a lot of rooms, roommates and departments within and outside of the LUMC. Different people in different periods have contributed (in) directly to this thesis. Mention a couple of them would do others shortage so I keep it to: Bedankt, Thanks, Danke, Merci, Grazie, Gracias, Domo arigatou, Terima Kasih and Xièxie.

Next to the LUMC, I did spend some time abroad in both the Princess Margaret Cancer Center in Toronto and the University Medical Center Göttingen. Ralph and Azusa thanks for hosting me, doing all the experiments together and for taking care of me outside work hours. Frauke, Joanna, Anne and others thank you for your hospitality, I always felt very welcome when I was at your place.

In general, I want to thank all the partners from the H2020 MSCA-RISE PRISAR project. Working together with you inside this project has widened my scientific view in multiple directions. I really liked the interaction with all the different disciplines. I also want to thank all the co auteurs for the research we performed together, our cooperation yielded great publications.

Eline, Ellart, Gertjan, Ilse, Lianne, Lieke, Maartje, Wina en Yolanda bedankt voor jullie luisterend oor de afgelopen jaren, maar ook voor de gezelligheid en de momenten van ontspanning samen, vaak met een lekker hapje en/of drankje.

De meiden van de handbal wil ik ook bedanken dat ze me de kans gaven om mijn frustraties af te reageren op de bal. Hierbij hebben vooral de keepers het soms zwaar te verduren gehad. Sorry hiervoor, ik beloof vanaf nu beterschap!

Pap, Mam en Rick, bedankt voor jullie steun en dank dat jullie altijd achter me blijven staan. Soms konden jullie niet meer doen dan alleen luisteren maar nu kunnen jullie er ook naar kijken!

